UNIVERSITÀ DEGLI STUDI DI TRIESTE

UNIVERSITÀ DEGLI STUDI DI TRIESTE

XXXVIII CICLO DEL DOTTORATO DI RICERCA IN

Scienze Della Terra, Fluidodinamica e Matematica.
Interazioni e Metodiche

Reservoir Characterization and Monitoring for Subsurface Storage using Deep Learning Tools

Settore scientifico-disciplinare: **GEOS-04/B**

DOTTORANDO
Giovanni Pantaleo

COORDINATORE
Prof. Stefano Maset

SUPERVISORE DI TESI
Prof. Michele Pipan

CO-SUPERVISORE DI TESI
Prof. Emanuele Forte

ANNO ACCADEMICO 2024/2025

Reservoir Characterization and Monitoring for Subsurface Storage using Deep Learning Tools

Giovanni Pantaleo

XXXVIII cycle of PhD program in
Earth Science, Fluid Dynamics and Mathematics.
Interactions and Methods
Department of Mathematics, Informatics and Geosciences
University of Trieste
Trieste, Italy

October 2025

Supervisor Prof. Michele Pipan
Co-Supervisor Prof. Emanuele Forte

Contents

Abstract

The PhD thesis discusses the integration of data-driven approaches such as Deep Learning (DL) with physics-driven methods including Full-Waveform Inversion (FWI) and rock-physics modelling to advance geophysical monitoring for Carbon Capture and Storage (CCS) and Underground Hydrogen Storage (UHS). Motivated by the urgent need to reduce atmospheric carbon-dioxide (CO_2) and to enable safe subsurface storage technologies, this work emphasizes the advantages of DL in geophysics in improving interpretation accuracy, reducing subjectivity, and enabling cost-effective time-lapse surveys. We developed a data-driven workflow to map time-lapse seismic gathers directly to CO_2 saturation. A U-Net architecture enriched with multi-scale features via the Continuous Wavelet Transform (CWT) improves sensitivity to subtle and spatially variable plume signatures, providing more accurate fluid saturation estimates. A cost-effective monitoring strategy is then introduced based on pre-trained convolutional encoders arranged in a Siamese architecture to extract baseline versus monitor features. UMAP projects the high dimensional embeddings to a lower dimensional space, enhancing time lapse evolution tracking and supporting rapid anomaly screening and detection. This framework highlights baseline-monitor differences and reduces the need for dense data acquisition and manual screening. This approach is at first demonstrated on synthetic datasets, and then validated on a time-lapse Distributed Acoustic Sensing (DAS) seismic dataset from a controlled CO_2 injection at the Svelvik CO_2 Field Lab, Norway. As part of the PhD program, I led the SBEM (Svelvik Borehole Electromagnetic Monitoring) project in collaboration with SINTEF, during which both electromagnetic (GPR and ERT) and seismic (cross-well and VSP) data were acquired using hydrophones and Distributed Acoustic Sensing (DAS). This campaign provided the experimental dataset used for validating the proposed monitoring framework. The results demonstrated robust injected fluid detection at lower acquisition density and provided a real-world testbed for evaluating plume evolution. Furthermore, the thesis introduces a rock-physics-parametrized FWI that performs inversion directly for a petrophysical parameter, such as saturation, thereby mitigating the cross-talk typical of multi-parameter seismic inversions. This formulation, implemented through automatic differentiation, is applied to an underground gas storage scenario, showing improved recovery of saturation-related variations. Furthermore, frequency-dependent effects arising from patchy gas saturation are analysed, with emphasis on

wave-induced fluid flow and resulting dispersion/attenuation in the seismic band. The results demonstrate that intermediate gas saturations can maximize signal attenuation and must be incorporated into the inversion schemes to enhance feasibility studies for monitoring purposes. In summary, this PhD thesis highlights how DL and physics-driven methods can be integrated to handle complex time-lapse seismic datasets, extracting crucial subsurface information for CCS and UHS monitoring, thereby supporting safer and more scalable geophysical reservoir assessment and monitoring.

Extended Abstract

Climate change caused by greenhouse gas emissions is one of the most urgent challenges of this century. Global average temperatures continue to exceed historical thresholds, and international roadmaps emphasize the importance of rapid decarbonization to achieve the goal of net-zero emissions by mid-century (IPCC, 2023). Geosciences play a central role in this transition, enabling underground solutions that reduce emissions and support a flexible, low-carbon energy system. Carbon Capture and Storage (CCS) is considered essential in many mitigation pathways because it permanently stores CO_2 in deep geological formations (reservoirs) and addresses hard-to-abate industrial sources. Underground Hydrogen Storage (UHS) complements this effort by providing large-scale seasonal energy storage that mitigates wind and solar variability and stabilises renewable energy systems. In parallel, advances in high-performance computing and deep learning now enable the processing of massive datasets and the training of complex models at affordable costs. This convergence is the basis for the present work. Within CCS and UHS seismic monitoring, this thesis aims to propose methods for enhancing the detection of subtle subsurface changes while reducing operational effort by combining data-driven learning with physics-based methods.

This thesis advances geophysical monitoring for CCS and UHS by combining data-driven methods with physics-based methods. The work is motivated by two practical needs: first, to detect and quantify subsurface changes linked to injected fluids with higher sensitivity and lower interpretative bias; second, to make fluid monitoring cost-effective so that it can scale from pilots to industrial deployments. To meet these needs, the thesis develops four complementary contributions: 1. Data-driven CO_2 storage monitoring, a supervised data-driven workflow that maps time-lapse seismic gathers directly to CO_2 saturation maps; 2. Cost-effective early leakage detection, a DL framework that help in detect changes from time-lapse seismic images based on pre-trained encoders and Uniform Manifold Approximation and Projection (UMAP) representations, validated on real seismic DAS cross-well data; 3. Rock-physics parametrized

Full-Waveform Inversion (FWI), that help in reducing cross-talk among elastic parameters during the inversion process, and obtain direct inversion of quantitative parameters related to the injection; 4. Seismic dispersion and attenuation related to hydrogen storage, a rock-physics analysis of frequency-dependent effects related to patchy gas saturation, which clarifies when dispersion and attenuation materially affect monitoring performance.

We first design a supervised workflow that infers spatial variations in CO_2 saturation from time-lapse seismic gathers. The method exploits a U-Net architecture augmented with multi-scale features derived via Continuous Wavelet Transform (CWT). The method combines the strengths of U-Net and CWT, where the U-Net encoder–decoder with skip connections preserves spatial detail and the CWT inputs highlight scale-specific patterns. The U-Net is trained on synthetic datasets where ground-truth saturation maps are known. Compared to a simple U-Net trained on raw gathers, the CWT-enhanced version improves sensitivity to weak anomalies and produces more accurate saturation maps that better align with the known fluid plume morphology. Beyond accuracy, the multi-scale responses allow a qualitative link between predicted saturation and observed time-lapse signal, which supports expert validation.

In the context of CCS monitoring, to reduce acquisition density and manual screening, we introduce a framework based on pre-trained models on non-seismic images in order to detect changes between time-lapse seismic surveys. Pre-trained encoders ResNet152 are arranged in a Siamese setup to embed baseline and monitor shot gathers into a high-dimensional feature space. UMAP is used to map those embeddings into a low-dimensional space where temporal evolution becomes visually and metrically separable. Unsupervised UMAP provides a neutral view of natural clusters. Supervised UMAP uses the labels from the training set only to refine class separation, thereby achieving greater class separation on unlabelled datasets. Because UMAP is not a classifier, we add a k-nearest neighbours classifier algorithm (k-NN) to assign class labels to unlabelled samples. The overall proposed framework is lightweight. It relies on fixed pre-trained encoders, minimal hyper-parameter tuning, and low dimensional inference, so it is both fast and transferable across different surveys.
As part of the PhD program, I led the SBEM (Svelvik Borehole Electromagnetic Monitoring) project, a geophysical campaign aimed at testing the integration of seismic and electromagnetic methods for the detection and quantification of CO_2 leakage at the Svelvik CO_2 Field Lab, in Norway. The project was carried out in collaboration with SINTEF, and both electromagnetic (GPR and ERT) and seismic (cross-well and VSP) data were acquired during a controlled CO_2 injection, using hydrophones and Distributed Acoustic Sensing (DAS). The resulting seismic time-lapse dataset served

as a key experimental benchmark for this research.
We used this dataset to validate the proposed deep learning framework on time-lapse Distributed Acoustic Sensing (DAS) cross-well data acquired during the controlled injection. Baseline and monitor surveys span pre-, during-, and post-injection periods, reflecting real operational constraints. In unsupervised settings, PCA and t-SNE offer limited or fragmented separation, whereas UMAP yields a clearer manifold structure. Baseline and monitor are not perfectly separated everywhere. Supervised UMAP fitted only on training data produces two compact clusters aligned with expected classes "no-leakage" versus "leakage", and places unlabelled and unseen test samples coherently in the learned space. A k-NN trained in the UMAP space improves accuracy, F1, and ROC-AUC relative to k-NN on the raw 2048-D embeddings, indicating that the learned embedding better separate different classes. Qualitatively, the embedding provides rapid detection of anomalies and a concise summary of monitoring performance, which is valuable for guiding targeted follow-up surveys.

In this thesis, we introduce a rock-physics parametrized FWI that inverts directly for the saturation petrophysical parameter rather than unconstrained elastic moduli. Rock-physics models, including Gassmann's relations, map saturation to elastic moduli, which are then used to generate the forward wavefield within the inversion procedure through automatic differentiation. Optimizing within this petrophysical space reduces the classic cross-talk among multiple elastic parameters and yields models that are expressed in terms of parameters describing the evolution of the injected fluid. Tests on an UHS scenario show improved recovery of saturation-related variations compared to the conventional parametrizations, resulting in more stable convergence and reduced ambiguity. Physics-constrained inversion ensures better interpretability and reduces parameter interference, which is critical when monitoring needs to inform risk decisions.

The thesis analyses the mesoscopic mechanisms that create dispersion and attenuation when gas saturation is spatially heterogeneous at scales comparable to the seismic wavelengths. Wave-induced fluid flow between regions with contrasting compressibility results in a frequency-dependent bulk modulus, which in turn causes phase shifts and amplitude attenuation within the frequency bands relevant to exploration-scale seismic surveys. Two practical implications follow. First, intermediate saturations can maximize attenuation, which means that time-lapse amplitude losses are not always simple proxies for increasing saturation. Second, ignoring these effects can bias both data-driven frameworks and physic-based inversions, particularly when training implicitly assumes a frequency independent behaviour. Incorporating these mechanisms, either through physics-informed priors during training stages, or through frequency-dependent rock-physics operators in inversion scheme such as FWI, improves feasibility studies for

monitoring purpose, while reducing systematic errors.

Together, these methods enable more reliable fluid detection with reduced monitoring efforts. Across synthetic and field settings, the contributions are complementary and cumulative. The U-Net with CWT improves mapping from gathers to saturation, achieving better alignment with target plume geometries and enhanced sensitivity to weak anomalies. The pre-trained Siamese ResNet152 with UMAP and k-NN pipeline turns high-dimensional features into a low-dimensional, human-interpretable map that separates baseline and monitor classes more clearly than PCA or t-SNE on the Svelvik seismic DAS dataset. The rock-physics constrained FWI improves recovery of saturation-driven changes in a storage scenario. The dispersion and attenuation study clarifies when frequency-dependent effects must be modelled explicitly to avoid over or under estimating changes.

The findings of this thesis highlight the benefits of integrating physics-based modelling with data-driven learning to achieve reliable, interpretable, and scalable monitoring of geological storage systems. By combining seismic inversion, rock-physics modelling, and machine learning, the proposed methodologies enhance sensitivity to subsurface changes while reducing acquisition and processing costs. The approaches developed in this work demonstrate that it is possible to improve both accuracy and efficiency in time-lapse seismic fluid monitoring. Furthermore, the same strategies can be effectively extended from CO_2 storage to underground hydrogen storage, and potentially to natural hydrogen exploration, emphasizing their versatility across the broader energy transition scenario.

Despite these advances, several open issues remain for future development. Data-driven models should be fine-tuned on large seismic datasets, improving their generalization to real monitoring scenarios. Self-supervised training on extensive unlabelled seismic datasets could further expand model applicability, reducing the dependence on labelled data. Injection logs from the Svelvik CO_2 Field Lab will be implemented in an additional regression task to link time-lapse embeddings to actual injection mass and pressure, improving the quantitative interpretability of the framework. In terms of physics, integrating frequency-dependent rock-physics models directly into the FWI scheme will help to capture realistic dispersion and attenuation effects. Meanwhile, adaptive learning of site-specific parameters will enhance the overall robustness of the model . Finally, as a key future step, the methodologies developed and validated so far on synthetic datasets will be applied to the seismic dataset collected at the Svelvik CO_2 Field Lab, providing a crucial benchmark of their performance under field conditions.

In conclusion, this thesis contributes to the development of a new generation of

geophysical monitoring strategies that balance physical interpretability with computational efficiency. By combining data-driven representations with physics-constrained formulations, the proposed methods provide reliable detection of subsurface changes while maintaining strong links to measurable geological parameters. These advances pave the way for more effective and affordable monitoring of CO_2 and H_2 storage, reinforcing the central role of geophysics in ensuring the safety, scalability, and public trust, which are crucial for a sustainable low-carbon energy future.

Bibliography

IPCC, 2023. Sections. In: Climate Change 2023: Synthesis Report. Contribution of Working Groups I, II and III to the Sixth Assessment Report of the Intergovernmental Panel on Climate Change [Core Writing Team, H. Lee and J. Romero (eds.)]. IPCC, Geneva, Switzerland, 1 pp. 35-115, doi: 10.59327/IPCC/AR6-9789291691647.

Acknowledgements

I am grateful to Prof. Michele Pipan for his trust, guidance, and continuous encouragement. His intellectual curiosity and broad vision have been instrumental in guiding this research and in fostering my development as both a scientist and a person.

My sincere thanks also go to Prof. Emanuele Forte, co-supervisor, for his valuable advice, insightful discussions, and continuous support in refining this work. His meticulous attention to detail and constructive feedback have greatly contributed to the quality of this thesis.

I am truly grateful to my colleagues and friends Elisa Ligas, Ary Leonel Miño, Attilio Molossi, and Giacomo Roncoroni for their collaboration, stimulating discussions, and friendship throughout these years. Their ideas and support have made this research not only more meaningful but also an enjoyable collective experience.

Finally, I wish to express my sincere appreciation to all the friends and researchers I have met during conferences, workshops, and fieldwork activities. The exchanges, discussions, and shared enthusiasm for research have greatly enriched both this work and my personal experience as a researcher.

List of Figures

List of Tables

List of Publications

Journal Paper

G. Pantaleo, A. Molossi, M. Pipan, *Estimation of CO_2 saturation maps from synthetic seismic data using a deep-learning method with a multi-scale approach*, Geoenergy, 2024, Vol. 2(1), https://doi.org/10.1144/geoenergy2023-057.

Peer-Reviewed Conference papers

G. Pantaleo, A. Molossi, M. Pipan, *Application of Deep Learning in the Estimation of CO_2 Saturation Maps*, European Association of Geoscientists & Engineers, 2023(1), 1–5, https://doi.org/10.3997/2214-4609.202335061.

G. Pantaleo, G. Roncoroni, M. Pipan, *Monitoring Elastic Parameters Changes during Underground Hydrogen Storage Using Rock Physics Parametrized FWI*, Fifth EAGE Global Energy Transition Conference & Exhibition (GET 2024), 2024(1), 1–5, https://doi.org/10.3997/2214-4609.202421200.

G. Pantaleo, M. Pipan, *Optimization of rock-physics inversion via FWI and deep learning tools*, The 43rd National Conference of the GNGTS, 11-14 Feb 2025, (1), 1–5, https://gngts.ogs.it/.

G. Pantaleo, M. Pipan, *Assessment of a deep learning framework for time-lapse seismic monitoring*, EGU General Assembly 2025, Vienna, Austria, 27 Apr–2 May 2025, EGU25-882, 2025, https://doi.org/10.5194/egusphere-egu25-882.

G. Pantaleo, M. Pipan, *Enhancing Early CO_2 Leakage Detection using Pre-Trained Deep Learning Models*, World CCUS Conference 2025, 2025(1): 1–5, EAGE, DOI to be assigned. Available at https://www.earthdoc.org/content/papers/10.3997/2214-4609.202522134

G. Pantaleo, M. Pipan, *Frequency-dependent seismic analysis for hydrogen storage in porous media*, Fifth International Meeting for Applied Geoscience and Energy (IMAGE25), 2025, DOI to be assigned. Available at https://imageevent.aapg.org/portals/26/abstracts/2025/4316783.pdf

Code availability

The Python codes used to compute gas properties based on the Peng–Robinson Equation of State are available at https://figshare.com/s/af33b896cd45ed71b4ab. These scripts were used to estimate the gas properties shown in Figure 2.2.3, and to calculate the effective fluid properties used in the fluid substitution analysis throughout all rock physics modelling presented in this thesis.

The U-Net implementation developed for CO_2 saturation mapping, presented in Chapter 3, is publicly available at https://github.com/GiovanniPantaleo/UNet-for-CO2-saturation-map-estimation.git.

Chapter 1

Overview

The current PhD work aims to analyse and improve methodologies for monitoring geological fluid storage sites, particularly for carbon-dioxide and hydrogen. This is pursued through data-driven approaches, such as Deep Learning (DL) tools, and their integration with physics-driven methods, including Rock-Physics Modelling (RPM) and Full-Waveform Inversion (FWI) of seismic data.

1.1 Motivations

Climate change driven by greenhouse gas emissions represents one of the most pressing present global challenges. Recent records confirm that global average temperatures are consistently breaking historical thresholds, with 2024 marking the first year when warming exceeded 1.5 °C above pre-industrial levels (IEAa, 2025). There is an urgent need to develop solutions that can reduce CO_2 in the atmosphere and lead the world towards a net-zero carbon and sustainable future by 2050. The current energy transition is driven by both environmental and societal imperatives, with geosciences expected to play a central role in this process. Their contribution spans from the sustainable sourcing of raw materials with reduced environmental impact, to the development of methods for the exploitation and storage of low-carbon energy, to the safe disposal of energy-related wastes. Energy use, including electricity, heat, and transport, accounts for 73.2% of global CO_2 emissions (IEA, 2017). Consequently, energy production and consumption practices remain the main drivers of climate change.

A technology that has been recognised as essential for achieving net-zero emissions is Carbon Capture and Storage (CCS) (de Coninck et al., 2018). Most scenarios developed by the Intergovernmental Panel on Climate Change (IPCC) that limit warming to around 1.5 °C incorporate CCS and highlight that "*CCS is unavoidable if net-zero CO_2 or GHG emissions are to be achieved*" (IPCC, 2022). CCS technologies involve capturing the CO_2 from power generation and hard-to-abate industries, and permanently storage in deep geological formations. Notably, some of the most ambitious IPCC pathways foresee a rapid scale-up of CCS, projecting that nearly 200 Gt of CO_2 from fossil fuels could be captured by 2100 (IPCC, 2023). These findings

underscore that without widespread CCS deployment, meeting global climate goals will remain highly challenging.

At the same time, rapid advances in digital technologies are opening new opportunities for geophysical climate monitoring. For instance, Europe's first exascale supercomputer launched in 2025, JUPITER, supports weather and climate research and provides unprecedented computational power for large-scale simulations (ECMWF, 2025). In parallel, Deep Learning (DL) has emerged as a powerful tool in the Earth Sciences (Camps-Valls et al., 2025). Together, these advances in AI and hardware enable the processing of massive datasets, the training of complex models, and the execution of complex simulations far more efficiently. This convergence offers a strong impetus to apply DL and HPC to geophysical monitoring and modelling in the Earth Sciences.

Important reasons to focus on CCS monitoring are to ensure safe site operations satisfying regulatory requirements, and at the same time to earns public confidence and address public concerns about possible leakage. While CCS has strong technical potential, public scepticism and lack of trust are still big challenges. People fear possible leaks or are sceptical about the technology not being fully tested, so it is essential to adopt rigorous monitoring strategies. For this reason, all regulatory frameworks require Measurement, Monitoring, and Verification (MMV) of CO_2 injections. Long-term monitoring can show that injected CO_2 remains underground. Using geophysical data and advanced algorithms, we can also detect anomalies quickly. This not only confirms that storage is safe but also builds confidence among people and stakeholders.

Alongside CCS, Underground Hydrogen Storage (UHS) is another promising option for integrating renewable energy. In this approach, excess electricity from wind or solar is used to produce hydrogen through electrolysis, which is then stored in deep geological formations. The hydrogen can later be recovered when needed, providing seasonal energy balancing Carbonero et al. (2024). Like CCS, UHS involves complex subsurface processes. Running detailed reservoir simulations is very computationally demanding, which slows down deployment. For this reason, there is growing interest in using AI to support faster, more efficient modelling and monitoring of UHS sites.

The knowledge developed on seismic exploration and rock physics methods for hydrocarbon exploration, CCS, and UHS can be directly transferred and adapted to emerging applications, particularly natural hydrogen exploration. One of the key challenges in this context is to understand the rock physical properties of hydrogen-bearing reservoir rocks and their sealing formations. Such characterization is essential to perform seismic-based reservoir assessment, evaluate caprock integrity, and support the identification and appraisal of potential hydrogen production reservoirs.

In conclusion, this thesis makes a contribution to the field of subsurface geophysical monitoring by advancing methods for characterising and quantifying processes associated with CO_2 and hydrogen storage. Guided by the goal of improving the reliability and efficiency of subsurface monitoring, I explored how machine learning can extract meaningful information directly from time-lapse active seismic data, developing and testing a data-driven framework for CO_2 plume

estimation (Chapter 3).
To make monitoring more efficient and cost-effective, I extended this concept into a pre-trained, lightweight architecture for automatic change detection (Chapter 4), which I then tested and validated on real cross-well Distributed Acoustic Sensing (DAS) data from the Svelvik CO_2 Field Lab.
To enhance the physical interpretability and the extraction of petrophysical information, I subsequently integrated rock-physics relationships into Full-Waveform Inversion (Chapter 5), leveraging automatic differentiation to enable the direct quantitative estimation of gas distribution rather than estimating it after the extraction of the elastic parameters response.
The subsequent chapter (Chapter 6) deepens the physical understanding of how gas distribution affects seismic responses through frequency-dependent dispersion and attenuation, a crucial aspect for realistic modelling and inversion.
Altogether, these researches build a coherent path from data-driven prediction to physics-based interpretation, demonstrating how both perspectives can converge toward safer and more efficient geological fluid storage monitoring.

1.2 Review of Chapters

A comprehensive description of the chapters of this thesis is provided hereafter. Each of the subsequent chapters contains published research paper as well as peer-reviewed extended abstracts of which I fully contributed to the study, discussions, manuscript writing and figures preparation. A preface has been added to the chapters to contextualise and describe the research carried out in more detail. Papers and extended abstracts are presented with their published content, with some minor editing to adapt them to the format of the thesis.

Chapter 2
In this chapter, we introduce the fundamental concepts of carbon-dioxide and hydrogen storage and their monitoring. After outlining the motivation behind these technologies, we provide a comprehensive state of the art of current monitoring methods, discussing why they are needed and how their implementation can be improved.

Chapter 3
In this chapter, we explore data-driven methodologies for CO_2 storage monitoring. We propose a deep learning approach to directly estimate the spatial distribution of the CO_2 plume from time-lapse seismic data, using a U-Net Convolutional Neural Network enhanced by multi-scale feature extraction using Continuous Wavelet Transform. Key findings of this chapter are presented in Pantaleo et al. (2023) and Pantaleo et al. (2024a).

Chapter 4
We design a cost-effective time-lapse monitoring strategy for CO_2 storage, using a pre-trained ResNet152 arranged in a Siamese setup, UMAP for visualization, and k-NN for classification. The framework automatically detect changes between baseline and monitor surveys, thereby reducing the need for dense acquisition and extensive manual analysis. We first presented this methodology in (Pantaleo and Pipan, 2025a) using a synthetic dataset, and further tested and validated it on seismic DAS cross-well data collected at the Svelvik CO_2 Field Lab, Norway.

Chapter 5
We present a novel full-waveform inversion approach parametrized through rock-physics relationships. The method directly inverts for petrophysical parameter using a rock-physics model that links saturation changes to elastic parameters changes. Leveraging automatic differentiation which is widely used in machine learning tasks, the inversion efficiently computes exact gradients through the coupled seismic and rock-physics domains, enabling a fully differentiable and computationally stable framework. This rock-physics parametrized FWI helps reduce ambiguity and crosstalk between parameters by focusing the inversion on changes caused by the injected gas in the reservoir. A preliminary application of this method to an underground gas storage scenario is described in Pantaleo et al. (2024b) and further work in Pantaleo and Pipan (2025c).

Chapter 6
This chapter examines the effects of patchy gas saturation on seismic wave propagation, with an emphasis on frequency-dependent phenomena. We investigate how the presence of hydrogen in heterogeneous distributions in porous media leads to significant dispersion of P-wave velocities and seismic attenuation. This is due to wave-induced fluid flow between more gas-saturated regions and less gas-saturated regions. We underscore the importance of incorporating dispersion and attenuation effects into monitoring and inversion workflows. Results of this approach are presented in Pantaleo and Pipan (2025b).

Chapter 7
In the final chapter, the geophysical campaign conducted at the Svelvik CO_2 Field Lab in Verket (Norway) is described. Time-lapse seismic surveys, including both Distributed Acoustic Sensing (DAS) and borehole hydrophone recordings, were collected before, during, and after a controlled CO_2 injection with the aim of developing and testing new monitoring methodologies for CCS.

Chapter 8
An overview of the work done during this work and a way forward for practical applications of the proposed methods is presented in this chapter, with a critical analysis of its future perspectives.

Bibliography

Gustau Camps-Valls, Miguel-Ángel Fernández-Torres, Kai-Hendrik Cohrs, Adrian Höhl, Andrea Castelletti, Aytac Pacal, Claire Robin, Francesco Martinuzzi, Ioannis Papoutsis, Ioannis Prapas, Jorge Pérez-Aracil, Katja Weigel, Maria Gonzalez-Calabuig, Markus Reichstein, Martin Rabel, Matteo Giuliani, Miguel D. Mahecha, Oana-Iuliana Popescu, Oscar J. Pellicer-Valero, Said Ouala, Sancho Salcedo-Sanz, Sebastian Sippel, Spyros Kondylatos, Tamara Happé, and Tristan Williams. 2025. Artificial intelligence for modeling and understanding extreme weather and climate events. *Nature Communications* 16, 1 (2025), 1919. https://doi.org/10.1038/s41467-025-56573-8

Alvaro Carbonero, Shaowen Mao, and Mohamed Mehana. 2024. Enabling Clean Energy Resilience with Machine Learning-Empowered Underground Hydrogen Storage. https://doi.org/10.48550/arXiv.2404.03222

Heleen de Coninck, Aromar Revi, Mustafa Babiker, Paolo Bertoldi, Marcos Buckeridge, Anton Cartwright, Wenjie Dong, James Ford, Sabine Fuss, Jean-Charles Hourcade, Desiree Ley, Reinhard Mechler, Peter Newman, Alina Revokatova, Sebastian Schultz, Linda Steg, and Taishi Sugiyama. 2018. Strengthening and Implementing the Global Response. In *Global Warming of 1.5°C: An IPCC Special Report on the Impacts of Global Warming of 1.5°C above Pre-industrial Levels and Related Global Greenhouse Gas Emission Pathways, in the Context of Strengthening the Global Response to the Threat of Climate Change, Sustainable Development, and Efforts to Eradicate Poverty*, V. Masson-Delmotte, P. Zhai, H.-O. Pörtner, D. Roberts, J. Skea, P. R. Shukla, A. Pirani, W. Moufouma-Okia, C. Péan, R. Pidcock, S. Connors, J. B. R. Matthews, Y. Chen, X. Zhou, M. I. Gomis, E. Lonnoy, T. Maycock, M. Tignor, and T. Waterfield (Eds.). Cambridge University Press, Cambridge, UK, 313–444. https://doi.org/10.1017/9781009157940.006

ECMWF. 2025. Reaching JUPITER: ECMWF celebrates the first European exascale supercomputer. ECMWF News. https://www.ecmwf.int/en/about/media-centre/news/2025/reaching-jupiter-ecmwf-celebrates-first-european-exascale

IEA. 2017. World Energy Outlook 2017, IEA, Paris. https://www.iea.org/reports/world-energy-outlook-2017. Accessed 16 Sep 2025.

IEAa. 2025. Global Energy Review 2025. https://www.iea.org/reports/global-energy-review-2025 Accessed 16 Sep 2025.

IPCC. 2022. Chapter 6: Energy systems. In *Climate Change 2022: Mitigation of Climate Change. Contribution of Working Group III to the Sixth Assessment Report of the Intergovernmental Panel on Climate Change*. Cambridge University Press, Cambridge. https://doi.org/10.1017/9781009157926.008

IPCC. 2023. *Climate Change 2022 – Impacts, Adaptation and Vulnerability: Working Group II Contribution to the Sixth Assessment Report of the Intergovernmental Panel on Climate Change*. Cambridge University Press, Cambridge University Press, Cambridge, UK and New York, NY, USA, 3056 pp. https://doi.org/10.1017/9781009325844

Giovanni Pantaleo, Attilio Molossi, and Michele Pipan. 2023. Application of Deep Learning in the Estimation of CO_2 Saturation Maps. In *EAGE Conference Proceedings*. European Association of Geoscientists & Engineers, EAGE, Porto, Portugal, 1–5. https://doi.org/10.3997/2214-4609.202335061

Giovanni Pantaleo, Attilio Molossi, and Michele Pipan. 2024a. Estimation of CO_2 Saturation Maps from Synthetic Seismic Data Using a Deep-Learning Method with a Multi-Scale Approach. *Geoenergy* 2, 1 (2024), 1–13. https://doi.org/10.1144/geoenergy2023-057

Giovanni Pantaleo and Michele Pipan. 2025a. Enhancing Early CO_2 Leakage Detection Using Pre-Trained Deep Learning Models. In *EAGE World CCUS Conference 2025 Conference Proceedings*, Vol. 2025. European Association of Geoscientists & Engineers, EAGE, Bergen, Norway, 1–5. DOI to be assigned. Available at https://www.earthdoc.org/content/papers/10.3997/2214-4609.202522134.

Giovanni Pantaleo and Michele Pipan. 2025b. Frequency-Dependent Seismic Analysis for Hydrogen Storage in Porous Media. In *International Meeting for Applied Geoscience and Energy (IMAGE25)*. SEG, Houston, TX, 1–5. DOI to be assigned. Available at https://imageevent.aapg.org/portals/26/abstracts/2025/4316783.pdf.

Giovanni Pantaleo and Michele Pipan. 2025c. Optimization of Rock-Physics Inversion via FWI and Deep Learning Tools. In *43rd National Conference of the GNGTS*. GNGTS, Bologna, Italy, 1–5. https://gngts.ogs.it/

Giovanni Pantaleo, Giacomo Roncoroni, and Michele Pipan. 2024b. Monitoring Elastic Parameters Changes During Underground Hydrogen Storage Using Rock Physics Parametrized FWI. In *EAGE GET24 Conference Proceedings*. European Association of Geoscientists & Engineers, EAGE, Rotterdam, The Netherlands, 1–5. https://doi.org/10.3997/2214-4609.202421200

Chapter 2

Introduction

Greenhouse gas (GHG) emissions are now higher than ever, causing visible climate change and creating strong pressure to cut emissions quickly. Scientists have shown that human activities are the main cause of global warming, with carbon dioxide (CO_2) and methane (CH_4) being the most important gases (Figure 2.0.1). These emissions come from more than a hundred years of burning fossil fuels, changing how land is used, and from the ways people live, consume, and produce goods (IPCC, 2022b). In the 2001 to 2020 period, the average global surface temperature was about 1 °C higher than in 1850–1900 (Figure 2.0.1). The temperature has been rising faster since 1970 than during any other 50-year period in at least the last 2000 years. International agreements such as the United Nations Framework Convention on Climate Change (UNFCCC), the Kyoto Protocol, and the Paris Agreement have raised national climate goals. At the same time, public awareness has grown, helping to speed up actions against climate change at many levels.

Between 2010 and 2019, many countries reduced their energy and carbon intensity, and some achieved absolute cuts in GHG emissions for more than ten years in a row (IPCC, 2023). This progress was mostly due to switching from coal to gas, slowing the growth of coal power plants, as well as using more renewable energy sources (IPCC, 2022b) (Figure 2.0.2). In addition, policies improved energy efficiency, slowed deforestation, and supported new technologies, which helped to avoid or reduce emissions. Still, if the global emission pledges announced by October 2021 are met, GHG levels in 2030 would probably cause global warming to rise above 1.5 °C during this century. This would also make it much harder to limit warming to below 2 °C (Figure 2.0.2). Up-to-date atmospheric greenhouse gas concentrations are reported by NOAA's Global Monitoring Laboratory portal (NOAA, 2025), which provides near-real-time GHGs data and clearly documents the persistent long-term increase in atmospheric GHGs.

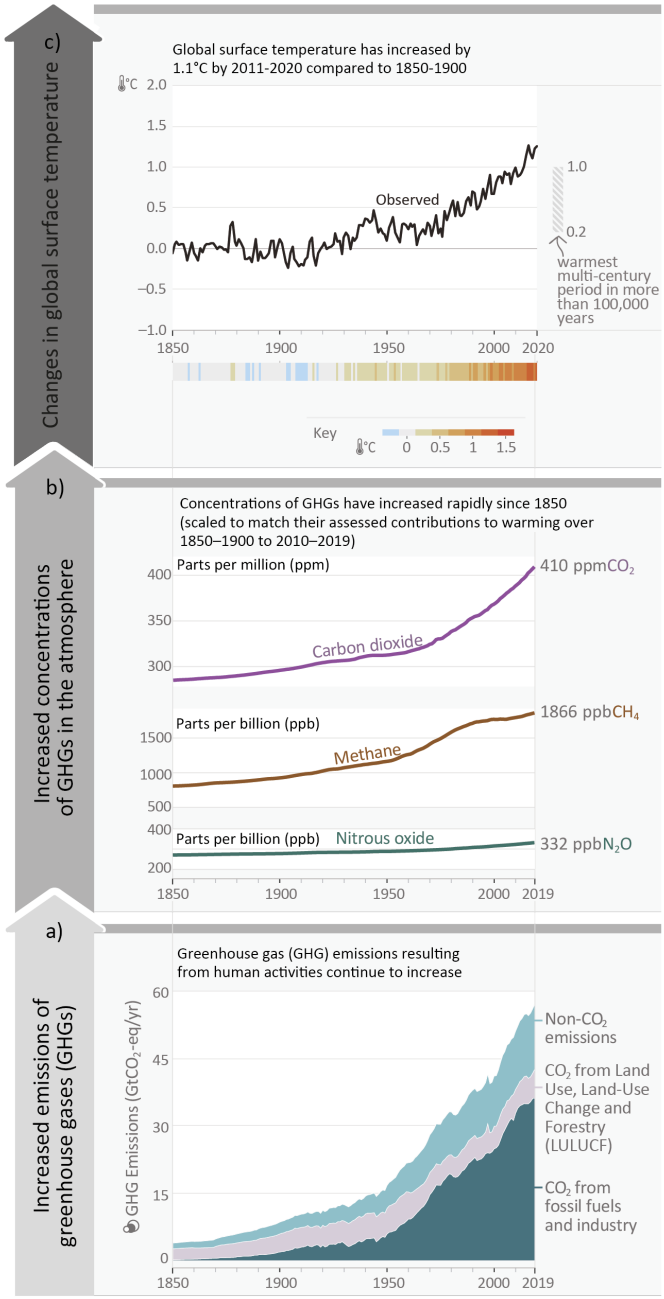

Figure 2.0.1: The chain of cause and effect from greenhouse gas (GHG) emissions to global warming. Adapted from IPCC (2023): (a) Global net human-caused GHG emissions have risen quickly in recent decades. These include CO_2 from fossil fuel burning and industry, net CO_2 from land use and forestry, CH_4, N_2O. (b) These emissions have increased the atmospheric concentration of several gases, especially the three main well-mixed GHGs: CO_2, CH_4, and N_2O (annual values shown). (c) Global surface temperature (shown as yearly anomalies relative to 1850–1900) has increased by about 1.1 °C since pre-industrial times.

To stop human-caused global warming, it is necessary to reach net zero CO_2 emissions, while also cutting other greenhouse gases (GHGs) strongly (IPCC, 2023). Pathways that keep warming within 1.5 °C or 2 °C require fast, deep, and in most cases immediate cuts in GHG emissions across all sectors (Figure 2.0.3). If warming first goes above these limits and then comes back down, the risks of possible irreversible impacts would increase. Global mitigation pathways that reach net zero CO_2 and GHG emissions involve moving away from the usage of fossil fuels without carbon capture and storage (CCS), while shifting to very low- or zero-carbon energy sources such as renewables or fossil fuels with CCS. They also include demand-side changes, higher efficiency, and strong cuts in GHG emissions (Figure 2.0.4). Both the IPCC and the IEA highlight hydrogen as a useful fuel and energy carrier, important for balancing energy systems in the short and long term (Clarke et al., 2022). As summarized in IPCC (2022a): "*Achieving net zero will be challenging and will require new production processes, low- and zero-emissions electricity, hydrogen, and, where necessary, carbon capture and storage.*"

As far as hydrogen, to really help the decarbonisation, it must be produced using zero- or very low-carbon sources. One option is green hydrogen, which can be made by splitting water (electrolysis) just with renewable electricity. Another option is producing hydrogen from biomass with CCS, which can even result in negative net emissions (del Pozo et al., 2021). A different pathway is blue hydrogen, made from natural gas combined with CCS, which can capture about 80–90% of the CO_2 released. In the Sustainable Development Scenario (SDS), providing universal access to energy at the lowest cost does not increase GHG emissions. By 2040, power generation is almost fully decarbonised, relying mostly on renewables (over 60%), nuclear power (15%), and CCS (6%) (Figure 2.0.4).

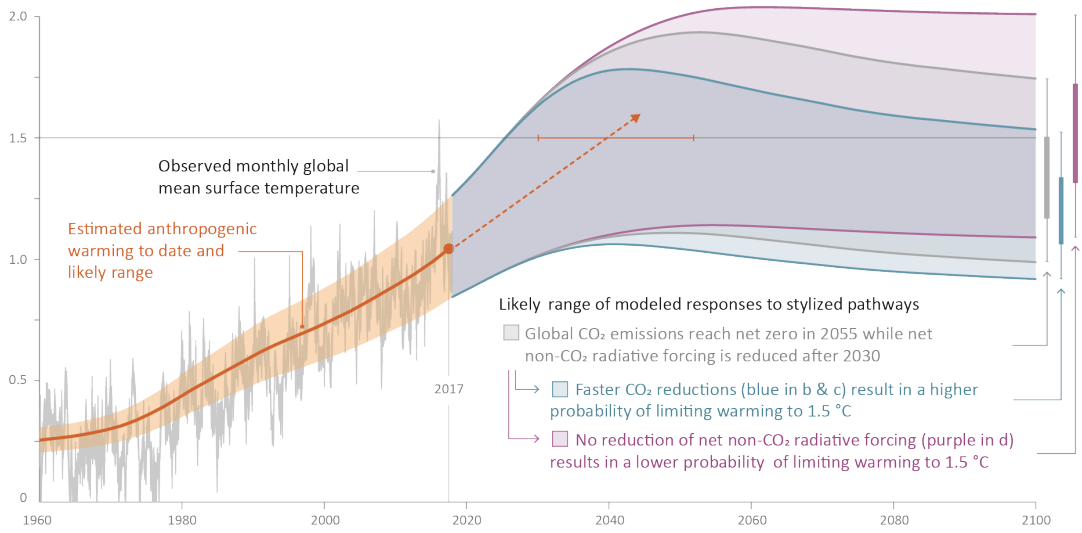

Figure 2.0.2: Observed global temperature change and modelled responses to anthropogenic emission and forcing pathways. Adapted from (IPCC, 2022b): the gray line shows observed monthly global mean surface temperature change. The solid orange line (to 2017) represents the estimated human-caused warming, with the shaded area giving the likely range. The orange dashed arrow and horizontal bar mark the central estimate and likely range of when 1.5 °C of warming would be reached if the current warming trend continues. On the right-hand side, vertical error bars show the likely ranges (thin lines) and central terciles (thick lines, 33rd–66th percentiles) of the projected warming in 2100 under the three different pathways.

Carbon capture and storage (CCS) can help to reduce emissions from large fossil-fuel energy plants and industrial sources, provided that suitable underground storage is available. Capturing CO_2 and injecting it underground is already a proven technology in gas processing and for enhanced oil recovery. However, compared to the oil and gas sector, CCS is less advanced in power generation and in industries such as cement and chemicals, where it is considered an essential mitigation tool (IEAb, 2025). The technical capacity for geological storage is estimated at around 1000 Gt of CO_2, which is more than enough to meet storage needs through 2100 for a 1.5°C pathway. Still, storage availability varies by region and may limit where CCS can be realistically applied (IEAb, 2025). If a site is chosen and managed carefully , CO_2 can be stored underground securely and permanently removed from the atmosphere. At present, CCS faces relevant barriers including technological, financial, institutional, environmental, and social challenges. Deployment rates are far lower than those required in pathways that keep global warming below 1.5–2 °C. However, stronger policies, innovation, and wider public support could help overcome these barriers. In the industrial sector, much greater use of CCS will be needed to capture around 19 Gt of CO_2 emissions from energy and industrial processes by 2040, compared to only 13 Gt in the Sustainable

Development Scenario (SDS) (IEAa, 2025).

Geological storage will likely play a major role in enabling the energy transition. In fact, many alternative energy sources such as hydrogen, bioenergy, or fossil fuels combined with CCS can only become truly carbon-neutral or carbon-negative if reliable CO_2 storage is available.

This thesis takes place within the wider energy transition, focusing on underground geological storage as a key technology for both emission reduction and energy system flexibility. Storing CO_2 underground ensures long-term permanence, which is necessary to offset remaining industrial emissions and to support carbon removal technologies. For hydrogen, large-scale underground storage can balance supply and demand, link different sectors, and decreasing the costs of deep decarbonisation in areas that are difficult to electrify. In both cases, careful site characterisation, monitoring, and risk management are essential to guarantee safe containment, reliable performance, and public acceptance. The following chapters present data-driven and physics-based methods for studying and monitoring reservoirs under CO_2 and hydrogen storage conditions, offering practical tools for a large-scale deployment.

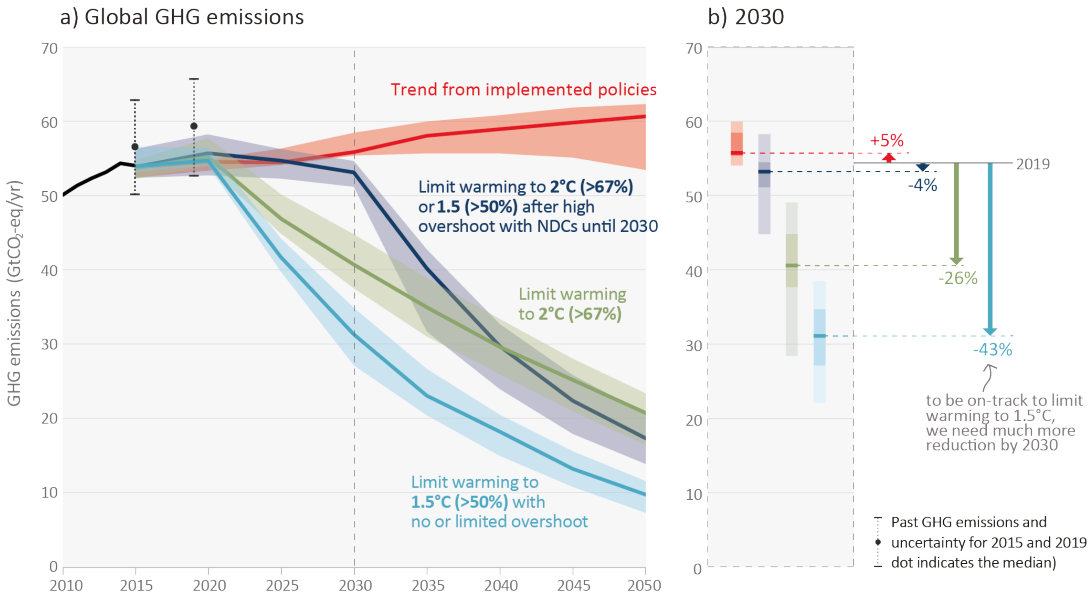

Figure 2.0.3: Global GHG emissions of modelled pathways (funnels in Panel a), and projected emission outcomes from near-term policy assessments for 2030 (Panel b). Panel a shows global GHG emissions over 2015-2050 for four types of assessed modelled global pathways. All these pathways assume immediate action after 2020 (IPCC, 2023).

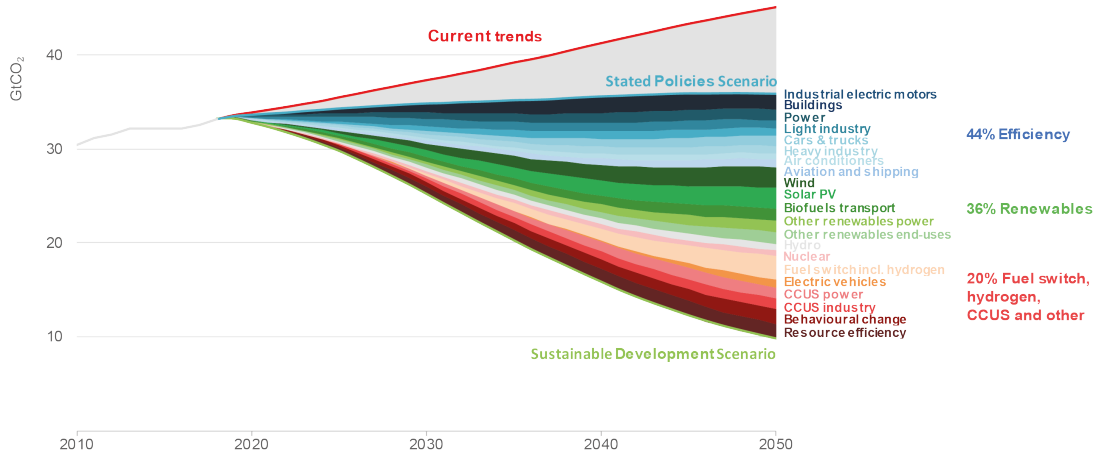

Figure 2.0.4: Energy-related CO_2 emissions and CO_2 emissions reductions by measure in the Sustainable Development Scenarios. CCS and hydrogen are identified as a significant actor to reach the IEA SDS. Image courtesy of IEA2020 (2020). $GtCO_2$ indicates gigatonnes of carbon dioxide.

2.1 Underground Geological Storage for the Energy Transition

Geological storage of energy-related fluids has emerged as a critical component of the clean energy transition. Carbon capture and storage (CCS) offers a way to directly reduce emissions by capturing CO_2 from industrial sources and injecting it into the subsurface to permanently isolate the CO_2 from the atmosphere. The Intergovernmental Panel on Climate Change (IPCC) emphasizes that CCS can be an effective measure to curb global warming and help limit temperature increase to 1.5 °C (IEA, 2021). Moreover, temporary Underground Hydrogen Storage (UHS) in geological formations is gaining attention as a way to enable large-scale utilization of hydrogen as a clean energy carrier by storing excess renewable energy for later use on demand (Figure 2.1.1).

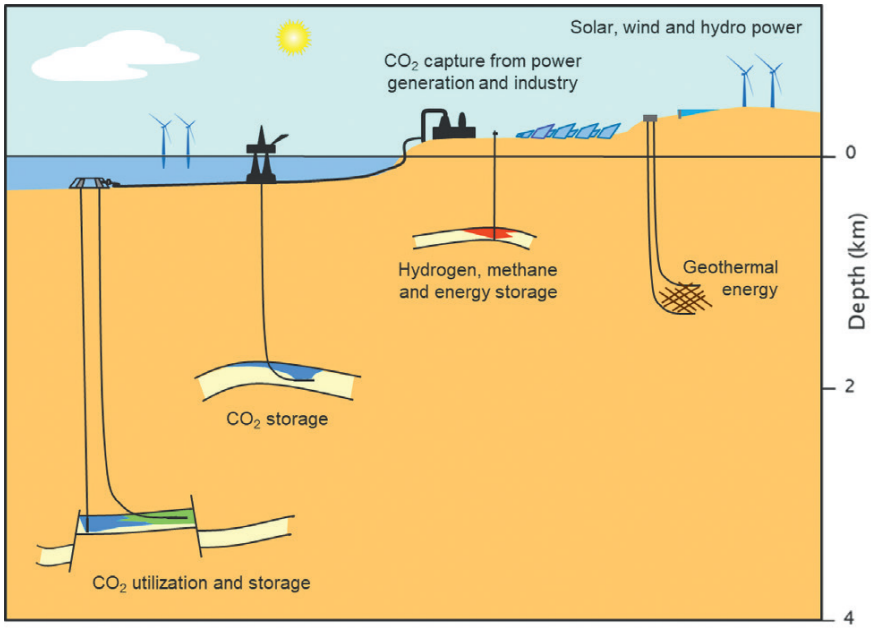

Figure 2.1.1: Sketch illustrating the range of renewable and low-carbon energy solutions likely to contribute during the energy transition (Furre et al., 2019).

The following sections introduce the concepts of CCS and UHS from a geophysical and geological perspective, highlighting the motivation, mechanisms, and case studies for each approach.

2.1.1 Carbon Capture and Storage (CCS)

Carbon capture and storage (CCS) is defined as the process of separating CO_2 from industrial or energy-related emissions to permanently storing it in deep underground

geologic formations. The goal is to prevent CO_2 from entering the atmosphere, thereby directly reducing the amount of GHG emissions. CCS enables continued operation of parts of industry and the energy sectors with hard-to-abate emissions, acting as a bridge technology in pathways to carbon neutrality (Bright and Lockwood, 2022). The main geological storage options in terms of their relative potential for storing large volumes of CO_2 are illustrated in Figure 2.1.2. However, two main classes of porous reservoirs can be identified (Ringrose, 2020):

- Saline aquifer formations: water-bearing formations known as saline aquifers offer the largest storage capacity for CO_2. These should not be confused with shallow freshwater aquifers; therefore, the term deep saline reservoirs is often preferred for clarity, even though saline aquifers remains widely used in the literature as a general term.

- Depleted hydrocarbon reservoirs: these formations represent a highly promising storage option, particularly in the longer term. Once oil or gas production has ceased, the depleted and well-characterized reservoirs can serve as excellent CO_2 storage sites, with much of the necessary infrastructure already available. Although the reduction in formation pressure may pose certain operational challenges, it can also facilitate long-term pressure management during storage.

The storage conditions are a key factor in CO_2 storage. CO_2 must stay in liquid or supercritical form, which requires storing it in reservoirs at least 800 m deep, under a pressure of 7.39 MPa, or more (Ringrose, 2020). At this depth and pressure, CO_2 has a higher density, which makes storage more efficient. The storage reservoir also needs to be sealed by a caprock to prevent CO_2 from migrating upwards and potentially reaching the surface.
Among all storage options, deep saline aquifers have the largest theoretical capacity worldwide and are the main focus for commercial CCS projects. In these aquifers, CO_2 is injected as a supercritical fluid that is lighter than the in-situ salty water (brine). Because of this, it rises and spreads beneath the sealing caprock. Over time, some of the CO_2 dissolves into the brine, and in some cases reacts with the rock minerals to form solid carbonates. Processes as structural trapping, solubility trapping, and mineral trapping work together to keep the CO_2 safely stored over the long term (Figure 2.1.3).

Geophysics and subsurface engineering are important in every stage of a CO_2 storage project, from choosing the site to project, operating and monitoring it for the long term. A well-known example is the Sleipner project in the North Sea, the world's first commercial CO_2 storage in a saline aquifer. Since 1996, Sleipner has injected about 0.9 million tonnes of CO_2 per year into the Utsira Sand formation, located 800–1000 m

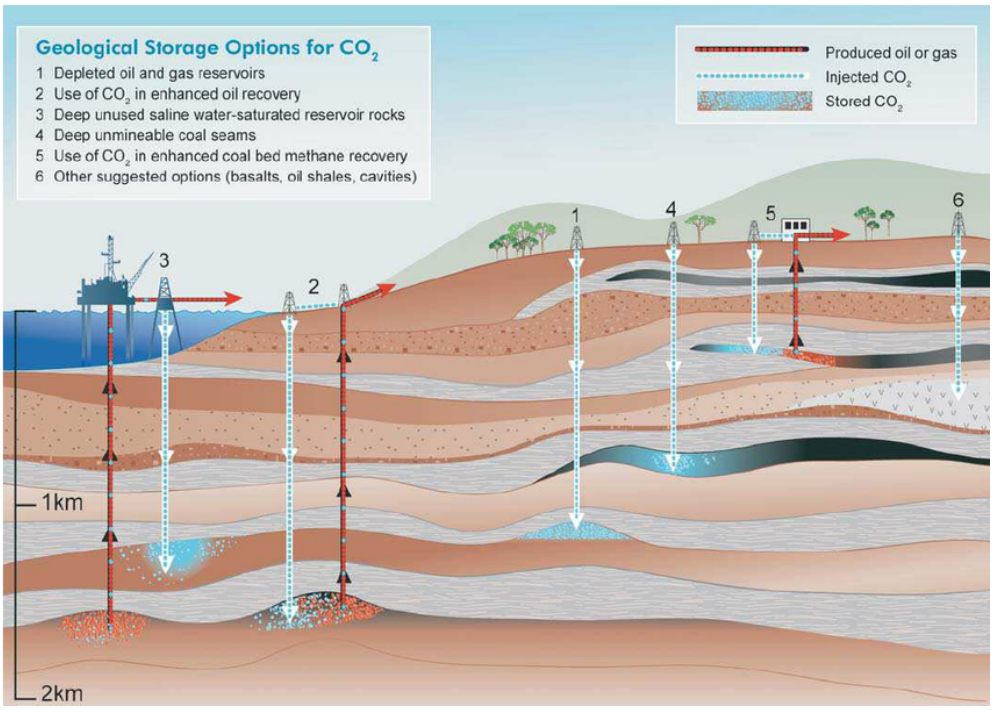

Figure 2.1.2: Schematic overview of geological storage options for CO_2 (Benson et al., 2005)

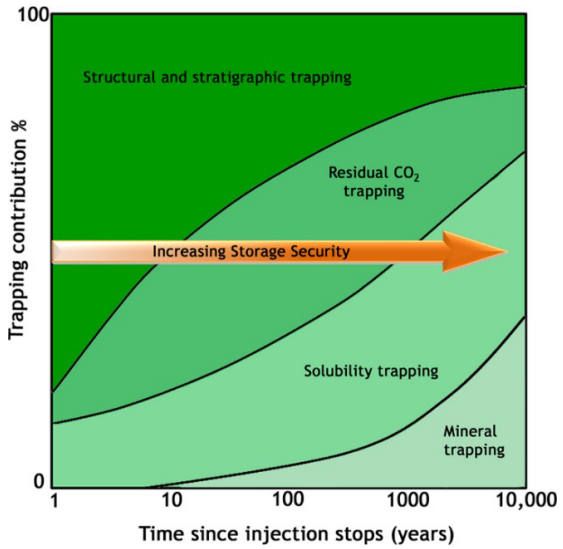

Figure 2.1.3: Relationship between the relative amount of CO_2 trapped by the different physical and chemical processes of trapping and time. The arrow shows the relative importance of the different trapping mechanisms over time (Benson et al., 2005).

below the seabed (Chadwick et al., 2004). Before injection started, a baseline seismic survey was carried out. Since then, repeated 3D seismic surveys (called time-lapse or 4D seismic) have been used to track how the CO_2 plume spreads within the formation (Warchoł et al., 2025). These surveys have been crucial for showing that the CO_2 is safely constrained, for estimating how much has been stored and where it is distributed. Similar monitoring programs, often including additional tools like pressure sensors, microseismic measurements, and soil gas surveys, have been used at other sites such as In Salah (Algeria), Snøhvit (Barents Sea), and Decatur (USA) (Ringrose, 2020). Together, these methods provide a complete picture of how the CO_2 behaves and flows underground.

2.1.2 Underground Hydrogen Storage (UHS)

Energy storage across multiple scales and technologies will play a key role in enabling a flexible, reliable, and responsive energy supply within a renewables-based net-zero system. It provides an essential buffer to balance the intermittency of renewable generation and to address the spatial and seasonal mismatches between energy production and demand (Gardiner et al., 2023; Kabuth et al., 2016). Energy storage operates cyclically, with energy temporarily stored and later released to satisfy specific demand requirements. Multiple storage options exist across different spatial and temporal scales, many of which rely on geoscientific understanding. These include established technologies such as subsurface pumped hydro, hydrogen, and natural gas storage, as well as emerging approaches like compressed air energy storage and gravity-based storage (Bauer et al., 2017).

As the world shifts toward renewable and low-carbon energy, hydrogen (H_2) is emerging as a versatile and clean energy carrier. Hydrogen options which might be considered to be "low carbon" include hydrogen generated from methane with associated CO_2 emissions captured via CCS, and hydrogen generated from electrolysis of water using just renewable energy. A crucial technology for future large-scale deployment of "hydrogen economy" is Underground Hydrogen Storage (UHS) (Miocic et al., 2023). Similar to today's natural gas storage, hydrogen can be temporary stored in subsurface reservoirs during peaks of renewable power production, and withdrawn when needed, acting as a buffer between supply and demand. Compared with above-ground pressurized tanks or liquid hydrogen facilities, underground storage offers far greater capacity and lower cost for bulk energy storage (Ali et al., 2025). Estimates suggest that the seasonal storage needs of a future hydrogen-rich energy system could reach dozens of terawatt-hours of energy, a scale that is achievable with underground methods (Williams et al., 2022; Ali et al., 2025). If implemented on a large scale, UHS would complement batteries and other storage technologies by covering multi-day to seasonal timescales that electrical

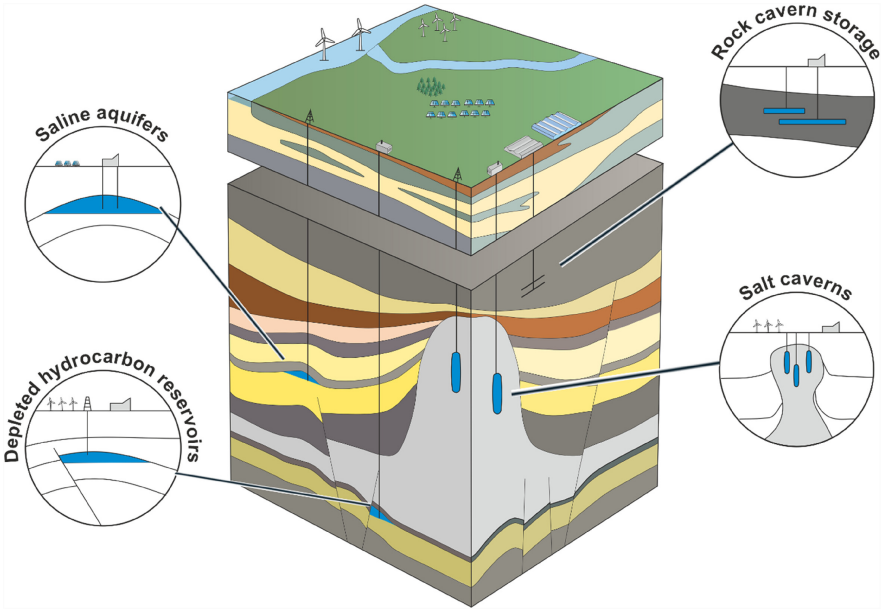

Figure 2.1.4: UHS options include storage in depleted hydrocarbon fields, saline aquifers, salt caverns, and rock caverns (Miocic et al., 2023).

storage alone cannot economically provide (Ali et al., 2025). Two primary geological pathways are being explored for UHS, each at a different stage of maturity (Figure 2.1.4):

- Salt caverns: this storage option is currently the most established (Londe, 2022), where hydrogen can be injected in an artificial cavern at high pressure, generally in the range of 100-200 bar or more, and later withdrawn with minimal losses because salt is effectively impermeable to hydrogen molecules (Londe, 2022; Ali et al., 2025). However, caverns have limited capacity, and there are geologic and geographic restrictions on the availability of sufficiently thick salt deposits.
- Porous rock reservoirs: this option is being explored as a cost-effective solution, which includes depleted hydrocarbon fields or deep saline aquifers (Tarkowski et al., 2021). In this case, hydrogen occupies the pore space of a permeable rock sealed by an overlying impermeable seal. Feasibility studies and small-scale field tests are currently underway, such as the Underground Sun Storage project in Austria (Underground Sun Storage project, USS) which is attempting to demonstrate the possibility to store, in a depleted gas field, a mixture of gas and hydrogen produced from solar energy.

In porous formations, hydrogen migrates according to the rock's hydraulic conductivity and trapping structures, and unlike CO_2 in CCS, which is intended to remain underground permanently, it must be repeatedly injected and extracted. This cyclic

operation leads to pressure and temperature fluctuations that can stress both the reservoir and the wells while also requiring that the purity and recoverability of the gas is preserved. For hydrogen energy storage, the goal is to withdraw as much of the injected hydrogen as possible on demand, and to maintain it as essentially pure, so cushion gases such as nitrogen or natural gas may be used to improve recovery (Krevor et al., 2023). Studies indicate that some hydrogen inevitably permanently remains in the reservoir after each cycle, and microbial or chemical processes that consume hydrogen or create contaminants must be controlled or accounted for to ensure that the extracted gas meets specific quality standards (Veshareh et al., 2022; Yuan et al., 2025). Ongoing research is investigating how hydrogen interacts with different reservoir rocks and brines, which will ultimately determine the suitability of specific geological formations for underground hydrogen storage and the best practices for managing them (Miocic et al., 2023).

Geoscience plays a key role in the prospecting and site selection of suitable sites for hydrogen storage, and the related operations and monitoring. Many techniques developed for CCS and natural gas storage are directly applicable to UHS. Baseline site characterization is essential to define the potential reservoir (trap) and identify any faults or pathways that could allow leakage. Active seismic monitoring during and after hydrogen injection can help track the movement of the gas plume, much as it does for CO_2 monitoring. A pocket of hydrogen in a porous rock creates an acoustic impedance contrast with brine-filled rock, which could appear as a time-lapse seismic anomaly. However, the signal is expected to be much weaker than for CO_2 because hydrogen is a much lighter gas (a small, low-density molecule) compared to CO_2 (McMahon et al., 2023). Pilot tests and modelling studies are needed to confirm whether hydrogen plumes can be reliably detected by seismic methods. In salt cavern storage, seismic imaging is less useful for observing the cavern's contents, so surface monitoring for leaking hydrogen, for example using gas sniffers or shallow borehole sensors, would likely be part of a comprehensive plan to provide early leak detection (Marianne et al., 2020). Moreover, there is potential of prospecting for naturally-occurring hydrogen from underground reservoirs (McMahon et al., 2023), where geophysics is essential for both characterization and monitoring of any leak of hydrogen in the atmosphere that must definitely be avoided (Ocko and Hamburg, 2022).

2.2 Geophysical Monitoring

Geophysical monitoring is essential for CCS and UHS projects to evaluate the overall storage capability and to ensure that injected gases remain contained and behave as expected. In CCS, robust Measurement, Monitoring and Verification (MMV) programs

are required to confirm injectivity potential, track the gas plume, and ensure Conformance and Containment (Ringrose, 2020). An additional key technical objective is Contingency, which involves the ability to react promptly to detected anomalies and to stop any leakage, if necessary. UHS operations present similar challenges, including potential leakage and induced seismicity, so regular geophysical monitoring is critical to detect and quantify the movement of the stored gas (Tarkowski et al., 2021). These monitoring activities provide confidence to regulators and stakeholders that the storage sites are secure and perform as intended (Figure 2.2.1).

A variety of geophysical techniques can be employed to observe subsurface changes during and after CO_2 or hydrogen injection (Figure 2.2.2). Key methods include:

- **Time-lapse gravity:** Repeated gravity measurements can reveal subtle changes in the gravitational field caused by density variations underground. Injecting low-density fluid in place of dense brine reduces subsurface mass, producing a measurable gravity decrease that can indicate fluid migration or leakage (Wilkinson et al., 2017). This approach offers a cost-effective way to detect plume movement or migration in overlying layers, but has intrinsic resolution limits.

- **Electrical and electromagnetic (EM) methods:** The injection of CO_2 or H_2 changes the electrical resistivity of reservoir rocks. For example, CO_2 is a dielectric and therefore increases the resistivity of a formation relative to the original saline water (Landro and Amundsen, 2018). Controlled-source EM surveys or electrical resistivity tomography can map the resulting resistive anomalies and delineate the plume extent, making EM an effective complement to seismic monitoring (Fawad and Mondol, 2021).

- **Passive seismic monitoring:** Passive (microseismic) monitoring involves recording small (micro) earthquakes triggered by the fluid injection. It serves to detect seismicity that might compromise caprock integrity, and discover a possible reactivation of fractures and faults (Davis et al., 2019), (Ringrose, 2020). An example of efficient microseismic monitoring for an onshore CCS site is the monitoring of In Salah CCS project in Algeria (Goertz-Allmann et al., 2014).

- **Active-source seismic monitoring:** Active seismic methods, especially time-lapse 3D seismic (or 4D seismic), are the primary tools for imaging and quantifying physical property changes in the subsurface. 4D seismic require a baseline survey recorded before injection, and repeated 3D surveys (monitoring) periodically thereafter. Differences between baseline and monitor surveys can reveal changes in the subsurface caused by changes in rock and fluid properties due to

the fluid injection. At the Sleipner CO_2 storage site in the North Sea, periodical 3D surveys where conducted from the 1994 baseline until 2010 and clearly mapped the growing CO_2 plume within the Utsira Formation (Furre et al., 2017). Active seismic methods can be deployed in various geometries, including surface surveys, borehole-based vertical seismic profiling (VSP), and cross-well imaging (Figure 2.2.2), all of which provide indirect measurements of the fluids presence and the impact on reservoir properties (Landro and Amundsen, 2018). The high sensitivity of seismic waves to fluid-induced changes makes this technique a cornerstone of any monitoring program. In practice, 4D seismic data are interpreted quantitatively with the aid of rock-physics models to convert observed seismic anomalies (amplitude, frequency, ...) into estimates of gas saturation and other reservoir changes (Fawad and Mondol, 2023).

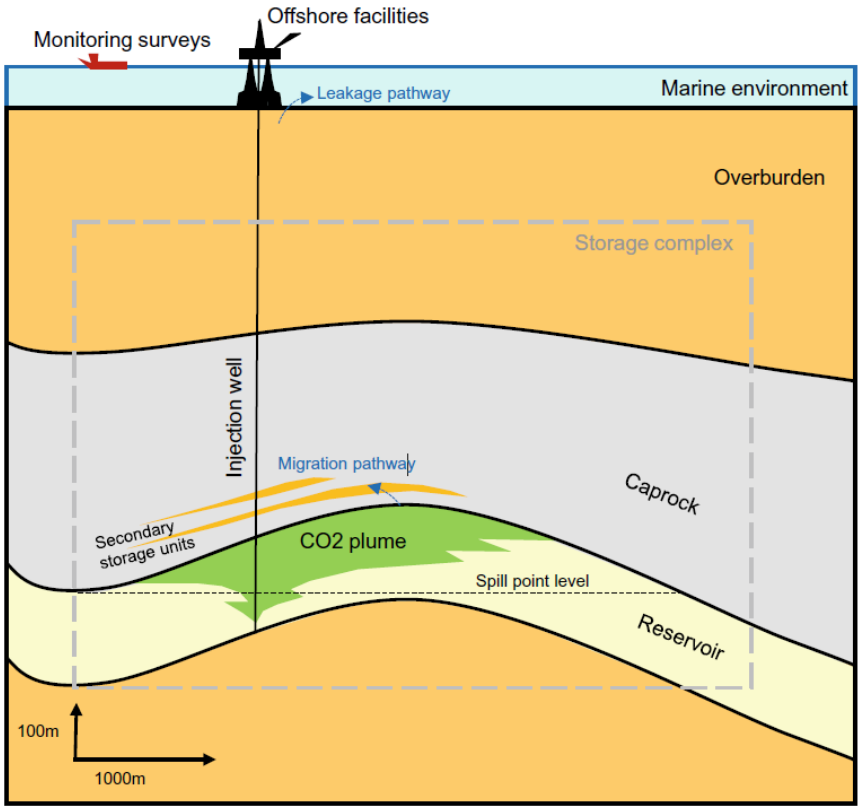

Figure 2.2.1: Conceptual cross-section of an offshore CO_2 storage site, illustrating the injection well, CO_2 plume evolution, potential migration and leakage pathways, and the role of geophysical monitoring. Modified from Ringrose (2020).

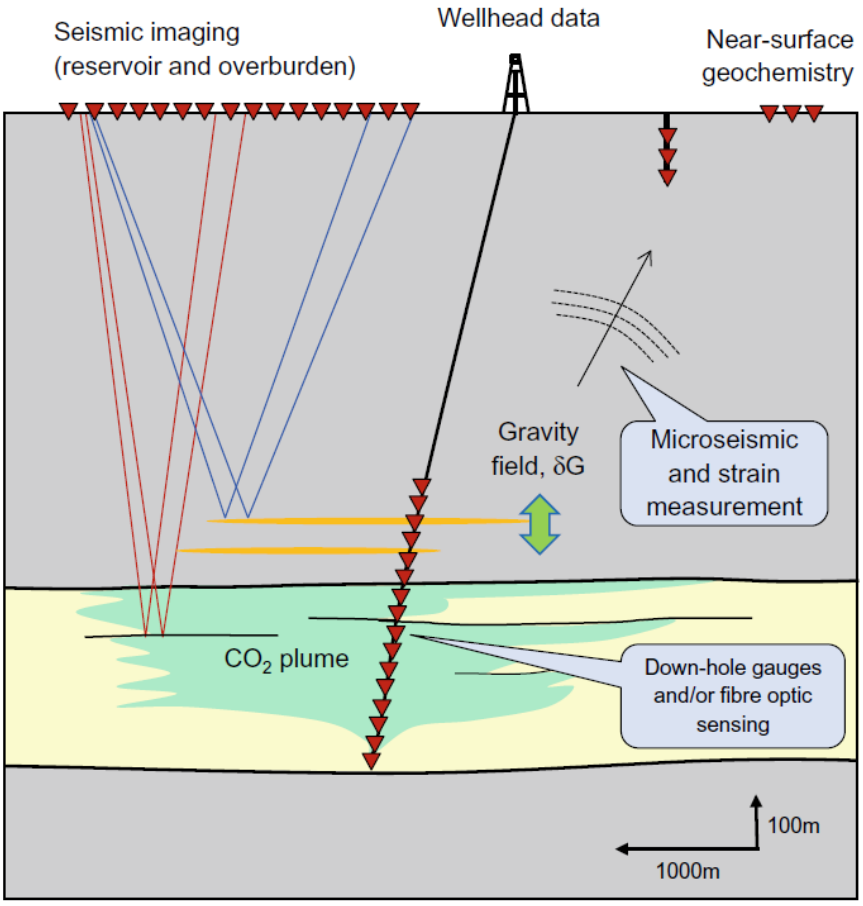

Figure 2.2.2: Idealised sketch of a CO_2 storage site monitoring programme (Ringrose, 2020).

2.2.1 Rock-Physics for seismic monitoring in porous media

Time-lapse seismic data are highly sensitive to variations in the elastic properties of reservoir rocks that occur during fluid injection. These variations are primarily controlled by changes in pore-fluid saturation and composition, as well as by stress and temperature perturbations associated with the introduction of fluids such as carbon-dioxide or hydrogen. The magnitude of the seismic response strongly depends on the mechanical properties of the storage reservoir: injections into saline aquifers, which are relatively soft rocks, typically produce strong time-lapse signals, whereas injections into depleted hydrocarbon reservoirs, which are typically stiffer, often yield weaker and more complex responses. In essence, seismic waves propagating through the subsurface respond to the effective elastic moduli of the combined rock-fluid system. Rock physics provides the theoretical framework to predict the effective elastic moduli of porous media containing different mixtures of minerals and fluids. Within this framework, partial or uniform fluid saturations can be represented by an equivalent effective fluid, which

establishes the quantitative link between changes in fluid saturation and observable seismic parameters such as travel time and amplitude. This relationship enables the interpretation of time-lapse seismic observations in terms of fluid migration, plume distribution, and storage performance (Creasy et al., 2024). Therefore, the role of rock physics is to investigate how seismic signatures evolve in response to changes in porosity, lithology, pressure and fluid composition. These predictive scenarios represent the "*What if*?" analyses of rock physics, providing a rigorous foundation for understanding and quantitatively interpreting reservoir monitoring data (Avseth et al., 2010a).

The impact of pore fluid changes is defined as *fluid substitution problem*. A pioneer study on the impact of fluid-filled pores on the elastic properties is the well-known *Gassmann fluid substitution theory* introduced by Gassmann (1951). Gassmann's substitution theory underlying several assumptions that were summarized by Wang (2001) as:

- The rock (both the matrix and the frame) is macroscopically homogeneous
- All the pores are interconnected or communicating.
- The pores are filled with a frictionless fluid (liquid, gas, or a mixture).
- The rock-fluid system under study is closed (conservative and undrained).
- The pore fluid does not interact with the solid in a way that would soften or harden the frame.

Moreover, Gassmann's theory is valid only for sufficiently low seismic frequencies because the pore pressure induced by the seismic wave must equilibrate throughout the pore network, considering frequency typically below 100 Hz. Its accuracy decreases as the frequencies increase toward sonic logging around 10^4 Hz, and laboratory ultrasonic measurements around 10^6 Hz. At these higher frequencies ranges the Gassmann's theory is no longer valid. However, in the context of CO_2 storage, these assumptions are frequently violated. Reservoir rocks often display heterogeneity in terms of permeability, and lithology, which lead to irregular and non-uniform migration of CO_2, as shown in both laboratory and field experiments (Nakagawa et al., 2013; Alemu et al., 2013). This scale-dependent saturation heterogeneity directly impacts the relationship between seismic velocity and CO_2 saturation, since a propagating seismic wave generates local differences in pore pressure that may not equilibrate.

Rock physics models are crucial for interpreting seismic monitoring data, as they provide the link between subsurface changes associated with CO_2 injection and their seismic signatures, ultimately enabling the conversion of seismic observations into CO_2

saturation maps. In particular, rock physics allows us to compute the effective elastic moduli of a rock, which quantify its overall stiffness. These moduli are not fixed properties, but vary systematically with changes in fluid content within the pore space, thereby capturing how the substitution of brine by CO_2 (or other fluids) modifies the seismic response of the reservoir.

Time-lapse seismic signatures are driven by the interaction between the dry-frame compliance and the compressibility contrast of the pore fluids. The elastic properties of the dry rock frame, namely the bulk modulus of the dry porous rock (K_{dry}), and shear modulus (G_{dry}), strongly depend on porosity (ϕ) and grain cementation. For limited porosity ranges, both K_{dry} and G_{dry} vary nearly linearly with porosity and can be reliably estimated from core data and well logs (Davis et al., 2019). Dry-frame moduli can also be predicted using rock-physics relations (i.e., the Krief model or the Hashin–Shtrikman bounds (Mavko et al., 2009)). While, the effective elastic moduli of a rock in terms of its constituents and pore space (K_m and G_m) are calculated using the Voigt–Reuss–Hill (VRH) average (Mavko et al., 2009). In what follows, we denote by K_m the bulk modulus of the solid matrix and by G_m its shear modulus. K_{m} is bounded between the Voigt (K_V) and Reuss (K_R) limits:

$$K_V = \sum_i f_i K_i, \qquad \frac{1}{K_R} = \sum_i \frac{f_i}{K_i}, \tag{2.1}$$

$$K_{\text{m}} = \frac{K_V + K_R}{2}, \tag{2.2}$$

where f_i is the volume fraction of the i-th mineral constituent. Analogously, the shear modulus of the solid matrix (G_m) is obtained by applying the same VRH averaging to the phase shear moduli G_i with volume fractions f_i. Elastic moduli are also stress-dependent: increasing pore pressure, the rock frame softens. The effective bulk modulus of fluid mixtures is obtained through the Reuss average (Eq. 2.3) (Mavko et al., 2009), and the mixture density is given by the Voigt average (Eq. 2.4):

$$\frac{1}{K_{\text{fluid}}} = \sum_j \frac{S_j}{K_j}, \tag{2.3}$$

$$\rho_{\text{fluid}} = \sum_j S_j \rho_j, \tag{2.4}$$

where S_j is the saturation of the j-th fluid, while K_j and ρ_j denote the bulk moduli and the density of the individual fluid phases, respectively. Once the effective fluid modulus

K_{fluid} is determined, the bulk modulus of a saturated rock K_{sat} can be estimated using Gassmann-Wood's (also called Biot-Gassmann-Hill model, BGH, (Hill, 1963)) relation (Mavko et al., 2009):

$$K_{\text{sat}} = K_{\text{dry}} + \frac{\left(1 - \frac{K_{\text{dry}}}{K_m}\right)^2}{\frac{\phi}{K_{\text{fluid}}} + \frac{1-\phi}{K_m} - \frac{K_{\text{dry}}}{K_m^2}}, \tag{2.5}$$

where K_m is the bulk modulus of the minerals making the rock frame (eq. 2.2). The wet-rock shear modulus is the same as the dry-rock modulus, i.e. $G = G_m$. The density of the solid mineral matrix ρ_{matrix} is instead obtained as the weighted average of the densities of the individual constituent minerals:

$$\rho_{\text{matrix}} = \sum_i f_i \, \rho_i. \tag{2.6}$$

The bulk rock density, ρ_{sat}, is defined considering both the grain density (ρ_{matrix}), and the density of the saturating fluids (ρ_{fluid}) as:

$$\rho_{\text{sat}} = (1 - \phi)\rho_{\text{matrix}} + \phi \, \rho_{\text{fluid}}. \tag{2.7}$$

Finally, putting all the pieces together, the P-wave velocity V_p of a saturated rock can be expressed as:

$$V_p = \sqrt{\frac{K_{\text{sat}} + \frac{4}{3}G}{\rho_{sat}}}, \tag{2.8}$$

where the bulk modulus K_{sat} and the density of the saturated rock ρ_{sat} are both influenced by the presence of fluids in the rock pore space. Similarly, the shear-wave velocity V_s is given by:

$$V_s = \sqrt{\frac{G}{\rho_{sat}}}, \tag{2.9}$$

where G is the shear modulus of the rock frame, generally considered unaffected by fluid substitution.

More advanced rock-physics models account for inhomogeneous fluid distributions through patchy saturation models, in which individual fluids occupy isolated patches.

White (1975) first introduced the mesoscopic-loss mechanism. Considering a periodic ensemble of spherical gas pockets in a water-saturated porous medium, White (1975) predicted the associated seismic attenuation and velocity dispersion. Later works generalized the concept to more realistic fluid arrangements, introducing patches of arbitrary shape (e.g., Johnson (2001); Pride et al. (2004); Toms et al. (2007)), then calculating P-wave attenuation and dispersion.

Particularly, Johnson (2001) introduced the dynamic bulk modulus $K(\omega)$, where ω is the angular frequency. $K(\omega)$ describes the crossover between the low frequency and the high frequency limits, respectively the BGW model and the BGH model (Hill, 1963). The first assumes uniform fluid pressure throughout the pore space, while the latter assumes there is insufficient time for pressure equilibration between fluid patches. $K(\omega)$ and the subsequent P-wave modulus ($E(\omega)$) are expressed as:

$$K(\omega) = K_{GH} - \frac{K_{GH} - K_{GW}}{1 - \xi + \xi\sqrt{1 - i\omega\tau/\xi^2}}, \tag{2.10}$$

$$E(\omega) = K(\omega) + \frac{4}{3}G_{dry}, \tag{2.11}$$

where G_{dry} denotes the dry shear modulus of the rock-frame, unaffected by fluid substitution. The parameters ξ and τ are derived independently from S/V and T (Johnson, 2001). They are not empirical fitting constants, instead, ξ represents a geometrical shape factor, while τ defines the characteristic frequency scale. If $\xi < 1$, the crossover region extends over a broad frequency range, whereas for $\xi > 1$ the transition becomes relatively narrow. The parameter S/V is controlled by the morphology of the patches, whereas T is related to the average patch size in a complex and non-local manner, which can only be resolved under simplified geometrical assumptions (Johnson, 2001). The complex P-wave velocity $V_{p,c}$ is then given by:

$$v_{p,c}(\omega) = \sqrt{\frac{E(\omega)}{\rho_{\text{sat}}}}. \tag{2.12}$$

From this expression, the frequency-dependent P-wave velocity is obtained as:

$$v_p(\omega) = \left[\text{Re}\left(\frac{1}{v_{p,c}(\omega)}\right)\right]^{-1}. \tag{2.13}$$

The associated attenuation factors for P-waves is defined by:

$$Q_p(\omega) = \frac{\mathrm{Re}\left(v_{p,c}^2(\omega)\right)}{\mathrm{Im}\left(v_{p,c}^2(\omega)\right)}. \tag{2.14}$$

Seismic properties of the fluids

Injection of fluids such as CO_2 or H_2, which have much lower bulk modulus and density than the in-situ brine they replace, causes a decrease in the acoustic impedance within the reservoir. To quantify this effect, accurate fluid properties estimation, specific to the site conditions is required. Figure 2.2.3 compares fluid properties from the National Institute of Standards and Technology (NIST) database with those calculated using the Peng–Robinson Equation of State (PR-EoS) (Peng and Robinson, 1976), as a function pressure and temperature, which in turn depend on depth. Specifically, the temperature T_c (eq. 2.15) and pore pressure p (eq. 2.16) variation with depth z is expressed as:

$$T_c = T_0 + Gz, \tag{2.15}$$

$$p = p_0 + \bar{\rho}_b g z, \tag{2.16}$$

where G is the geothermal gradient set to 25 °C/km, T_0 is the surface temperature, p_0 is the atmospheric pressure, $\bar{\rho}_b$ is the average brine density from the surface to depth z, and g is the gravitational acceleration. Brine properties was calculated using Batzle and Wang (1992) equations, who developed relationships for the density and sonic velocity of brines as a function of pressure, temperature, and salinity. Viscosity is essential for the quantification of seismic attenuation in the Johnson model. The viscosities of H_2 and CO_2 are determined as a function of pressure and temperature from the Lohrenz-Bray-Clark theory (Lohrenz et al., 1964).

The three panels in Figure 2.2.3 illustrate the depth dependence of density, acoustic velocity, and bulk modulus for brine, CO_2, and H_2. In Figure 2.2.3.a, brine density shows a slight, but systematic, decrease along the geothermal gradient. In contrast, CO_2 exhibits a strong non-linear increase in density, particularly between 0 and 1500 m depth, as it transitions from a gaseous state to a supercritical state. At greater depths, CO_2 density stabilises around values typical of liquid phase. Hydrogen, on the other hand, remains extremely light, being the density values orders of magnitude lower than both CO_2 and brine, showing only a weak increase with depth.
In Figure 2.2.3.b, the bulk modulus of brine increases with depth, reaching a maximum at intermediate depths before slightly decreasing at greater depth due to the dominance of thermal effects. For CO_2, the bulk modulus rises sharply up to 1000 m, reflecting the transition into the supercritical regime, and then continues to increase approximately

linearly with depth. Hydrogen maintains the same bulk modulus than CO_2 up to 1000 m, but increases gradually with pressure, although it remains much smaller than brine and CO_2 towards higher depths.
The velocity of acoustic waves in gases given by $V_g = \sqrt{K_g/\rho_g}$ is shown in Figure 2.2.3.c, where K_g and ρ_g are bulk modulus and density of the gas, respectively. CO_2 shows a sharp velocity decrease up to 1000 m, corresponding to the density transition observed in the top panel, after which its velocity grows more gradually. H_2 displays relatively low velocities across the depth range, with only a modest increase under higher pressure. The P-wave velocity of brine increases steadily with depth, reflecting the combined effects of rising pressure and moderate temperature increase.

The geophysical and rock-physics methodologies developed for fluid migration monitoring can also be effectively transferred to the exploration of naturally occurring geological hydrogen. Experience in monitoring the behaviour of injected CO_2 in porous media has advanced our ability to link fluid saturation and pressure changes to elastic and petrophysical property variations, which are observable through seismic imaging. Similar principles apply to natural hydrogen exploration, where seismic and rock physics methods are critical for delineating structural traps, identifying reservoir heterogeneities, and distinguishing between gas-bearing and non-gas lithologies (Li and Zhang, 2025). Furthermore, seismic monitoring complements potential-field and electromagnetic methods by imaging reservoir-scale accumulations and migration pathways, thereby reducing the overall exploration risk (Jackson et al., 2024; Su et al., 2025).

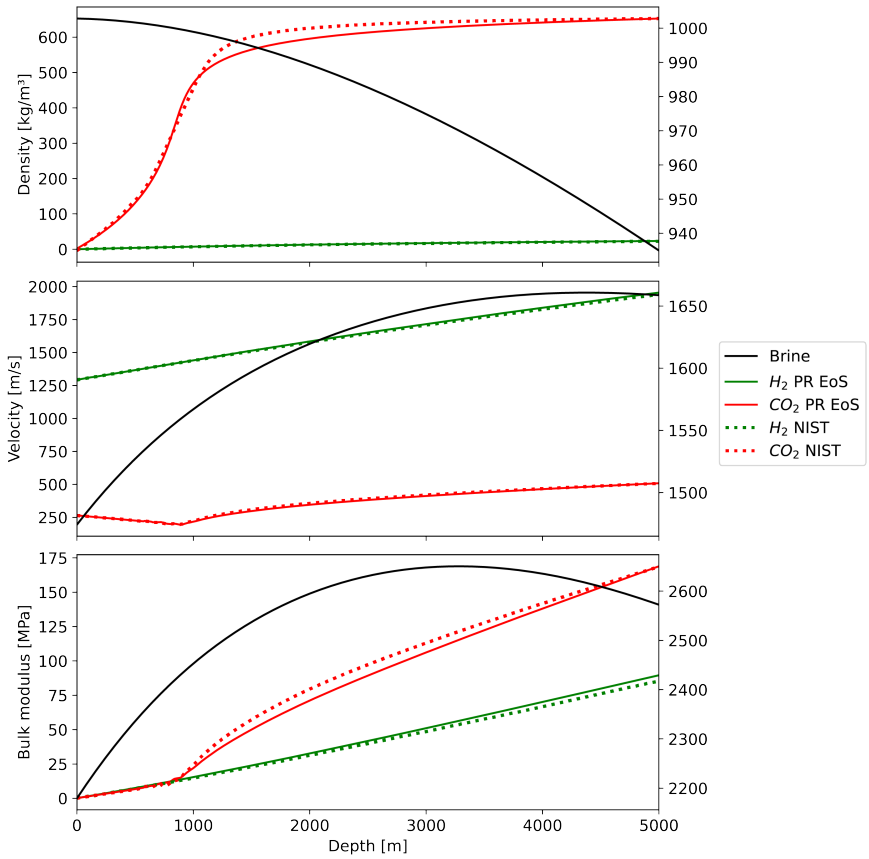

Figure 2.2.3: Gas properties of CO_2 and H_2 calculated using PR-EoS. Python codes used to compute PR-EoS are available at `figshare.com/s/af33b896cd45ed71b4ab`. Solid lines indicate properties calculated using PR-EoS, whereas dotted lines indicate data from NIST. NIST gas properties from `webbook.nist.gov/chemistry/fluid/` (Lemmon, 2010). Brine properties refer to the right-hand y-axis in each panel.

CO_2 and hydrogen-related elastic properties changes

Extensive research has been focused on understanding the elastic property changes associated with CO_2 storage. Field and laboratory studies consistently demonstrate measurable elastic changes during CO_2 injection. At Sleipner storage field, time-lapse seismic over more than two decades document plume growth and the associated elastic responses (Arts et al., 2008; Furre and Eiken, 2014). At the Ketzin storage site, rock-physics modelling combined with AVO/AVA analysis revealed that even low levels of CO_2 saturation cause measurable decreases in P-wave velocity. Laboratory experiments have confirmed these trends and shown that seismic response is strongly influenced by the spatial distribution of CO_2, whether it is uniformly mixed or irregular (Kazemeini et al., 2010; Kummerow and Spangenberg, 2011). At the Otway Project site, repeatable

4D surveys track small supercritical CO_2 injections and corresponding velocity/amplitude changes (Pevzner et al., 2017). A parallel research stream separates pressure and saturation effects on elastic properties using time-lapse AVO and time-shift methods (Landrø, 2001; Meadows, 2001), approaches that are now a standard in quantitative 4D interpretation. Integrated geomechanical monitoring at the In Salah project site showed that injection-induced pressure changes caused elastic deformation of the rock mass and, locally, permanent strain along pre-existing fractures, linking surface deformation, seismic velocity variations, and subsurface stress evolution (Vasco et al., 2008; Ringrose et al., 2013; Rinaldi and Rutqvist, 2013; Bohloli et al., 2017; White et al., 2014).

Building on these pioneering demonstrations, the main focus is now shifting towards large-scale commercial projects, which represent the next generation of CCS projects. The Northern Lights project, part of Norway's Longship CCS initiative, is the world's first open-source offshore CO_2 transport and storage development (EQUINOR, 2025b). Its Aurora site, located about 110 km offshore on the Horda Platform, targets a deep saline aquifer in the Lower Jurassic Dunlin Group at ∼2.6–2.7 km depth. Shallow-marine sandstones of the Johansen and Cook formations provide the primary reservoirs, sealed by the thick Drake shale (Legeay et al., 2024). Phase 1 started the injection in late august 2025, storing about 37.5 Mt of CO_2 at ∼1.5 Mt/yr using one main and one contingent injector, while a planned Phase 2 aims to exceed ∼5 Mt/yr, starting from the second half of 2028 (EQUINOR, 2025a). A comprehensive monitoring program, combining a 2022 high-resolution 3D seismic baseline, repeated active and passive seismic surveys, continuous in-well pressure/temperature measurements, fibre-optic DAS, and environmental surveys, will track plume migration and ensure containment throughout operations and post-closure (Legeay et al., 2024; Acuna et al., 2024a,b).

Limited work has focused on rock-physics analyses of how hydrogen influences the elastic properties of gas-bearing reservoir rocks, but recent studies have begun to fill this gap. In fact, recent research has advanced the understanding of how hydrogen injection alters subsurface elastic properties and how these changes can be monitored seismically. Li and Bhattacharya (2024) show, through rock-physics modelling and AVA/AVO simulations, that hydrogen saturation non-linearly reduces P-wave velocity, being most sensitive at low saturations, while S-wave velocity and density decrease more linearly, producing distinctive amplitude-versus-angle responses at reservoir-caprock interfaces. Complementing this physics-based approach, Gao et al. (2024) develop a machine-learning framework that links rock-physics models of H_2-saturated rocks to synthetic seismic waveforms, enabling detection and characterization of leakage even from spatially limited time-lapse data.

Further confirmation is provided by laboratory measurements. Bijay et al. (2024) demonstrated, through ultrasonic experiments on Berea sandstone cores, that P-wave velocity non-linearly decreases with increasing hydrogen saturation, showing a total reduction of about 3.5% at 36% H_2 saturation relative to the fully water-saturated state. They also observe a marked drop in waveform amplitude, indicating stronger attenuation with rising gas content. Using a Gassmann fluid-substitution framework, they found that the measured velocities fall between the Voigt and Reuss boundaries, suggesting a predominantly patchy fluid distribution inside the specimen. These findings show that P-wave velocity is sensitive to hydrogen saturation and support the use of 4D seismic surveys to track hydrogen plume migration and detect potential leakage in underground hydrogen storage reservoirs.

2.2.2 Deep Learning Tools for Seismic Monitoring

Convolutional Neural Network (CNN)

Convolutional Neural Networks (CNNs) have emerged as a dominant architecture within the field of deep learning, particularly for image recognition and classification tasks. A CNN is designed to process images, allowing it to automatically learn and extract hierarchical features from raw digital data. This process begins at the input layer, where the image is fed into the system, followed by several convolutional and pooling layers (Figure 2.2.4). Convolutional layers apply a series of filters to detect various features like edges or textures, effectively reducing the input dimensionality. Pooling layers further downsample the output to diminish computational load and focus on the most significant information while retaining features invariant to scale and position (Li et al., 2022).

CNNs are usually trained with supervised learning, where the network learns from labelled datasets. During training, the model updates its filters and weights to reduce prediction errors (Yamashita et al., 2018). In this way, the CNN learns the most important features automatically, without the need for manual feature engineering. The flattened feature vector acts as a compressed representation of the input, containing its most important information in a smaller form (Shen et al., 2020). This representation is then used by the dense layers to make predictions, such as assigning the image to a class. CNNs utilize back-propagation for training, adjusting weights based on the error in prediction outcomes, which enables effective learning of complex patterns from labelled training datasets (Yamashita et al., 2018). Over the years, various advanced architectures of CNNs have been developed to enhance performance across multiple computer vision tasks. Prominent examples include VGGNet, GoogLeNet, and ResNet, each contributing unique design innovations that address challenges related to depth, efficiency, and feature learning in CNNs (Guo and Zhang, 2019).

A pivotal CNN architecture is U-Net (Ronneberger et al., 2015), which was primarily designed for the task of image segmentation, which involves separating and labelling different regions or objects within an image. It is characterized by its distinctive U-shaped design, which consists of an encoder-decoder structure (Figure 2.2.5). The encoder gradually compresses the input image, extracting features through multiple convolutional and pooling layers, while the decoder progressively reconstructs the image to generate an accurate segmentation map. This architecture uses skip connections, which allow feature maps from earlier layers in the encoder to be concatenated with corresponding layers in the decoder, facilitating high-resolution outputs and improving segmentation accuracy, particularly in medical images. These skip connections help the model recover fine details that were lost when the image was reduced. This design allows U-Net to make pixel-level predictions with high accuracy. Because of its efficiency and skip connections, U-Net works well even with smaller training datasets, which is why it is popular in areas like medical imaging, where labelled data are limited (Ronneberger et al., 2015).

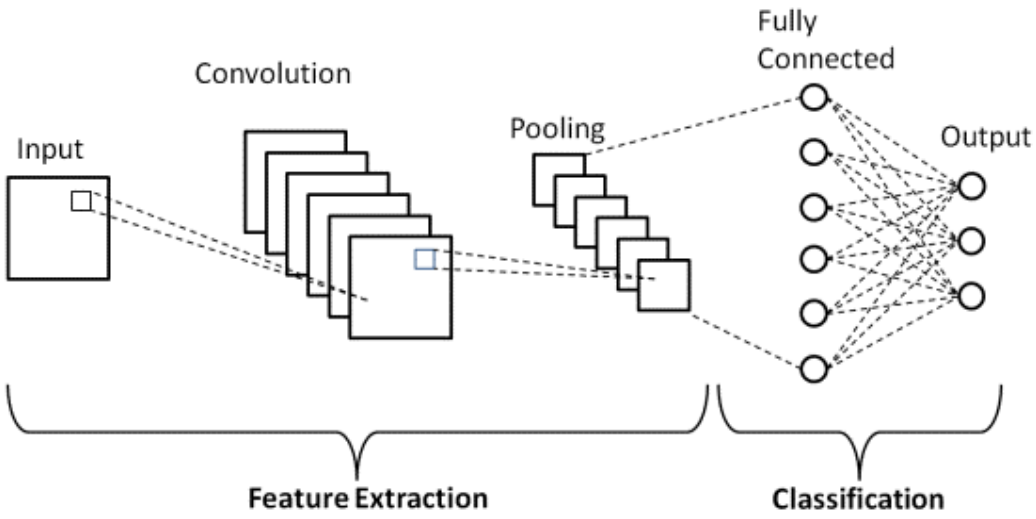

Figure 2.2.4: Basic CNN architecture (Phung and Rhee, 2019).

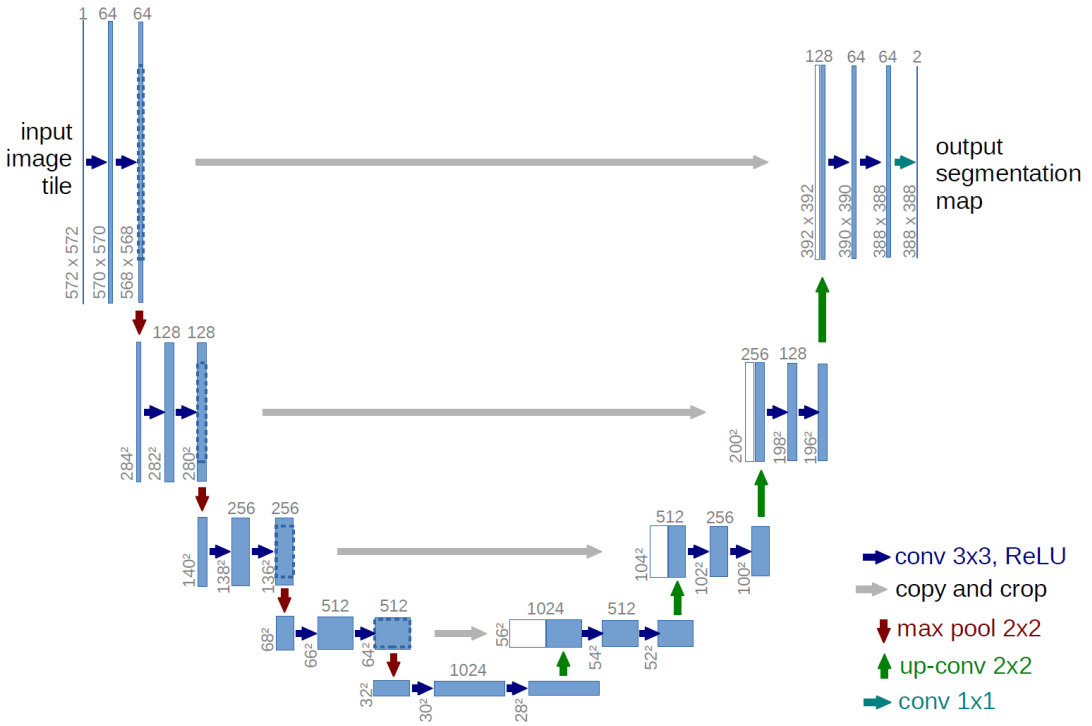

Figure 2.2.5: U-Net architecture for image segmentation. Source (Ronneberger et al., 2015): each blue box corresponds to a multi-channel feature map. The number of channels is denoted on top of the box. The x-y-size is provided at the lower left edge of the box. White boxes represent copied feature maps. The arrows denote the different operations.

Uniform Manifold Approximation and Projection (UMAP) for dimensionality reduction

Unlike a CNN, which learns a direct mapping between inputs and outputs, UMAP is an unsupervised method for visualizing and exploring data. It is a non-linear dimensionality reduction algorithm that transforms data from a high-dimensional space into a lower-dimensional representation, most commonly in two or three dimensions, while preserving the essential structure of the dataset. In practice, this means that UMAP produces a two-dimensional map in which points that were close in the original space remain close, whereas points that were dissimilar are placed farther apart. This property makes UMAP a powerful tool for visualization because it reveals clusters and patterns even in complex datasets that cannot be observed in very high dimensions. Compared to the earlier t-SNE algorithm, UMAP tends to preserve the global structure of the data more effectively, maintaining meaningful distances between distant clusters, and it is computationally more efficient, which makes it suitable for large-scale applications (McInnes et al., 2018).

UMAP operates by constructing a nearest-neighbour graph in the high-dimensional space and then computing a low-dimensional embedding that preserves this structure. The algorithm ensures that points that are close in the original space remain close in the two- or three-dimensional representation, while points that are distant in the original space are also kept apart in the embedding (Theodo, 2024). In this way, UMAP is able to preserve both the fine-scale clustering of very similar samples, which appear as compact groups, and the broader-scale separation between different regions of the data, which remain clearly distinct. The resulting visualization highlights clusters and patterns that may not be visible in the original high-dimensional space and facilitates the identification of natural groupings or anomalous samples (Figure 2.2.6).

By utilizing UMAP for dimensionality reduction of embeddings from the latent space of CNNs, researchers can uncover significant clusters and intrinsic structures in data that may otherwise remain obscured in higher dimensions. This aspect of UMAP is particularly beneficial for enhancing the interpretability of CNNs, which are often seen as "black boxes" due to their inherent complexity. The adoption of UMAP in conjunction with CNN embeddings fosters a better understanding of the learned representations and aids in the refinement of model performance through subsequent analysis and visualization.

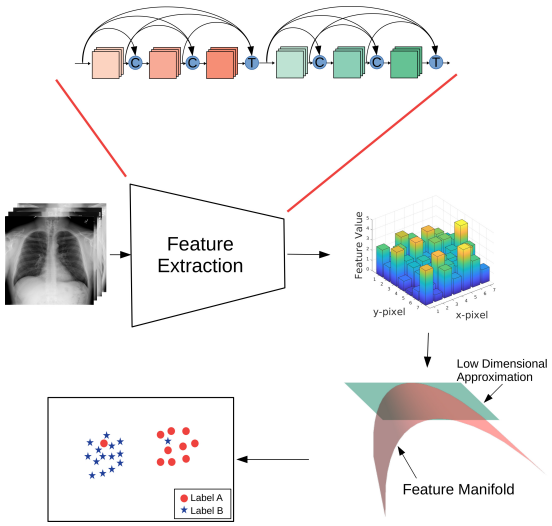

Figure 2.2.6: Schematic example of a framework proposed by Islam and Fleischer (2025) for feature extraction and dimensionality reduction using medical images. Image features extracted from a pre-trained neural network are projected onto a low-dimensional space (2-D plane) using UMAP.

In the domain of representation learning, autoencoders (AEs) play a crucial role. An autoencoder is a specific type of neural network that learns a compact representation of input data, which can subsequently be used to reconstruct the original input (Goodfellow et al., 2016). The typical structure of an autoencoder consists of an encoder, which compresses the input data into a latent vector, a bottleneck layer called a hidden latent vector, and a decoder that attempts to reconstruct the original data from this representation (Alain and Bengio, 2014) (Figure 2.2.7). AE with a single hidden layer in the encoder and decoder can be represented by the following equations:

$$z = \sigma\left(W_{\text{encoder}} x + b_{\text{encoder}}\right), \tag{2.17}$$

$$\hat{x} = \sigma\left(W_{\text{decoder}} z + b_{\text{decoder}}\right), \tag{2.18}$$

where x represents the input vector, z represents the bottleneck low-dimensional feature space, σ is an activation function, and W and b are the weight and bias parameters, respectively. Equation (2.17) is used by the encoder network to map the input features into low-dimensional features, while the decoder network uses Equation (2.18) to recover the original data x from the projected low-dimensional features z. This encoding-decoding process is fundamental for tasks such as feature extraction and data compression, positioning autoencoders as essential components in various machine learning applications, including features detection and image compression.

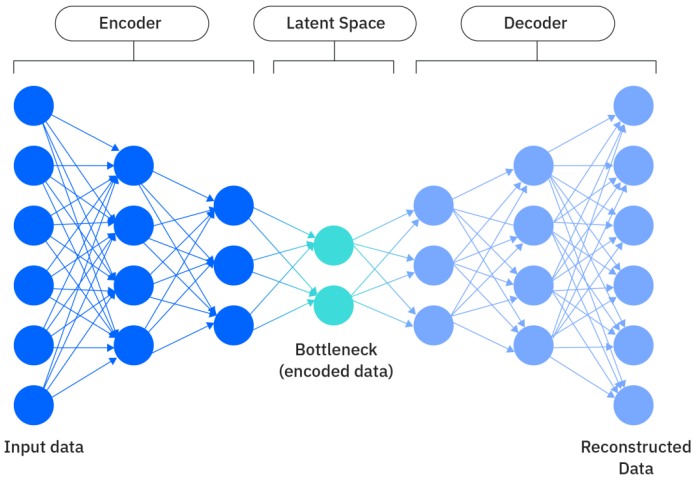

Figure 2.2.7: General structure of an autoencoder (AE).

In specific applications, the encoder in frameworks like ResNet (Figure 2.2.8) (He et al., 2016), is utilized to progressively downsample input images, and extract higher-level features and representations. These latent representations can be effectively used as inputs for downstream tasks or are further analysed using dimensionality reduction techniques like UMAP to identify relationships and patterns within the data. Moreover, UMAP and autoencoders can integrate seamlessly to enhance representation learning. For instance, the latent space generated by a CNN can be refined using UMAP, revealing complex relationships and clusters that improve the interpretability and usability of CNN embeddings. This integration between UMAP and autoencoders facilitates innovative approaches to data analysis, enabling researchers to leverage high-dimensional embeddings for various applications, including medical imaging, data visualization, and anomaly detection.

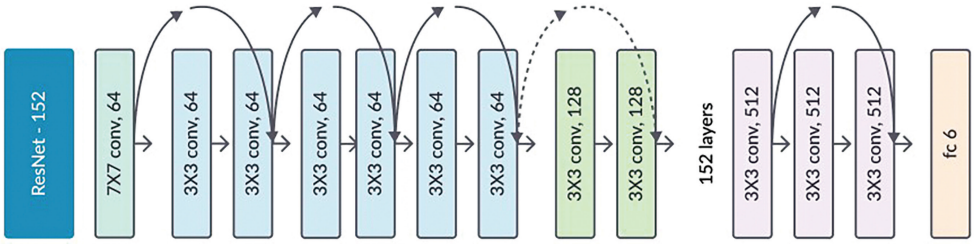

Figure 2.2.8: ResNet-152 neural network architecture (He et al., 2016).

2.2.3 Automatic Differentiation for Full-Waveform Inversion

Full-waveform inversion (FWI) is a seismic imaging method that estimates subsurface parameters by minimizing the misfit between recorded seismic wavefield and simulated wavefield solving the wave equation. In general, FWI leverages the full information content of the wavefield to recover high-resolution models of the elastic moduli (Tarantola, 1984; Pratt, 1999; Virieux and Operto, 2009). In seismic monitoring, time-lapse FWI can sharpen sensitivity to fluid-induced changes, improving the resolution of seismic velocity changes associated with evolving fluids saturation. The FWI problem can be defined as follows:

$$\mathbf{m}_{\text{FWI}} = \arg\min_{\mathbf{m}} \phi_{\text{FWI}}(\mathbf{m}) = \arg\min_{\mathbf{m}} \tfrac{1}{2} \left\| \mathbf{f}(\mathbf{m}) - \mathbf{d}_{\text{obs}} \right\|_2^2, \tag{2.19}$$

where $\mathbf{f}(\mathbf{m})$ denotes the acoustic or elastic forward-modeling operator that solves the wave equation for model $\mathbf{m}$, and $\mathbf{d}_{\text{obs}}$ are the observed data. In practice, estimating $\mathbf{m}_{\text{FWI}}$ requires iterative, gradient-based algorithms and repeated evaluations of the objective function, each involving the numerical solution of thousands of wave equations. Moreover, ϕ_{FWI} typically admits multiple local minima, which makes the final solution

sensitive to the initial model choice (Virieux and Operto, 2009).

Traditionally, the gradient of the FWI objective function is derived through the adjoint-state method (Chavent et al., 1975), which requires both the derivation and the implementation of the adjoint equations associated with the chosen partial differential equation. Modern differentiable programming frameworks such as PyTorch (Paszke et al., 2019) provide reverse-mode automatic differentiation, also called autograd, which computes gradients through complex computational chains once the forward pass has been defined. Automatic Differentiation (AD) is an efficient way to compute gradients by applying the chain rule: the forward-pass computation is traced and the gradient at the final step is propagated back through each operator and parameter in the computational graph (Figure 2.2.9). This mechanism is the foundation of neural network training. Neural networks can be regarded as nested functions with parameters, consisting of weights and biases stored in tensors. Forward propagation produces predictions through successive linear transformations and non-linear activations, while backward propagation adjusts the parameters in proportion to the error by accumulating derivatives of the loss with respect to the trainable variables. The resulting gradients are then passed to gradient-based optimizers, which aim to reduce the discrepancy between predictions and ground-truth labels. Numerical simulations governed by partial differential equations share the same compositional structure, consisting of sequences of linear and non-linear transformations. An example is the finite-difference time-domain method (Yee, 1966), which applies finite-difference operators across consecutive time steps to solve time-dependent equations (Hughes et al., 2019). In seismic applications, forward simulations specify quantities such as wave velocity, source location or source-time functions in order to generate predicted signals. The gradients of data misfits with respect to these parameters can be computed automatically through AD, and incorporated into the same gradient-based optimization framework.

In the context of AD and its application within deep learning, the use of frameworks like PyTorch facilitates the reverse-mode back-propagation to compute gradients of a scalar loss function concerning model variables. This method processes the recorded computation graph without requiring manual derivation of adjoint equations, significantly simplifying the implementation of gradient-based optimization techniques (Richardson, 2018). The implications of employing AD in this manner are threefold:

- **Reduced development burden**: the same code used for the forward modelling is leveraged to automatically derive gradients. This eliminates complexity and potential errors involved in manually coding the adjoint equations (Richardson, 2018).

- **GPU efficiency**: PyTorch exploit GPU efficiency through parallelized computations allowing deep learning models to run efficiently (Paszke et al., 2019). This enhancement is particularly beneficial when handling large datasets or complex models that require extensive computation.
- **Flexible parametrization**: AD allows the inversion parameters to be defined in any differentiable form, including petrophysical variables such as porosity, saturation, or fluid moduli. These can be linked to elastic parameters through rock-physics relationships, ensuring physical consistency and reducing parameter cross-talk during inversion.

The flexible parametrization provides a natural bridge between automatic differentiation and rock-physics–constrained inversion. A rock-physics operator $\boldsymbol{\mathcal{G}}$ maps petrophysical parameters $\boldsymbol{\theta}$ (e.g., porosity, saturation) to elastic parameter $\mathbf{m}$, such that $\mathbf{m} = \mathcal{G}(\boldsymbol{\theta})$. When $\mathcal{G}$ is embedded in the computational graph, its derivatives are automatically propagated during back-propagation, enforcing physically consistent updates in $\boldsymbol{\theta}$ throughout the inversion process.

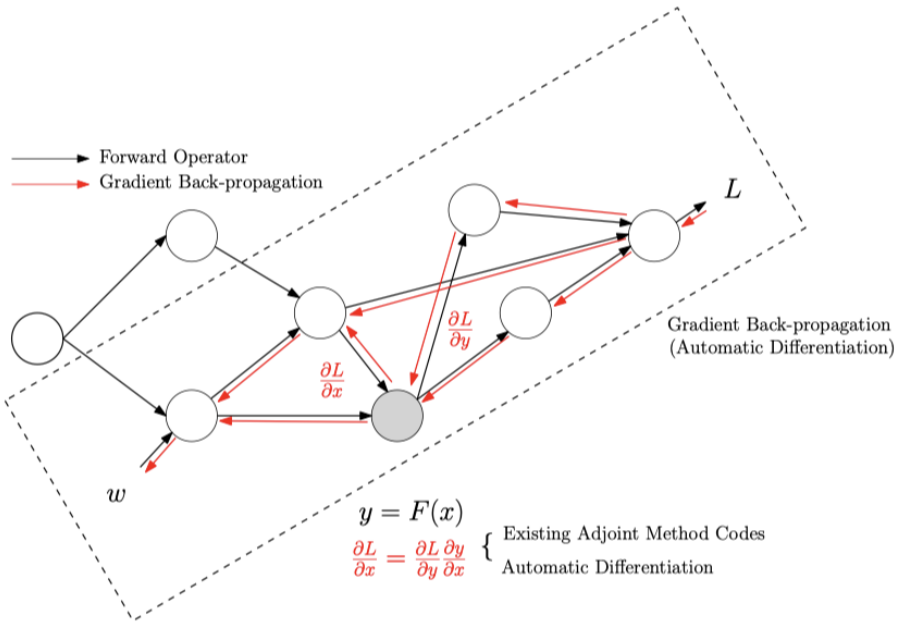

Figure 2.2.9: Computational graph representation of the forward and backward passes in automatic differentiation. Black arrows denote the forward operator, which maps input parameters w through successive operations to produce the output L. Red arrows illustrate the reverse-mode gradient back-propagation, where derivatives of the loss with respect to intermediate variables are propagated backward through the graph according to the chain rule. Image courtesy of Li (2023).

In recent years, the integration of rock physics into FWI methodologies has significantly enhanced geophysical exploration, particularly in tasks related to reservoir characterization and monitoring. In fact, rock physics establishes a quantitative relationship between the physical properties of rocks and the elastic properties inverted from geophysical data, improving the interpretation of seismic features and quantifying the subsurface physical parameters. Key studies have highlighted the crucial role of rock physics in linking geological features with geophysical targets, providing a quantitative bridge between rock properties and the elastic attributes inferred from seismic data (Mardan et al., 2023; Hu et al., 2021, 2022). Embedding rock-physics models within FWI frameworks further enhances subsurface characterization, particularly for reservoir monitoring, by translating seismic amplitudes (as well as other signal properties) into meaningful physical parameters (Avseth, 2010; Grana, 2014; Avseth et al., 2010b; Nasser and Sinton, 2012; Munyithya et al., 2019). Bayesian and probabilistic approaches further extend this concept by quantifying uncertainty in petrophysical predictions. For example, Queiroz and Grana (2025) proposed a Bayesian seismic–petrophysical inversion using non-linear rock-physics models, enabling robust estimation of reservoir parameters even in complex lithologies such as carbonates. Similarly, Rock Physics Templates (RPTs) provide a statistical framework for interpolating rock properties across lithologies, enhancing predictions in data-sparse areas (Hernandez et al., 2016).

Integrating these models directly into differentiable FWI pipelines marks a major step forward. Instead of inverting for elastic parameters and interpreting them afterward, the inversion can target petrophysical quantities directly, while keeping the physical relationships enforced through differentiable rock-physics operators. This end-to-end differentiable inversion ensures physically consistent updates, reduces non-uniqueness, and makes the results easier to interpret. In addition, combining AVO analysis with rock-physics models in differentiable frameworks has proven effective for estimating reservoir properties such as lithology and fluid saturation (Jensen et al., 2016; He et al., 2011; Grana et al., 2012). Thanks to GPU acceleration and the flexibility of deep-learning frameworks, these physics-informed inversion approaches can now be efficiently implemented and applied even to large-scale, time-lapse monitoring problems (Weinzierl and Wiese, 2021).

2.3 Conclusions

This introductory chapter has explained the scientific,social and environmental reasons for studying underground geological storage as part of the energy transition, with a focus on carbon capture and storage (CCS) and underground hydrogen storage (UHS).

Greenhouse gas emissions, primarily carbon-dioxide and methane, represent the dominant driver of contemporary climate change. Their continued accumulation in the atmosphere has led to unprecedented global temperature increases and poses major challenges for energy systems and society. International agreements and climate policies have already stimulated the progress in reducing emissions through energy efficiency, fuel substitution, and the expansion of renewables sources. However, current commitments remain insufficient to keep global warming within the limits of 1.5–2 °C, highlighting the urgent need for additional measures. Among the portfolio of mitigation strategies, CCS and UHS emerge as central technologies for enabling a secure and flexible low-carbon energy system. CCS provides a pathway to permanently dispose of large volumes of CO_2, mitigating emissions from hard-to-abate sectors such as heavy industry and fossil-fuel power generation. UHS, on the other hand, enables seasonal and large-scale storage of hydrogen, a clean energy carrier that can complement renewables and facilitate deep decarbonisation. Together, these two approaches extend the role of the subsurface from a source of hydrocarbons to a long-term enabler of climate mitigation and energy transition.

Both CCS and UHS depend critically on geological storage integrity. Site characterization, injectivity assessment, and secure containment over decades to centuries require detailed geophysical and geochemical understanding. Time-lapse geophysical monitoring has already proven effective in pioneering CCS projects where seismic surveys have provided direct evidence of safe containment and plume migration. Equivalent monitoring strategies will be essential for hydrogen storage, though technical challenges such as cyclic injection, weaker seismic contrasts, and microbial interactions remain active areas of research. Rock-physics provides the theoretical framework to link subsurface fluid and rock properties with geophysical observables. By quantifying how elastic moduli, density, and velocity respond to changes in saturation, pressure, and temperature, rock physics allows seismic data to be translated into estimates of CO_2 or hydrogen distributions. This capability underpins both monitoring and risk assessment, ensuring that subsurface storage operates within safe and predictable boundaries.

Recent advances in machine learning, automatic differentiation, and differentiable programming offer powerful new tools to integrate rock physics, seismic monitoring, and inversion. By combining physics-based modelling with data-driven approaches, it is becoming possible to improve resolution, reduce uncertainties, and develop monitoring systems that are both robust and adaptive. In particular, the use of automatic differentiation and deep learning opens opportunities for efficient gradient-based inversion and interpretation of complex datasets.

Bibliography

C Acuna, S Foss, A Furre, I Torsnes, L Fenstad, G Apeland, S Way, and P Glenister. 2024a. The Northern Lights Seismic Monitoring Plan and its 4D Baseline: Ready to Ensure Safe Operations. In *85th EAGE Annual Conference & Exhibition*. European Association of Geoscientists & Engineers, European Association of Geoscientists & Engineers, Oslo, Norway, 1–5. https://doi.org/10.3997/2214-4609.202410441

C Acuna, M Vinchon, A Furre, I Torsnes, and N Thomson. 2024b. Northern Lights CCS Monitoring: a Plan in Continuous Evolution. In *85th EAGE Annual Conference & Exhibition-Workshop Programme*. European Association of Geoscientists & Engineers, European Association of Geoscientists & Engineers, Oslo, Norway, 1–5. https://doi.org/10.3997/2214-4609.2024101838

Guillaume Alain and Yoshua Bengio. 2014. What regularized auto-encoders learn from the data-generating distribution. *J. Mach. Learn. Res.* 15, 1 (Jan. 2014), 3563–3593. https://doi.org/10.48550/arXiv.1211.4246

Binyam L Alemu, Eyvind Aker, Magnus Soldal, Øistein Johnsen, and Per Aagaard. 2013. Effect of sub-core scale heterogeneities on acoustic and electrical properties of a reservoir rock: A CO2 flooding experiment of brine saturated sandstone in a computed tomography scanner. *Geophysical Prospecting* 61, 1 (2013), 235–250. https://doi.org/10.1111/j.1365-2478.2012.01061.x

M. Ali et al. 2025. Recent progress in underground hydrogen storage – a review. *Energy & Environmental Science* 18, 18 (2025), 5740–5810. https://doi.org/10.1039/D4EE04564E

Rob Arts, Ole Eiken, A. Chadwick, et al. 2008. Ten years of experience of monitoring CO_2 injection in the Sleipner project. *Energy Procedia* 1, 1 (2008), 2029–2035. https://doi.org/10.1016/j.egypro.2009.01.264

Per Avseth. 2010. *Explorational Rock Physics – The Link Between Geological Processes and Geophysical Observables*. Springer Berlin Heidelberg, Berlin, Heidelberg, 403–426. https://doi.org/10.1007/978-3-642-02332-3_18

Per Avseth, Tapan Mukerji, and Gary Mavko. 2010a. *Quantitative seismic interpretation: Applying rock physics tools to reduce interpretation risk*. Cambridge university press, Cambridge. https://doi.org/10.1017/CBO9780511600074

Per Avseth, Tapan Mukerji, Gary Mavko, and Jack Dvorkin. 2010b. Rock-physics diagnostics of depositional texture, diagenetic alterations, and reservoir heterogeneity in high-porosity siliciclastic sediments and rocks — A review of selected models and suggested work flows. *GEOPHYSICS* 75, 5 (2010), 75A31–75A47. https://doi.org/10.1190/1.3483770

Michael Batzle and Zhijing Wang. 1992. Seismic properties of pore fluids. *Geophysics* 57, 11 (1992), 1396–1408. https://doi.org/10.1190/1.1443207

Sebastian Bauer, Andreas Dahmke, and Olaf Kolditz. 2017. Subsurface energy storage: geological storage of renewable energy—capacities, induced effects and implications. *Environmental Earth Sciences* 76, 20 (2017), 695. https://doi.org/10.1007/s12665-017-7007-9

Sally Benson, Jason Anderson, Stefan Bachu, Hassan Bashir Nimir, Biswajit Basu, John Bradshaw, Gota Deguchi, John Gale, Gabriela von Goerne, W Heidug, S Holloway, et al. 2005. Underground geological storage. In *IPCC special report on carbon dioxide capture and*

storage,. Cambridge University Press, Cambridge, 195–276. https://www.ipcc.ch/report/carbon-dioxide-capture-and-storage/underground-geological-storage/

Bijay, Luke P. Frash, Neala M. Creasy, Chelsea W. Neil, Prakash Purswani, Wenfeng Li, Meng Meng, Uwaila Iyare, and Michael R. Gross. 2024. Laboratory study of cyclic underground hydrogen storage in porous media with evidence of a dry near-well zone and evaporation induced salt precipitation. *International Journal of Hydrogen Energy* 71 (2024), 515–527. https://doi.org/10.1016/j.ijhydene.2024.05.234

Bahman Bohloli, Philip Ringrose, Lars Grande, and Bamshad Nazarian. 2017. Determination of the fracture pressure from CO2 injection time-series datasets. *International Journal of Greenhouse Gas Control* 61 (2017), 85–93. https://doi.org/10.1016/j.ijggc.2017.03.025

M. Bright and T. Lockwood. 2022. What does the latest IPCC report say about carbon capture? Clean Air Task Force. https://www.catf.us/2022/04/what-does-latest-ipcc-report-say-about-carbon-capture/

R.A. Chadwick, R. Arts, O. Eiken, et al. 2004. 4D seismic imaging of an injected CO_2 plume at the Sleipner Field, North Sea. In *Petroleum Geology Conference series*. Vol. 6. Geological Society, London, London, UK, 1385–1399. https://nora.nerc.ac.uk/id/eprint/7003/

G. Chavent, M. Dupuy, and P. Lemmonier. 1975. History Matching by Use of Optimal Theory. *Society of Petroleum Engineers Journal* 15, 01 (02 1975), 74–86. https://doi.org/10.2118/4627-PA

Leon Clarke, Yi-Ming Wei, Angel de la Vega Navarro, Amit Garg, Andrea N Hahmann, Smail Khennas, Inês ML Azevedo, Andreas Löschel, Ajay Kumar Singh, Linda Steg, et al. 2022. Energy systems. In *Climate Change 2022: Mitigation of Climate Change. Working Group III Contribution to the IPCC Sixth Assessment Report*. Cambridge University Press, Cambridge, 613–746. https://doi.org/10.1017/9781009157926.008

Neala Creasy, Lianjie Huang, Erika Gasperikova, William Harbert, Tom Bratton, and Quanlin Zhou. 2024. CO2 rock physics modeling for reliable monitoring of geologic carbon storage. *Communications Earth & Environment* 5 (06 2024). https://doi.org/10.1038/s43247-024-01493-6

Thomas L Davis, Martin Landrø, and Malcolm Wilson. 2019. *Geophysics and Geosequestration*. Cambridge University Press, Cambridge. https://doi.org/10.1017/9781316480724

Carlos Arnaiz del Pozo, Schalk Cloete, and Ángel Jiménez Álvaro. 2021. Carbon-negative hydrogen: Exploring the techno-economic potential of biomass co-gasification with CO2 capture. *Energy Conversion and Management* 247 (2021), 114712. https://doi.org/10.1016/j.enconman.2021.114712

EQUINOR. 2025a. *First CO2 volumes stored at Northern Lights*. Technical Report. Equinor ASA. https://www.equinor.com/news/20250825-first-co2-volumes-stored-at-northern-lights.

EQUINOR. 2025b. *The Northern Lights project*. Technical Report. Equinor ASA. https://www.equinor.com/energy/northern-lights..

Manzar Fawad and Nazmul Haque Mondol. 2021. Monitoring geological storage of CO2: a new approach. *Scientific Reports* 11, 1 (2021), 5942. https://doi.org/10.1038/s41598-021-85346-8

Manzar Fawad and Nazmul Haque Mondol. 2023. Quantifying Saturation in the Sleipner CO2 Storage:

A Rock Physics-Based Approach for Seismic Data Analysis. *CSEG Recoder* 1, 1 (2023), 1–22. https://shorturl.at/FCupH

Anne-Kari Furre, Ola Eiken, Håvard Alnes, Jonas Nesland Vevatne, and Anders Fredrik Kiær. 2017. 20 years of monitoring CO2-injection at Sleipner. *Energy procedia* 114 (2017), 3916–3926. https://doi.org/10.1016/j.egypro.2017.03.1523

A-K Furre, R Meneguolo, Philip Ringrose, and S Kassold. 2019. Building confidence in CCS: from Sleipner to the Northern Lights project. *First Break* 37, 7 (2019), 81–87. https://doi.org/10.3997/1365-2397.n0038

Anne-Marie Furre and Ole Eiken. 2014. Time-lapse seismic data from the Sleipner CO_2 storage project: A review. *Energy Procedia* 63 (2014), 5380–5387. https://doi.org/10.1016/j.egypro.2014.11.570

Kai Gao, Neala M. Creasy, Lianjie Huang, and Michael R. Gross. 2024. Underground hydrogen storage leakage detection and characterization based on machine learning of sparse seismic data. *International Journal of Hydrogen Energy* 61 (2024), 137–161. https://doi.org/10.1016/j.ijhydene.2024.02.296

Nicholas J. Gardiner, Jennifer J. Roberts, Gareth Johnson, Daniel J. Smith, Clare E. Bond, Rob Knipe, Stuart Haszeldine, Sarah Gordon, and Megan O'Donnell. 2023. Geosciences and the Energy Transition. *Earth Science, Systems and Society* 3, 1 (2023), 10072. https://doi.org/10.3389/esss.2023.10072

Fritz Gassmann. 1951. Elastic Waves Through a Packing of Spheres. *GEOPHYSICS* 16, 4 (1951), 673–685. https://doi.org/10.1190/1.1437718

Bettina P. Goertz-Allmann, Daniela Kühn, Volker Oye, Bahman Bohloli, and Eyvind Aker. 2014. Combining microseismic and geomechanical observations to interpret storage integrity at the In Salah CCS site. *Geophysical Journal International* 198, 1 (05 2014), 447–461. https://doi.org/10.1093/gji/ggu010

Ian Goodfellow, Yoshua Bengio, and Aaron Courville. 2016. *Deep Learning*. MIT Press, Cambridge, MA. http://www.deeplearningbook.org.

Dario Grana. 2014. Probabilistic approach to rock physics modeling. *GEOPHYSICS* 79, 2 (2014), D123–D143. https://doi.org/10.1190/geo2013-0333.1

Dario Grana, Marco Pirrone, and Tapan Mukerji. 2012. Quantitative log interpretation and uncertainty propagation of petrophysical properties and facies classification from rock-physics modeling and formation evaluation analysis. *GEOPHYSICS* 77, 3 (2012), WA45–WA63. https://doi.org/10.1190/geo2011-0272.1

Guodong Guo and Na Zhang. 2019. A survey on deep learning based face recognition. *Comput. Vis. Image Underst.* 189, C (Dec. 2019), 37 pages. https://doi.org/10.1016/j.cviu.2019.102805

Fu-Bang He, You Jun, and Kai-Yuan Chen. 2011. Gas Sand Distribution Prediction by Prestack Elastic Inversion Based on Rock Physics Modeling and Analysis. *Applied Geophysics* 8, 3 (2011), 197–205. https://doi.org/10.1007/s11770-011-0285-1

Kaiming He, Xiangyu Zhang, Shaoqing Ren, and Jian Sun. 2016. Deep Residual Learning for Image

Recognition. In *2016 IEEE Conference on Computer Vision and Pattern Recognition (CVPR)*. IEEE, NEW YORK, 770–778. https://doi.org/10.1109/CVPR.2016.90

William Marin Hernandez, Paola Newton, and Mario Di Luca. 2016. *Upscaled rock-physics templates for seismic reservoir characterization in thin-sand reservoirs*. SEG, Dallas, 3433–3437. https://doi.org/10.1190/segam2016-13971147.1

R. Hill. 1963. Elastic properties of reinforced solids: Some theoretical principles. *Journal of the Mechanics and Physics of Solids* 11, 5 (1963), 357–372. https://doi.org/10.1016/0022-5096(63)90036-X

Qi Hu, Dario Grana, and Kristopher A Innanen. 2022. Feasibility of seismic time-lapse monitoring of CO2 with rock physics parametrized full waveform inversion. *Geophysical Journal International* 233, 1 (11 2022), 402–419. https://doi.org/10.1093/gji/ggac462

Qi Hu, Scott Keating, Kristopher A. Innanen, and Huaizhen Chen. 2021. Direct updating of rock-physics properties using elastic full-waveform inversion. *GEOPHYSICS* 86, 3 (2021), MR117–MR132. https://doi.org/10.1190/geo2020-0199.1

Tyler W. Hughes, Ian A. D. Williamson, Momchil Minkov, and Shanhui Fan. 2019. Wave physics as an analog recurrent neural network. *Science Advances* 5, 12 (2019), eaay6946. https://doi.org/10.1126/sciadv.aay6946

IEA. 2021. Net Zero by 2050: A Roadmap for the Global Energy Sector. IEA Report. https://iea.blob.core.windows.net/assets/deebef5d-0c34-4539-9d0c-10b13d840027/NetZeroby2050-ARoadmapfortheGlobalEnergySector_CORR.pdf

IEA2020. 2020. *Outlook for biogas and biomethane: prospects for organic growth*. OECD Publishing, Paris. https://www.iea.org/reports/outlook-for-biogas-and-biomethane-prospects-for-organic-growth

IEAa. 2025. Global Energy Review 2025. https://www.iea.org/reports/global-energy-review-2025 Accessed 16 Sep 2025.

IEAb. 2025. CCUS projects around the world are reaching new milestones. https://www.iea.org/commentaries/ccus-projects-around-the-world-are-reaching-new-milestones IEA Commentary, 30 April 2025.

IPCC. 2022a. The evidence is clear: the time for action is now. We can halve emissions by 2030. https://www.ipcc.ch/2022/04/04/ipcc-ar6-wgiii-pressrelease/. Accessed 16 Sep 2025.

IPCC. 2022b. *Mitigation Pathways Compatible with 1.5°C in the Context of Sustainable Development*. Cambridge University Press, Cambridge, 93–174. https://doi.org/10.1017/9781009157940.004

IPCC. 2023. Sections. In: Climate Change 2023: Synthesis Report. Contribution of Working Groups I, II and III to the Sixth Assessment Report of the Intergovernmental Panel on Climate Change [Core Writing Team, H. Lee and J. Romero (eds.)]. https://www.ipcc.ch/report/ar6/syr/. , 35–115 pages. https://doi.org/10.59327/IPCC/AR6-9789291691647 Accessed 16 Sep 2025.

Mohammad Tariqul Islam and Jason W. Fleischer. 2025. Outlier Detection in Large Radiological Datasets Using UMAP. In *Topology- and Graph-Informed Imaging Informatics*, Chao Chen, Yash

Singh, and Xiaoling Hu (Eds.). Springer Nature Switzerland, Cham, 111–121. https://doi.org/10.48550/arXiv.2407.21263

O. Jackson, S. R. Lawrence, I. P. Hutchinson, A. E. Stocks, A. C. Barnicoat, and M. Powney. 2024. Natural hydrogen: Sources, systems and exploration plays. *Geoenergy* 2, 1 (2024), 1–9. https://doi.org/10.1144/geoenergy2024-002

Erling Hugo Jensen, Tor Arne Johansen, Per Avseth, and Kenneth Bredesen. 2016. Quantitative interpretation using inverse rock-physics modeling on AVO data. *The Leading Edge* 35, 8 (2016), 677–683. https://doi.org/10.1190/tle35080677.1

David Linton Johnson. 2001. Theory of frequency dependent acoustics in patchy-saturated porous media. *The Journal of the Acoustical Society of America* 110, 2 (2001), 682–694. https://doi.org/10.1121/1.1381021

Alina Kabuth, Andreas Dahmke, Christof Beyer, Lars Bilke, Frank Dethlefsen, Peter Dietrich, Rainer Duttmann, Markus Ebert, Volker Feeser, Uwe-Jens Görke, Ralf Köber, Wolfgang Rabbel, Tom Schanz, Dirk Schäfer, Hilke Würdemann, and Sebastian Bauer. 2016. Energy storage in the geological subsurface: dimensioning, risk analysis and spatial planning: the ANGUS+ project. *Environmental Earth Sciences* 76, 1 (2016), 23. https://doi.org/10.1007/s12665-016-6319-5

S. H. Kazemeini, C. Juhlin, A. Giese, and B. Norden. 2010. Time-lapse seismic monitoring of CO_2 injection into a saline aquifer at Ketzin, Germany. *Geophysical Prospecting* 58, 5 (2010), 871–883. https://doi.org/10.1111/j.1365-2478.2010.00874.x

Samuel Krevor, Heleen De Coninck, Sarah E Gasda, Navraj Singh Ghaleigh, Vincent de Gooyert, Hadi Hajibeygi, Ruben Juanes, Jerome Neufeld, Jennifer J Roberts, and Floris Swennenhuis. 2023. Subsurface carbon dioxide and hydrogen storage for a sustainable energy future. *Nature Reviews Earth & Environment* 4, 2 (2023), 102–118. https://doi.org/10.1038/s43017-022-00376-8

Juliane Kummerow and Erik Spangenberg. 2011. Experimental studies on CO_2–brine–rock interaction at Ketzin storage site: Impact on petrophysical properties. *International Journal of Greenhouse Gas Control* 5, 4 (2011), 1004–1011. https://doi.org/10.1016/j.ijggc.2011.03.012

M. Landrø. 2001. Discrimination between pressure and fluid saturation changes from time-lapse seismic data. *Geophysics* 66, 3 (2001), 836–844. https://doi.org/10.1190/1.1444973

Martin Landro and Lasse Amundsen. 2018. *Introduction to exploration geophysics with recent advances*. Bivrost Geo, Riga, Latvia. https://books.google.it/books/about/Introduction_to_Exploration_Geophysics_w.html?id=avPEvQEACAAJ&redir_esc=y

E Legeay, M Vinchon, L Fritz, and J Adam. 2024. Detailed Geological Characterization of the Aurora CO2 Storage Site, Northern North Sea. In *Fifth EAGE Global Energy Transition Conference & Exhibition (GET 2024)*, Vol. 2024. European Association of Geoscientists & Engineers, EAGE, Rotterdam, The Netherlands, 1–5. https://doi.org/10.3997/2214-4609.202421120

Eric W Lemmon. 2010. Thermophysical properties of fluid systems. https://webbook.nist.gov/chemistry/fluid/

Chao Li and Shuvajit Bhattacharya. 2024. *Seismic amplitude variation with angle response of hydrogen-saturated rock: Implications on subsurface monitoring*. SEG, Houston, TX, 104–108. https://doi.org/10.1190/image2024-4100439.1

Dongzhi Li. 2023. FwiFlow.jl Documentation (Version 0.2). https://github.com/lidongzh/FwiFlow.jl/blob/master/docs/src/index.md. Accessed: September 16, 2025.

Y. Li and M. Zhang. 2025. Geologic hydrogen exploration by imaging key hydrogen system components using multiple geophysical methods. *Journal of Geophysics and Engineering* 22, 3 (2025), 952–961. https://doi.org/10.1093/jge/gxaf047

Zewen Li, Fan Liu, Wenjie Yang, Shouheng Peng, and Jun Zhou. 2022. A Survey of Convolutional Neural Networks: Analysis, Applications, and Prospects. *IEEE Transactions on Neural Networks and Learning Systems* 33, 12 (2022), 6999–7019. https://doi.org/10.1109/TNNLS.2021.3084827

John Lohrenz, Bruce G Bray, and Charles R Clark. 1964. Calculating viscosities of reservoir fluids from their compositions. *Journal of Petroleum Technology* 16, 10 (1964), 1171–1176. https://doi.org/10.2118/915-PA

L. Londe. 2022. Four ways to store large quantities of hydrogen. Geostock Group technical article. https://www.geostockgroup.com/en/four-ways-to-store-large-quantities-of-hydrogen/

Amir Mardan, Bernard Giroux, Gabriel Fabien-Ouellet, and Mohammad Reza Saberi. 2023. Monitoring fluid saturation in reservoirs using time-lapse full-waveform inversion. *Geophysical Prospecting* 71, 6 (2023), 1012–1029. https://doi.org/10.1111/1365-2478.13363

van Unen Marianne, van der Valk Kaj, Brunner Logan, and Groenenberg Remco. 2020. *Inventory of risks associated with underground storage of compressed air (CAES) and hydrogen (UHS), and qualitative comparison of risks of UHS vs. underground storage of natural gas (UGS).* Technical Report TNO2020 R12005. TNO – Netherlands Organisation for Applied Scientific Research, The Hague, The Netherlands. 47 pages. https://repository.tno.nl/SingleDoc?find=UID%204a8bfbac-9b18-4499-945c-807c6ca7872e

Gary Mavko, Tapan Mukerji, and Jack Dvorkin. 2009. *The Rock Physics Handbook: Tools for Seismic Analysis of Porous Media* (2 ed.). Cambridge University Press, Cambridge. https://doi.org/10.1017/CBO9780511626753

Leland McInnes, John Healy, Nathaniel Saul, and Lukas Großberger. 2018. UMAP: Uniform Manifold Approximation and Projection. *Journal of Open Source Software* 3, 29 (2018), 861. https://doi.org/10.21105/joss.00861

Christopher J. McMahon, Jennifer J. Roberts, Gareth Johnson, Katriona Edlmann, Stephanie Flude, and Zoe K. Shipton. 2023. Natural hydrogen seeps as analogues to inform monitoring of engineered geological hydrogen storage. *Geological Society, London, Special Publications* 528, 1 (2023), 461–489. https://doi.org/10.1144/SP528-2022-59

Melissa A. Meadows. 2001. Time-lapse seismic monitoring of CO_2 injection: Pressure and saturation effects. *The Leading Edge* 20, 12 (2001), 1350–1355. https://doi.org/10.1190/1.1487166

Johannes Miocic, Niklas Heinemann, Katriona Edlmann, Jonathan Scafidi, Fatemeh Molaei, and Juan Alcalde. 2023. Underground hydrogen storage: a review. *Geological Society, London, Special Publications* 528, 1 (2023), 73–86. https://doi.org/10.1144/SP528-2022-88

J. M. Munyithya, C.N. Ehirim, and Tamunonengiyeofori Dagogo. 2019. Rock Physics Models and Seismic Inversion in Reservoir Characterization, "MUN" Onshore Niger Delta Field. *International Journal of Geosciences* 10 (2019), 981–994. https://doi.org/10.4236/ijg.2019.1011056

Seiji Nakagawa, Timothy J Kneafsey, Thomas M Daley, Barry M Freifeld, and Emily V Rees. 2013. Laboratory seismic monitoring of supercritical CO2 flooding in sandstone cores using the Split Hopkinson Resonant Bar technique with concurrent X-ray computed tomography imaging. *Geophysical Prospecting* 61, 2-Rock Physics for Reservoir Exploration, Characterisation and Monitoring (2013), 254–269. https://doi.org/10.1111/1365-2478.12027

Mosab Nasser and John B. Sinton. 2012. *Integrating rock physics and full elastic modeling for reservoir characterization.* SEG, San Antonio, TX, 2886–2890. https://doi.org/10.1190/1.3627794

NOAA. 2025. NOAA Global Monitoring Laboratory - Trends in Atmospheric Carbon Dioxide (CO_2). https://gml.noaa.gov/ccgg/trends/. Accessed 10 Oct 2025.

Ilissa B Ocko and Steven P Hamburg. 2022. Climate consequences of hydrogen emissions. *Atmospheric Chemistry and Physics* 22, 14 (2022), 9349–9368. https://doi.org/10.5194/acp-22-9349-2022, 2022

Adam Paszke, Sam Gross, Francisco Massa, Adam Lerer, James Bradbury, Gregory Chanan, Trevor Killeen, Zeming Lin, Natalia Gimelshein, Luca Antiga, Alban Desmaison, Andreas Köpf, Edward Yang, Zach DeVito, Martin Raison, Alykhan Tejani, Sasank Chilamkurthy, Benoit Steiner, Lu Fang, Junjie Bai, and Soumith Chintala. 2019. *PyTorch: an imperative style, high-performance deep learning library.* Curran Associates Inc., Red Hook, NY, USA, 1–12. https://doi.org/10.48550/arXiv.1912.01703

Ding-Yu Peng and Donald B Robinson. 1976. A new two-constant equation of state. *Industrial & Engineering Chemistry Fundamentals* 15, 1 (1976), 59–64. https://doi.org/10.1021/i160057a011

Roman Pevzner, Brian Gurevich, et al. 2017. 4D seismic monitoring of supercritical CO_2 injection at the Otway Project. *International Journal of Greenhouse Gas Control* 63 (2017), 150–161. https://doi.org/10.1016/j.ijggc.2017.05.014

Van Hiep Phung and Eun Joo Rhee. 2019. A High-Accuracy Model Average Ensemble of Convolutional Neural Networks for Classification of Cloud Image Patches on Small Datasets. *Applied Sciences* 9, 21 (2019), 4500. https://doi.org/10.3390/app9214500

R. G. Pratt. 1999. Seismic waveform inversion in the frequency domain, Part 1: Theory and verification in a physical scale model. *Geophysics* 64, 3 (1999), 888–901. https://doi.org/10.1190/1.1444597

S. R. Pride, J. G. Berryman, and J. M. Harris. 2004. Seismic attenuation due to wave-induced flow. *Journal of Geophysical Research: Solid Earth* 109, B1 (2004). https://doi.org/10.1029/2003JB002639

Luiz E. S. Queiroz and Dario Grana. 2025. Bayesian Seismic–Petrophysical Inversion for Rock and Fluid Properties and Pore Aspect Ratio in Carbonate Reservoirs. *Geophysical Prospecting* 73, 6 (2025), e70041. https://doi.org/10.1111/1365-2478.70041

A. Richardson. 2018. Seismic Full-Waveform Inversion Using Deep Learning Tools and Techniques. https://doi.org/10.48550/arXiv.1801.07232 arXiv:1801.07232 [physics.geo-ph]

Antonio P Rinaldi and Jonny Rutqvist. 2013. Modeling of deep fracture zone opening and transient ground surface uplift at KB-502 CO2 injection well, In Salah, Algeria. *International Journal of Greenhouse Gas Control* 12 (2013), 155–167. https://doi.org/10.1016/j.ijggc.2012.10.017

Philip Ringrose. 2020. *How to store CO2 underground: Insights from early-mover CCS projects*. Vol. 2191-5369. Springer, Switzerland. 1–129 pages. https://doi.org/10.1007/978-3-030-33113-9

PS Ringrose, AS Mathieson, IW Wright, F Selama, Olav Hansen, R Bissell, N Saoula, and John Midgley. 2013. The In Salah CO2 storage project: lessons learned and knowledge transfer. *Energy Procedia* 37 (2013), 6226–6236. https://doi.org/10.1016/j.egypro.2013.06.551

Olaf Ronneberger, Philipp Fischer, and Thomas Brox. 2015. U-Net: Convolutional Networks for Biomedical Image Segmentation. In *Medical Image Computing and Computer-Assisted Intervention – MICCAI 2015*, Nassir Navab, Joachim Hornegger, William M. Wells, and Alejandro F. Frangi (Eds.). Springer International Publishing, Cham, 234–241. https://doi.org/10.48550/arXiv.1505.04597

Yujun Shen, Jinjin Gu, Xiaoou Tang, and Bolei Zhou. 2020. Interpreting the latent space of gans for semantic face editing. In *Proceedings of the IEEE/CVF conference on computer vision and pattern recognition*. IEEE, Seattle, WA, USA, 9243–9252. https://doi.org/10.48550/arXiv.1907.10786

Y. Su, S. Wu, J. Sun, X. Wu, Y. Huang, J. Chen, and R. Christiansen. 2025. Natural hydrogen exploration by joint sparse inversion of geophysical measurements and integrated geological interpretation. *International Journal of Hydrogen Energy* 173 (2025), 151040. https://doi.org/10.1016/j.ijhydene.2025.151040

A. Tarantola. 1984. Inversion of seismic reflection data in the acoustic approximation. *Geophysics* 49, 8 (1984), 1259–1266. https://doi.org/10.1190/1.1441754

Radosław Tarkowski, Barbara Uliasz-Misiak, and Piotr Tarkowski. 2021. Storage of hydrogen, natural gas, and carbon dioxide–Geological and legal conditions. *International Journal of Hydrogen Energy* 46, 38 (2021), 20010–20022. https://doi.org/10.1016/j.ijhydene.2021.03.131

Theodo. 2024. Dimensionality reduction for exploration and curation of datasets. Theodo Blog. https://blog.theodo.com/2024/03/dimensionality-reduction-for-exploration-and-curation-of-datasets/

Julianna Toms, Tobias M Müller, and Boris Gurevich. 2007. Seismic attenuation in porous rocks with random patchy saturation. *Geophysical Prospecting* 55, 5 (2007), 671–678. https://doi.org/10.1111/j.1365-2478.2007.00644.x

Underground Sun Storage project, USS. 2025. Underground Sun Storage project in Austria. www.uss-2030.at. Accessed 16 Sep 2025.

D. Vasco, A. Rucci, A. Ferretti, and F. Novali. 2008. Satellite-based measurements of surface deformation reveal injection-induced fault reactivation. *Geophysics* 73, 6 (2008), WA113–WA122. https://doi.org/10.1190/1.2981184

Moein Jahanbani Veshareh, Thaysen Eike Marie, and Nick Hamidreza M. 2022. Feasibility of hydrogen storage in depleted hydrocarbon chalk reservoirs: Assessment of biochemical and chemical effects. *Applied Energy* 323 (2022), 119575. https://doi.org/10.1016/j.apenergy.2022.119575

Jean Virieux and Stephane Operto. 2009. An overview of full-waveform inversion in exploration geophysics. *GEOPHYSICS* 74, 6 (2009), WCC1–WCC26. https://doi.org/10.1190/1.3238367

Zhijing (Zee) Wang. 2001. Fundamentals of seismic rock physics. *GEOPHYSICS* 66, 2 (2001), 398–412. https://doi.org/10.1190/1.1444931

Michał Jakub Warchoł, Anna Pontén, and Anne-Kari Furre. 2025. Stratigraphic Controls on CO2 Migration at Sleipner: An Example From a Basin-Floor Fan of the Utsira Formation. *Basin Research* 37, 1 (2025), e70018. https://doi.org/10.1111/bre.70018 e70018 BRE-119-2024.R1.

Wolfgang Weinzierl and Bernd Wiese. 2021. Deep learning a poroelastic rock-physics model for pressure and saturation discrimination. *GEOPHYSICS* 86, 1 (2021), MR53–MR66. https://doi.org/10.1190/geo2020-0049.1

JE White. 1975. Computed seismic speeds and attenuation in rocks with partial gas saturation. *Geophysics* 40, 2 (1975), 224–232. https://doi.org/10.1190/1.1440520

Joshua A White, Laura Chiaramonte, Souheil Ezzedine, William Foxall, Yue Hao, Abelardo Ramirez, and Walt McNab. 2014. Geomechanical behavior of the reservoir and caprock system at the In Salah CO2 storage project. *Proceedings of the National Academy of Sciences* 111, 24 (2014), 8747–8752. https://doi.org/10.1073/pnas.131646511

Mark Wilkinson, Julien Mouli-Castillo, P Morgan, and Rami Eid. 2017. Time-lapse gravity surveying as a monitoring tool for CO2 storage. *International Journal of Greenhouse Gas Control* 60 (2017), 93–99. https://doi.org/10.1016/j.ijggc.2017.03.006

John D.O. Williams, J.P. Williamson, Daniel Parkes, David J. Evans, Karen L. Kirk, Nixon Sunny, Edward Hough, Hayley Vosper, and Maxine C. Akhurst. 2022. Does the United Kingdom have sufficient geological storage capacity to support a hydrogen economy? Estimating the salt cavern storage potential of bedded halite formations. *Journal of Energy Storage* 53 (2022), 105109. https://doi.org/10.1016/j.est.2022.105109

Rikiya Yamashita, Mizuho Nishio, Richard Do, and Kaori Togashi. 2018. Convolutional neural networks: an overview and application in radiology. *Insights into Imaging* 9 (06 2018). https://doi.org/10.1007/s13244-018-0639-9

Kane Yee. 1966. Numerical solution of initial boundary value problems involving maxwell's equations in isotropic media. *IEEE Transactions on Antennas and Propagation* 14, 3 (1966), 302–307. https://doi.org/10.1109/TAP.1966.1138693

Lin Yuan, Adel Najafimarghmaleki, Amirhossein Meysami, and Hassan Dehghanpour. 2025. Evaluating Fluid/Rock Interactions for Energy Storage in Salt Caverns – Part II: Effect of Hydrogen on Salt Rock Dissolution in Brine. *Energy & Fuels* 39, 6 (2025), 3140–3156. https://doi.org/10.1021/acs.energyfuels.4c04506

Chapter 3

Data-driven CO_2 storage monitoring

Traditionally, the interpretation of time-lapse seismic data for CO_2 saturation estimation relies on physics-based inversion workflows. Techniques such as amplitude inversion or Full-Waveform Inversion (FWI), are used to infer changes in reservoir properties and fluid saturations. However, these conventional inversion approaches are computationally intensive, often requiring numerous processing steps, strong a priori information, and iterative optimizations. These limitations pose challenges for timely and reliable CO_2 plume quantification and evolution, especially when quick decisions are needed during monitoring. Given these challenges, there is a clear rationale for exploring data-driven approaches that can streamline or bypass the traditional inversion process.

In recent years, deep learning (DL) has shown promise in geophysical applications, offering a way to directly map observed data to subsurface properties. The core idea of our proposed methodologies is to train a neural network, specifically a U-Net model, to learn the complex non-linear relationship between seismic measurements and CO_2 saturation distribution, thus essentially performing an implicit inversion. Once trained, such a model can rapidly predict a saturation map from new seismic inputs, potentially providing near-real-time insights. A key component of this data-driven strategy is the use of multi-scale features extraction to make the seismic input more amenable to learning. Raw seismic shot gathers are high-dimensional and contain information across various scales and frequencies. To distil the most relevant features, the method leverages the two-dimensional Continuous Wavelet Transform (2D-CWT) as a pre-processing step. The 2D-CWT decomposes each shot gather into a set of scale-dependent images, effectively highlighting patterns at different resolution levels. This multi-scale representation enriches the input to the neural network by providing

a separate channel for each wavelet scale, which can accentuate subtle amplitude variations associated with CO_2 saturation changes. Indeed, by converting seismic data into wavelet coefficient maps, the network is presented with more informative and distinguishable features, enhancing its ability to learn the mapping to saturation. In practice, a U-Net model can be supplied with multi-channel inputs that include both the original seismic data and several 2D-CWT transformed images, corresponding to multiple wavelet scales. This multi-scale approach enables the network to simultaneously capture large-scale plume trends and fine-scale details, improving the robustness and accuracy of the CO_2 saturation predictions.

However, it should be noted that, despite the theoretical generality of DL models, geological variability often makes these solutions site-specific and site-dependent, thus preventing geophysical generalizations. For instance, the seismic response to a CO_2 plume can differ greatly from one storage site to another due to differences in reservoir depth, lithology, background seismic velocity, and fluid properties. Consequently, a network trained on one dataset may not perform well if straightforwardly applied to a different site. To address this issue, the adopted workflow emphasizes training the model on site-specific synthetic data, i.e. data that realistically mimic the target field's conditions. Typically, this involves using reservoir simulation or fluid substitution modelling to properly simulate CO_2 saturation distributions and the corresponding changes in seismic properties, then forward-modelling the seismic response using wave propagation simulations. For example, the studies in this chapter use synthetic time-lapse seismic data created by applying Gassmann's fluid substitution to a baseline reservoir model and then generating synthetic seismic shot gathers via 2D finite-difference acoustic modelling. The neural networks are then trained on pairs of such simulated seismic gathers and their known CO_2 saturation maps, ensuring that the learned mapping is tailored to the specific geological setting of interest. This site-calibrated training approach acknowledges that while the DL architecture may be general, its application must be tuned to the site-specific seismic signature of CO_2 saturation to produce reliable results.

Once developed, these data-driven methods can serve as a complementary tool to physics-based inversion for CO_2 monitoring, offering significant gains in efficiency and automation. After the one-time high cost of training, the inference of saturation maps from new seismic surveys can be almost instantaneous, circumventing the heavy computational cost of running a full inversion for each repeated survey. Moreover, the automated nature of the DL predictor reduces the need for intensive human interpretation at every monitoring timestep. The network applies the learned criteria to output a saturation map, which can then be checked, validated, or refined by experts if needed. Overall, the integration of machine learning into the monitoring

toolbox promises a more efficient, rapid, and potentially automated assessment of CO_2 plume development, greatly enhancing the responsiveness of CCS monitoring programs.

3.1 Application of deep learning in the estimation of CO_2 saturation maps

CO_2 saturation estimation during the monitoring of a carbon-dioxide storage project using traditional inversion techniques can be an intensive task due to the processing steps and inversion workflows involved. In our work, we propose a deep-learning algorithm based on the U-Net architecture, to develop a method for automatic prediction of the spatial distribution of CO_2 saturation from time-lapse seismic data. We suggest using continuous wavelet transform (CWT) to optimize features extraction from the recorded seismic shot gathers. In fact, CWT could provide more informative and distinguishable images. The method is tested on synthetic time-lapse seismic data generated by applying the Gassmann fluid substitution equation to calculate the post-injection P-wave velocity model used to perform the 2D finite-difference acoustic modelling. The neural network has been trained on pairs of synthetic seismic shot gathers and corresponding CO_2 saturation maps, along with pairs of CWT coefficient maps and CO_2 saturation maps. The results of this work indicate the prospective utility of CWT in producing more informative images for the prediction of CO_2 saturation maps through deep learning algorithm like U-net.

Application of deep learning in the estimation of CO_2 saturation maps

G. Pantaleo, A. Molossi, M. Pipan

Extended abstract presented at the Fifth EAGE Conference on Petroleum Geostatistics, Volume 2023, p.1-5, 27^{th}-30^{th} November 2023, Porto, Portugal
doi: https://doi.org/10.3997/2214-4609.202335061

Key Words
CO_2 storage monitoring; *time-lapse seismic*; *Continuous Wavelet Transform*; *Deep Learning,*

Introduction

Carbon capture and storage (CCS) has emerged as one of the key technologies that is likely to reduce carbon dioxide emissions into the atmosphere. CO_2 is captured from power plants and industrial processes, and therefore safely and long-term stored in deep geological formations. Porous and permeable saline aquifers are suitable geological storage sites due to their vast storage capacity and no commercial value. The time-lapse seismic method is being widely used to monitor the evolution of the injected gas. Seismic waves detect changes in reflection events, which are associated with CO_2 saturation related to changes in petrophysical parameters (Chadwick et al., 2004b). High-resolution monitoring is mandatory to detect changes in the reservoir due to gas injection. Several works in the literature focused on CO_2 saturation estimation. They face complex inverse problems and use data-driven seismic imaging techniques (e.g., Meadows and Cole, 2013). Queißer and Singh (2013) derived CO_2 saturation from velocity models obtained using FWI. Hu et al. (2022) applied an FWI scheme integrated with rock physics for the prediction of the spatial distribution of CO_2 saturation from synthetic time-lapse seismic data. Traditional inversion techniques require a large amount of computational time and intensive human interactions. Recently, carbon storage monitoring problems have attracted the attention of deep learning. Leong et al. (2022) developed a network to directly image CO_2 saturation using multiphysics data. Yan et al. (2022) proposed a deep-learning workflow that predicts pressure and CO_2 saturation from rock properties, wells, and operational controls, while Um et al. (2022a) proposed a multiphysics network that enhances CO_2 saturation prediction.

In this abstract, a deep neural network based on the U-Net architecture (Ronneberger et al., 2015) is presented. The network predicts CO_2 saturation spatial distribution

maps from raw seismic data. Performances of neural network predictions will be compared, involving two different types of learning input: seismic shot gathers and continuous wavelet transform (CWT) coefficient maps.

Methods

We approached our purpose by designing synthetic geological models with realistic petrophysical characteristics and performing finite-difference acoustic modelling. To achieve the most realistic modelling, we based our pre-injection P-wave velocity model on P-wave wireline log data from exploration well 15/9-13 located in the Sleipner storage field in the North Sea. Therefore, the reservoir storage layer represents an unconsolidated sandstone reservoir with the same petrophysical characterization as the Utsira Sand, a regional saline aquifer in the North Sea (Chadwick et al., 2004b). The geological model was developed and created using the open-source geological modelling software GemPy (de la Varga et al., 2019). We generated a three-dimensional synthetic geological model with shape $n_x = 100$, $n_y = 100$, and $n_z = 100$. Thus, we derived the P-wave baseline model corresponding to the pre-injection stage. Then, we generated 20 P-wave monitor models (hereinafter referred to as "reservoir realizations") in which the P-wave of the sandstone reservoir varies with CO_2 saturation level. Each reservoir realization corresponds to a 5% CO_2 saturation increment within a range from 0 to 100%.

The Gassmann equation (Eq. (3.1)) relates the saturated bulk modulus of the rock (K_{sat}) to porosity (ϕ), the bulk modulus of the porous frame (K_{dry}), the mineral matrix (K_{matrix}), and the pore-filling fluids (K_{fl}) (Gassmann, 1951).

$$K_{\text{sat}} = K_{\text{dry}} + \frac{\left(1 - \frac{K_{\text{dry}}}{K_{\text{matrix}}}\right)^2}{\frac{\phi}{K_{\text{fl}}} + \frac{1-\phi}{K_{\text{matrix}}} - \frac{K_{\text{dry}}}{K^2_{\text{matrix}}}}, \tag{3.1}$$

$$V_p = \sqrt{\frac{K_{\text{sat}} + \frac{4}{3}\mu}{\rho_b}}. \tag{3.2}$$

Once the new bulk modulus and density are calculated, the corresponding P-wave velocity is obtained using Eq. (3.2), where ρ_b is the bulk density (Batzle and Wang, 1992), and μ is the shear modulus, assumed constant after fluid substitution.

We used Devito (Louboutin et al., 2019) to perform 2D finite-difference acoustic modelling for each P-wave velocity model to generate synthetic shot gathers, using a Ricker wavelet with a central frequency of 15 Hz. Furthermore, 2D modelling eases the problem complexity and reduces the computation time. Each synthetic shot gather has shape $n_x = 100$, $n_t = 511$. To match the size of the corresponding CO_2 saturation

map, we resized the shot gathers so that $n_x = n_t = 100$. Thus, our dataset consists of 100 gathers for each reservoir realization, resulting in 2000 pairs of shot gathers and CO_2 saturation maps. The dataset was randomly split into 80% for training and 20% for validation and test, resulting in 1600 training data and 400 test data.

Lastly, the synthetic seismic shot gathers have been examined using the continuous wavelet transform (CWT), which is a mathematical tool used for feature extraction from time series. The CWT convolves a time series signal with an arbitrarily chosen mother wavelet. After selecting the mother wavelet, a sequence of scaled and shifted wavelets is generated which yields different CWT coefficient values (Sinha et al., 2005; Wang et al., 2009). The values of the scaling and translation factors are continuous, which means that there can be an infinite number of wavelets. For our purpose, we used a scale factor equal to 1 to obtain more detail in the time domain at a wider scale. We used the Mexican Hat wavelet as mother wavelet. Thus, we obtain an image with the same shape as the original shot gather including the CWT coefficient, which could generate more informative images.

We developed a deep-learning algorithm based on U-Net (Ronneberger et al., 2015). The neural network has been trained using two different input/output configurations: the pair shot gathers and saturation maps, and the pair CWT coefficient maps and saturation maps. We preferred to use U-Net due to the multiscale nature of the encoder–decoder architecture. U-Net performs image segmentation to extract features from the input image at a pixel level and to output a segmentation map where each element indicates which class that pixel belongs to. Our neural network architecture consists of contracting and expansive paths (Figure 3.1.1). The contracting path consists of three 3×3 convolutional layers followed by ReLU activation and 2×2 max pooling as down-sampling. At each down-sampling step we double the number of feature channels. The expansive path is specular and consists of up-sampling of the feature map, followed by a 3×3 convolution that halves the number of feature channels, and a concatenation with the corresponding feature map from the contracting path. At the final layer a 1×1 convolution is used to map the features of the corresponding classes, followed by pixel-wise softmax combined with the categorical cross-entropy loss function (Mannor et al., 2005). As optimizer, we used Adam (Kingma and Ba, 2014), a method for stochastic optimization of a parametrized objective function.

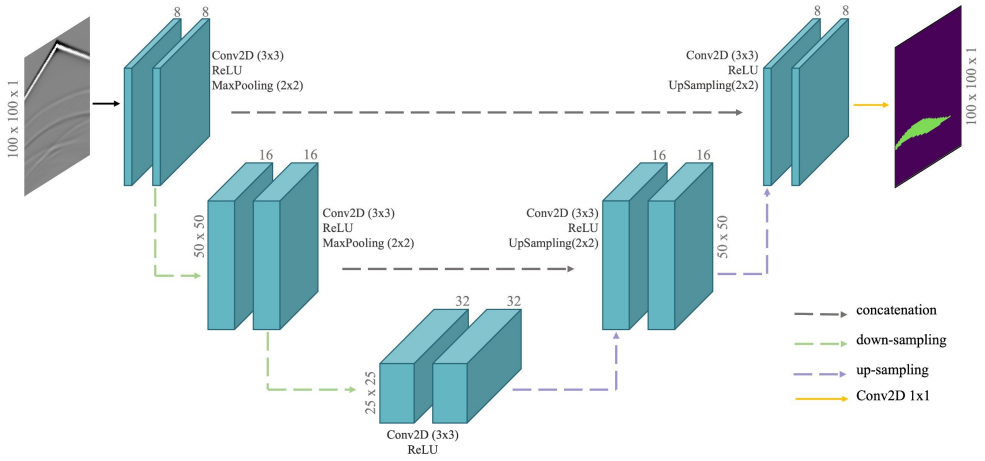

Figure 3.1.1: U-shaped deep-learning architecture used in our method. Each box corresponds to a multi-channel feature map, where the number on the top of the box is the number of filters at each convolution layer. The size of the image is denoted at the edges of the box.

Results and Discussion

The neural network trained with different input learning datasets produces predictions with different accuracy as shown in Figure 3.1.2. The neural network predicts the saturation level with higher accuracy by considering CWT coefficient maps as learning input, achieving a maximum error of 5%. The error is calculated as the mean of the squares of the differences between the ground truth and the predicted values (i.e., Mean Squared Error, MSE). On the contrary, training the network with shot gathers achieves errors $> 5\%$. Better accuracy in predicting the spatial distribution of CO_2 is achieved with the network trained using CWT maps, as shown in the uncertainty maps in Figure 3.1.2.

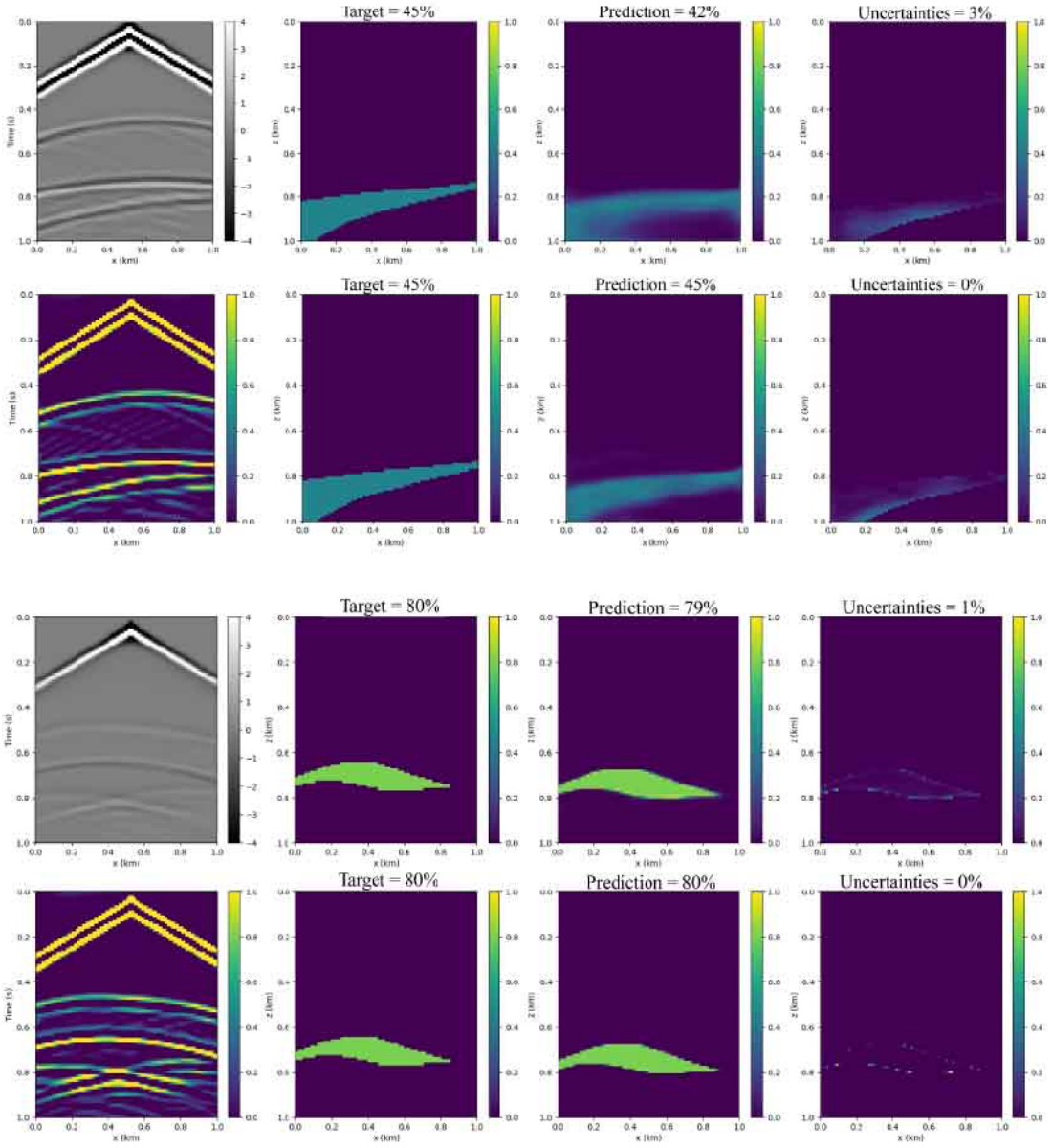

Figure 3.1.2: Four examples of predictions from our neural network. For both panels, in the first row there are the shot gather as input learning data, CO_2 saturation spatial distribution map as target, predicted CO_2 saturation spatial distribution map, and the uncertainty map to highlight the uncertainties of the prediction. In the second row are the predictions related to the neural network trained with the CWT coefficient maps.

Conclusions

We propose a deep-learning based method to predict CO_2 saturation spatial distribution maps from time-lapse seismic gathers. We generated a baseline geologic model with a reservoir layer with petrophysical characteristics related to a deep saline aquifer

in the North Sea. Then, we created 20 monitor models representing 20 different post-injection saturation levels. We used the monitor velocity models, computed using the Gassmann fluid substitution equation (Gassmann, 1951), to generate acoustic modelling to simulate seismic field data. We processed the shot gathers by computing the continuous wavelet transform to obtain more informative images. For our purpose, we developed a U-shaped neural network. We trained the neural network giving as input both shot gathers and CWT coefficient maps, coupled with CO_2 saturation maps. Despite the preliminary nature of this work, the results support the potential of these deep-learning methods in CO_2 saturation prediction and suggest the potential use of CWT to generate more informative images for the estimation of CO_2 saturation maps using DL-based methods such as U-Net.

3.2 Estimation of CO_2 saturation maps from synthetic seismic data using a deep-learning method with a multi-scale approach

In the context of Carbon Capture and Storage (CCS), monitoring the behaviour of CO_2 within subsurface reservoirs is pivotal for efficient and safe storage operations. This study proposes a new approach to enhance the accuracy of predicting CO_2 saturation maps directly from shot gathers, using a combination of deep learning (DL) and feature extraction methods. We employ a U-Net model, specifically tailored to solve regression tasks, and two-dimensional continuous wavelet transform (2D-CWT) to analyse shot gathers at different scales. We introduce a novel approach using multi-channel input data for the DL model, combining shot gathers and CWT images. The DL model was trained and tested using both single channel and multichannel input. The single channel datasets included shot gathers and CWT images at the first scale, while the multi-channel datasets integrated shot gathers with either two or four scales of CWT. We conducted a sensitivity analysis on the number of training epochs to compare the performance of the model with multichannel and single channel input. Additionally, a Transfer Learning approach was implemented to improve performance in noisy conditions by leveraging knowledge from a pre-trained model on noise-free images. Monte Carlo dropout was used to predict pixel-scale variability and provided a prediction variability with a standard deviation ranging from 0.019 to 0.194, enhancing the robustness of CO_2 saturation estimates. Our results suggest that combining feature extraction using 2D-CWT with the U-Net architecture improves the prediction performance of CO_2 saturation in a synthetic CCS model. Additionally, using multi-channel input instead of single channel is more efficient as it requires less training and prediction time to achieve comparable results. This confirms the effectiveness of 2D-CWT as a pre-processing technique, contributing valuable insights and advances in the field of data-driven geophysical inversion problems.

Estimation of CO_2 saturation maps from synthetic seismic data using a deep-learning method with a multi-scale approach

G. Pantaleo, A. Molossi, M. Pipan

Geoenergy, Volume 2, Issue 1
doi: https://doi.org/10.1144/geoenergy2023-057

Key Words

CO_2 storage monitoring; *time-lapse seismic*; *Continuous Wavelet Transform*; *Deep Learning*

Highlights

- U-Net predicts CO_2 saturation maps directly from time-lapse seismic gathers.
- 2D-Continuous Wavelet Transform inputs increase prediction accuracy versus raw gathers.
- Uncertainty maps quantify prediction confidence for high-resolution CO_2 monitoring.

Introduction

In the ongoing global effort to mitigate climate change and reduce greenhouse gas emissions, Carbon Capture and Storage (CCS) has emerged as a key technology. The basic idea behind CCS is capturing the CO_2 where it is produced by human activities (i.e. large industrial process facilities, such as fossil fuel power plants, steel mills, cement plants and refineries) and long-term storing in underground geological sites. Suitable storage reservoirs are deep saline aquifers, depleted oil and gas fields, and coal deposits. Indeed, saline aquifers are considered a crucial option for CO_2 storage due to their vast storage capacity and lack of commercial value. One significant advantage is their easy accessibility from most existing CO_2 capture sites, which makes the CO_2 sequestration process highly convenient. Deep saline aquifers located at depths not greater than 1000 m below ground level, are highly porous and permeable, making them particularly suitable locations for CO_2 storage (Gunter et al., 2004). Saline aquifers hold the potential to store up to 10,000 gigatons of CO_2, equivalent to 20–500% of the projected emissions by 2050 (Davidson and Smith, 2001). Once the CO_2 is injected within the reservoir, monitoring and verification techniques are needed to ensure safe and long-term storage. Geophysical methods are used to estimate stored CO_2 mass, to

monitor the migration of gas in the storage sites, and to detect possible leakage (Ajayi et al., 2019). Successful verification of simulations through monitoring would provide researchers with greater confidence in using simulation tools (Ajayi et al., 2019).

Numerous techniques can be employed to monitor the CO_2 plume within the reservoir. In 4-D mode, i.e. multi multi-offset and multi-azimuth (3-D) data acquisition repeated over time (time-lapse), seismic methods are effective for tracking the movement of the injected plume and detecting gas leakages. Specifically, 2-D time-lapse seismic monitoring can provide valuable data on the behaviour of the injected plume. This technique is particularly beneficial in areas with observation wells, where cross-well seismic technology can be used to identify leakages and trace the migration path of CO_2. Additionally, seismic monitoring tools can be integrated with gravimetry to observe in-situ changes in the density of underground fluids (Nooner et al., 2007). The results from gravimetric monitoring offer reliable inputs for flow simulations, enhancing the overall understanding of the subsurface dynamics (Ajayi et al., 2019). The time-lapse seismic method is widely used for reservoir characterization in CO_2 storage projects, and subsequently for monitoring storage operations (Arts et al., 2004; Chadwick et al., 2006; Osdal et al., 2013). In such applications, high-resolution seismic imaging is mandatory, as the main objective is to diagnose the spatial distribution of the injected gas plume to evaluate the injection and prevent leaks. The time-lapse reflection seismic method employs seismic waves to detect changes in subsurface physical and petrophysical properties over time, and to delineate the boundaries of CO_2 plumes (Arts et al., 2004; Chadwick et al., 2010). In a CCS context, these changes are associated with the displacement of the brine with the gas within the pore space, involving changes in relative saturation level and corresponding changes in parameters such as seismic velocities and properties such as rock density (Chadwick et al., 2004a). These parameters play a crucial role while monitoring a CCS project. The estimation of velocity and attenuation through seismic inversion allows to make quantitative analysis of CO_2 volumes and migration (Furre et al., 2017).

The CCS pioneer project and first commercial-scale offshore storage operation is the Sleipner CCS project (Ringrose, 2020). This project is the longest running in the world. In fact, it has been active since 1994 and the subsurface of this site has been under monitoring for over 20 years. An extensive geophysical and environmental monitoring programme has been deployed to monitor this injection site, such as 3-D seismic and gravimetric surveys, wellhead, and seabed monitoring. Time-lapse seismic imaging at Sleipner was very successful as it provided crucial information to researchers regarding the physics of the storage process and played a vital role in convincing authorities and the public about the effectiveness of storage efforts (Ringrose, 2020). A correct

estimation of the evolution of CO_2 saturation in the reservoir is crucial in a CCS project and can be obtained through seismic inversion methods. Unlike modelling, seismic inversion aims to obtain the unknown elastic parameters of an underground volume from seismic data. Conventional seismic inversion methods are well established in the scientific literature and achieve high degrees of accuracy in the estimation of elastic parameters. Chadwick et al. (2004a) determined the total injected CO_2 volume at the Sleipner Field by employing seismic data inversion. They utilized relationships between the thickness of the CO_2 layer and seismic wave reflection amplitude, as well as travel time differences, as independent parameters in their analysis. Meadows and Cole (2013) analysed 4D seismic data to detect CO_2 leaks and monitor variations in saturation levels and pressure over time. They calculated the temporal variations of impedance and utilized this information to deduce alterations in pore pressure and CO_2 saturation. The results aligned well with both the petrophysical model and reservoir flow simulations. However, they remarked that the inversion results related to changes in CO_2 saturation exhibited more variability compared to those associated with effective pressure changes. Queißer and Singh (2013) derived CO_2 saturation using elastic 2D time-domain full waveform inversion (FWI) in a time-lapse manner, by relating velocity change to free CO_2 saturation using a rock physics model. In their study, Dupuy et al. (2017) conducted a quantitative seismic analysis of CO_2 at the Sleipner storage site. They integrated high-resolution seismic waveform tomography with uncertainty quantification and rock physics inversion. Employing FWI, they determined P-wave velocity and applied advanced rock physics models to estimate CO_2 saturation. The sensitivity tests on the rock physics inversion indicated the reliability of saturation estimates for low levels of CO_2 saturation, whereas the reliability diminished for high levels of CO_2 saturation. Ivandic et al. (2018) analysed amplitude versus offset (AVO) responses from 3D time-lapse seismic surveys at the Ketzin pilot site to quantitatively assess CO_2 saturation changes. Hu et al. (2022) developed a methodology based on the application of a rock-physics parameterized FWI scheme that allows to directly update reservoir properties, such as base-line porosity and lithology parameters and use them as input to predict CO_2 saturation from monitor data. Their tests on synthetic time-lapse generated from the Johansen Formation model showed that both the errors in baseline model estimates and the errors in monitor data could compromise the recovered CO_2 saturation model.

However, traditional methods, also referred to as model-driven, are inefficient in terms of computational resources and require intensive human interactions. Model-driven methods are being replaced by data-driven methods such as Machine Learning (ML) and Deep Learning (DL) techniques, due to higher efficiency, reduction of time-consuming tasks, and ability to discover complex patterns in images avoiding tedious

manual tasks. Seismic pattern recognition plays a vital role in geosciences, especially in the analysis of subsurface structures and reservoir characterization. Bagheri and Riahi (2015) focused on seismic facies analysis from well logs using a supervised classification scheme with various machine learning techniques, for qualitative mapping of the reservoir facies distribution. In a subsequent paper Bagheri and Riahi (2017) explored modelling reservoir facies using seismic data with missing attributes through dissimilarity-based classification. Moreover, Tavakolizadeh and Bagheri (2022) investigated multi-attribute selection for salt dome detection based on support vector machine (SVM) and multilayer perceptron (MLP) machine learning techniques. Recently, carbon storage monitoring problems have drawn attention to this field. Araya-Polo et al. (2018) proposed the training of a deep neural network to overcome FWI processes in velocity model building for hydrocarbon exploration. The task involves predicting velocity models from shot gathers, where the network estimates the relationship between input and output during a training phase. Wang et al. (2020) trained a ML classifier on a large collection of labeled forward models from simulated surface seismic, to infer leakage and CO_2 saturation levels along a leaky well. Yan et al. (2022) proposed a DL workflow that predicts temporal and spatial evolution of pressure and CO_2 saturation from rock properties, well measurements, and operational controls. Um et al. (2022b) proposed a multi-physics network that enhances CO_2 saturation prediction by jointly analysing seismic, electromagnetic, and gravity data. Feng (2023) developed an unsupervised learning approach for inverting reservoir porosity and CO_2 saturation from post-stack data using generative adversarial networks, enabling ensemble predictions and uncertainty analysis. Liu et al. (2023) combined neural networks for model reparameterization and differentiable programming for inverse modeling, developing a differentiable physics model for large-scale joint inverse problems that assimilates time-lapse seismic and resistivity data.

In this study we propose a novel approach that leverages two-dimensional continuous wavelet transform (2D-CWT) and U-Net model to provide more accurate predictions of CO_2 saturation directly from seismic shot gathers, acquired during the monitoring phase of a CCS site. The proposed approach includes 2D-CWT to obtain diverse scales of shot gathers, which were used as training input data to the U-Net. The DL model is trained and tested using four different datasets: two with single-channel images (shot gathers and CWT images separately) and two with multi-channel images (shot gathers combined with two and four scales of CWT images). Additionally, the impact of noisy input data is considered, and Monte Carlo dropout is used to provide pixel-scale prediction of variability. We believe that this new approach can be easily implemented in a conventional seismic data processing workflow. The addition of the CWT preprocessing step can increase the time and computational cost. The prediction step is

essential to have an initial hypothesis of the saturation model on which further analyses can then be carried out. The limitations of this approach can be related to the site dependence of the trained model. Thus, a site-specific training dataset is needed for the site under monitoring. This paper is divided into four main sections. The first part gives a description of the methodology and theory, starting from the synthetic data generation aimed at obtaining synthetic seismic data, a brief introduction to 2D-CWT used to extract features from shot gather images, an overview on the datasets used to train and test the models, and an explanation about the proposed model architecture and the training and test procedures. The second part shows the results of the CO_2 saturation maps prediction using the proposed models and datasets, where both qualitative and quantitative evaluations are reported. Discussion and conclusions report a critical analysis of results in the third and fourth parts.

Methods and theory

The proposed method belongs to the supervised learning technique, where the training dataset and the network architecture are two key factors. This section illustrates how we constructed the training dataset, starting with geological modelling up to traditional forward modelling based on the finite-difference scheme. A multi-scale feature extraction strategy based on wavelet transform is proposed to help the network learn information features more easily through more informative images. The proposed deep learning architecture is then presented and further implemented with the Transfer Learning (TL) strategy which can overcome the limitations in the prediction from more complex datasets.

Synthetic seismic data generation

A data-driven method needs a large amount of data to learn the nonlinear relationship between input and output. We then generated synthetic seismic data to build a large training database and overcome the difficult access to time-lapse field seismic data. The geological model was designed and built with the use of GemPy (de la Varga et al., 2019), an open-source 3D geological modelling package for Python. Our model consists of five slightly folded layers. Geological layers and seismic velocities are based on sonic log data from the 15/9-13 exploration well located in the Sleipner storage field in the North Sea (Figure 3.2.1). The five layers are: water, sediments, upper shale, sandstone, and lower shale. The corresponding P-wave velocity of the synthetic pre-injection model are 1500, 1750, 2500, 2120, 2500 m/s. The reservoir storage layer represents an unconsolidated sand reservoir with the same petrophysical characterization as the Utsira sand, a regional deep saline aquifer in the North Sea (Chadwick et al., 2004a). The CO_2 plume in the reservoir layer was simulated creating a three-dimensional CO_2 lens body at the top of the sand layer, below the upper shale, and assumes various

shapes, sizes, and locations.

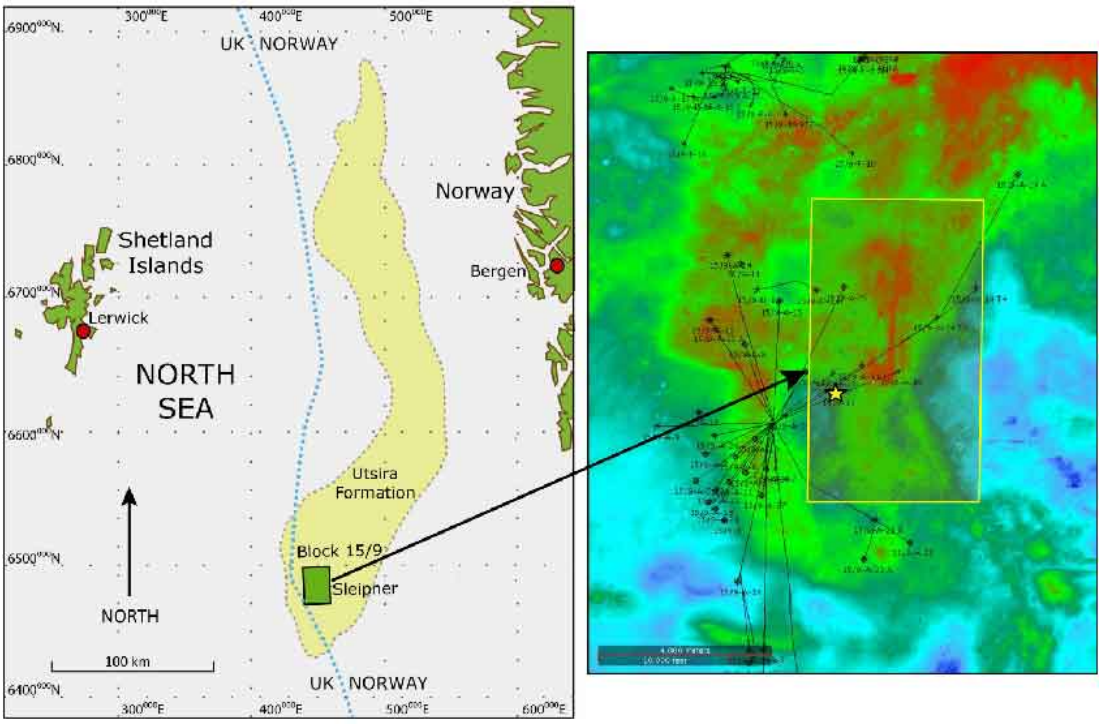

Figure 3.2.1: Location maps of the Sleipner injection site. (a) Location map of the Utsira Formation (yellow shape) in the North Sea and the green box highlights the Sleipner site on offshore Norway. (b) Traveltime map of Top Utsira horizon showing the area covered by the time-lapse seismic data (yellow square); the yellow star shows the location of the 15/9-13 exploration well (modified after Hermanrud et al. (2009)).

CO_2 and water saturation ranges from 0 to 100% in the sediments to evaluate the effects of replacing water with gas. We have generated a rock physics model based on the Biot–Gassmann theories (Gassmann, 1951; Biot, 1956). This model follows some basic assumptions: the media is homogeneous and isotropic, the pore space is completely connected, and no chemical interaction between the grains and the fluid phases happens. Gassmann equation relates the saturated bulk modulus of the rock (K_{sat}) to its porosity (ϕ), the bulk modulus of the porous rock frame (K_{dry}), the bulk modulus of the mineral matrix (K_{matrix}) and the bulk modulus of the pore-filling fluids (K_{fl}). Once the new bulk modulus and bulk density of the saturated rock after fluid substitution are calculated (Eq. (3.3)), the corresponding P-wave velocity is calculated by Eq. (3.4) where ρ_{b} is the bulk density of the rock which can be calculated from fluid density using the Batzle and Wang relation (Batzle and Wang, 1992), while μ is the shear modulus which remains constant after fluid substitution.

$$K_{\text{sat}} = K_{\text{dry}} + \frac{\left(1 - \frac{K_{\text{dry}}}{K_{\text{matrix}}}\right)^2}{\frac{\phi}{K_{\text{fl}}} + \frac{1-\phi}{K_{\text{matrix}}} - \frac{K_{\text{dry}}}{K^2_{\text{matrix}}}}, \tag{3.3}$$

$$V_p = \sqrt{\frac{K_{\text{sat}} + \frac{4}{3}\mu}{\rho_b}}. \tag{3.4}$$

Using the rock physics model, we investigated a homogeneous saturation distribution scenario, that is a uniform mix of brine and CO_2. Our rock physics model requires information regarding lithostatic pressure and rock temperature which affect the fluid substitution simulation. To make the simulation more realistic, 8 MPa and 28 °C has been set respectively, which correspond to a hydrostatic pore pressure and temperature at the top of the Utsira storage complex (Alnes et al., 2011). Figure 3.2.2 shows the variations in P-wave velocity, S-wave velocity, and rock density versus CO_2 saturation (S_{CO_2}) for the homogeneous saturation model calculated for a sandstone. P-wave velocity changes significantly when the fluid changes from pure brine to brine with low CO_2 saturation, while it changes much less when the CO_2 saturation increases further. In fact, looking at the shape of the curve, for values of S_{CO_2} greater than about 0.5, the S_{CO_2} estimate from P-wave velocity might be not well constrained. In contrast, S-wave velocity increases with CO_2 saturation and exhibits direct proportionality, as depicted in Figure 3.2.2.b. Another parameter analysed here is rock density, which decreases proportionally with increasing CO_2 saturation, as shown in Figure 3.2.2.c. Solving the inverse problem to estimate CO_2 saturation is not an easy task. In fact, this process is subject to several sources of uncertainty. A fundamental issue is the choice of an adequate rock physics model to quantify CO_2 saturation. Using average mixing theory such as the one used in this work is a strong approximation, because it involves calculating an average modulus of the fluid and using it as input to the Gassmann equation. To build our training dataset, we have created twenty three-dimensional P-wave velocity models corresponding to an equal number of saturation scenarios. Each realization has the same geometry: the three-dimensional model extends 1000 m along each dimension and is formed by 10×10×10 m grid cells. Therefore, the size of the structured grid is 100 points along each direction, i.e. $n_x = n_y = n_z = 100$. We sliced the 3D volume into 2D vertical images along z–x cross section. Then, we performed 2D finite-difference acoustic-wave forward modelling for each of the 2D seismic velocity models using the Devito software (Louboutin et al., 2019) to generate synthetic shot gathers. Devito is a domain-specific language for implementing high-performance, finite-difference, partial differential equation solvers. We have positioned the seismic source at a depth of 20 meters, and set the peak wavelet frequency to 30 Hz, which is the dominant frequency

of the Sleipner seismic data (Furre and Eiken, 2014). A total of 100 receiving stations placed at the same depth as the source were used, with a spacing between the receiver station of 10 m. 2D acoustic modelling was performed to reduce problem complexity and computation time. In fact, modelling the propagation of seismic approximated by the acoustic wave equation (Tarantola, 1984) assumes only P-waves and requires fewer computational resources and parameters than the solution of the elastic equation. In reflection seismic terminology, the assembly of signals acquired by an array of receivers from a single source position is known as shot gather. Our learning dataset consists of 100 shot gathers for each saturation scenario (corresponding to the two-dimensional seismic modelling every 10 meters along the y-direction), resulting in 2000 shot gather training images. In Figure 3.2.3 an example of 2D velocity model (Figure 3.2.3.a) and the corresponding synthetic shot gather (Figure 3.2.3.c) are shown. Each 2D velocity model is coupled with the corresponding 2D saturation model (Figure 3.2.3.b). They have the same geometry as the velocity models but are filled with saturation values, i.e. zero for water, sediments, upper shale, lower shale and variable SCO_2 value from 0 to 1 for the sand reservoir layer. From Figure 3.2.3.b, it is evident how the area occupied by CO_2 is limited, leading to a number of zero elements much higher than the number of non-zero elements, as a sparse matrix.

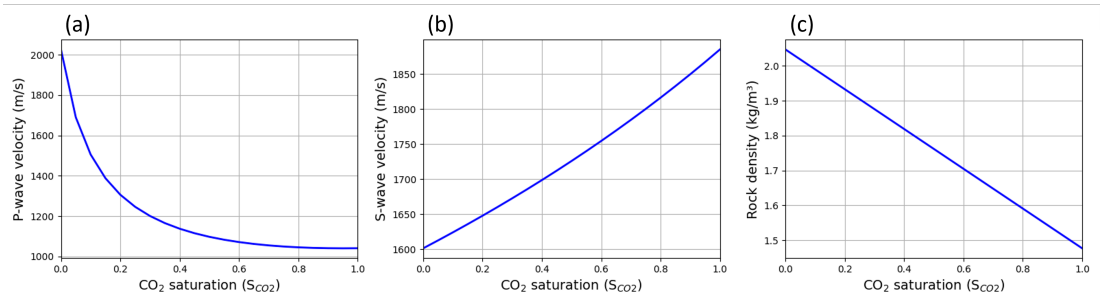

Figure 3.2.2: Effect of CO_2 saturation on P-wave velocity (a), S-wave velocity (b), and rock density (c) in the simulated sandstone with uniform saturation distribution.

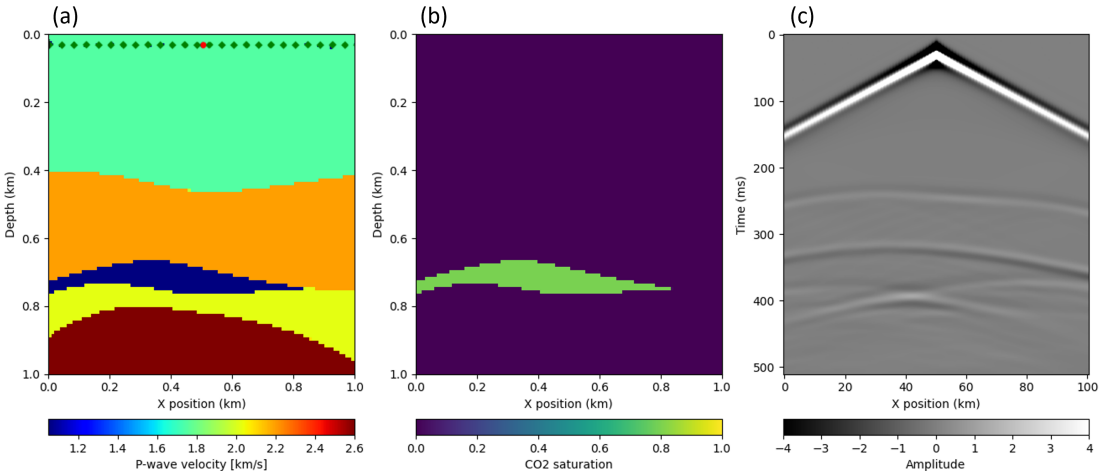

Figure 3.2.3: Examples of cross-sectional view of the synthetic dataset. (a) 2D P-wave velocity model extracted from the 3D model. (b) Corresponding CO_2 saturation map. (c) Common shot gathers obtained from seismic forward modelling. The green and red symbols in (a) represent receivers and seismic source respectively.

Two-dimensional Continuous Wavelet Transform

In this study, we explored the use of Continuous Wavelet Transform (CWT) to evaluate how the wavelet function at different scales could enhance the features and information extraction from the shot gather images. CWT is a transform used in signal analysis and processing which is similar to the Fourier Transform (FT). It can be used as a multi-scale analysis tool that allows to analyse nonstationary signals by convolving the input signal to a stretched and compressed analysing (mother) wavelet by varying its scales. The main applications of CWT are pattern recognition, feature extraction and object detection. While FT assumes stationary processes underlying the geophysical time series, CWT can analyse dynamic signals and retain the time domain information as well. Moreover, CWT allows to extract more discriminatory features from images, compared to the Discrete Wavelet Transform (DWT) (Reddy et al., 2014). Several authors have worked with CWT applied to geoscience datasets, using both one-dimensional and two-dimensional transformations. Application fields are oceanography and meteorology data analysis (Wang and Lu, 2010; Meyers et al., 1993), image processing, astronomy, and fluid dynamics (Antoine et al., 2004), application to the periodic fluctuation in sea surface temperature and air pressure in the equatorial Pacific Ocean (Torrence and Compo, 1998), anomalous zone localization and denoising in seismic data (Ali et al., 2020; Huot et al., 2019). In this work we focus on the use of the two-dimensional CWT (2D-CWT), which is a natural extension of the one-dimensional CWT. It can be generally defined as follows (Wang and Lu, 2010):

$$(Wf)(a,b,\theta) = \langle\, f,\, \psi_{a,b,\theta}\,\rangle, \tag{3.5}$$

$$\psi_{a,b,\theta}(x) = a^{-1}\,\psi\Big[\,R_\theta^{-1}\Big(\frac{x-b}{a}\Big)\Big]\,, \tag{3.6}$$

where $f \in L^2(\mathbb{R}^2)$ is a two-dimensional signal function; ψ is the wavelet mother function; $a > 0$ is the scale parameter; $\mathbf{b} \in \mathbb{R}^2$ is the position vector; R_θ is the standard rotation matrix of rotating angle θ; and the angle brackets $\langle \cdot, \cdot \rangle$ denote the scalar product of the Hilbert space. Many 2D wavelets have been proposed in literature; for an overview of the most popular see (Wang and Lu, 2010). We chose the 2D Mexican hat wavelet (hereinafter called Mexh) since it is well-known as a good wavelet for edge and contour features detection (Marr and Hildreth, 1980). The scales are arbitrary but can be translated into frequencies for a better understanding. The physical frequency of the wavelet depends on wavelet type and sampling period. With Mexh and a sampling period of 0.012 seconds, the smaller scale (i.e. scale 1 which corresponds to higher wavelet frequency) corresponds to an equivalent pseudo-frequency of about 20 Hz. Using these parameters, no aliasing is expected. The frequency decreases by increasing the scale factor since the wavelet has been stretched, making it sensitive to lower frequencies in the signal and extract features at greater scale. We have analysed each of the 2000 synthetic shot gathers with 2D-CWT. In this way we have defined a new dataset consisting of CWT images showing the wavelet coefficients. The resulting dataset is hereinafter called CWT dataset.

Training and testing datasets

Our proposed model architecture was trained and tested on four different datasets. Each dataset is composed by input training images and output target images, where the input images are the processed seismic data, and the output ones are CO_2 saturation maps. From here on we will refer to the different datasets with the following abbreviations: SG, CWT, SGCWT, SGN. SG contains shot gather images, CWT the CWT of the shot gathers, SGCWT2 and SGCWT4 contain two and four input channels respectively, where the first channel is the shot gather while the additional ones are the CWT of the shot gathers at scales from 1 to 4. Eventually the SGN dataset contains shot gathers with additional random noise. SGCWT was tested to investigate whether simultaneous extraction of information from shot gathers and CWT images lead to improved prediction accuracy compared with the separate SG or CWT datasets. In this study, the desired target output are CO_2 saturation maps. Therefore, each dataset is coupled with a target output dataset consisting of CO_2 saturation maps. Each dataset is randomly split into 80% for training and 20% for validation and test. Considering both datasets, up to the 95th percentile the values are predominantly 0, while from the

95th percentile onwards there is a well-distributed range of SCO_2 values between 0.05 and 1 (Figure 3.2.4). This leads to an imbalanced dataset (or as mentioned before sparse matrix). This is reasonable considering the CO_2 saturation map in Figure 3.2.3 where the pixels representing the CO_2 plume are considerably less than the total number of pixels within the image.

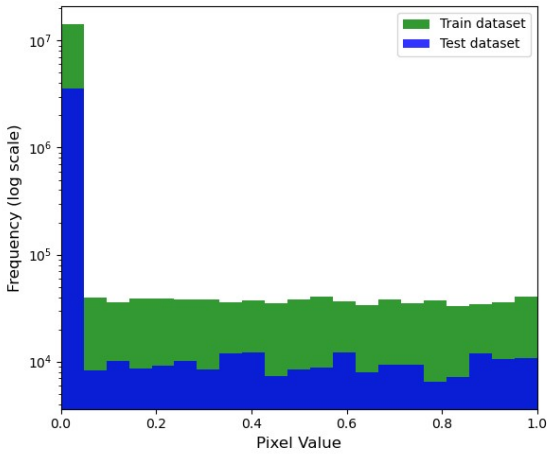

Figure 3.2.4: Frequency of occurrences in the training set and in the testing set within each CO_2 saturation level.

Architecture of the proposed U-Net and training procedures

Deep Learning (DL) is a subset of Machine Learning (ML), which stands out for the use of Deep Neural Networks (DNNs). This approach is particularly suited to distinguishing complex patterns and representations from data, finding application in various fields such as image recognition and natural language processing. When the input is a set of images, DL can provide models that exploit the hierarchical structure within the images, such as local combinations of edges and patterns to achieve a desired output. Within the broad panorama of DL, a noteworthy architecture suitable for semantic segmentation tasks is the U-Net (Ronneberger et al., 2015). This convolutional neural network configuration is characterized by its peculiar U-shaped structure, which includes both a contraction and expansion paths. The combination of these paths facilitates the integration of context information and the preservation of high-resolution details, a unique strength of the U-Net architecture. The model architecture used in this paper, inspired by the original U-Net, has been modified to solve an image-to-image regression tasks, by considering a single output channel and a regression loss. The model has been organized as encoder and decoder setup (Figure 3.2.5). The encoder path extracts high-level features from the input image. Each encoder block consists of 3×3 convolution layers followed by ReLU activation function (Rectified Linear Unit, this function introduces non-linearity into the network to better generalize the training

data), and 2×2 max pooling operation as down-sampling mechanism. On the other hand, the decoder path enables precise localization and recover object dimensions and detail. The decoder blocks are specular and consists of 2×2 up-sampling operations of the feature map, then it is concatenated with the corresponding feature map from the contracting path. Finally, 3×3 convolutions are used where each convolution is followed by ReLU activation function. Each convolutional layer is followed by a dropout layer with a dropout rate of 0.5. This implies that each neuron has a 50% probability of being temporarily deactivated, forcing the network to learn to be robust even without the presence of specific neurons during each training iteration. At the final layer, a 1×1 convolution is used to map the features, followed by ReLU combined with the mean-square-error (MSE) loss function. As optimizer, we used Adamax with a batch size of 32 and a learning rate of 1e−4. The prediction performance of the models after the training phase is evaluated at the pixel level by comparing the predictions with the reference data using MSE and adjusted R^2 regression metrics. The mean-square error (MSE) is computed as the sum of the squared differences between the corresponding pixel values in reference and predicted images. The adjusted R^2, instead, is a modified version of R^2 (Nagelkerke, 1991), adjusted for the number of predictors in the model, therefore considering the complexity of the model. This metric measures how well the model predicts an outcome, i.e. the closer the value is to 1, the more accurate is the prediction. The following equation are the explanation of MSE error (Eq. 3.7) and adjusted R^2 (Eq. 3.8):

$$\text{MSE} = \frac{1}{n}\sum_{i=1}^{n}(y_i - \hat{y}_i)^2, \tag{3.7}$$

$$R^2 = 1 - \frac{\sum_{i=1}^{n}(y_i - \hat{y}_i)^2}{\sum_{i=1}^{n}(y_i - \bar{y})^2}, \qquad R^2_{\text{adj}} = 1 - \frac{(1-R^2)(n-1)}{n-k-1}, \tag{3.8}$$

where n represents the total number of pixels in the images, y_i represents the pixel values in the target images, $\hat{y}_i$ represents the pixel values in the predicted images, $\bar{y}$ is the mean of the target values, k is the number of predictors in the analysis. A data augmentation function was implemented in the model to introduce robustness and variations in the training process. Data augmentation is a common technique used during training of deep learning models to improve model generalization through manipulation of input data by applying random, but realistic, transformations. This process can help improve the performance of the model even when limited training data are available. In this work, we will apply random rotation which randomly rotates images during training, and random contrast which randomly adjusts contrast of the images by a random factor.

Typically, dropout levels help improve model generalization by randomly and with a certain frequency setting to zero a fraction of the input units during training. This might prevent the network from relying too much on specific features or relationships in the training data. In this work, these layers are used as a method to estimate the model uncertainty, that is generally not captured by deep-learning tools (Gal and Ghahramani, 2016; Sicking et al., 2020; Feng et al., 2021). The so called "Monte Carlo Dropout" method (hereinafter referred as MCD) maintains the activation of the dropout layers both during the training phase and during testing. The prediction is then repeated iteratively for an arbitrary number of forward steps and the results averaged. In addition to mean, Standard Deviation (SD) can be computed. It measures the dispersion of a data set relative to its average.

To create a more complex dataset, we added Gaussian random noise to the shot gather images. We hypothesize that using TL by fine-tuning, the pre-training model can teach the network to learn to predict CO_2 saturation maps using noisy input images with reduced learning time. This contrasts with the laborious and computationally intensive process of building a model from scratch. The subsequent fine-tuning phase facilitates the rapid adaptation of the network to the specific features present in the noisy images. Consequently, transfer learning has the potential to alleviate the considerable resource demands associated with the use of highly realistic synthetic data for supervised training. There are several approaches and steps to use TL. We have kept the layers trainable along both the encoder and decoder path. Therefore, the architecture of the pretrained model remains unvaried. We just updated the weights during back-propagation, allowing the layers to adapt to the new task while retaining the pretrained knowledge. During the experiments presented in this paper, the network architecture and training hyperparameters of the network were held constant. They were selected based on trial-and-error optimization for the datasets considered in this study, while considering the trade-off between network complexity and processing speed.

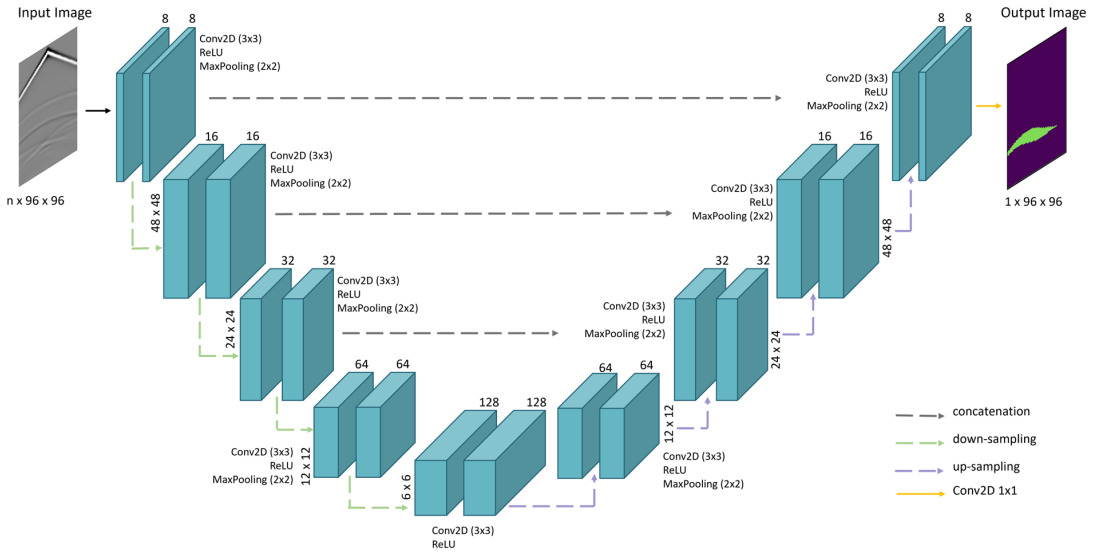

Figure 3.2.5: U-Net architecture used to train our models. Each box corresponds to a multichannel feature map, where the number on the top of the box is the number of filters at each convolution layer. The size of the image is denoted at the edges of the box. At the bottom of input image there is the input size accepted by the model, where n is the number of channels; the output size instead is always the same.

Results

In this section, we evaluate the performance of the proposed models. Overall, we have five training scenarios with the same network architecture. Four scenarios were trained from scratch on SG, CWT, SGCWT2, and SGCWT4 datasets, from here on referred to as SGNet, CWTNet, SGCWT2Net and SGCWT4Net, respectively. The fifth was pretrained on SGNet and then tuned on a noisy dataset, in the following referred to as TL-SGNet. Each network is trained for 200 epochs with a learning rate of 10^{-4}, except for SGNet, SGCWT2Net and SGCWT4Net which were submitted to a sensitivity analysis to the number of epochs. The statistical error metrics used for the quantitative comparison between the ground truth CO_2 saturation maps and the predicted images are MSE and adjusted R^2. Moreover, the MCD method was adopted to have an estimation of uncertainty of the prediction using the SGNet. The synthetic shot gathers obtained simulating a reflection seismic field experiment have 100 traces, and each trace has 511 samples. We cropped the images to a size of 96 $\times$ 96 due to the architecture of our U-Net. Given four sets of two-dimensional MaxPooling layers along the encoder path, the input dimensions should be multiples of 24 for an optimal performance and to reconstruct at UpSampling layers along the decoder path. In fact, an input size of 96 $\times$ 96 is acceptable since all the dimensions can be divided by 24. Subsequently, the CWT images obtained applying two-dimensional wavelet analysis algorithm measure 96 $\times$ 96, as the target output CO_2 saturation maps.

Table 3.1: Evaluation metrics results of the proposed models for SGNet in the first row, CWTNet in the second row, SGCWT2Net in the third row, and SGCWT4Net in the fourth row. Each model was trained for 200 epochs.

Model	Adjusted R^2	MSE	Train time–prediction time [s]
SGNet	0.967	2.124×10^{-4}	385.35–0.221
CWTNet	0.987	1.819×10^{-4}	385.33–0.219
SGCWT2Net	0.986	2.041×10^{-4}	412.11–0.251
SGCWT4Net	0.973	2.838×10^{-4}	505.92–0.548

Training scenarios evaluation

After obtaining the trained networks, we used the test dataset to predict the CO_2 saturation maps in a synthetic CO_2 geological storage project and to evaluate the performance. Table 3.1 summarizes the evaluation metrics values after model evaluation of the deployed networks. Training time and prediction time are also reported, that can be helpful to provide a deeper insight about the influence of different datasets on the training and prediction process. Error analysis on individual images can provide detailed insights that goes beyond aggregate evaluations on test data. To provide a measure of error for each output image and represent the overall discrepancy between target and predicted values, we calculated pixel-wise MSE between ground truth images and network output. Basically, MSE measures how much a prediction deviates, on average, from the actual values. Figure 3.2.6 shows the distribution of the MSE overall the datasets and models trained with 200 epochs. Each box within the boxplots represents the distribution of MSE errors for each specific saturation level. Figure 3.2.6.a-b-c-d show the MSE distribution for SGNet, CWTNet, SGCWT2Net, SGCWT4Net, respectively. By analysing the boxplots, a pattern in the distribution of errors can be identified. It is worth noting that in all the models the error remains relatively low up to saturation levels between 0.5 and 0.6. Instead, for higher saturation levels the average error and boxplot size increases.

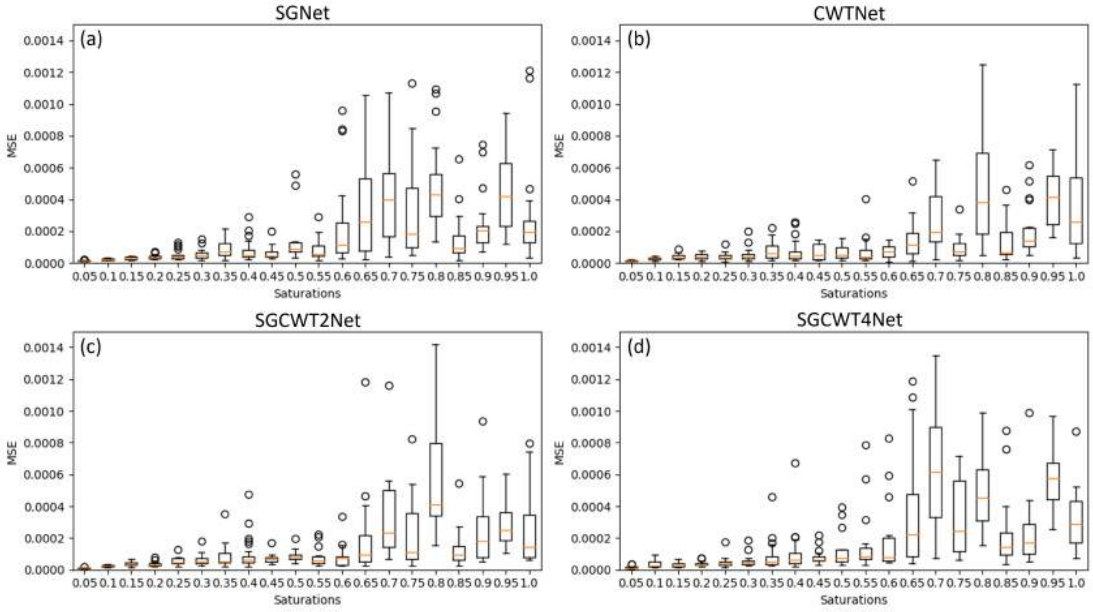

Figure 3.2.6: Box plots of the distribution of MSE of the prediction results on the testing set for various CO_2 saturation values. The horizontal line within each box refers to the median. The lower and upper whiskers are the minimum and maximum values, respectively.

Furthermore, a qualitative evaluation of the proposed method is provided through the visualizations of CO_2 saturation map prediction and corresponding residual error (Figure 3.2.7). Figure 3.2.7 shows SGNet and CWTNet predictions of different plume shapes and CO_2 saturation levels, along with corresponding ground truth and residual error map. The latter was calculated as the difference between ground truth and predicted images. Residual error maps provide some information about prediction accuracy. In fact, the shape of the plume is almost always correctly predicted, except for some edge parts of the plume where errors are more widely distributed. Also, for the saturation level value, errors are more distributed at the edges of the plume rather than in the central part. These observations are valid for both SGNet and CWTNet, but with greater inaccuracies for SGNet.

Table 3.2: Evaluation metrics results of the proposed models for different number of epochs: SGNet in the first row, SGCWT2Net in the second row, and SGCWT4Net in the third row.

	Adjusted R^2			MSE		
Epochs	50	100	200	50	100	200
SGNet	0.931	0.949	0.967	7.49×10^{-4}	2.24×10^{-4}	2.12×10^{-4}
SGCWT2Net	0.972	0.978	0.986	4.03×10^{-4}	2.07×10^{-4}	2.04×10^{-4}
SGCWT4Net	0.964	0.966	0.973	4.07×10^{-4}	2.79×10^{-4}	2.83×10^{-4}

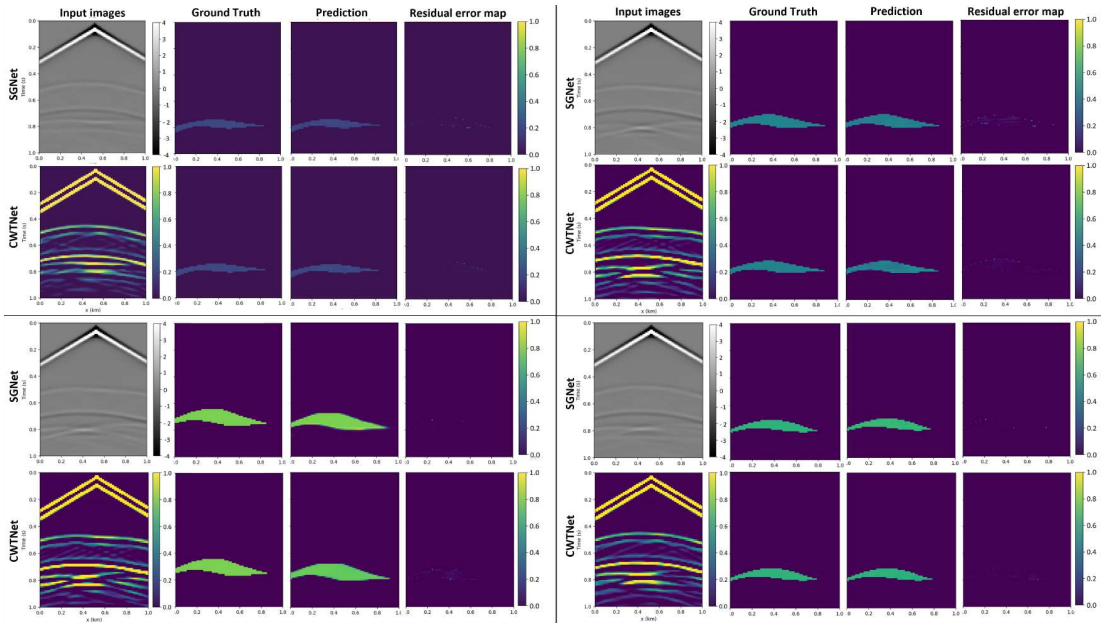

Figure 3.2.7: Examples of CO_2 saturation maps prediction using SGNet and CWTNet. From left to right: the shot gathers input to the predictive model, the ground truth, the predicted CO_2 saturation map, and the residual error map.

A sensitivity analysis on the number of epochs by training SGNet, SGCWT2Net and SGCWT4Net with 50, 100 and 200 epochs was performed to test whether the multichannel approach brings improved prediction accuracy. Once the networks were trained, we used the test datasets to evaluate the performance. The MSE calculated on the prediction results of the models are showed in Table 3.2. The results of the sensitivity analysis show that higher adjusted R^2 score is achieved using SGCWT2Net and SGCWT4Net with a reduced number of training epochs. In fact, the adjusted R^2 score is comparable when the networks are trained for either 100 or 200 epochs. However, with 50 epochs, the R^2 score for SGCWT2Net and SGCWT4Net is higher compared to those obtained from SGNet.

To evaluate the effects of more complex input data to the predictive model, we contaminated the images of the SG dataset with Gaussian noise with zero mean and standard deviation of 10%. In this way, we can evaluate how the SGNet predicts whether receive as input more complex images. However, after training with appropriate data, a model can effectively predict CO_2 saturation maps with high accuracy and have a good robustness against noise. To efficiently train the network to predict CO_2 saturation map from noisy shot gathers, we proposed the use of Transfer Learning. We used the same architecture and all parameters from SGNet trained on SG dataset. We used the SGNet as pretrained model, then we performed a fine-tuning of the pretrained model on the noisy shot gather images, obtaining the TL-SGNet model. The learning rate is set to 10^{-6} while the other training settings are the same as those for the SGNet. TL-SGNet was pretrained for 200 epochs on the original training set, followed by 100 epochs fine-tuning on 1200 complex synthetic images. After model evaluation, the metrics showed a value of 0.8689 for R^2, and 0.0042 for MSE. While training and prediction time of 89.71 and 0.218 seconds, respectively. Figure 3.2.8.a shows a comparison of CO_2 saturation maps predicted from noisy shot gathers using both SGNet and TL-SGNet. Figure 3.2.8.b shows the MSE distribution for the prediction from noisy shot gathers using SGNet. In Figure 3.2.8.b, the error distribution is homogeneous by varying the CO_2 saturation level, in contrast to what is shown in Figure 3.2.7.c or 5. In fact, even in the predictions with TL-SGNet, it can be seen that the error starts to increase when CO_2 saturation values above 0.5–0.6 are reached (Figure 3.2.8.c), which is a peculiarity we had noticed in the models trained with noise-free images. Therefore, this characteristic seems to have been transferred to the model re-trained with the noisy data. The pre-trained model, however, show an improvement in the prediction from noisy shot gathers respect to the prediction using SGNet. This performance improvement is gained from incorporating pre-trained SGNet model in our proposed model, which allowed for better generalization ability. Moreover, we trained our proposed model from scratch using noisy shot gathers as training input. The resulting training time is about 496.85 seconds, the metrics evaluation results in MSE of 0.0415, and R^2 of 0.28. These results suggest that, at least regarding our proposed network architecture, the use of a complex dataset to train a model may not be efficient from the perspective of the use of computational resources and the time required for the network to learn the relationships between input and output.

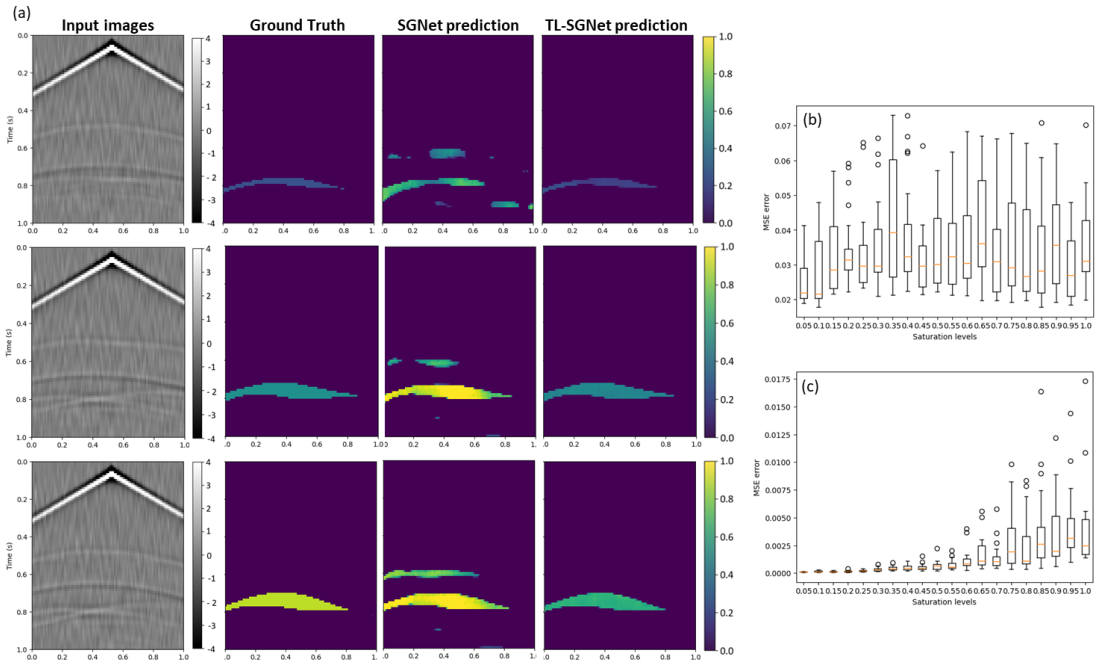

Figure 3.2.8: Examples of the prediction results using SGNet and TL-SGNet on noisy shot gathers. (a) Examples of CO_2 saturation maps prediction. For each row from the left: the noisy shot gathers used as input images, the ground truth, the prediction using SGNet, and the prediction using the fine-tuned SGNet, TL-SGNet. (b) Box plot of the distribution of MSE of the prediction results on the noisy shot gathers using SGNet for various CO_2 saturation values. (c) Box plot of the distribution of MSE of the prediction results on the noisy shot gathers using TL-SGNet for various CO_2 saturation values. The horizontal line within each box refers to the median. The lower and upper whiskers are the minimum and maximum values, respectively.

When the MCD method is adopted, several outputs are produced for a given input. Subsequently, an uncertainty analysis can be performed on the results to quantify the variability of the output. In this work, we performed 30 predictions. Thus, we have a distribution of CO_2 saturation at each pixel for each predicted map and we can calculate a mean CO_2 saturation map and SD map. The mean CO_2 saturation map is considered the output of the model ('MCD prediction' in Figure 3.2.9), while the SD map represents the variability of the CO_2 saturation value for each pixel of the image ('SD map' Figure 3.2.9). Thus, the SD images represents the variability of the predictions for each pixel across the MCD predictions, providing information on the variability of the model prediction for each pixel. Analysing the SD maps, the highest SD values occur at the edges of the plume rather than in the central part of the plume. This suggests that the model faces difficulty in delineating the outer part of the plume and estimating the saturation value at its edges, resulting in a maximum SD value of 0.16. Figure 3.2.10 shows the variability of SD obtained across 30 predictions using

MCD, for each of the CO_2 saturation level. Here the SD values are the maximum value of SD within each SD image across the MCD predictions. These values demonstrate that the predicted values are close to each other and have low SD. In fact, the SD lies within 0.019 to 0.194.

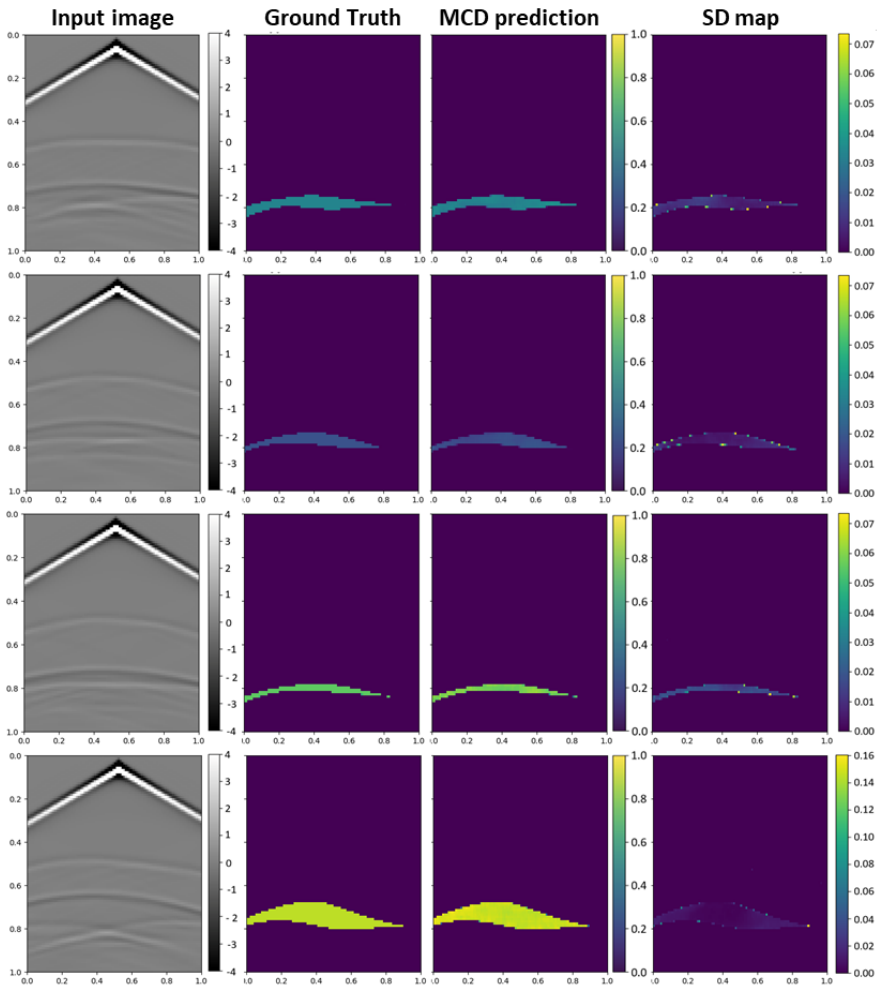

Figure 3.2.9: Examples of CO_2 saturation maps predicted using MCD method. From left to right: the shot gathers input to the predictive model, the ground truth, the mean of the predictions recovered from MCD method, and the Standard Deviation map.

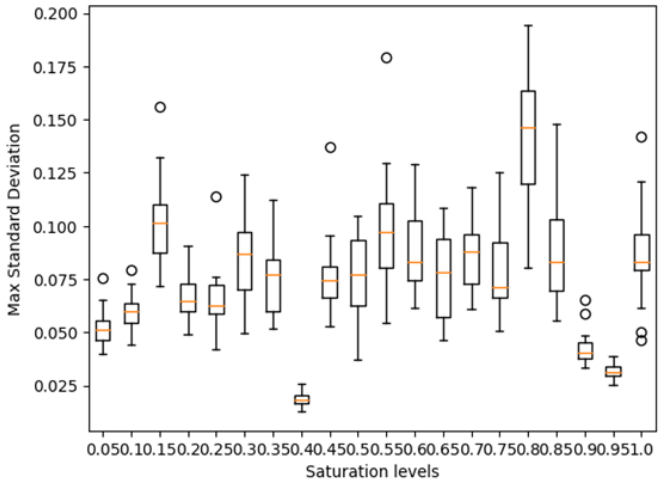

Figure 3.2.10: Box plot of the distribution of SD of the prediction results using SGNet with MCD method, for various CO_2 saturation values. The horizontal line within each box refers to the median. The lower and upper whiskers are the minimum and maximum values, respectively.

Discussion

The purpose of this work was to prove the feasibility of using a multi-scale approach combining two-dimensional Continuous Wavelet Transform with U-Net model, to estimate more accurate maps of the spatial distribution of CO_2 saturation from 2-D synthetic shot gathers. In this analysis, we compare the performance of multiple model training procedures, and we try to identify a procedure that predicts CO_2 saturation maps more efficiently and with higher accuracy. The main purpose of our deep-learning algorithm is to skip the processing and inversion procedures which are conventionally performed for CO_2 saturation inversion using seismic gathers. The 2D-CWT was evaluated as a potential tool to extract features from shot gather images at different scales. The datasets used to train and test our models consists of shot gather images, CWT images, and two datasets composed by multichannel images. The first channel is the shot gather and the other ones are CWT of the shot gathers at progressively increasing scales. MSE and adjusted R^2 have been used as evaluation metrics and to evaluate the performance of the models. The models were tested on the respective test set. The evaluation metrics results indicate that the use of CWT images as training data and as input to the predictive model provides better performance in terms of image prediction accuracy compared to shot gathers. Both SGNet and CWTNet have more difficulty in predicting plume edges, rather than the central body, both in terms of plume shape and saturation value. However, higher inaccuracies were found in the predictions with SGNet. In addition, a sensitivity analysis on the number of epochs was conducted using the models trained with shot gathers and multichannel datasets. The results of this

analysis show that predictions obtained with models trained for 200 epochs have comparable average errors, with no substantial difference. In contrast, predictions performed with models trained for 50 epochs show lower error when using multichannel images as training data. This suggests that the model, despite the reduced number of epochs, leverage its ability to capture information at different scales even from multichannel images. Thus, it learns complementary information from shot gathers and CWT images simultaneously, maximizing the utilization of input data. The models trained on multichannel images, incorporating shot gather and CWT images, outperformed traditional approaches, demonstrating the effectiveness of the proposed methodology in accurately predicting CO_2 saturation maps. To evaluate the predictions of the models, we calculated the pixel-wise MSE between ground truth images and prediction results. While MSE values are generally low, a noteworthy observation is their distinctive distribution as CO_2 saturation varies (Figure 3.2.6 and Figure 3.2.8.b-c). Specifically, the variability of MSE remains constant up to CO_2 saturation values of about 0.6, beyond which it begins to increase. According to our interpretation, this behaviour of the MSE is not random. Indeed, Figure 3.2.2 shows how the P-wave velocity of a sandstone rapidly decreases up to CO_2 saturation values of 0.6, after which it stabilizes, becoming nearly constant for higher saturation levels. Consequently, this phenomenon results in stable P-wave velocity values beyond a saturation of 0.6, most probably due to the rock-physics model used. Therefore, the prediction results are affected by the rock physics model used to estimate seismic velocities after CO_2 fluid replacement, from which synthetic seismic acquisition was performed to obtain shot gathers. As a result, the seismic response will also show low variability and the shot gathers will be hardly discernible. These observations lead to further investigations into the P-wave velocity–CO_2 saturation relationship, which is critical to generate rock-physics models as realistic as possible. The Transfer Learning technique was employed to leverage the knowledge acquired from the model pretrained with noise-free shot gathers and transfer it to predict CO_2 saturation maps from noisy shot gathers. The improvement in prediction performance is noticeable after fine-tuning the pre-trained model, with respect to prediction performed on noisy shot gather using the pre-trained model. Even in predictions using the fine-tuned model, higher MSE values result at high saturation values, as observed for the pre-trained model. Thus, this feature also seems to have been transferred to the model retrained with the noisy data. This saves not only time and computational resources, but also exploits prior knowledge gained in the network, facilitating more effective solutions to complex inversion problems. The adoption of the MCD method in our study allows a thorough exploration of prediction uncertainty and model variability. Thirty predictions provide a robust distribution of CO_2 saturation values at each pixel for every predicted map. The analysis of the SD maps reveals

the model prediction variability at the pixel level, supplying crucial information on the confidence and stability of predictions. The obtained SD values (Figure 3.2.10), ranging from 0.019 to 0.194, indicate a high level of agreement among predictions. In summary, the uncertainty analysis using the MCD method underscores the model's consistency and reliability in estimating CO_2 saturation levels, reinforcing its credibility. Moreover, this approach also faces challenges, notably in capturing subtle differences in features and patterns due to limited variability among images. Augmenting the dataset with more diverse examples could address this limitation, enhancing the model's generalization capabilities. Further research into different rock-physics modelling approaches could refine synthetic modelling, improving the accuracy and generalization of predictive models. Another limitation of this method is the exclusive development and implementation on synthetic data, which are scalable, allowing the dimensions to be adjusted to facilitate training. In the future, we are planning to test these models on field seismic data, although accessing pre-stack seismic data of a CO_2 sequestration context is challenging. Related to this, an additional limitation of this approach could be related to the dependence of the DL model on the site being analyzed, thus making accurate site modeling necessary to train the DL model.

Conclusions

This work presents a novel approach to CO_2 saturation inversion that integrates deep learning techniques with two-dimensional Continuous Wavelet Transform. The U-Net model was trained using both single channel input (shot gathers or CWT at the first scale) and multichannel input that combine shot gathers with CWT at different scales. The prediction performances were evaluated using evaluation metrics such as MSE and adjusted R^2. Our results indicate that using 2D-CWT as input to the U-Net model improves the quality of saturation map predictions. This approach not only improves prediction accuracy, requires less training time than using shot gather input to achieve similar results. This methodology extracts features from seismic records producing more informative images that enhance the predictive capabilities of the model when used as input during the training phase. The results of a sensitivity analysis on the number of epochs underline that a strategic approach to epoch selection significantly contributes to optimizing model performance, especially when multichannel images are used as input. Synthetic Gaussian noise was added to the shot gathers to evaluate the performance of the model trained on noisy images. To achieve better performance, the pre-trained model was fine-tuned to increase the accuracy of the predictions from noisy shot gathers, emphasizing the value of Transfer Learning in seismic inverse problems. Furthermore, the incorporation of the Monte Carlo Dropout (MCD) method emerged as a pivotal strategy for uncertainty analysis. By analysing the standard deviation (SD) maps, we obtained information on the variability of the model's predictions and

infer how the model achieves high level of agreement among predictions. This method contributes to the robustness of the model by providing a tool to evaluate uncertainty in CO_2 saturation predictions. In addition, different approaches to rock-physics modelling could be considered in the inversion process to refine the synthetic modelling, thereby improving the accuracy and generalization of the predictive model. Our results suggest that 2D-CWT can be implemented in a seismic data processing workflow to provide interesting insights in the context of CO_2 injection monitoring. Moreover, the implementation of a DL model is efficient for solving data-driven geophysical inversion problems, despite the initial high computational effort required for model training and the need for a site-dependent subsurface model. Moving forward, addressing challenges related to dataset diversity and exploring alternative rock-physics modelling approaches will be crucial for advancing the capabilities of deep learning models in CO_2 saturation inversion. Furthermore, testing these models on pre-stack field data is crucial to assess the actual applicability of this method. Future developments will undoubtedly progress in this direction, as we believe that this holistic approach will be instrumental in advancing the adaptability of deep learning models for CO_2 saturation inversion to field data.

Computer code availability The developed U-Net code is publicly available at https://github.com/GiovanniPantaleo/U-Net-for-CO2-saturation-map-estimation.git.

Bibliography

T. Ajayi, J. S. Gomes, and A. Bera. 2019. A review of CO_2 storage in geological formations emphasizing modeling, monitoring and capacity estimation approaches. *Petroleum Science* 16 (2019), 1028–1063. https://doi.org/10.1007/s12182-019-0340-8

A. Ali, Sheng-Chang Chen, and M. Shah. 2020. Continuous wavelet transformation of seismic data for feature extraction. *SN Applied Sciences* 2 (2020), 1835. https://doi.org/10.1007/s42452-020-03618-w

Håvard Alnes, Ola Eiken, Scott Nooner, G. Sasagawa, Torkjell Stenvold, and Mark Zumberge. 2011. Results from Sleipner gravity monitoring: Updated density and temperature distribution of the CO2 plume. *Energy Procedia* 4 (12 2011), 5504–5511. https://doi.org/10.1016/j.egypro.2011.02.536

J.-P. Antoine, R. Murenzi, P. Vandergheynst, and S. T. Ali. 2004. *Two-Dimensional Wavelets and their Relatives*. Cambridge University Press, Cambridge. https://doi.org/10.1017/CBO9780511543395

M. Araya-Polo, J. Jennings, A. Adler, and T. Dahlke. 2018. Deep-learning tomography. *The Leading Edge* 37 (2018), 58–66. https://doi.org/10.1190/tle37010058.1

R. Arts, O. Eiken, A. Chadwick, P. Zweigel, L. van der Meer, and B. Zinszner. 2004. Monitoring of CO_2 injected at Sleipner using time-lapse seismic data. *Energy* 29 (2004), 1383–1392. https://doi.org/10.1016/j.energy.2004.03.072

M. Bagheri and M. A. Riahi. 2015. Seismic facies analysis from well logs based on supervised classification scheme with different machine learning techniques. *Arabian Journal of Geosciences* 8 (2015), 7153–7161. https://doi.org/10.1007/s12517-014-1691-5

M. Bagheri and M. A. Riahi. 2017. Modeling the facies of reservoir using seismic data with missing attributes by dissimilarity based classification. *Journal of Earth Science* 28 (2017), 703–708. https://doi.org/10.1007/s12583-017-0797-6

M. Batzle and Z. Wang. 1992. Seismic properties of pore fluids. *Geophysics* 57, 11 (1992), 1396–1408. https://doi.org/10.1190/1.1443207

M. A. Biot. 1956. Theory of Propagation of Elastic Waves in a Fluid-Saturated Porous Solid. I. Low-Frequency Range. *The Journal of the Acoustical Society of America* 28 (1956), 168–178. https://doi.org/10.1121/1.1908239

A. Chadwick, R. Arts, O. Eiken, P. Williamson, and G. Williams. 2006. Geophysical monitoring of the CO_2 plume at Sleipner, North Sea. In *Advances in the Geological Storage of Carbon Dioxide*. Springer, Dordrecht, 303–314. https://doi.org/10.1007/1-4020-4471-2_25

R. Chadwick, G. Williams, N. Delépine, V. Clochard, K. Labat, S. Sturton, M.-L. Budensiek, M. Dillen, M. Nickel, A. Lima, R. Arts, F. Neele, and G. Rossi. 2010. Quantitative analysis of time-lapse seismic monitoring data at the Sleipner CO_2 storage operation. *The Leading Edge* 29 (2010), 170–177. https://doi.org/10.1190/1.3304820

R. A. Chadwick, R. Arts, O. Eiken, G. A. Kirby, E. Lindeberg, and P. Zweigel. 2004a. 4D Seismic Imaging of an Injected CO_2 Plume at the Sleipner Field, Central North Sea. In *Geological Society, London, Memoirs*. Vol. 29. Geological Society of London, London, 311–320. https://doi.org/10.1144/GSL.MEM.2004.029.01.29

R. A. Chadwick, P. Zweigel, U. Gregersen, G. A. Kirby, S. Holloway, and P. N. Johannessen. 2004b. Geological reservoir characterization of a CO2 storage site: The Utsira Sand, Sleipner, northern North Sea. *Energy* 29, 9-10 (2004), 1371–1381. https://doi.org/10.1016/j.energy.2004.03.071

P. Davidson, J. Freund and A. Smith. 2001. *Putting carbon back in the ground*. Technical Report. IEA, Cheltenham, UK. https://publications.ieaghg.org/docs/general_publications/putcback.pdf

M. de la Varga, A. Schaaf, and F. Wellmann. 2019. GemPy 1.0: open-source stochastic geological modeling and inversion. *Geoscientific Model Development* 12, 1 (2019), 1–32. https://doi.org/10.5194/gmd-12-1-2019

B. Dupuy, A. Romdhane, P. Eliasson, E. Querendez, H. Yan, V. A. Torres, and A. Ghaderi. 2017. Quantitative seismic characterization of CO_2 at the Sleipner storage site, North Sea. *Interpretation* 5 (2017), SS23–SS42. https://doi.org/10.1190/INT-2017-0013.1

Runhai Feng. 2023. Physics-informed deep learning for rock physical inversion and its uncertainty analysis. *Geoenergy Science and Engineering* 230 (2023), 212229. https://doi.org/10.1016/j.geoen.2023.212229

R. Feng, D. Grana, and N. Balling. 2021. Uncertainty quantification in fault detection using convolutional neural networks. *Geophysics* 86 (2021), 41–48. https://doi.org/10.1190/geo2020-0424.1

A.-K. Furre and O. Eiken. 2014. Dual sensor streamer technology used in Sleipner CO_2 injection monitoring. *Geophysical Prospecting* 62 (2014), 1075–1088. https://doi.org/10.1111/1365-2478.12120

A.-K. Furre, O. Eiken, H. Alnes, J. N. Vevatne, and A. F. Kiær. 2017. 20 Years of Monitoring CO_2-injection at Sleipner. *Energy Procedia* 114 (2017), 3916–3926. https://doi.org/10.1016/j.egypro.2017.03.1523

Yarin Gal and Zoubin Ghahramani. 2016. Dropout as a Bayesian Approximation: Representing Model Uncertainty in Deep Learning. In *Proceedings of The 33rd International Conference on Machine Learning (Proceedings of Machine Learning Research, Vol. 48)*, Maria Florina Balcan and Kilian Q. Weinberger (Eds.). PMLR, New York, New York, USA, 1050–1059. https://proceedings.mlr.press/v48/gal16.html

F. Gassmann. 1951. Elastic waves through a packing of spheres. *Geophysics* 16 (1951), 673–685. https://doi.org/10.1190/1.1437718

W. D. Gunter, S. Bachu, and S. Benson. 2004. The role of hydrogeological and geochemical trapping in sedimentary basins for secure geological storage of carbon dioxide. In *Geological Society, London, Special Publications*. Vol. 233. Geological Society of London, London, 129–145. https://doi.org/10.1144/GSL.SP.2004.233.01.09

C. Hermanrud, T. Andresen, O. Eiken, H. Hansen, A. Janbu, J. Lippard, H. N. Bolås, T. H. Simmenes, G. M. G. Teige, and S. Østmo. 2009. Storage of CO_2 in saline aquifers–Lessons learned from 10 years of injection into the Utsira Formation in the Sleipner area. *Energy Procedia* 1 (2009), 1997–2004. https://doi.org/10.1016/j.egypro.2009.01.260

Q. Hu, D. Grana, and K. A. Innanen. 2022. Predicting the time-evolution of CO_2 saturation through a combination of rock physics and full-waveform inversion. In *Second International Meeting for Applied Geoscience & Energy, SEG Technical Program Expanded Abstracts*. Society of Exploration Geophysicists, Houston, TX, 3419–3423. https://doi.org/10.1190/image2022-3745280.1

F. Huot, B. Biondi, A. Lichnewsky, and C. Boneti. 2019. Automatic denoising by 2-D continuous wavelet transform. In *SEG Technical Program Expanded Abstracts 2019*. Society of Exploration Geophysicists, San Antonio, TX, 3944–3948. https://doi.org/10.1190/segam2019-3213958.1

M. Ivandic, P. Bergmann, J. Kummerow, F. Huang, C. Juhlin, and S. Lueth. 2018. Monitoring CO_2 saturation using time-lapse amplitude versus offset analysis of 3D seismic data from the Ketzin CO_2 storage pilot site, Germany. *Geophysical Prospecting* 66 (2018), 1568–1585. https://doi.org/10.1111/1365-2478.12666

D. P. Kingma and J. Ba. 2014. Adam: A method for stochastic optimization. *arXiv preprint arXiv:1412.6980* abs/1412.6980 (2014), 1–15. https://doi.org/10.48550/arXiv.1412.6980

Z. X. Leong, T. Zhu, and A. Y. Sun. 2022. Estimating CO2 saturation maps from seismic data using deep convolutional neural networks. In *Second International Meeting for Applied Geoscience & Energy*. Society of Exploration Geophysicists and American Association of Petroleum Geologists, Houston, TX, 510–514. https://doi.org/10.1190/image2022-3746727.1

M. Liu, V. Divakar, D. Grana, and T. Mukerji. 2023. Joint Inversion of Geophysical Data for Geologic Carbon Sequestration Monitoring: A Differentiable Physics-Informed Neural Network

Model. *Journal of Geophysical Research: Solid Earth* 128, 3 (2023), e2022JB025372. https://doi.org/10.1029/2022JB025372

M. Louboutin, M. Lange, F. Luporini, N. Kukreja, P. A. Witte, F. J. Herrmann, P. Velesko, and G. J. Gorman. 2019. Devito (v3.1.0): an embedded domain-specific language for finite differences and geophysical exploration. *Geoscientific Model Development* 12 (2019), 1165–1187. https://doi.org/10.5194/gmd-12-1165-2019

S. Mannor, D. Peleg, and R. Rubinstein. 2005. The cross entropy method for classification. In *Proceedings of the 22nd International Conference on Machine Learning*. ACM, Bonn, Germany, 561–568. https://doi.org/10.1145/1102351.1102422

D. Marr and E. Hildreth. 1980. Theory of edge detection. *Proceedings of the Royal Society of London. Series B, Biological Sciences* 207 (1980), 187–217. https://doi.org/10.1098/rspb.1980.0020

M. A. Meadows and S. P. Cole. 2013. 4D seismic modeling and CO_2 pressure-saturation inversion at the Weyburn Field, Saskatchewan. *International Journal of Greenhouse Gas Control* 16 (2013), S103–S117. https://doi.org/10.1016/j.ijggc.2013.01.030

S. D. Meyers, B. G. Kelly, and J. J. O'Brien. 1993. An Introduction to Wavelet Analysis in Oceanography and Meteorology: With Application to the Dispersion of Yanai Waves. *Monthly Weather Review* 121 (1993), 2858–2866. https://doi.org/10.1175/1520-0493(1993)121<2858:AITWAI>2.0.CO;2

N. J. D. Nagelkerke. 1991. A note on a general definition of the coefficient of determination. *Biometrika* 78, 3 (1991), 691–692. https://doi.org/10.1093/biomet/78.3.691

S. Nooner, O. Eiken, C. Hermanrud, G. Sasagawa, T. Stenvold, and M. Zumberge. 2007. Constraints on the in-situ density of CO_2 within the Utsira formation from time-lapse seafloor gravity measurements. *International Journal of Greenhouse Gas Control* 1 (2007), 198–214. https://doi.org/10.1016/S1750-5836(07)00018-7

B. Osdal, H. M.Zadeh, S. Johansen, and D. Gilding. 2013. CO2 Saturation and Thickness Prediction from 4D Seismic Data at Snřhvit Field. *EAGE* 1, 1 (2013). https://doi.org/10.3997/2214-4609.20130854

M. Queißer and S. C. Singh. 2013. Full waveform inversion in the time lapse mode applied to CO_2 storage at Sleipner. *Geophysical Prospecting* 61 (2013), 537–555. https://doi.org/10.1111/j.1365-2478.2012.01072.x

V. K. Reddy, K. K. Siramoju, and P. Sircar. 2014. Object Detection by 2-D Continuous Wavelet Transform. In *2014 International Conference on Computational Science and Computational Intelligence*. IEEE, Las Vegas, NV, USA, 162–167. https://doi.org/10.1109/CSCI.2014.34

P. Ringrose. 2020. *How to Store CO_2 Underground: Insights from early-mover CCS Projects*. Springer International Publishing, Cham. https://doi.org/10.1007/978-3-030-33113-9

Olaf Ronneberger, Philipp Fischer, and Thomas Brox. 2015. U-Net: Convolutional Networks for Biomedical Image Segmentation. In *Medical Image Computing and Computer-Assisted Intervention – MICCAI 2015*, Nassir Navab, Joachim Hornegger, William M. Wells, and Alejandro F. Frangi (Eds.). Springer International Publishing, Cham, 234–241. https://doi.org/10.48550/arXiv.1505.04597

J. Sicking, M. Akila, T. Wirtz, S. Houben, and A. Fischer. 2020. Characteristics of Monte Carlo Dropout in Wide Neural Networks. *arXiv preprint arXiv:2007.05434* 1 (2020), 1–14. https://doi.org/10.48550/arXiv.2007.05434

S. Sinha, P. S. Routh, P. D. Anno, and J. P. Castagna. 2005. Spectral decomposition of seismic data with continuous-wavelet transform. *Geophysics* 70, 6 (2005), P19–P25. https://doi.org/10.1190/1.2127113

A. Tarantola. 1984. Inversion of seismic reflection data in the acoustic approximation. *Geophysics* 49, 8 (1984), 1259–1266. https://doi.org/10.1190/1.1441754

N. Tavakolizadeh and M. Bagheri. 2022. Multi-attribute Selection for Salt Dome Detection Based on SVM and MLP Machine Learning Techniques. *Natural Resources Research* 31 (2022), 353–370. https://doi.org/10.1007/s11053-021-09973-8

C. Torrence and G. P. Compo. 1998. A Practical Guide to Wavelet Analysis. *Bulletin of the American Meteorological Society* 79 (1998), 61–78. https://doi.org/10.1175/1520-0477(1998)079<0061:APGTWA>2.0.CO;2

E. S. Um, D. Alumbaugh, M. Commer, S. Feng, E. Gasperikova, Y. Li, Y. Lin, and S. Samarasinghe. 2022b. Deep learning multiphysics network for imaging CO_2 saturation and estimating uncertainty in geological carbon storage. *Geophysical Prospecting* 72 (2022), 183–198. https://doi.org/10.1111/1365-2478.13257

E. S. Um, D. Alumbaugh, M. Commer, S. Feng, E. Gasperikova, Y. Li, and S. Samarasinghe. 2022a. Deep learning multiphysics network for imaging CO2 saturation and estimating uncertainty in geological carbon storage. *Geophysical Prospecting* 72, 1 (2022), 183–198. https://doi.org/10.1111/1365-2478.13257

N. Wang and C. Lu. 2010. Two-Dimensional Continuous Wavelet Analysis and Its Application to Meteorological Data. *Journal of Atmospheric and Oceanic Technology* 27 (2010), 652–666. https://doi.org/10.1175/2009JTECHA1338.1

X. Wang, J. Gao, Y. He, and W. Wang. 2009. 2D seismic attributes extraction based on two-dimensional continuous wavelet transform. In *SEG Technical Program Expanded Abstracts 2009*, Vol. 28. Society of Exploration Geophysicists, Houston, TX, 3650–3654. https://doi.org/10.1190/1.3255625

Z. Wang, R. Dilmore, and W. Harbert. 2020. Inferring CO_2 saturation from synthetic surface seismic and downhole monitoring data using machine learning for leakage detection at CO_2 sequestration sites. *International Journal of Greenhouse Gas Control* 100 (2020), 103115. https://doi.org/10.1016/j.ijggc.2020.103115

B. Yan, B. Chen, D. R. Harp, W. Jia, and R. J. Pawar. 2022. A robust deep learning workflow to predict multiphase flow behavior during geological CO_2 sequestration injection and Post-Injection periods. *Journal of Hydrology* 607 (2022), 127542. https://doi.org/10.1016/j.jhydrol.2022.127542

Chapter 4

Cost-effective early-leakage detection

Early detection of CO_2 leakage is a key requirement for ensuring the long-term safety and integrity of geological storage sites. Seismic monitoring is among the most reliable tools for tracking subsurface CO_2 flow, as it provides direct sensitivity to fluid substitution and pressure changes within the reservoir and the overburden. However, the use of time-lapse (4D) seismic surveys for early leakage detection beyond the primary storage complex remains challenging. Conventional approaches rely on repeated full-scale acquisitions and manual interpretation, which are costly and time-consuming, and often limited by low signal-to-noise ratios and subtle temporal variations in the recorded signals. These factors hinder the ability to detect weak leakage signatures in their early stages, when mitigation strategies would be most effective.

Traditional monitoring workflows are also constrained by the need for dense data coverage and domain-specific inversion schemes. In many cases, early-stage leakage or migration produces seismic changes that are too subtle to be resolved through standard amplitude- or traveltime-based analyses alone. Moreover, the increasing volume of seismic data collected in modern monitoring programs calls for methods that can efficiently extract informative patterns without extensive manual intervention in a less subjective way. This has led to growing interest in automated, data-driven approaches capable of identifying and quantifying time-lapse changes directly from seismic images.

Recent advances in DL have shown strong potential for improving seismic interpretation, particularly through Convolutional Neural Networks (CNNs) that can learn hierarchical features from complex image-like data. Yet, training such networks from scratch typically requires large labelled datasets and significant computational resources, which

are rarely available in the context of CO_2 storage monitoring. An alternative is to exploit the representational power of pre-trained CNNs, which have already learned generic visual features from large-scale natural image datasets. These pre-trained models can serve as fixed feature extractors, allowing the transfer of learned representations to new domains, such as seismic monitoring, with minimal additional training.

By adapting pre-trained architectures to seismic data, we encode time-lapse seismic images into high-dimensional feature spaces that can capture subtle waveform variations linked to subsurface changes. When combined with dimensionality reduction techniques, these embeddings can support both qualitative visualization and, most importantly, quantitative change detection. In this context, pre-trained deep networks provide a computationally efficient path toward automated fluid anomaly detection, potentially transforming time-lapse seismic monitoring into a faster, more scalable, and cost-effective early-warning system for CO_2 leakage.

4.1 Enhancing early CO_2 leakage detection using pre-trained deep learning models

This study presents a deep learning framework for early CO_2 leakage detection from time-lapse seismic data, leveraging a pre-trained ResNet152 model originally trained for natural images classification. The framework integrates forward seismic modelling, deep feature extraction, and leakage mass prediction. ResNet152 is adapted to extract embeddings from time-lapse seismic shot gathers, which are compared using a Siamese network setup. Time-lapse embeddings are projected into a 2D latent space using UMAP, enabling anomaly detection and temporal pattern analysis. A Multilayer Perceptron (MLP) regressor is then trained to estimate leakage mass from the extracted embeddings. Tests on synthetic datasets from the Kimberlina CO_2 storage site simulations show that the model effectively captures the temporal evolution of seismic signal related to CO_2 leakage, particularly during the early stages. UMAP projections reveal clear separability between baseline, no-leakage, and leakage scenarios. Despite being trained on non-seismic data, the model produces informative embeddings that fully support leakage detection. The MLP regressor achieves satisfactory performance even under realistic noise levels. This framework demonstrates the potential of using pre-trained CNNs for seismic monitoring tasks, and is extendable to other architectures. It offers computational efficiency and generalization that are essential for providing an early-warning tool to flag anomalies and guide targeted surveys.

Enhancing early CO_2 leakage detection using pre-trained deep learning models

G. Pantaleo, M. Pipan

Extended abstract presented at the World CCUS Conference 2025, Volume 2025, 1^{st}-4^{th} September 2025, Bergen, Norway

doi: https://doi.org/10.3997/2214-4609.202522134

Available at:

https://www.earthdoc.org/content/papers/10.3997/2214-4609.202522134

Key Words

Time-lapse seismic monitoring; *CCS leakage detection*; *UMAP dimensionality reduction*; *Pre-trained NN*

Introduction

Underground carbon-dioxide storage plays a crucial role to play in meeting net-zero emissions targets by 2050. The diffusion of Carbon Capture and Storage (CCS) technologies is often hampered by cost constraints, particularly during the characterization and monitoring phase of deep reservoirs, such as aquifers or depleted gas fields. For this reason, there is an urgent need to develop cost-effective monitoring strategies that primarily target key structures and ensure CO_2 containment within the storage complex. Time-lapse seismic monitoring is a widely adopted approach, but its application for early leakage and migration detection beyond the designated storage complex remains challenging due to acquisition challenges, noise interference, and subtle signal changes. This work aims to develop a Deep Learning (DL) framework that could be both computationally cost-effective and efficient for early detection of CO_2 leakage during time-lapse seismic surveys. We explore the potential of using pre-trained Convolutional Neural Networks (CNNs), specifically ResNet152 (He et al., 2016), originally trained on the ImageNet dataset (Deng et al., 2009). Using a pre-trained model, one can avoid the training phase from scratch, which is a computationally expensive and data-intensive task. Instead, we leverage the deep representations and weights learned by the model from a different dataset and task, adapting them to identify changes in time-lapse seismic data, and to provide an initial quantitative estimation of CO_2 leakage. We adapted ResNet152 to extract meaningful features from seismic images and

to monitor the evolution of seismic data over time. To test the proposed framework, we consider hypothetical well leakage scenarios for a candidate CCS site near Kimberlina, CA, USA. We used a dataset based on 3D numerical multi-phase flow simulations (Buscheck et al. (2019); Yang et al. (2019)). These simulations model CO_2 and brine leakage from a legacy well into overlying shallow aquifers. The model domain includes three overlying aquifer layers, while excluding the CO_2 injection well, storage reservoir, and primary seal (see Yang et al. (2019) for further details of the Kimberlina model). The dataset comprises 1000 simulations, which each contain a unique aquifer heterogeneity, aquifer and caprock permeability. The output time steps are every 10 years between 0-200 years. The simulation outputs considered in this work comprise CO_2 saturation maps and CO_2 leakage mass for each time step. The saturation maps were converted into P-wave velocity models using rock physics models, providing the input for forward seismic modeling. The CO_2 leakage mass values were used as targets for training a regressor, enabling the framework to provide a final quantitative estimate of the detected leakage.

Deep Learning Framework

We designed a framework that integrates physics-based seismic modeling to simulate time-lapse seismic surveys, with feature extraction and anomaly detection techniques. Seismic data were generated through seismic acoustic forward modeling based on the P-wave velocity models constructed by Wang et al. (2021), for each simulation time step. A total of 21000 forward modeling was performed using a cross-well survey configuration with 3 sources and 50 receivers for each timestep. Gaussian noise at different signal-to-noise ratios (SNR = 30, 20, 5) was added to simulate realistic acquisition conditions, and evaluate the impact of seismic noise on regressor prediction performance. A Siamese neural network architecture (Chicco, 2020) was implemented using a pre-trained ResNet152 as the feature extractor (Figure 4.1.1). The original ResNet152, trained for image classification on natural images, was modified by removing its final fully connected classification layer. The output of the last convolutional block, a 2048-dimensional feature vector, was used as the embedding representation of the input seismic data. Each input consists of three shot gather images combined into a single 3-channel image. The model processes pairs of time-lapse seismic data, a baseline survey and a monitor survey, to produce embeddings that capture key features of each input. The Siamese setup consists of two identical pre-trained ResNet152 models, with the same configuration, parameters, and weights, operating in parallel. This setup ensures consistent and reliable comparison of the resulting embeddings. From the resulting embeddings, we compute the Euclidean distance to quantify the degree of change between the baseline and monitor images. These high-dimensional embeddings are then reduced to a two-dimensional latent space using Uniform Manifold Approximation and

Projection (UMAP, McInnes et al. (2018)), enabling cluster visualization and anomaly detection. Finally, a multilayer perceptron (MLP) regressor is trained to predict the leakage mass, a physically interpretable parameters derived from flow simulations. This final step is crucial, as it can also provide quantitative information for decision-making in seismic monitoring.

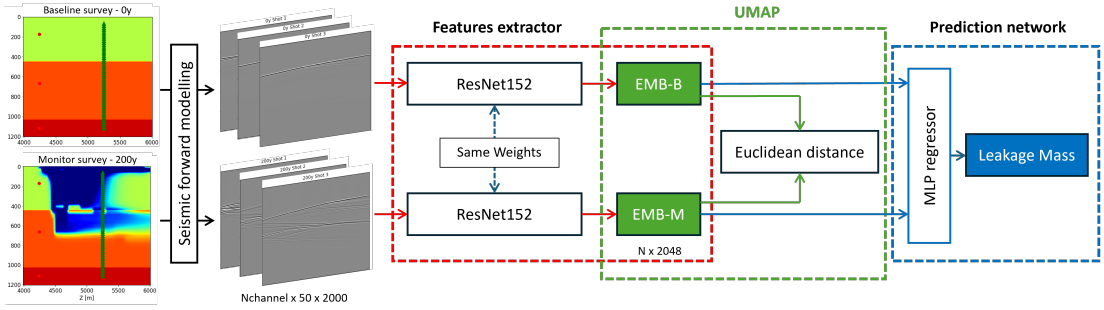

Figure 4.1.1: Overview of the proposed DL framework for time-lapse seismic monitoring. From left: examples of P-wave velocity models from baseline (0 years) and monitor (200 years) surveys used as input to forward modeling to generate synthetic seismic shot gathers. These are processed by a Siamese ResNet152 to extract embeddings (EMB-B and EMB-M, with dimensions batch size $\times$ 2048); then they are compared via Euclidean distance and projected into a 2D latent space using UMAP; the Multilayer Perceptron (MLP) regressor predicts the CO_2 leakage mass from the embeddings.

Early leakage detection and leakage mass prediction

The UMAP space was constructed using embeddings from both baseline and monitor surveys. These projections provide insight into how the Siamese ResNet152 is able to extract deep and meaningful features of the input data in relation to CO_2 leakage progression. In the training set (Figure 4.1.2 left), embeddings from baseline surveys form a well-defined cluster, while monitor embeddings, colored by survey time, are progressively distributed along a certain trajectory. The size of each marker reflects the Euclidean distance between the monitor embedding and its corresponding baseline embedding, larger markers indicate greater deviation. This distribution aligns with simulation time, suggesting that the model captures the temporal evolution of leakage scenarios, particularly at early timesteps such as 10 and 20 years after injection (t10 and t20 in Figure 4.1.2). In contrast, later timesteps become increasingly dispersed in the latent space, indicating greater variability and change as leakage progresses. In the test set (Figure 4.1.2 right), we projected the unseen embeddings into the same UMAP latent space. Embeddings from monitors without leakage remain close to the baseline cluster, while those from leakage scenarios project into a separate region, forming a structure similar to that observed for the training set. This demonstrates the ability of the model to generalize and the stability of the embedding space, although

ResNet152 was originally trained for classification task on non-seismic images. These results indicate that the extracted embeddings are meaningful and discriminative for the task of leakage detection.

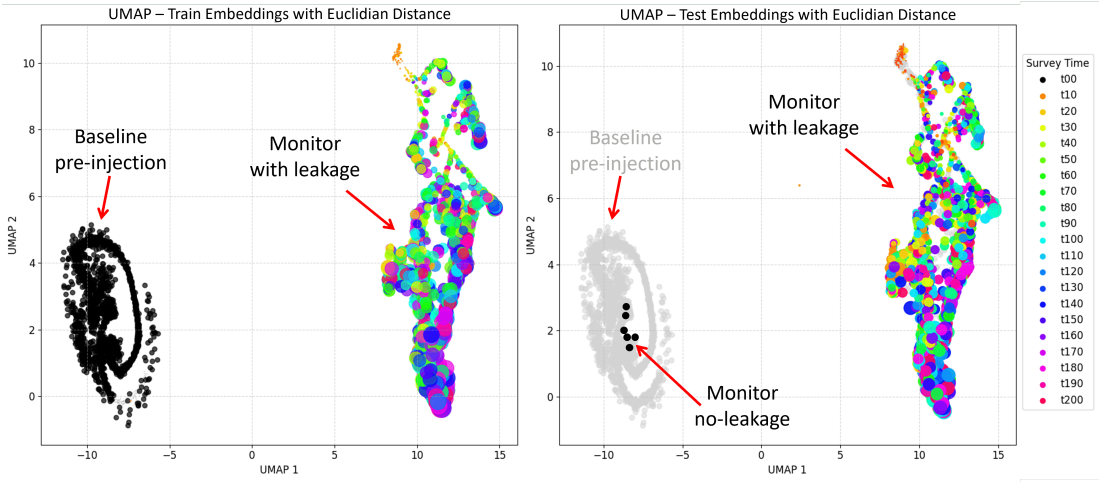

Figure 4.1.2: UMAP projections of train (left) and test (right) embeddings. Baseline and no-leakage monitors cluster together, while leakage scenarios form a distinct cluster, highlighting the ability of the model to separate leakage and no-leakage surveys.

As the noise level increases (i.e., lower SNR), the global structure of the UMAP embeddings becomes progressively less defined and harder to interpret (Figure 4.1.3). At high SNR (SNR = 30), the latent space maintains a coherent structure, with visible separation between different surveys. However, at SNR = 20, the clustering begins to degrade, and by SNR = 5, the separation between leakage and no-leakage scenarios becomes indiscernible. This degradation in the latent space could affect downstream tasks, such as regression or classification. In the final stage of our framework, the embeddings are used as input to a regression model that predicts leakage mass for each time-lapse survey analyzed. The predicted versus true values are shown in Figure 4.1.4. At SNR = 30, the regressor achieves good accuracy, with a coefficient of determination $R^2 = 0.77$, with predicted leakage mass closely matching ground truth values. At SNR = 20, the model maintains good predictive performance ($R^2 = 0.61$), particularly for lower leakage mass values, although it tends to underestimate larger leakage events. At SNR = 5, the correlation between predicted and true leakage mass is strongly reduced ($R^2 = 0.08$). This highlights the reduced ability of the model to generalize under high-noise conditions and underscores the importance of robust denoising and preprocessing techniques when applying the framework to real field data.

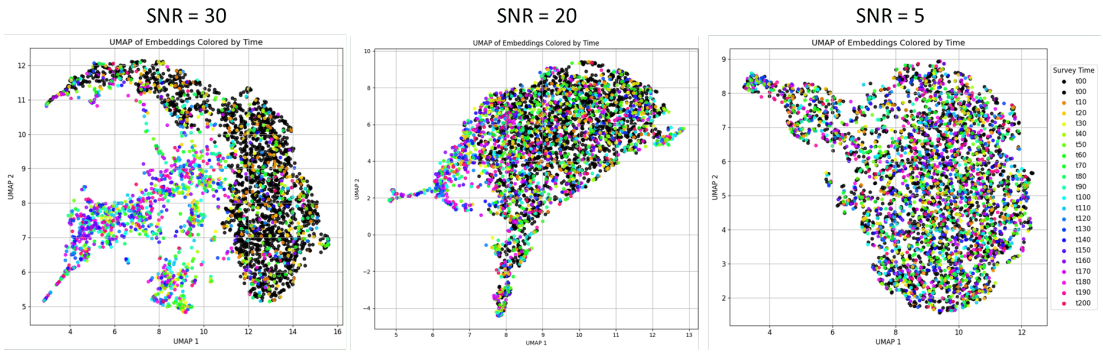

Figure 4.1.3: Impact of seismic noise on UMAP embeddings structure. Lower SNR leads to less structured embeddings with the global structure is no more preserved.

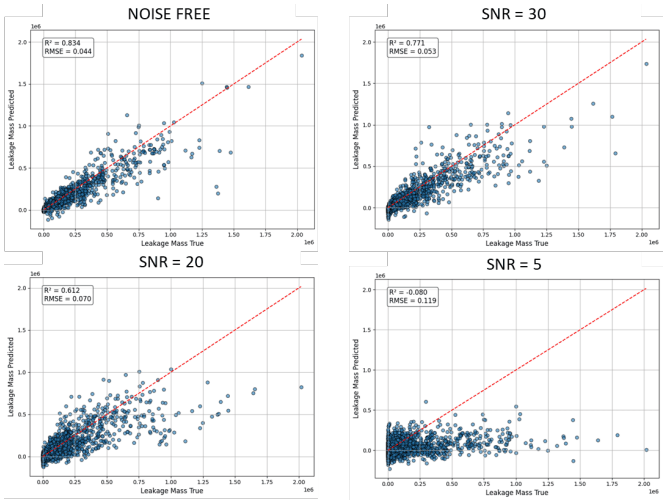

Figure 4.1.4: Impact of seismic noise on regressor prediction performance. As the SNR decreases, the predicted vs. true leakage values become less correlated.

Conclusions

This study demonstrates that a pre-trained ResNet152, originally developed for natural image classification, can successfully extract meaningful features from synthetic time-lapse seismic shot gathers. The model is capable of capturing subtle variations in the seismic response associated with CO_2 leakage, particularly in the early stages of migration. Although not trained on geophysical data, the extracted embeddings proved effective in detecting time-lapse seismic changes. The use of UMAP for dimensionality reduction offered a powerful tool for visual interpretation of the latent space, clearly separating baseline, no-leakage, and leakage scenarios. The embedding structure also reflected temporal progression, with early timesteps appearing more compact and later timesteps becoming increasingly dispersed as leakage advanced. In addition to qualitative analysis, the MLP regressor demonstrated that the embeddings extracted

by the ResNet152 model are informative to support quantitative estimation of CO_2 leakage mass. The MLP regressor, trained on these embeddings, maintains predictive capability in the presence of moderate levels of noise, indicating that the learned representations capture relevant features of the seismic data despite the absence of domain-specific training. The proposed approach is generalizable and can be extended to other pre-trained CNNs. Variants of ResNet (e.g., ResNet50, ResNet101) or alternative architectures such as DenseNet, EfficientNet, or Vision Transformers trained on natural image datasets could be tested to further improve feature extraction performance, embedding robustness, and computational efficiency. Overall, the proposed DL framework offers a promising and computationally efficient approach for early leakage detection in time-lapse seismic monitoring. Although it may not replace conventional monitoring systems, it could have strong potential as a complementary early-warning or decision-support tool to flag anomalies and guide targeted surveys.

4.2 CO_2 migration detection with Time-Lapse seismic DAS using pre-trained deep learning models: a case study from the Svelvik CO_2 Field Lab

In this chapter, we preliminary test the framework proposed in Pantaleo and Pipan (2025) using time-lapse seismic DAS data collected during a controlled CO_2 injection at the Svelvik CO_2 Field Lab, Verket (Norway), in May and June 2025. As discussed in Section 4.1, the main objective of this framework is to efficiently and cost-effectively detect changes in time-lapse (TL) seismic images, without training a deep-learning model from scratch. Instead, we leverage feature-extraction capabilities already learned by the ResNet152, simultaneously extracting meaningful features from TL seismic gathers adopting a Siamese NN setup. Then, the extracted high-dimensional features are reduced and approximated to 2-D employing UMAP, enhancing dataset interpretability detecting CO_2-related changes due to traveltime/amplitude changes in the TL seismic gathers. This method fits in the 'trigger-survey' concepts, where additional surveys can be scheduled only when an anomaly is detected.

Monitoring CO_2 Migration with Time-Lapse DAS Using Pre-Trained Deep Learning Models: Insights from the Svelvik CO_2 Field Lab

Key Words

Distributed Acoustic Sensing (DAS); *Time-lapse seismic monitoring*; *CO_2 storage leakage detection*; *UMAP dimensionality reduction*; *Pre-trained neural networks*

Introduction

A prominent reason behind the recent progress in detecting changes from seismic data is the growing availability of time-lapse seismic datasets. For machine learning models to perform reliably in this field, these datasets must be representative of the geological conditions and acquisition settings of interest. Labels in such datasets are often derived from expert interpretations or automated detection tools. These labels typically indicate whether significant changes have occurred between two time-lapse surveys.

For seismic images, visual inspection remains useful for exploring and verifying data. However, processing and inversion of seismic datasets for use in tomographic or imaging workflows to detect patterns of changes is a labor-intensive task requiring significant human effort. Driven by the growing need for enhanced data exploration and efficient interpretation of complex datasets, data-driven visualization approaches have gained increasing attention. Among these, non-linear dimensionality reduction techniques have proven particularly effective for representing complex relationships within seismic data. Popular methods are non-linear dimensionality reduction methods, such as t-distributed stochastic neighbor embedding (t-SNE), which transform high-dimensional data into two-dimensional representations that retain the original similarity structure, thereby facilitating 2D visual exploration of complex seismic datasets. Recent studies have demonstrated the value of such dimensionality reduction algorithms for seismic change detection. Zheng et al. (2025) applied t-SNE to high-dimensional seismic waveforms, producing clear 2D clusters that improved feature extraction and reservoir prediction. Jun and Cho (2021) used t-SNE to compare feature distributions of time-lapse seismic surveys, guiding data augmentation and enhancing 4D repeatability. In a related geophysical context, Portes et al. (2025) created an interactive 2D atlas of attribute maps using t-SNE, showing how such embeddings can reveal subsurface patterns in seismic-like images.

Building upon the success of t-SNE, Uniform Manifold Approximation and Projection (UMAP) has emerged as a powerful alternative, attracting considerable attention for its solid algebraic and topological foundations as well as its computational efficiency. Recent studies have demonstrated the versatility of UMAP for a wide range of seismic applications. Chai et al. (2025) applied UMAP to over 1400 hours of continuous seismic data from an industrial facility in Texas, successfully identifying clusters related to background noise, vehicle traffic, and previously unrecognized sources, thus illustrating the potential of unsupervised learning for automatic pattern discovery in continuous records. In the context of microseismic monitoring, Chakravarty and Misra (2023) and Misra and Chakravarty (2024) employed UMAP to project high-dimensional accelerometer and hydrophone data acquired during hydraulic stimulation experiments into low-dimensional manifolds, effectively distinguishing fracture networks and assigning fracture-plane labels through a semi-supervised propagation scheme. At a larger exploration scale, Zheng et al. (2025) integrated UMAP with convolutional neural networks (CNNs) for seismic waveform feature extraction and reservoir characterization, demonstrating superior accuracy and computational efficiency compared to traditional non-linear embedding methods such as t-SNE, LLE, and Isomap. Collectively, these studies highlight UMAP's robustness and flexibility in extracting meaningful representations from complex seismic data, enabling both qualitative interpretation and quantitative subsurface analysis across different acquisition scales and geological settings.
In this chapter, we propose a new integrated model based on ResNet152 and UMAP as an early detector for CO_2 leakage, using TL shot gathers. ResNet152, originally trained for classification on the ImageNet dataset (Deng et al., 2009), demonstrates high potential in extracting useful low-dimensional features for monitoring purpose without the need for a feature extraction training stage. Particularly, the features have been extracted from the final layer, after removing the final fully connected classification layer of the network, where the features of the input images are generally most discriminating. The Siamese setup consists of two identical feature extractor with the same configuration, parameters, and weights. Each branch operate in parallel and independently on baseline and monitor shot. This setup ensures consistent and reliable comparison of the extracted embeddings, which can be then used to compute the Euclidean distance quantifying the degree of change between baseline and monitor shots.

Field site and instrumentation overview

The time-lapse seismic dataset analysed in this study was acquired in a cross-well configuration at the Svelvik CO_2 Field Lab (Figure 4.2.1; see Chapter 7 for the geological and geographical context), covering the pre-injection, injection, and post-injection phases of the CO_2 experiment. The CO_2 is injected through the injection well (#2) at 65 m depth in a sandstone aquifer. The injection well is surrounded by four monitoring

wells (M1 to M4) equipped with fibre-optic DAS (Figure 4.2.1) down to a depth of approximately 100 m. In each seismic survey the source was deployed in M4, while the Distributed Acoustic Sensing (DAS) using fibre-optic cables is installed within the casing of all monitoring wells in two configurations: linear (LIN) and helically wound cables (HWC).

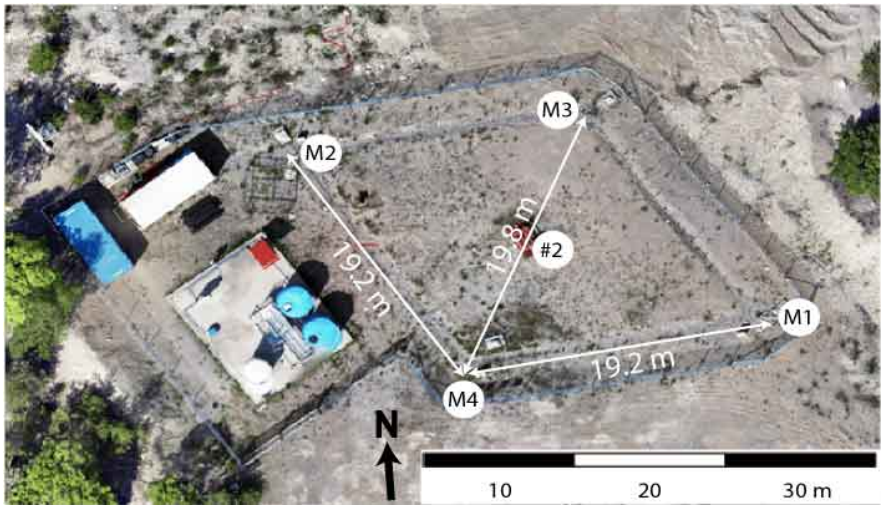

Figure 4.2.1: Overview of the Svelvik CO_2 Field Lab. M1 to M4 are the monitoring wells, #2 is the injection well. The seismic source was deployed in M4.

Findings from several past monitor surveys during injection experiments (Jordan et al., 2022) have demonstrated the same site behaviour once CO_2 is injected: The CO_2 migrates upwards from the injection point and moves northward, accumulating below a clay-rich layer at approximately 37 m depth in correspondence with well M3 (Figure 4.2.2). The CO_2 accumulates below this layer as long as the injection is ongoing. Once the injection stops, the CO_2 continues to move northward and toward the surface, no longer being detected by the monitoring wells (Barbosa et al., 2024). This well-characterized stratigraphic-guided CO_2 migration can be leveraged to develop methodologies aimed at leakage detection and leakage quantification, simulating leakage scenario from a deep storage reservoir. Moreover, this is the perfect situation to test the framework proposed in Pantaleo and Pipan (2025) because of the DAS configuration which ensure high-repeatability due to the fibre-optic cable installed behind-casing. In this way, higher DAS data quality is achieved due to higher coupling with the surrounding rock formation and reduced depthing problems causing tension issues (Willis et al., 2021). Thus, any changes within the data should be strictly related to changes in fluid saturation or pressure changes due to CO_2 injection.

The injection ran for four days, from 30/05 at 16:52 to 03/06 at 16:50 (see Table 7.1).

Accordingly, the surveys on 28/05 and 30/05 serve as the pre-injection baseline (BL1 and BL2, respectively). Surveys from 31/05 to 03/06 correspond to the during-injection period (MO1 to MO4), and the survey on 04/06 represents the post-injection survey (MO5). The last monitor survey planned for 05/06 was cancelled due to a P-wave source failure. Shot coverage varies by day, with shallowest and deepest source depths missing and present only on selected monitor dates. See Table 7.1 for detailed schedule. In this chapter, we analyze the baseline and monitor shot gathers with our framework to assess its ability to detect time-lapse changes, specifically elated to CO_2 induced effects. For this study, we consider only data recorded along the linear DAS cable.

Table 4.1: Injection phase, source depth, and sensors coverage by survey date. Gray cells indicate periods of source failure. HP stand for hydrophones.

		28/05 BL1	30/05 BL2	31/05 MO1	01/06 MO2	02/06 MO3	03/06 MO4	04/06 MO5	05/06 MO6
Injection phase	pre- during- post-								
Source Depth [m]	3–34 35–45 46–55								

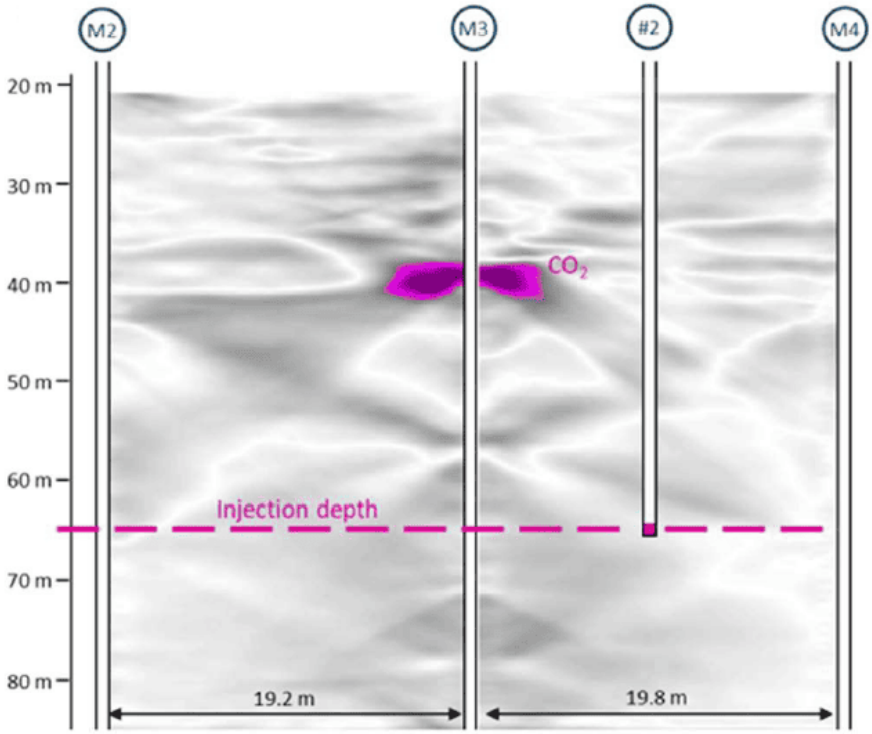

Figure 4.2.2: Cross sections of 4D time lapse velocity anomalies observed during past CO_2 injection derived from seismic first-arrival-time tomography (Jordan et al., 2022).Pink areas indicate time-lapse low-velocity anomalies, corresponding to velocity decreases of at least 3%. Source: Jordan et al. (2022)

Seismic dataset overview

Figure 4.2.3 shows time-lapse shots recorded with the linear DAS cable in well M3 at four source depths (15, 35, 45, and 55 m), displayed from top to bottom in rows (a)–(d). The datasets were pre-processed through the following steps: (1) stacking six repeated shots acquired keeping the source at the same depth; (2) stacking of the downgoing and upgoing DAS segments for both LIN and HWC configurations; (3) band-pass filter 100–1700 Hz to remove diffuse high-frequency noise. Data quality improves increasing the depth of the source point. This would be due to less consolidated subsurface at shallow depths causing a not proper propagation of the seismic wave. Following preprocessing, the TL gathers were directly fed into the proposed framework for subsequent feature extraction and dimensionality reduction. The seismic dataset contains 53 baseline shots and 158 monitor shots, the first covering two days, the latter covering 5 days of repeated surveys. In this study, the monitor surveys will be considered as "CO_2 leakage" scenarios. Further details on the workflow and the linear versus helical DAS response are provided in Chapter 7.

A visual analysis of the time-lapse shots in Figure 4.2.3 reveals several features that reflect the well-known behaviour of subsurface CO_2 migration, as established in previous experiments at the field site. These changes are evident from MO1 in Figures 4.2.3a–c, and then remain consistent through MO4 and MO5. Black circles highlights new reflection events become evident between 0.01 and 0.03 seconds. A strong linear signal, already visible in BL1 and BL2 and highlighted by the black arrows, is preliminarily interpreted as a guided wave. It appears to be generated near or at the surface from the direct wave and then to propagate downward along the entire length of well M3 as a direct arrival. In fact, its travel-time increases linearly with increasing depth along the well. Particularly, black arrows point out amplitude variations of this guided wave, where the amplitude gradually decreases from MO1 over the injection period. Green arrows indicate a new event originating from the same guided wave at approximately 35–40 m depth, propagating upward along the cable. This new event might indicate the interaction between the guided wave and the accumulation of CO_2 beneath the clay layer at approximately 37 m depth in well M3, causing some type of refraction or reflection.

DL Framework Implementation and Workflow

We modified the framework introduced in Section 4.1 (Figure 4.1.1), adapting it for the dataset we are analysing here. Firstly, we consider a single-channel seismic shot gather as input image of each branch of the Siamese model, instead of a multi-channel image composed by n-shot gathers. Secondly, we do not use the Multilayer Perceptron (MLP) regressor because we have not yet been provided with the CO_2 mass injection logs needed to train it and make predictions. This will be a task we will perform as soon as we have the data logs available. Thus, the proposed framework comprises two main components: (i) a Siamese architecture built from twin ResNet152 backbones for feature extraction and similarity analysis, and (ii) UMAP for dimensionality reduction and clustering. Each component plays a distinct role in building a robust and adaptable framework for analysing time-lapse datasets and improving the accuracy of similarity assessments. In the following, we will describe each component of the framework.

ResNet and Feature Extraction

We use a ResNet-152 backbone (He et al., 2016) to turn each input image into a 2048-dimensional feature vector taken from the last global average pooling. The model represents the image as a point in a 2048-dimensional feature space, where each coordinate corresponds to one learned high-level feature. ResNet-152 was pre-trained on the ImageNet dataset (Russakovsky et al., 2015) for natural images classification. We removed the final classifier and keep the output vector after global average pooling as the feature vector. This produces a 2048-dimensional embedding for every shot. We

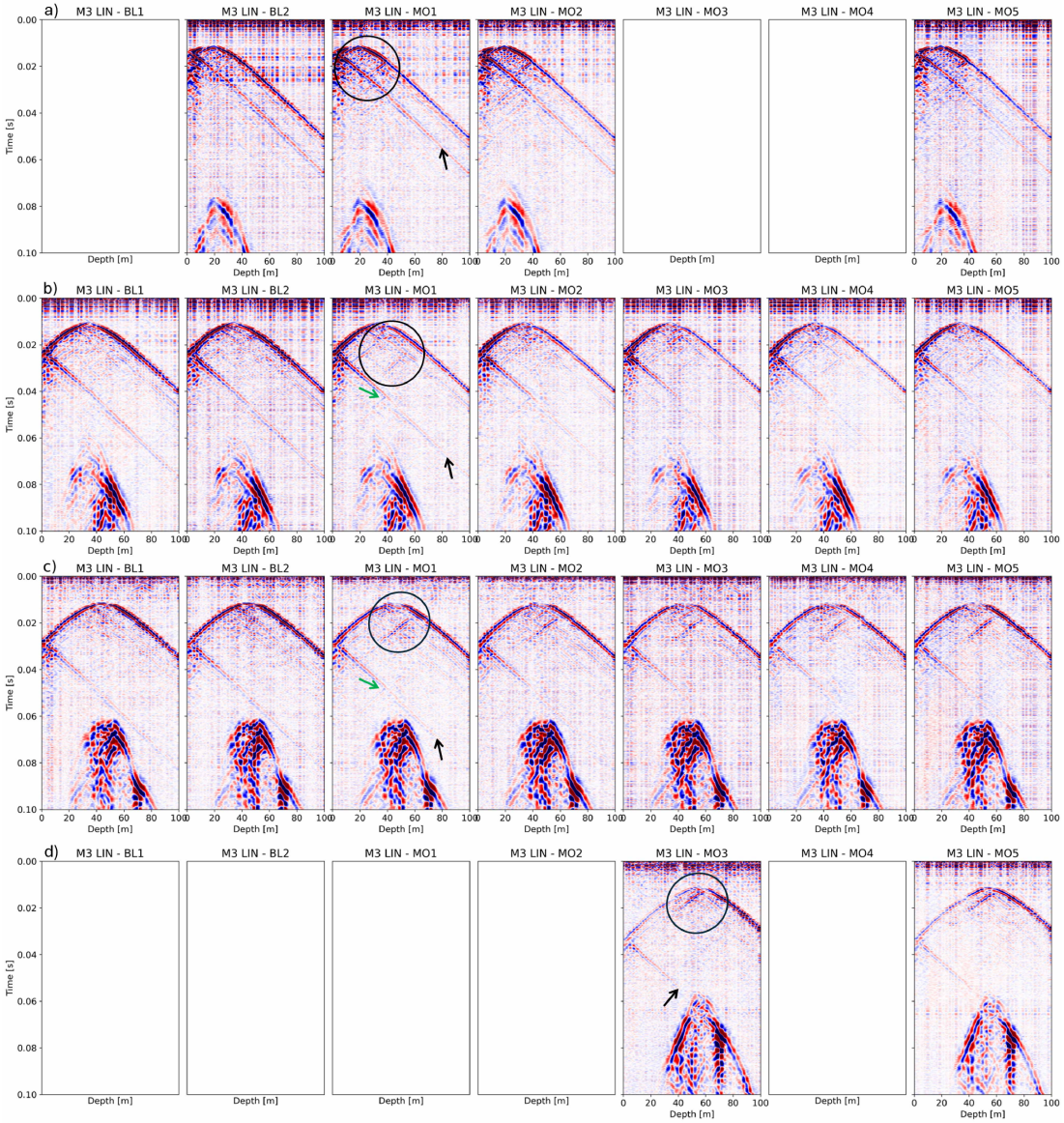

Figure 4.2.3: Shot gathers recorded with LIN DAS in M3. BL1 and BL2 correspond to pre-injection surveys, MO1 to MO4 to injection-phase surveys, and MO5 to the post-injection survey. Panels (a) to (d) show shot points at 15, 35, 45, and 55 m depth, respectively. The DAS cable covers the entire depth of the well M3, from the surface down to 100 m. The blank spaces indicate days when no seismic surveys were conducted at those depths (see Table 7.1 for source depth coverage).

selected ResNet-152 after testing the other published ResNet depths (18, 34, 50 and 101 layers), available in PyTorch deep learning library. In our experiments, ResNet-152 consistently capture patterns in the data that are useful for later stages. It is deep enough to capture the patterns in our seismic images without becoming unstable, thanks to residual skip connections (He et al., 2016). Empirically, deeper residual architectures learn features and produce more informative embeddings (He et al., 2016). Overall, while other backbones (including shallower ResNet or DenseNet) can be used, ResNet-152 offered the best trade-off between representation quality and computational cost for our dataset. The rest of the framework does not depend on this specific choice, so switching to another backbone is straightforward if future datasets suggest it.

Siamese Neural Network (SNN)

Two twin backbones are then arranged in a SNN setup, to assess the similarity between image pairs, e.g., baseline and monitor shot gathers. The SNN architecture consists of two identical ResNet-152 with the same weights arranged in two branches (Figure 4.2.4). Each branch takes one image and produces the resulting high-dimensional embedding vector. Because the weights are identical, the two branches extract features in the same way. If the inputs come from the same class, their embeddings should be close. If they are different, the embeddings should be far apart. After feature extraction, we compare the two resulting embeddings with Euclidean Distance (Shahtalebi et al., 2020; Ramirez-Rodriguez et al., 2024):

$$\mathrm{D}_w = \|\mathbf{E}(monitor) - \mathbf{E}(baseline)\|_2 \tag{4.1}$$

where $\mathbf{E}(baseline)$ is the baseline embedding from the first branch, while $\mathbf{E}(monitor)$ is the monitor embedding from the second branch. Then, D_w measure how similar the embeddings are. A small D_w suggests no differences between the two inputs, while a large D_w suggests differences between the inputs, so different class. This approach works well even with limited data and has shown good transfer across domains such as medical imaging and bioinformatics (Bhagwat et al., 2018; Giverts et al., 2022).

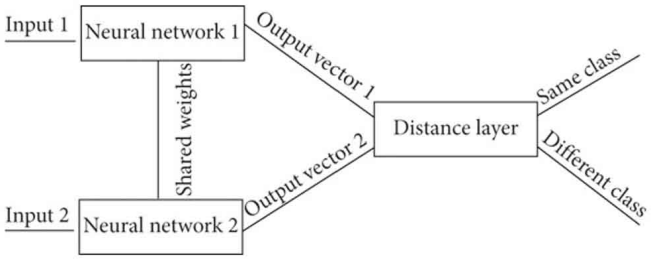

Figure 4.2.4: Siamese Network Networks architecture used to find the similarity of two inputs by comparing their feature vectors.

Uniform Manifold Approximation and Projection (UMAP)

For dimensionality reduction and data clustering and visualization of the high-dimensional embeddings produced by the feature extraction process, we use UMAP (McInnes et al., 2018). UMAP is a powerful technique that excels in preserving both local and global structure in the data while embedding it in a lower-dimensional space. This allows for easier interpretation and analysis of the relationships captured by the SNN. UMAP operates by constructing a fuzzy topological representation on the high-dimensional data and optimizing the low-dimensional representation to maintain the topological structure.

We first run unsupervised UMAP to get a neutral view and to check whether the two classes *no-leakage* for baseline shots, and *leakage* for monitor shots, naturally form two separate clusters. Since we know the actual class for each samples, we decided to use this information performing Supervised UMAP. In this way, we can train a UMAP space with training embeddings and the corresponding training labels (e.g., no-leakage / leakage), and then use that supervised learned space to embed new unlabelled test data. We would like to achieve much better class separation, fitting the reducer on the training set providing the training labels so that no-leakage and leakage images are clustered differently. We split the dataset into 70% training and 30% testing, yielding 37 baseline and 110 monitor samples for training, and 16 baseline and 48 monitor samples for testing.

After feature extraction and embedding space reduction, k-Nearest Neighbors (k-NN) (Cover and Hart, 1967) was adopted as final classifier to address the classification challenges of the two possible classes. Basically, k-NN assigns the class label of the majority of the K-nearest patterns in data space (Kramer, 2013). We performed this classification task in both representation spaces: (i) the high-dimensional embeddings produced by the ResNet encoder, and (ii) the low-dimensional embeddings after UMAP. In the high-D space, k-NN operates directly on the 2048-D vectors, providing a baseline that tests whether the raw deep features already separate the two classes. In the UMAP

space, k-NN naturally exploits the neighborhoods that supervised UMAP has organized by label clustering same class samples together.

For k-NN hyper-parameters selection we use GridSearchCV from scikit-learn (Pedregosa et al., 2011). The search space includes the number of Neighbors (1,3,5,7,9,11,15,21), the weight function used in prediction (uniform or distance), and metric used for distance computation (euclidean, manhattan, or minkowski). We evaluate multiple metrics, including accuracy, F1, and ROC-AUC. We apply this protocol identically in both spaces (raw 2048-D embeddings and UMAP-reduced embeddings) to ensure a fair comparison. Finally, we evaluate both k-NN variants on the same test dataset and the results are evaluated through accuracy, F1, and ROC-AUC, which lets us quantify the added value of UMAP over the raw high-dimensional features.

Results

Because our ResNet encoder is not pre-trained on seismic data, its features may not fully capture the patterns most relevant to key seismic changes. We therefore start by using UMAP in an unsupervised setting to visualize and cluster the embeddings without labels. Next, to sharpen class separation, we use the available categorical labels and apply supervised UMAP aiming to enhance the embedding geometry so that the two classes become more distinct.

First, we compare UMAP with two commonly used dimensionality reduction techniques in machine learning, PCA (Abdi and Williams, 2010) and t-SNE (van der Maaten and Hinton, 2008) (Figure 4.2.5). Each point is a seismic shot embedded from the ResNet encoder. Black circles are the 11 baseline shots from 28/05, while black squares are the 42 baseline shots from 30/05. The other coloured points represent the monitor shots acquired on later dates, with colour indicating the acquisition date so that points with the same colour correspond to the same survey. For the purpose of this study we treat them as a "leakage" scenario and expect them to form their own cluster apart from the baselines, due to changes in the shot gathers such as new diffractions/reflections, amplitude changes and travel-time changes due to the presence of CO_2 (see examples of time-lapse changes from shot gathers in Figure 4.2.3).

In Figure 4.2.5.a, PCA shows a broad, overlapping cloud with little separation among dates or between baseline and monitor. Variance is spread across many directions and the first two components are not enough to reveal structure. t-SNE (Figure 4.2.5.b) starts to organize the manifold and partially isolates one monitor date as a side cluster, but the overall arrangement is still fragmented and hard to interpret globally. UMAP (Figure 4.2.5.c) provides the cleanest view: points align along a smoother manifold and date-wise bands are more evident. Nevertheless, baseline and monitor are not yet

cleanly separated everywhere. In short, for our seismic dataset UMAP works better than PCA and somewhat more interpretable than t-SNE, but the class structure is still not perfect organized.

Figure 4.2.6.a reproposes the unsupervised UMAP from Figure 1 to provide a neutral view of natural groupings. Figure 4.2.6.b shows supervised UMAP, where we fit the reducer on the training set only, using the training labels (no-leakage and leakage). Supervision training pulls same-class samples together and pushes different classes apart in the learned 2-D geometry, so "no-leakage" and "leakage" become much easier to separate. Thus, the supervised UMAP preserves the important neighbourhood structure while producing two clean, well-isolated clusters aligned with our labels.
However, UMAP is not a classifier. UMAP learns an embedding, not a decision rule from coordinates to class. To turn this geometric separation into quantitative predictions we combine the embedding with the k-Nearest Neighbors (k-NN) classifier. k-NN is recognized as a lazy learner (Aha, 1997) that classify unlabelled observations based on the majority of the K-nearest labelled examples.

Figure 4.2.7 reports the k-NN decision regions learned in the supervised-UMAP space. We first fit supervised UMAP on the training set only, then transform train and test, and finally train/evaluate k-NN in this 2-D space. The shaded background shows the two decision regions; points close to the boundary are the most ambiguous. A small number of samples are misclassified (n=5), mostly near the interface between clusters or as clear outliers. This confirms that k-NN provides a simple, locality-aware rule that is consistent with the geometry learned by UMAP, turning a visual separation into measurable performance.

To quantify to what extent the use of UMAP has increased the accuracy of classification with k-NN, we run the same k-NN protocol in two domains. First, using the raw 2048-D ResNet embeddings, and second, using the UMAP-reduced embeddings. Hyperparameters are selected with a grid search algorithm, evaluating accuracy, F1, and ROC-AUC. Table 4.2 lists the selected settings. This evaluation performed on the same train/test split allows us to attribute any performance difference to the UMAP representation. The k-NN classifier operating in the UMAP space outperforms the same model in the raw 2048-D embedding space (Table 4.3). Accuracy rises from 0.781 (Raw + k-NN) to 0.871 (UMAP + k-NN), F1 increases from 0.815 to 0.866, and ROC-AUC improves markedly from 0.725 to 0.928. The large gain in ROC-AUC indicates much better class separability when decisions are made in the supervised-UMAP geometry, consistent with the visual two-cluster structure seen in Figure 4.2.6. In short, UMAP provides a representation that makes local neighborhoods more class-consistent, and k-NN is able to exploit that structure to deliver higher and more robust performance.

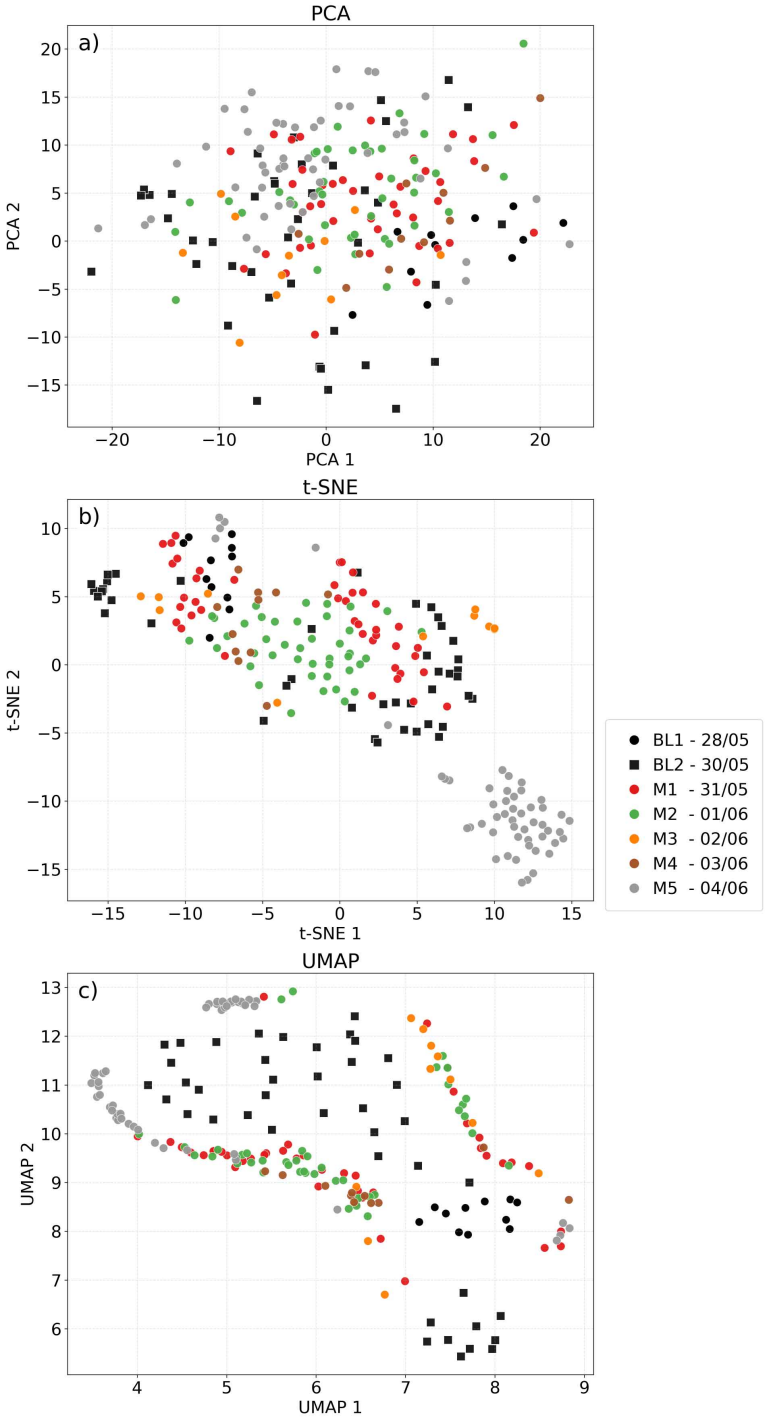

Figure 4.2.5: Comparison of PCA(a), t-SNE (b), and UMAP (c) 2D projections of the ResNet embeddings. Markers: black circles denote 11 baseline shots from 28/05; black squares represents 42 baseline shots from 30/05; coloured points indicate 158 monitor shots from later dates.

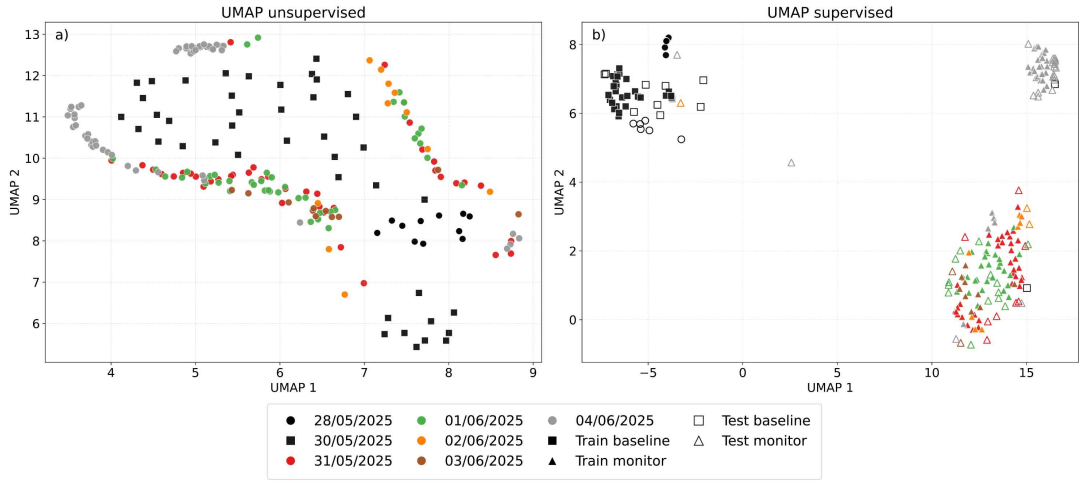

Figure 4.2.6: Comparison of unsupervised UMAP (a) and supervised UMAP (b). Legend distinguishes train/test and survey dates. Supervised UMAP produces two distinct clusters aligned with the two classes.

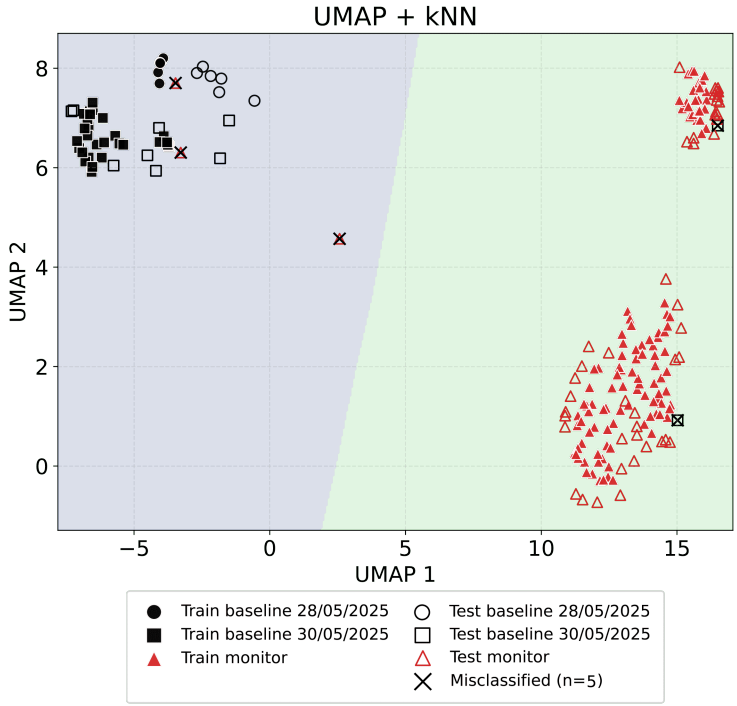

Figure 4.2.7: UMAP + k-NN decision regions. k-NN trained in the supervised UMAP space: UMAP is fit on train dataset with labels, then test dataset is transformed into the learned space. Train baseline points (filled circles/squares) and train monitor points (filled triangles) define the learned space. Test samples are shown with hollow markers. The shaded background shows the decision regions of k-NN. Five test samples were misclassified and marked with a black "**x**". This pairing turns the geometric separation given by UMAP into a simple, locality-aware decision rule.

Table 4.2: Selected hyperparameters after optimization using GridSearch for the proposed methods.

Method	k	min_dist	metric	n_components	weights	random_state
UMAP	15	0.1	euclidean	2	—	42
Raw k-NN	5	—	manhattan	—	uniform	—
UMAP + k-NN	3	—	euclidean	—	uniform	—

Table 4.3: Comparison of k-NN classification in raw space and in the UMAP-reduced space.

Method	Accuracy	F1	ROC-AUC
Raw + k-NN	0.781	0.815	0.725
UMAP + k-NN	0.871	0.866	0.928

Discussion and Conclusions

This chapter showed that a lightweight pipeline composed by ResNet-152 features extractor, UMAP for dimensionality reduction, and a simple k-NN classifier can identify changes from time-lapse DAS cross-well data without training a DL model from scratch. Unsupervised comparisons indicated that UMAP gives a clearer and more interpretable organization of the embeddings than PCA and t-SNE, although baseline and monitor shot gathers were not perfectly separated everywhere. Adding labels only on the training set performing supervised UMAP produced two compact clusters aligned with the expected classes (no-leakage vs leakage). Since UMAP is not a classifier, we paired the embedding with k-NN to turn geometric separation into quantitative decisions. Running the same k-NN algorithm in both domains, firstly raw 2048-D embeddings and, secondly UMAP-reduced embeddings showed consistent gains in the low-D space. Accuracy metrics confirms that supervised UMAP enhances class separability while preserving neighbourhood structure, and that a locality-aware rule like k-NN can exploit this structure effectively.

The approach is fast to set up, robust, and easy to interpret. However, there are limits. The encoder is pre-trained on natural images rather than seismic images, therefore some features may not detects changes in the subsurface optimally. Furthermore, data quality varies with source depth depending on the source/rock coupling, but we assume that time-lapse recordings shot at the same depth are equally affected by noise sources and therefore share the same noise features.

Despite the limits, the proposed framework is site-independent, scalable, and computationally efficient. Using pre-trained encoders, requires minimal tuning, and can be

scaled to new surveys without re-training. Future work will test seismic-pretrained encoders and alternative backbones to better align features with subsurface changes. Moreover, once the injection logs are available, we will add a regression head to relate the embedding geometry to CO_2 mass and pressure. We will also evaluate uncertainty and calibrate k-NN decisions, and extend the analysis to additional sites and acquisition geometries. Together, these steps move the framework beyond solely detect and visualize task toward an operational monitoring tool for CO_2 storage surveillance. This makes it suitable as a preliminary tool in a CO_2 storage monitoring portfolio to verify storage and minimize the risk of leakage. Moreover, it can be extended to other fibre-optic downhole monitoring methods, such as Vertical Seismic Profile (VSP), both onshore and offshore. DAS acquisition offers several advantages over conventional sensors, especially when the cable is permanently installed within the borehole casing, ensuring high repeatability. Used as an early-warning tool for time-lapse change detection, it can highlight possible warning and then guide targeted surveys where necessary.

Bibliography

Hervé Abdi and Lynne J. Williams. 2010. Principal component analysis. *WIREs Computational Statistics* 2, 4 (2010), 433–459. https://doi.org/10.1002/wics.101

David W. Aha. 1997. Lazy learning. In *Lazy learning*. Springer, Dordrecht, IV–424. https://doi.org/10.1007/978-94-017-2053-3

Nicolás D. Barbosa, Andrew Greenwood, Eva Caspari, Michael Jordan, Marcin Ireneusz Duda, Bastien Dupuy, Amir Ghaderi, and Peder Eliasson. 2024. *The potential of borehole seismic monitoring techniques at the field scale for leakage and well integrity assessment in CO2 injection projects*. SEG, Houston, TX, 425–429. https://doi.org/10.1190/image2024-4099280.1

Nikhil Bhagwat, Joseph D. Viviano, Aristotle N. Voineskos, and M. Mallar Chakravarty. 2018. Modeling and Prediction of Clinical Symptom Trajectories in Alzheimer's Disease Using Longitudinal Data. *Plos Computational Biology* 1 (2018), 1–25. https://doi.org/10.1371/journal.pcbi.1006376

T. A. Buscheck, K. Mansoor, X. Yang, H. Wainwright, and S. Carroll. 2019. Downhole pressure and chemical monitoring for CO_2 and brine leak detection in aquifers above a CO_2 storage reservoir. *International Journal of Greenhouse Gas Control* 91 (2019), 102812. https://doi.org/10.1016/j.ijggc.2019.102812

Chengping Chai, Omar Marcillo, Monica Maceira, Junghyun Park, Stephen Arrowsmith, James O. Thomas, and Joshua Cunningham. 2025. Exploring Continuous Seismic Data at an Industry Facility Using Unsupervised Machine Learning. *The Seismic Record* 5, 1 (01 2025), 64–72. https://doi.org/10.1785/0320240046

Aditya Chakravarty and Siddharth Misra. 2023. Characterizing the Stimulated Reservoir Volume Using Manifold Learning on 3d Motions of Microseismic Sources. In *ADIPEC (Abu Dhabi International Petroleum Exhibition and Conference)*. ADIPEC, Abu Dhabi, UAE, D021S064R002. https://doi.org/10.2118/216500-MS

D. Chicco. 2020. Siamese neural networks: an overview. In *Artificial Neural Networks* (3 ed.). Methods in Molecular Biology, Vol. 2190. Humana Press, New York, NY, 73–94. https://doi.org/10.1007/978-1-0716-0826-5_3

T. Cover and P. Hart. 1967. Nearest neighbor pattern classification. *IEEE Transactions on Information Theory* 13, 1 (1967), 21–27. https://doi.org/10.1109/TIT.1967.1053964

J. Deng, W. Dong, R. Socher, L.-J. Li, K. Li, and L. Fei-Fei. 2009. ImageNet: A large-scale hierarchical image database. In *2009 IEEE Conference on Computer Vision and Pattern Recognition (CVPR)*. IEEE, Miami, FL, USA, 248–255. https://doi.org/10.1109/CVPR.2009.5206848

Pavel Giverts, Ksenia Sorokina, and Vladimir Fedorenko. 2022. Examination of the possibility to use Siamese networks for the comparison of firing pin marks. *Journal of Forensic Sciences* 67, 6 (2022), 2416–2424. https://doi.org/10.1111/1556-4029.15143

Kaiming He, Xiangyu Zhang, Shaoqing Ren, and Jian Sun. 2016. Deep Residual Learning for Image Recognition. In *2016 IEEE Conference on Computer Vision and Pattern Recognition (CVPR)*, Vol. 1. 2016 IEEE Conference on Computer Vision and Pattern Recognition (CVPR), Las Vegas, 770–778. https://doi.org/10.1109/CVPR.2016.90

Michael Jordan, Peder Eliasson, Wolfgang Weinzierl, Cathrine Ringstad, Martin Raphaug, Alv-Arne Grimstad, and Cornelia Schmidt-Hattenberger. 2022. Learnings from the Pre-ACT campaign at the Svelvik CO2 Field Lab, In GHGT-16 conference. *Available at SSRN: https://ssrn.com/abstract=4286508* 1, 1–8. https://doi.org/10.2139/ssrn.4286508

Hyunggu Jun and Yongchae Cho. 2021. Repeatability enhancement of time-lapse seismic data via a convolutional autoencoder. *Geophysical Journal International* 228, 2 (10 2021), 1150–1170. https://doi.org/10.1093/gji/ggab397

Oliver Kramer. 2013. *K-Nearest Neighbors*. Springer Berlin Heidelberg, Berlin, Heidelberg, 13–23. https://doi.org/10.1007/978-3-642-38652-7_2

Leland McInnes, John Healy, Nathaniel Saul, and Lukas Großberger. 2018. UMAP: Uniform Manifold Approximation and Projection. *Journal of Open Source Software* 3, 29 (2018), 861. https://doi.org/10.21105/joss.00861

Siddharth Misra and Aditya Chakravarty. 2024. Fracture Monitoring and Characterization Using Unsupervised Microseismic Data Analysis. In *International Petroleum Technology Conference (IPTC International Petroleum Technology Conference, Vol. International Petroleum Technology Conference)*, International Petroleum Technology Conference (Ed.). IPTC, Dhahran, Saudi Arabia, D021S087R003. https://doi.org/10.2523/IPTC-24412-MS

Giovanni Pantaleo and Michele Pipan. 2025. Enhancing Early CO_2 Leakage Detection Using Pre-Trained Deep Learning Models. In *EAGE World CCUS Conference 2025 Conference Proceedings*, Vol. 2025. European Association of Geoscientists & Engineers, EAGE, Bergen, Norway, 1–5. DOI to be assigned. Available at https://www.earthdoc.org/content/papers/10.3997/2214-4609.202522134.

F. Pedregosa, G. Varoquaux, A. Gramfort, V. Michel, B. Thirion, O. Grisel, M. Blondel, P. Prettenhofer, R. Weiss, V. Dubourg, J. Vanderplas, A. Passos, D. Cournapeau, M. Brucher, M. Perrot, and E. Duchesnay. 2011. Scikit-learn: Machine Learning in Python. *Journal of Machine Learning Research* 12 (2011), 2825–2830. https://doi.org/10.5555/1953048.2078195

Leonardo Portes, Guillaume Pirot, Michel M Nzikou, Jeremie Giraud, Mark Lindsay, Mark Jessell, and Edward Cripps. 2025. Feature fusion-enhanced t-SNE image atlas for geophysical features discovery. *Scientific Reports* 15, 1 (2025), 17152. https://doi.org/10.1038/s41598-025-01333-3

Ana Elena Ramirez-Rodriguez, Rodrigo Eduardo Arevalo-Ancona, Héctor Pérez-Meana, Manuel Cedillo-Hernandez, and Mariko Nakano-Miyatake. 2024. AISMSNet: Advanced Image Splicing Manipulation Identification Based on Siamese Networks. *Applied Sciences* 1 (2024), 1–20. https://doi.org/10.3390/app14135545

Olga Russakovsky, Jia Deng, Hao Su, Jonathan Krause, Sanjeev Satheesh, Sean Ma, Zhiheng Huang, Andrej Karpathy, Aditya Khosla, Michael Bernstein, Alexander C. Berg, and Li Fei-Fei. 2015. ImageNet Large Scale Visual Recognition Challenge. arXiv:1409.0575 [cs.CV] https://arxiv.org/abs/1409.0575

Soroosh Shahtalebi, Amir Asif, and Arash Mohammadi. 2020. Siamese Neural Networks for EEG-based Brain-computer Interfaces. In *2020 42nd Annual International Conference of the IEEE Engineering in Medicine & Biology Society (EMBC)*. EMBC, Montreal, 442–446. https://doi.org/10.1109/EMBC44109.2020.9176001

Laurens van der Maaten and Geoffrey Hinton. 2008. Visualizing Data using t-SNE. *Journal of Machine Learning Research* 9, 86 (2008), 2579–2605. http://jmlr.org/papers/v9/vandermaaten08a.html

Z. Wang, R. Dilmore, W. Harbert, L. Huang, Y. Lin, S. Feng, and S. Wang. 2021. Kimberlina 1.2 Velocity Models. U.S. Department of Energy, National Energy Technology Laboratory (NETL). https://doi.org/10.18141/1832899

Mark E. Willis, Andreas Ellmauthaler, Xiang Wu, and Michel J. LeBlanc. 2021. *Important Aspects of Acquiring Distributed Acoustic Sensing (DAS) Data for Geoscientists*. American Geophysical Union (AGU), 111 River Street, Hoboken, NJ 07030, USA, Chapter 2, 33–44. https://doi.org/10.1002/9781119521808.ch2

X. Yang, T. A. Buscheck, K. Mansoor, Z. Wang, K. Gao, L. Huang, D. Appriou, and S. A. Carroll. 2019. Assessment of geophysical monitoring methods for detection of brine and CO_2 leakage in drinking water aquifers. *International Journal of Greenhouse Gas Control* 90 (2019), 102803. https://doi.org/10.1016/j.ijggc.2019.102803

Lifu Zheng, Hao Yang, and Guichun Luo. 2025. Seismic Waveform Feature Extraction and Reservoir Prediction Based on CNN and UMAP: A Case Study of the Ordos Basin. *Applied Sciences* 15, 13 (2025), 1–14. https://doi.org/10.3390/app15137377

Chapter 5

Rock-Physics parametrized FWI

Traditionally, changes in reservoir fluids have been inferred from seismic data using a two-step inversion workflow. First, seismic observations are inverted for elastic parameters such as P- and S-wave velocities or impedances. Then, rock-physics relations are applied to link these elastic properties to reservoir characteristics like fluid saturation. Although this approach is logical and conceptually simple, it has significant drawbacks. Separating seismic inversion and rock-physics modelling introduces additional uncertainty, since errors in the elastic model directly affect the estimated saturations. In addition, conventional elastic Full-Waveform Inversion (FWI) often suffers from parameters cross-talk, where changes in one elastic property can be interpreted as changes in another. This overlap between elastic parameters makes it difficult to correctly separate their individual contributions to the seismic response, which is on the other hand essential to actually extract the complete and correct information from the seismic data. These ambiguities may not become evident until the rock-physics step, resulting in non-unique or biased saturation estimates. The sequential nature of the process also makes it slower and more reliant on manual interpretation, limiting its use for fast or automated monitoring.

Recent developments aim to overcome these issues by integrating rock-physics parametrization directly into the FWI workflow. In a rock-physics parametrized FWI, the subsurface is modelled in terms of reservoir properties such as fluid saturation, porosity, or lithology, rather than just elastic parameters. By embedding rock-physics relations like Gassmann's equations and fluid mixing laws into the inversion scheme, the resulting models remain more physically consistent and directly linked with the real reservoir behaviour (Keating and Innanen, 2019). Moreover, this integration reduces inter-parameter crosstalk and allows the inversion to isolate the seismic effects of fluid saturation more accurately (Hu et al., 2022). Consequently, the output is not just

an elastic model but a quantitative estimation of the injected fluid volume. In other words, the inversion retrieves saturation directly, eliminating the need for a separate conversion/correlation from velocity to saturation after the data inversion.

A novel aspect of this work is the implementation of automatic differentiation within the rock-physics–parametrized FWI framework, enabling efficient and exact computation of the gradients that couple seismic responses with petrophysical parameters. This allows the inversion to be fully differentiable and easily extendable to complex rock-physics formulations, improving computational efficiency.

Synthetic studies have shown that this parametrized FWI approach yields cleaner and more accurate models with fewer artifacts compared to conventional elastic FWI (Singh et al., 2018; Zhang et al., 2018; Mardan et al., 2023). However, its reliability depends strongly on the quality of the underlying rock-physics model (and to the quality of the seismic data). To predict seismic changes during gas injection, it is essential to include realistic in-situ conditions such as pressure variations, heterogeneity, and residual fluid saturations. In particular, estimating the residual gas saturation (i.e., the fraction of pore space that remains occupied by native gas or trapped hydrogen) is critical, as even a small immobile gas fraction can significantly affect rock compressibility and seismic velocity. Therefore, the success of this inversion strategy depends on using a rock-physics framework that properly represents in-situ multiphase behaviour, ensuring that the link between saturation and elastic response is physically accurate. When these conditions are met, rock-physics parametrized FWI becomes a powerful and efficient method for seismic monitoring of underground hydrogen storage.

5.1 Monitoring elastic parameters changes during underground hydrogen storage using rock physics parametrized FWI

This study proposes a workflow based on the integration of full-waveform inversion (FWI), rock physics modeling (RPM) and gas property modeling for monitoring changes in elastic medium parameters due to hydrogen injection. A rock physics model including the Gassmann equation and fluid mixing laws has been implemented, which accurately links rock physical properties to elastic properties. The parameterized approach is based on optimizing fluid saturation to reduce crosstalk between model parameters during the inversion process, while simultaneously providing a quantitative estimation of the fluid within the reservoir. The synthetic models show that parameterized inversion produces higher accuracy and fewer artifacts than conventional FWI. Our results underscore the importance of an appropriate RPM to reflect real subsurface conditions and proper fluid mixing laws. Therefore, FWI parameterization provides an efficient technique for monitoring hydrogen storage sites in depleted gas fields to ensure efficient storage.

Monitoring elastic parameters changes during underground hydrogen storage using rock-physics parametrized FWI

G. Pantaleo, G. Roncoroni, M. Pipan

Extended abstract presented at Fifth EAGE Global Energy Transition Conference & Exhibition (GET 2024), 4^{th}-7^{th} November 2024, Volume 2024.
doi: https://doi.org/10.3997/2214-4609.202421200

Key Words
Rock-physics inversion; *UHS monitoring*; *Automatic Differentiation (AD)*; *Full-Waveform Inversion (FWI)*

Introduction

Hydrogen production is becoming increasingly important in the perspective of a low-carbon society. For seasonal storage of renewable energy, large-scale storage of hydrogen is one strategy to help ensure that energy supply can always meet the energy demand (Miocic et al., 2023). Depleted gas fields are commonly used for gas storage, where the remaining native gas is mainly methane. This gas acts as a cushion gas and plays a significant role in storage and recovery processes and in maintaining sufficient pressure within the storage reservoir (Cao et al., 2020). Seismic monitoring is essential for tracking reservoir dynamics and detecting anomalies. One of the most widely used monitoring methods is full-waveform inversion (FWI). This is a robust technique that aims to produce high-resolution images of the subsurface and track changes in reservoir properties over time (Jean and Stephane (2009); Balhareth and Landrø (2016)). The utilization of FWI in reservoir monitoring involves the simultaneous estimation of model properties, including elastic and rock physics properties, thus providing a comprehensive understanding of reservoir dynamics (Mardan et al., 2023). In this study, we propose an inversion workflow that combines rock physics modelling, gas properties modelling and FWI, aimed at recovering elastic parameters through the optimization of a rock physics parameter (saturation) related to the injected hydrogen into a depleted gas reservoir. Our purpose is to define an inversion algorithm that can focus on updating a specific subsurface property independently, thereby reducing the undesirable crosstalk between different model parameters. Crosstalk refers to the fact that different combinations of different parameters can cause a similar seismic response (Yang et al.,

2018).

Methods

To perform a rock physics parametrized FWI, a rock physics model (RPM) is needed to map the rock physics properties to the elastic properties. A parametrized FWI requires realistic parameters to be determined. The effective moduli of the rock were estimated using the Krief model (Krief et al., 1990) for dry-rock moduli, and the Voigt-Reuss-Hill method (Hill, 1952) for average moduli of the grain. The grain density is computed as a weighted average of mineral densities. We consider that the solid material consists of a mix of clay and quartz grains, with porosity equal to 0.22. The effective fluid bulk modulus of the fluid mixture is determined using Brie mixing law (Brie et al., 1995). This law allows to simulate patchy fluid mixture through an empirical exponent e which can vary between 1 and 40. Low values correspond to patchy mixing of the fluid phases, and high values correspond to uniform mixing. The proposed fluid mixing exponent used in this work is 3, a semi-patchy mixing behavior. The effective fluid density was calculated through arithmetic average. In a field study, this patchiness exponent could be inverted along as other parameters for a better resolution of the inversion. Finally, the dry elastic properties of the rock matrix and the bulk modulus of the saturating fluid were combined with the Gassmann equation (Gassmann, 1951) to calculate the elastic moduli of saturated rock. According to Gassmann equation, the shear modulus of the saturated rock is the same as that of the dry rock.

Thermodynamic properties of the pore fluid under consideration have been computed using the Peng-Robinson equation of state (EoS), the most widely used in oil and gas industry. The main outputs from EoS equations are the bulk modulus and the density of the gases. These properties have been calculated as a function of pressure and temperature, considering average geothermal gradient of 25 °C/km and lithostatic pressure gradient with an average density of 2200 kg/m^3. Figure 5.1.1.a-b show density and bulk modulus variation with depth for the gases considered in this study. Methane was chosen as the model compound that represents the residual natural gas. A residual gas saturation of 0.15 has been considered to simulate the depleted gas reservoir. Typical residual gas saturation values ranged from 0.10 to 0.31 (Lin et al., 2024; Suzanne et al., 2003). Sediments and gas properties have been calculated to quantify the changes in elastic medium properties caused by hydrogen substitution. Figure 5.1.1.c-d illustrate the variation of the elastic parameters as a function of methane saturation (S_{CH_4}) for reservoir rock initially fully saturated with brine. Figure 5.1.1.e-f, instead, show the variation of the elastic parameters as a function of hydrogen saturation (S_{H_2}) for reservoir rock initially saturated with a brine-methane mixture at 0.15 methane saturation. It is noteworthy that increasing the hydrogen saturation in the reservoir rock leads to

a general increase in the P-wave velocity of the rock. This is because hydrogen has higher velocity than methane because of its low density, where the velocity of the gas can be calculated as the ratio of the bulk modulus to the density of the gas.

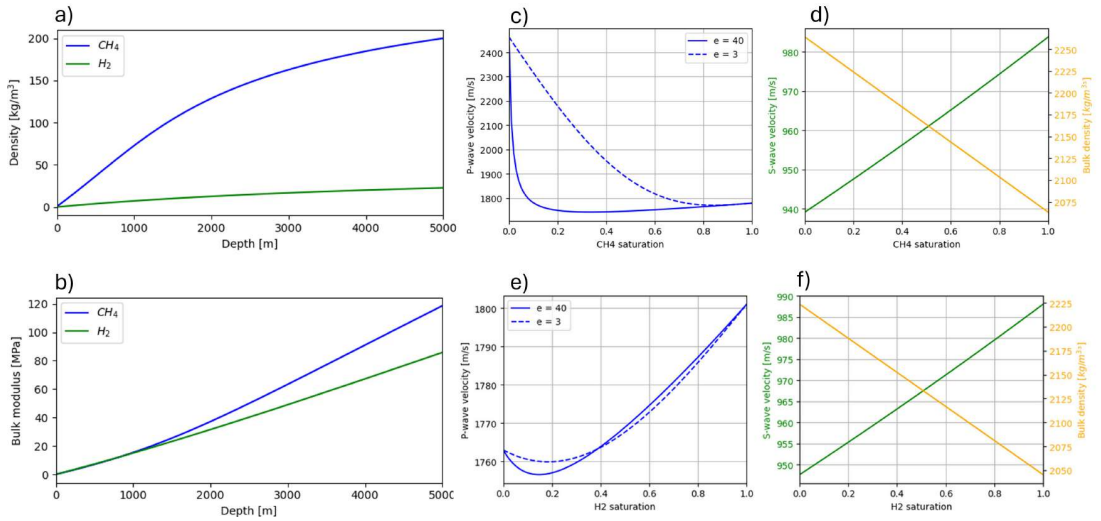

Figure 5.1.1: Variation of density (a) and bulk modulus (b) of methane (blue line) and hydrogen (green line) as a function of depth; c) P-wave velocity as a function of CH_4 saturation; d) S-wave velocity (green line), and bulk density (orange line) as a function of CH_4 saturation; e) P-wave velocity as a function of H_2 saturation; f) S-wave velocity (green line) and bulk density (orange line) as a function of H_2 saturation. In e-f) the parameters at S_{H_2}=0 corresponds to the simulated depleted reservoir (brine-methane mixture at S_{CH_4}=0.15. In c-e) solid lines represent uniform mixing (e=40), while dotted lines represent patchy mixing (e=3).

The synthetic model used in this study is a simplified representation of hydrogen storage in a depleted gas reservoir, emphasizing changes in the elastic and petrophysical parameters of the medium and fluids. For a more realistic representation of the hydrogen distribution within the reservoir, a dynamic flow simulation is necessary. We performed our elastic FWI experiments using Deepwave python package (Richardson, 2025). Observed prestack data was generated through an elastic propagator using a Ricker wavelet with a central frequency of 20 Hz, 40 explosive shots and 80 receivers. A finite-difference method is used to solve the elastic equation with Perfectly Matched Layer implemented. The optimization of the gradient during the FWI process is formulated in terms of saturation, where the baseline saturation model is required to be updated. The elastic properties were initialized based on the initial saturation model using our RPM function. It is assumed that the baseline models are exactly known before starting hydrogen injection. The LBFGS (Limited-memory Broyden-Fletcher-Goldfarb-Shanno) optimizer was employed to iteratively update the saturation model (Dai and He, 2023). In each iteration, the elastic properties were calculated from the

updated saturation, and the elastic wave propagation was simulated. Then, the mean-squared-error loss was calculated between observed and simulated prestack data. The calculated gradients of the loss function with respect to the model parameters guide the optimization process, updating the saturation and subsequently the elastic properties. To reduce the cycle-skipping problem we started the inversion process using a low cutoff frequency of 10 Hz, to a maximum of 40 Hz. A 6th order Butterworth filter was used to ensure numerical stability. In our approach, petrophysical properties such as porosity, mineralogy, and matrix properties remain constant over time. This implies that any observed variation in the elastic properties is exclusively due to changes in fluid saturation rather than changes in the rock matrix itself. We first estimated the baseline elastic models and rock physics parameters considering a brine-methane mixture. Then, monitor models were estimated using the RPM simulating hydrogen substitution with the brine-methane mixture. This step allows realistic estimation of elastic property changes due to fluid substitution, reflecting the new fluid composition in the reservoir. Our RPM does not consider any interaction between brine-hydrogen or methane-hydrogen.

Results and Discussion

Test on 2-D synthetic data

To investigate the performance of the methodology, a simple synthetic model with 100×100 grid cells and three layers was used. In the baseline model, the deeper layer presents an anticlinal fold which contains a gas cap filled by the residual brine-methane mixture. The reservoir is connected to an aquifer saturated with brine at the bottom of the model. The lithologies overlying the reservoir are modelled as filled by brine. In the monitor model, we represented the effect of hydrogen substitution with a representative extent and variation of parameters during the monitoring phase. The saturation level of the monitor model was chosen arbitrarily. The saturation distribution within the reservoir in the monitor model is guided by Perlin noise (Perlin, 2002), a noise generation algorithm used in computer graphics to create natural-looking textures and patterns. Thus, a random distribution of saturation values between 0.7 and 0.8 was defined, simulating a more realistic and heterogeneous distribution. Conventional and rock physics parameterized FWI is performed to monitor elastic parameters changes due to hydrogen injection. The elastic parameters estimated from inverted saturation are shown in Figure 5.1.2.d-f, as well as the elastic parameters inverted with conventional elastic FWI (Figure 5.1.2.g-i). Considering conventional FWI, the changes in velocity and density models are recovered in terms of localization of the changes, but not appropriately in terms of values. In contrast, parametrized inversion shows high accuracy for both location and values recovery. In fact, even the thinner edges of the gas body were reconstructed. The models of both inversions contain artifacts, although the

models of conventional inversion are more contaminated. In addition, the parametrized inversion better recovers the background of the models.

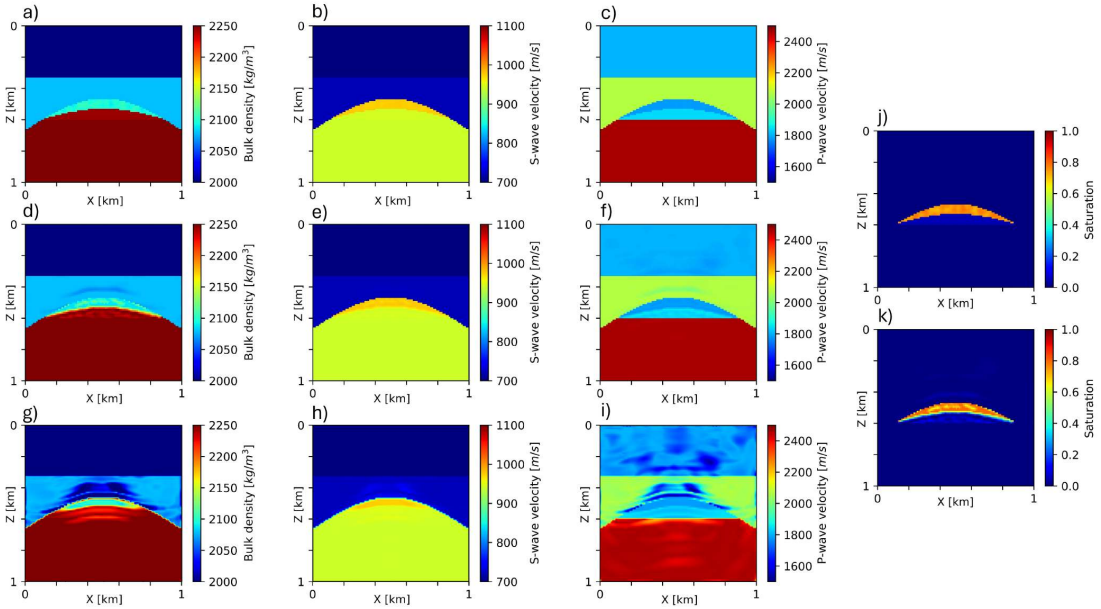

Figure 5.1.2: Elastic and rock physics properties of the synthetic model. a-c) true monitor elastic models; d-f) inverted models using rock physics parametrized FWI; g-i) inverted models using conventional FWI; j) true monitor saturation model; k) inverted monitor saturation model using rock physics parametrization.

Conclusions

The full-waveform inversion is an essential technique for accurately characterizing subsurface properties and for reservoir monitoring. Using a synthetic model, we demonstrate that by incorporating rock physics modelling and gas properties modelling within the inversion process, crosstalk between parameters can be minimized, allowing more accurate and robust inversion results. The results obtained with this type of parameterization confirms that a direct and accurate estimation of gas saturation can be obtained, in contrast to the conventional elastic inversion. The approach described in this work can be easily adapted to hydrogen leakage detection from the reservoir into the caprock, and subsequent quantitative evaluation. In this case, the RPM must include sediments and gas properties related to different thermodynamic and petrophysical properties of the caprock, to quantify the elastic property changes caused by hydrogen leakage. In conclusion, by leveraging the capabilities of FWI to integrate rock physics, its implementation for monitoring elastic and rock physics properties in a hydrogen storage scenario can improve fluid movement monitoring, ensuring efficient hydrogen storage.

5.2 Optimization of rock-physics inversion via FWI and deep learning tools

This work introduces a rock–physics–parametrized Full Waveform Inversion (FWI) framework for quantitative reservoir monitoring in subsurface storage applications. The proposed workflow is fast, accurate, and reduces subjectivity compared to conventional two–step procedures that first invert for elastic properties and then map them to petrophysical parameters. We couple seismic forward modelling with a differentiable rock–physics operator that links elastic parameters to fluid saturation, and implement the entire chain in an automatic–differentiation environment (PyTorch/Deepwave). This permits efficient gradient evaluation without adjoint coding and stabilizes the optimization against parameter cross–talk. The proposed framework was tested on synthetic model of cyclic hydrogen storage in a depleted carbonate reservoir, simulating a surface seismic survey. The results show that the method retrieves spatially consistent saturation maps and associated elastic contrasts, with fewer artefacts than traditional elastic-FWI.

The approach scales on GPUs, adapts naturally to multi-scale frequency strategies, and is readily extendable to alternative rock–physics parametrizations and mixing laws. These results highlight the potential of rock–physics–aware inversion as a practical tool for high–fidelity, automated monitoring of subsurface energy–storage operations.

Optimization of rock-physics inversion via FWI and deep learning tools

G. Pantaleo, M. Pipan

Extended abstract presented at The 43rd National Conference of the GNGTS (GNGTS 2025) - 11^{th}-14^{th} February 2025, Bologna, Italy
doi: to be assigned
Available at: to be assigned

Key Words
Rock-physics parametrization; *Hydrogen storage monitoring*; *Automatic Differentiation (AD)*; *Full-Waveform Inversion (FWI)*

Introduction

In the context of energy storage, such as CO_2 and hydrogen storage, the seismic reflection method is essential for tracking reservoir dynamics and detecting anomalies within the storage complex. Additionally, there is a growing need for cost-effective and time-efficient algorithms to facilitate long-term monitoring of storage reservoirs. We present a novel framework for inverting quantitative rock-physics parameters from seismic data by coupling Full-Waveform Inversion (FWI) and rock-physics modelling (RPM). FWI is an ill-posed, nonlinear optimization problem that iteratively minimizes the misfit between observed and simulated seismic data (Jean and Stephane, 2009). In standard FWI, the adjoint-state method is typically used to calculate the gradient of the cost function with respect to model parameters. However, since all operations involved in simulating wave propagation are differentiable, Automatic Differentiation (AD) can be used to compute the gradient of the cost function efficiently. AD, a tool commonly used in deep learning, automates the computation of gradients without requiring manual implementation of adjoint equations (Richardson, 2018). Our objective is to assess the performance of rock-physics parameterizations in elastic FWI for hydrogen storage monitoring. In this way, we aim to reduce undesirable crosstalk between different elastic model parameters during inversion. To achieve this, we implement a flexible and efficient rock-physics inversion framework that combines with FWI and operates effectively on GPUs. The proposed framework was tested on synthetic model of cyclic H_2 storage in a depleted carbonate reservoir, simulating a surface seismic survey. An

Appropriate RPM is employed to account for the complex characteristics of the storage reservoir, ensuring realistic modelling.

Methods

The modelling workflow combines a realistic static model of a depleted carbonate reservoir with a 3D simulation of cyclic H_2 storage to replicate experimental conditions as closely as possible. From this simulation, a 2D vertical slice passing through the injection/extraction well was extracted for testing with our framework. Geophysical parameters are then constructed through forward rock-physics modelling, followed by seismic forward modelling to generate synthetic datasets. Finally, the inversion framework is applied to monitor datasets, aiming to provide dynamic changes in fluid saturation and location of the plume within the reservoir. Rock-physics modelling plays a crucial role in the parametrization of FWI, acting as a bridge between rock-physics properties and elastic properties. An RPM tailored for carbonate reservoir was adopted, following the DEM-Gassmann approach (Sun et al., 2012). This approach predicts effective moduli for dry pores while accounting for different pore shapes and types, and subsequently saturates them with the desired fluid mixture using Gassmann's low-frequency relations. For matrix moduli, the Voigt-Reuss-Hill averaging method (Hill, 1952) was adopted, while the effective bulk modulus of the fluid mixture was calculated using Wood's equation for homogeneous mixing and the Brie equation (Brie et al., 1995) for patchy mixing. A semi-patchy mixing was applied (Figure 5.2.1). Methane (CH_4) was selected as the residual natural gas in the depleted reservoir (Figure 5.2.1.a), and the thermodynamic properties of both methane and hydrogen were computed using the Peng-Robinson equation of state (EoS). This study focuses on a three-phase fluid system consisting of brine, methane, and hydrogen. To enable realistic modeling of H_2 storage, various levels of saturation of the in-situ brine-methane mixture were analyzed to assess their influence on P-wave velocity as hydrogen enters the system (Figure 5.2.1.b).

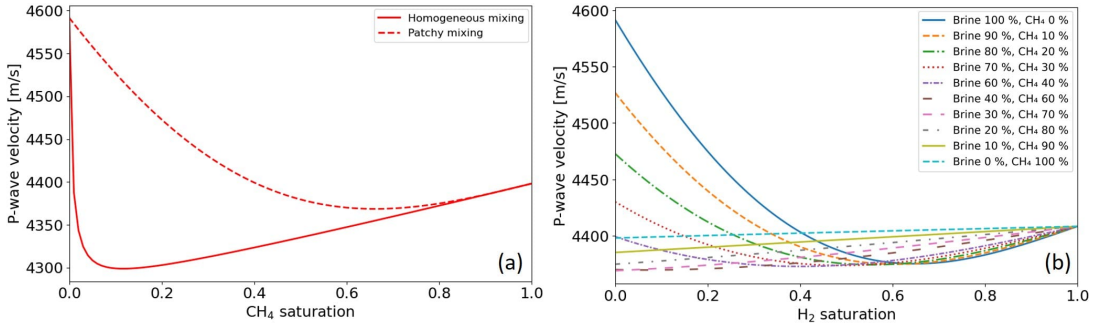

Figure 5.2.1: P-wave velocity as a function of CH_4 (a) and H_2 saturation (b) in the carbonate reservoir under consideration. In (a), CH_4 replace in-situ brine; in (b) each line represents a different saturation level of the residual in-situ brine-methane mixture. Even small amounts of H_2 significantly impact P-waves velocity, which becomes less sensitive as the medium becomes fully saturated with H_2. Moreover, higher CH_4 saturation results in smaller velocity change due to H_2 substitution. The relationship in (b) assumes patchy mixing for both the residual CH_4 and post-H_2 injection mixtures.

In traditional FWI, the objective is to invert seismic data d to estimate subsurface elastic properties m (e.g., V_p, V_s, ρ) using seismic forward modelling F. However, this approach does not directly incorporate rock-physics relationships, which link elastic properties to rock-physics parameters such as fluid saturation s. To overcome this limitation, we introduce a rock-physics parameterization R that directly connects seismic data to fluid saturation:

$$\text{syn} = F(m) \; ; \; m = R(s) \; ; \; \text{syn} = F(R(s)).$$

By combining F with R within an automatic-differentiation framework (PyTorch), we can efficiently compute the gradient of the objective function with respect to s:

$$\nabla_s \mathcal{L} = \frac{\partial \mathcal{L}(d, \text{syn})}{\partial s}.$$

Here, $\mathcal{L}$ is the loss function (mean-squared error, MSE) that quantifies the discrepancy between the observed seismic data d and the simulated data syn. The operator ∇_s denotes the gradient of the loss with respect to s. The optimization problem is solved using the L-BFGS optimizer (Limited-memory Broyden–Fletcher–Goldfarb–Shanno).

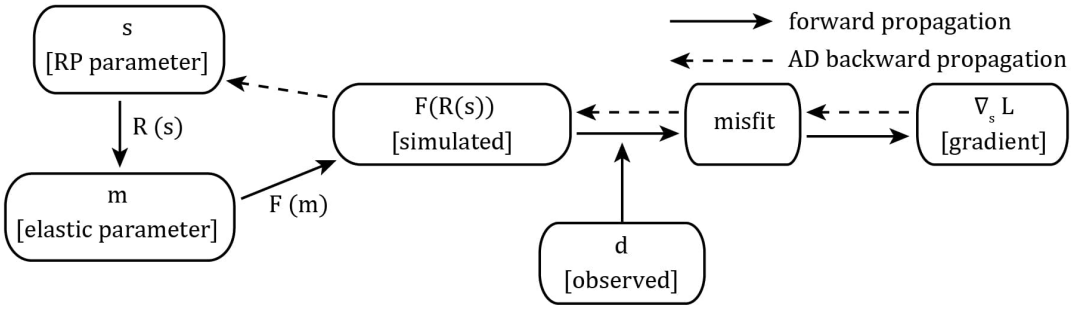

Figure 5.2.2: Workflow of proposed framework with RP parameterization using AD. The parameter s is mapped to elastic properties m through the rock-physics model R. These elastic properties are then passed into the forward modelling operator F to produce simulated seismic data (syn). The misfit between the simulated data and the observed data d is computed based on the objective function. Gradients of the loss function are then propagated backward via AD to iteratively update the model parameter s.

The inversion experiments were conducted using the Deepwave python package (Richardson, 2025), which integrates 2D elastic wave propagation modules with PyTorch. Two key assumptions were made: (1) the baseline (pre-injection) elastic models are assumed to be known and serve as the starting models for the inversion; (2) petrophysical properties such as porosity and matrix moduli remain constant over time. These assumptions ensures that variations in the elastic properties are attributed solely to changes in fluid saturation, without contributions from the rock matrix. The monitor (post-injection) seismic data were simulated using monitor elastic models derived from saturation maps produced by dynamic reservoir simulations, using the RPM to translate fluid saturation into elastic properties.

Results

Traditional and rock-physics parameterized FWI were performed and compared to assess their ability to accurately determine the distribution of H_2 within the reservoir and enable quantitative inversion. In traditional FWI, the inversion starts with a smoothed version of the baseline velocity model, while the parameterized FWI starts with the residual CH_4 saturation model of the depleted reservoir. A total of 140 receivers and 40 sources were deployed at intervals of 20 m and 80 m, respectively, using a Ricker source with a dominant frequency of 40 Hz. Both inversion methods were run for 200 epochs on a GPU. To mitigate the cycle-skipping problem, a multiscale approach was adopted, by inverting from a low frequency of 10 Hz to a maximum of 80 Hz to solve fine structures. Figure 5.2.3.e-g illustrates the velocity and density models recovered from the inverted saturation model (Figure 5.2.3.h) using the rock-physics parametrized inversion approach. These inverted models closely match the true ones (Figure 5.2.3.a-d),

with low residual error primarily concentrated in the right part of the model due to challenges posed by steep layers and limited source/receiver coverage (Figure 5.2.3.i-l). In contrast, the elastic models inverted with traditional FWI are shown in Figure 3m-o. Despite having the same runtime, the traditional FWI produces less accurate elastic models with significant artefacts compared to those obtained through rock-physics parameterized FWI. This difference is attributed to the slower convergence of traditional FWI, resulting from the simultaneous inversion of multiple elastic variables. As a second step following the traditional inversion, we derived the saturation model by applying point-by-point mapping to the velocity changes between the inverted monitor model and the pre-injection model. The velocity-saturation relationship depicted in Figure 5.2.1.b served as the reference for this mapping. The result, as expected, reveal hydrogen saturation map with significant errors, primarily due to the low-quality elastic inversion.

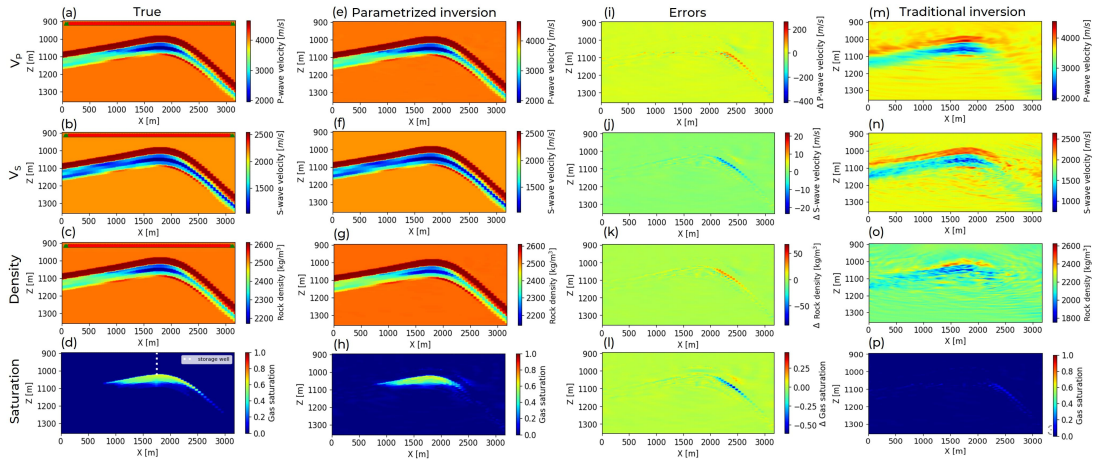

Figure 5.2.3: (a-d) True monitor elastic and saturation models of the synthetic reservoir; (e-h) inverted models obtained using rock-physics parametrized FWI; (i-l) residual error of the rock-physics parametrized FWI; (m-o) inverted models using traditional FWI approach; (p) saturation model obtained by applying point-by-point mapping to the velocity changes between the inverted elastic monitor model (m) and the pre-injection model. The green triangles and red dots in panels (a-c) represent receivers and sources, respectively.

The RPM guides the inversion by determining how changes in saturation influence the elastic response and, consequently, affect the inversion outcome. Small changes in hydrogen saturation affect velocity differently depending on the adopted mixing law, causing either significant or minimal variations. This highlights the need for a calibrated RPM and careful management of saturation updates during FWI optimization. Additionally, the non-linear saturation-velocity relationship can destabilize the gradient of the cost function, complicating convergence and requiring careful handling to

ensure accuracy and stability.

Conclusions

In this work, we developed a 2D elastic Full-Waveform Inversion (FWI) with rock-physics parametrization to directly estimate hydrogen saturation cyclically stored in a realistic depleted gas reservoir using prestack seismic data. A tailored DEM-Gassmann rock-physics model was combined within an Automatic Differentiation-based FWI framework to perform the inversion. The proposed framework demonstrated higher accuracy and efficiency compared to traditional FWI, both in terms of computational requirements and inversion precision. By directly inverting for reservoir properties, the framework eliminates the need for explicit derivations and bypasses the conventional two-step inversion process. However, the feasibility of the proposed method depends on prior knowledge or reasonable assumptions about the initial fluid distribution and rock matrix properties, which are often well-constrained in scenarios such as depleted gas reservoirs.

Bibliography

H. Balhareth and M. Landrø. 2016. Sensitivity analysis and application of time-lapse full-waveform inversion: synthetic testing and field data example from the North Sea, Norway. *Geophysical Prospecting* 64 (2016), 1183–1200. https://doi.org/10.1111/1365-2478.12251

A. Brie, F. Pampuri, A. Marsala, and O. Meazza. 1995. Shear sonic interpretation in gas-bearing sands. In *SPE Annual Technical Conference and Exhibition*. OnePetro, Dallas, Texas, SPE–30595–MS. https://doi.org/10.2118/30595-MS

C. Cao, J. Liao, Z. Hou, H. Xu, F. Mehmood, and X. Wu. 2020. Utilization of CO_2 as cushion gas for depleted gas reservoir transformed gas storage reservoir. *Energies* 13 (2020), 576. https://doi.org/10.3390/en13030576

M. Dai and B. He. 2023. Studies on modified limited-memory BFGS method in full waveform inversion. *Frontiers in Earth Science* 10 (2023), 1–11. https://doi.org/10.3389/feart.2022.1047342

F. Gassmann. 1951. Elastic waves through a packing of spheres. *Geophysics* 16 (1951), 673–685. https://doi.org/10.1190/1.1437718

R. Hill. 1952. The elastic behaviour of a crystalline aggregate. *Proceedings of the Physical Society. Section A* 65, 5 (1952), 349. https://doi.org/10.1088/0370-1298/65/5/307

Qi Hu, Dario Grana, and Kristopher A Innanen. 2022. Feasibility of seismic time-lapse monitoring of CO2 with rock physics parametrized full waveform inversion. *Geophysical Journal International* 233, 1 (11 2022), 402–419. https://doi.org/10.1093/gji/ggac462

Virieux Jean and Operto Stephane. 2009. An overview of full-waveform inversion in exploration geophysics. *GEOPHYSICS* 74, 6 (2009), WCC1–WCC26. https://doi.org/10.1190/1.3238367

Scott Keating and Kristopher A. Innanen. 2019. Parameter crosstalk and modeling errors in viscoacoustic seismic full-waveform inversion. *GEOPHYSICS* 84, 4 (2019), R641–R653. https://doi.org/10.1190/geo2018-0410.1

M. Krief, J. Garat, J. Stellingwerff, and J. Ventre. 1990. A petrophysical interpretation using the velocities of P and S waves (full waveform sonic). *The Log Analyst* 31 (1990), 355–369. https://api.semanticscholar.org/CorpusID:127038729

B. Lin, Y. Wei, S. Gao, L. Ye, H. Liu, W. Zhu, J. Zhang, and D. Han. 2024. Current progress and development trend of gas injection to enhance gas recovery in gas reservoirs. *Energies* 17 (2024), 1595. https://doi.org/10.3390/en17071595

A. Mardan, B. Giroux, G. Fabien-Ouellet, and M. R. Saberi. 2023. Monitoring fluid saturation in reservoirs using time-lapse full-waveform inversion. *Geophysical Prospecting* 71 (2023), 1012–1029. https://doi.org/10.1111/1365-2478.13363

Johannes Miocic, Niklas Heinemann, Katriona Edlmann, Jonathan Scafidi, Fatemeh Molaei, and Juan Alcalde. 2023. Underground hydrogen storage: a review. *Geological Society, London, Special Publications* 528, 1 (2023), 73–86. https://doi.org/10.1144/SP528-2022-88

Ken Perlin. 2002. Improving noise. In *Proceedings of the 29th Annual Conference on Computer Graphics and Interactive Techniques* (San Antonio, Texas) *(SIGGRAPH '02)*. Association for Computing Machinery, New York, NY, USA, 681–682. https://doi.org/10.1145/566570.566636

Alan Richardson. 2018. Seismic Full-Waveform Inversion Using Deep Learning Tools and Techniques. arXiv:1801.07232 [physics.geo-ph] https://arxiv.org/abs/1801.07232

Alan Richardson. 2025. *Deepwave*. Zenodo. https://doi.org/10.5281/zenodo.17107997

Sagar Singh, Ilya Tsvankin, and Ehsan Zabihi Naeini. 2018. Bayesian framework for elastic full-waveform inversion with facies information. *The Leading Edge* 37, 12 (2018), 924–931. https://doi.org/10.1190/tle37120924.1

S. Z. Sun, H. Wang, Z. Liu, Y. Li, X. Zhou, and Z. Wang. 2012. The theory and application of DEM–Gassmann rock-physics model for complex carbonate reservoirs. *The Leading Edge* 31 (2012), 152–158. https://doi.org/10.1190/1.3686912

K. Suzanne, G. Hamon, J. Billiotte, and V. Trocme. 2003. Experimental relationships between residual gas saturation and initial gas saturation in heterogeneous sandstone reservoirs. In *SPE Annual Technical Conference and Exhibition*. Society of Petroleum Engineers, Denver, Colorado, SPE–84038–MS. https://doi.org/10.2118/84038-MS

P. Yang, R. Brossier, L. Métivier, J. Virieux, and W. Zhou. 2018. A time-domain preconditioned truncated Newton approach to viscoacoustic multiparameter full waveform inversion. *SIAM Journal on Scientific Computing* 40, 4 (2018), B1101–B1130. https://doi.org/10.1137/17M112612

Zhen-dong Zhang, Tariq Alkhalifah, Ehsan Zabihi Naeini, and Bingbing Sun. 2018. Multiparameter elastic full waveform inversion with facies-based constraints. *Geophysical Journal International* 213, 3 (03 2018), 2112–2127. https://doi.org/10.1093/gji/ggy113

Chapter 6

Seismic dispersion and attenuation during hydrogen storage

Understanding how seismic waves are affected by dispersion and attenuation in partially gas-saturated rocks is crucial for new energy applications and specifically for underground hydrogen storage. To develop and validate these technologies, it is essential to know how partial gas saturation changes the elastic properties of reservoir rocks, since this knowledge is the base to design and implement reliable seismic monitoring methods. A key process in gas-bearing rocks is called mesoscopic patchy saturation, where gas and liquid phases form separate patches that are larger than individual pores but smaller than the seismic wavelength. When a seismic wave travels through such a rock, it creates pressure differences between gas-rich and liquid-rich patches. These pressure gradients drive fluid flow from the more compressible gas-rich zones to the less compressible liquid-rich ones. This movement of fluids causes an overall P-wave attenuation, which means energy loss, making the velocity dispersive, meaning that it depends on the frequency. Classic work by White (1975) showed that fluid heterogeneity, such as the presence of gas pockets within brine, can produce strong P-wave attenuation and elastic modulus dispersion at seismic frequencies relevant to field conditions. The strength and pattern of these effects depend on factors such as gas saturation, the size and shape of the patches, and the permeability/hydraulic conductivity of the rock.
Accurately modelling these dispersion and attenuation phenomena is therefore crucial for improving inversion workflows and constraint seismic interpretation. Incorporating frequency-dependent rock physics into seismic inversion algorithms can enable more quantitative retrieval of fluid properties from field data. For example, full-waveform

inversion schemes could integrate frequency-dependent attenuation and velocity trends, thereby leveraging the information content of dispersive seismic signals. By accounting for wave-induced fluid flow effects, such inversion approaches would better constrain the spatial distribution of gas saturation and even pore-fluid pressure changes. In time-lapse seismic monitoring of underground hydrogen storage, this means that small variations in waveform frequency content and amplitude can be linked to changes in gas saturation within the reservoir. Recent experimental and numerical studies support this idea (Kimura, 2014; Borgomano et al., 2017; Chapman et al., 2022; He et al., 2021; Sun et al., 2022), showing that frequency-dependent attenuation and dispersion measurements can be directly related to fluid saturation patterns. Overall, modelling the seismic response of patchy saturation enables more robust and frequency-aware inversion and interpretation, which are crucial for reliable monitoring of injected gases such as CO_2 and H_2.

In summary, the extended abstract presented in this chapter demonstrates that the injection of hydrogen into a brine-saturated formation will induce measurable dispersion and attenuation effects in the seismic frequency band. The insights from this study will inform future works integrating frequency-dependent attenuation and dispersion into inversion algorithms, ultimately enhancing our ability to track subsurface gas plumes and verify the integrity and efficiency of UHS operations.

6.1 Frequency-dependent seismic analysis for hydrogen storage in porous media

This work focus on the effects of mesoscopic hydrogen distributions on seismic attenuation and velocity dispersion, particularly under patchy saturation in saline aquifers and depleted gas reservoirs. Adopting a frequency-dependent rock physics forward modelling, spherical and fractal fluid patches are modelled in sandstone and limestone under different porosity and permeability scenarios. Attenuation and velocity dispersion are evaluated across saturation levels and frequency ranges. We note that limited hydrogen saturation induces strong attenuation within the seismic frequency band for saline aquifers, and depleted gas reservoir under low porosity- permeability conditions. The presence of cushion gas, such as CO_2, induce a slightly reduced attenuation than pure hydrogen. Wave dispersion and attenuation are diagnostic of hydrogen saturation and distribution. Thus, the sensitivity of time-lapse seismic surveys should be carefully assessed for the specific case. Incorporating mesoscopic effects and patch geometries can enhance UHS monitoring, supporting safe and accurate reservoir monitoring.

Frequency-dependent seismic analysis for hydrogen storage in porous media

G. Pantaleo, M. Pipan

Extended abstract presented at International Meeting for Applied Geoscience & Energy (IMAGE25), 25^{th}-28^{th} August 2025, Houston (TX)

doi: to be assigned

Available at:

https://imageevent.aapg.org/portals/26/abstracts/2025/4316783.pdf

Key Words

Underground Hydrogen Storage (UHS); *Wave-induced fluid flow*; *Seismic wave attenuation and dispersion*; *Rock-physics modelling*

Introduction

Hydrogen (H_2) is considered a key energy carrier in the transition to a low-carbon energy system. Underground hydrogen storage (UHS) offers a solution to store surplus renewable energy for later use during high demand. Among the potential geological formations, salt caverns, depleted gas field, and saline aquifers offer the volumes required for large-scale and long-term storage. Although salt caverns provide excellent containment, depleted gas fields and saline aquifers are advantageous due to their larger capacity, they require minimal artificial construction, and their geology is usually well understood. During the injection and withdrawal processes, cushion gas as methane and carbon-dioxide (CO_2) plays a crucial role to maintain reservoir pressure and enhance hydrogen recovery. In practical scenarios, the injection of CO_2 not only serves as cushion gas, but also allows CO_2 sequestration practices, maximizing the geological storage benefits (Miocic et al., 2023). Monitoring the storage site to ensure containment and detect potential leakage is essential. Seismic methods, particularly time-lapse seismic surveys, are well-established for CO_2 storage and are now being explored for hydrogen storage. CO_2 injection is known to alter the seismic response by modifying fluid saturation, which in turn affects elastic and attenuation properties of the rock. Besides conventional elastic properties (P- and S-wave velocities, and density), extracting parameters describing attenuation mechanism as quality factor (Q-factor) can enhance quantitative estimation. In this context, including the attenuation parameter in an inversion scheme as Full-Waveform Inversion (FWI) will likely produce a more correct reconstruction of the mesoscale properties (Queißer and Singh, 2013). Further study on mesoscopic effects due to CO_2 injection revealed that wave-induced fluid flow

in patchy-saturated media as the Utsira Formation, is a significant source of seismic attenuation (Rubino et al., 2011). These effects are pronounced in media with heterogeneities at scales between pore size and seismic wavelengths (White, 1975; Picotti et al., 2010a). Such mesoscopic effects are also expected in hydrogen storage scenarios. Bijay et al. (2024) demonstrated through ultrasonic experiments that P-wave velocity is sensitive to hydrogen saturation in sandstone cores, supporting the feasibility of seismic monitoring for hydrogen storage. White (1975) first predicted attenuation and seismic wave dispersion in patchy-saturated porous media, and Johnson (2001) later improved White's theory to arbitrary shape of the periodic patches. In this study, we investigate the attenuation and velocity dispersion of compressional waves propagating through rocks with heterogeneous distributions of hydrogen, cushion gas, and brine within the pore space. We explore various saturation levels and geometric configurations of the saturated patches, focusing on two key UHS scenarios: depleted gas reservoirs and saline aquifers.

Theory and Methods

To evaluate the frequency-dependent effect of patchy fluid distribution on seismic data, we adopt the approach proposed by Johnson (2001), applicable at intermediate frequencies. Johnson developed a model describing the transition between the Biot–Gassmann–Wood (BGW) low-frequency limit, which assumes uniform fluid pressure throughout the pore space, and the Biot–Gassmann–Hill (BGH) high-frequency limit, where there is insufficient time for pressure equilibration between fluid patches (Mavko et al., 2009). Thus, Johnson (2001) proposed a dynamic bulk modulus that describes the crossover between these two end-members, given by (6.1):

$$K(\omega) = K_{\mathrm{GH}} - \frac{K_{\mathrm{GH}} - K_{\mathrm{GW}}}{1 - \xi + \xi\sqrt{1 + \mathrm{j}\,\frac{\tau}{\xi}}}, \tag{6.1}$$

where $\mathrm{j} = \sqrt{-1}$ is the imaginary unit, ξ is a shape parameter, and τ sets the frequency scale. Both ξ and τ are obtained in terms of the dry-rock moduli, porosity (ϕ), permeability (κ), fluid viscosity (η), the shape factor S/V, and the size factor T. Here S/V is the ratio of the surface area of a patch to its volume and depends on the patch shape, while T is governed by the mean patch size (Johnson, 2001). K_{GH} is the effective bulk modulus at the high-frequency limit given by Hill's equation for a non-equilibrated (undrained) fluid distribution, and K_{GW} is the effective bulk modulus at the low-frequency limit given by Wood's equation for a fully equilibrated fluid system (Mavko et al., 2009). Attenuation and velocity dispersion in the intermediate-frequency range are governed by the size and distribution of the fluid patches. Following Johnson's conceptual model, we represent patchy saturation as a regular distribution

of spherical gas-saturated regions surrounded by brine-saturated regions. The inner sphere has radius R_a, and the outer sphere has radius R_b, with $R_b > R_a$ (White, 1975; Johnson, 2001). A useful parameter to describe the frequency transition is the critical diffusion length,

$$L_c = \sqrt{\frac{D}{\omega}}, \tag{6.2}$$

where ω is the angular frequency and D is the diffusivity. The diffusivity D is defined, for each fluid, in terms of rock permeability, fluid viscosity, and the elastic moduli of the solid grains and dry matrix (e.g., Picotti et al. (2010b)). When the diffusion length becomes comparable to the patch size, the response transitions between the low- and high-frequency limits due to mesoscopic patches. The frequency-dependent dynamic bulk modulus then yields the complex P-wave velocity

$$v_c(\omega) = \sqrt{\frac{K(\omega) + \frac{4}{3}\,\mu_m}{\rho_b}}, \tag{6.3}$$

where μ_m is the dry shear modulus and ρ_b is the bulk density of the saturated rock. Finally, the phase velocity v_p and the attenuation factor Q as functions of frequency are (Picotti et al., 2010b):

$$v_p = \Big[\mathrm{Re}\Big(\frac{1}{v_c(\omega)}\Big)\Big]^{-1}, \qquad Q = \frac{\mathrm{Re}\big(v_c^2(\omega)\big)}{\mathrm{Im}\big(v_c^2(\omega)\big)}. \tag{6.4}$$

Attenuation and dispersion effects are strongly influenced by porosity, permeability, and fluid viscosity. A decrease in porosity implies changes in both permeability and dry-rock moduli. For sandstone we use the Kozeny–Carman relation:

$$\kappa = B\,d^2\,\frac{\Phi^3}{(1-\Phi)^2},$$

where B is a constant, d is a grain (or pore) size, and Φ is porosity (Mavko et al., 2009). For limestone we use (Yu et al., 2014):

$$\kappa = 0.0012\,\mathrm{e}^{\,63.34\,\Phi}.$$

Viscosities for the individual fluid phases are computed with the Lohrenz–Bray–Clark model (Lohrenz et al., 1964) as a function of gas density. The effective viscosity of a two-phase mixture is modeled as (Teja and Rice, 1981):

$$\eta_f = \eta_2 \left(\frac{\eta_1}{\eta_2}\right)^{S_1},$$

where η_1 and η_2 are the viscosities of the first and second fluid, respectively, and S_1 is the saturation of the first fluid. For the saline-aquifer scenario, fluid properties are computed using the Peng–Robinson equation of state assuming $P \approx 8$ MPa and $T \approx 29°$C. Brine and in-situ gas properties for the limestone reservoir are taken from Yu et al. (2014), whereas hydrogen properties are calculated at 20 MPa and 75°C. See Table 6.1 for the fluid physical properties.

We perform forward rock-physics modeling (RPM) to simulate the frequency-dependent response of hydrogen injection in Utsira-like sandstone and Metajan-like limestone formations. The petrophysical parameters for the Utsira sandstone are based on Chadwick et al. (2004), whereas those for the Metajan limestone are taken from Yu et al. (2014). The effective mineral mixture $(K_m,\ \mu_m,\ \rho_m)$ and the dry-rock moduli $(K_d,\ \mu_d)$ are computed using the Voigt–Reuss–Hill average and the Krief model, respectively (Mavko et al., 2009). Heterogeneities in the rock matrix are neglected to focus exclusively on loss mechanisms associated with fluid-saturation effects. The shear modulus is assumed constant ($\mu_m = \text{const.}$), as it is not directly influenced by fluid variations. Chemical interactions between phases are neglected. See Table 6.2 for rock-physical properties.

To investigate how mesoscopic energy loss mechanisms are affected by patch geometry, we also consider fractal patch shapes. Following (Picotti et al., 2010b) and (Gei et al., 2024), fractal patch geometry is introduced by keeping the size factor T constant while increasing the shape factor S/V of the initial spherical patch by a factor of 10 (see (Johnson, 2001) for T and S/V definitions). Moreover, different fluid mixtures and rock frame stiffness conditions were assumed, and corresponding wave attenuation and dispersion sensitivity was calculated. As indicated in Table 6.2, Sand1 and Sand2 indicate soft and stiff saline aquifers, with 29% and 19% porosity, respectively. While Lime1 and Lime2 indicates soft and stiff depleted gas reservoir, with 16% and 8%, respectively.

Each scenarios were evaluated as partially saturated with pure hydrogen, or with a mixture of 50% hydrogen and 50% cushion gas (hereafter referred to as hydrogen mixture). For saline aquifers the cushion gas is CO_2, while for depleted reservoirs is the in-situ gas (data from Yu et al. (2014)).

Table 6.1: Pore-fluid physical parameters used in this work. Cushion gas is CO_2 for saline aquifer, and in-situ gas for limestone reservoir.

	Saline aquifer		
	Brine	Cushion gas	H_2
K_f [GPa]	2.31	0.014	0.012
ρ_f [g/cm^3]	1.00	0.332	5.99×10^{-3}
η_f [Pa·s]	8×10^{-4}	3.86×10^{-5}	8.28×10^{-6}
Limestone gas reservoir			
K_f [GPa]	2.51	0.081	0.031
ρ_f [g/cm^3]	1.04	0.17	0.013
η_f [Pa·s]	1×10^{-3}	1.5×10^{-4}	8.98×10^{-6}

Table 6.2: Rock physical parameters used in this work.

	Saline aquifer		**Limestone gas reservoir**	
	Sand1	Sand2	Lime1	Lime2
ϕ [%]	29	19	16	8
K_m [GPa]	39.66		71.90	
μ_m [GPa]	36.58		29.61	
ρ_m [g/cm^3]	2.65		2.70	
k [mD]	0.41	0.08	0.30	0.19
K_d [GPa]	1.78	8.61	24.81	36.75
μ_d [GPa]	1.03	5.02	11.79	17.46
R_b [m]	0.25		0.105	

Results

Frequency-dependent P-wave velocity dispersion and Q-factor attenuation were computed on the basis of Johnson's spherical and fractal patch geometries. Results are displayed in Figure 6.1.1 for saline aquifer scenarios, and Figure 6.1.2 for depleted gas reservoir scenarios.

Figure 6.1.1.a shows the P-wave velocity as a function of gas saturation at the corresponding relaxation peak frequency (~ 30 Hz) for the soft (Sand1 - red curves) and stiff (Sand2 - blue curves) sandstone models. In both lithologies, velocity decreases with increasing gas saturation. This change is emphasized when fractal patch geometries are assumed, particularly in the softer sandstone. At low saturations, the hydrogen

mixture deviates from the pure hydrogen trend, especially in the stiff sandstone.
Figure 6.1.1.b shows the attenuation curves (1000/Q) corresponding to the relaxation peak frequency for each scenario. Maximum attenuation for spherical patches occurs at approximately 10% gas saturation, then decreases with increasing saturation. Fractal patches shift the attenuation peak toward lower saturation levels and exhibit lower attenuation.
Figure 6.1.1.c and 6.1.1.d examine the frequency-dependence attenuation and P-wave velocity dispersion corresponding to 10%, 30%, and 55% gas saturation (pure hydrogen: lines; hydrogen mixture: markers), assuming spherical patches. In Figure 6.1.1.c the attenuation peaks at $\sim$ 10 % gas saturation falls within the seismic frequency range (5-300 Hz), for both sandstones. As saturation increases, the relaxation peak reaches low attenuation and shift towards higher frequencies.
In Figure 6.1.1.d, velocity dispersion curves highlight the transition from the low BGW limit to the high BGH limit at intermediate frequencies. This transition is governed by the mesoscopic patches whose size is comparable to the critical diffusion length Lc. For instance, the velocity transition at the low limit is located at $\sim 5\,\mathrm{Hz}$, corresponding to $L_c \approx 0.56\,\mathrm{m}$, while the patch radius Rb = 0.25 m, satisfying the condition $R_b < L_c$ for partial fluid pressure equilibration.
Figure 6.1.2.a presents the P-wave velocity as a function of gas saturation for soft and stiff limestone. Velocity decreases with gas saturation in both cases, with more significant changes observed in the softer limestone. This effect is emphasized when fractal patch geometries are assumed, particularly for the stiffer limestone.
In Figure 6.1.2.b, the attenuation response at the corresponding frequency peak is reached at about 10% saturation for spherical patches, while at lower saturation level for fractal patches. In both cases the attenuation decreases with increasing saturation. For spherical scenarios, the hydrogen mixture shows lower attenuation than pure hydrogen at relatively low saturation, with this difference diminishing towards higher saturations.
Figure 6.1.2.c displays the attenuation over frequency for gas saturations of 10%, 30%, and 55%. In the soft limestone, attenuation peaks lie at frequencies higher than the seismic band. Increasing gas saturation the peak moves towards higher frequencies, and the dispersion curves cover broader frequency range. The stiff limestone, with lower porosity and permeability, shows the relaxation peak for 10% saturation shifted towards the seismic range ($\sim 30\,\mathrm{Hz}$), and the maximum loss decreases. Same shift is observed for 30% and 55% saturation scenarios, where the maximum loss decreases, and the peak is shifter to lower frequencies.
Figure 6.1.2.d shows the P-wave velocity dispersion curves. As gas saturation increases,

the dispersion range broadens and the BGH limit shifts to higher frequencies. This indicates that the medium shows mesoscopic loss mechanisms across a broader frequency range. The low frequency transition limit is located at approximately 5 Hz for the stiff limestone and 1000 Hz for the soft limestone. These transition frequencies correspond to critical diffusion lengths of Lc = 0.03 m and Lc = 0.019 m, respectively, while the patch radius Rb = 0.0105 m in both cases remain smaller than Lc, validating the presence of partial fluid pressure equilibration at lower frequencies.

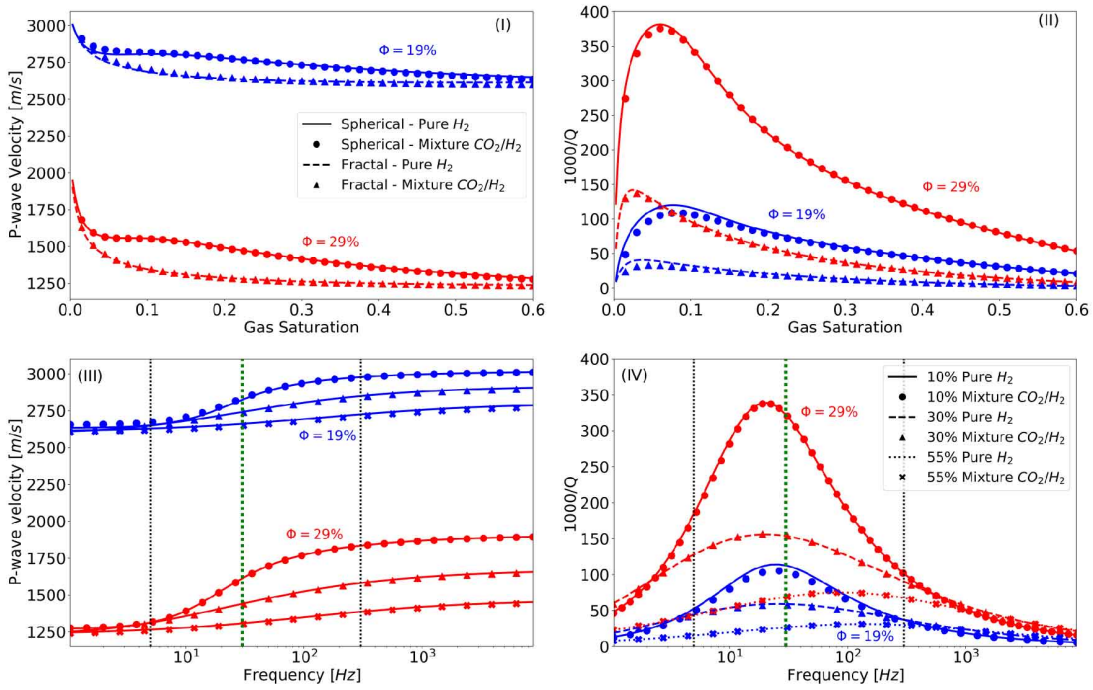

Figure 6.1.1: P-wave velocity (a) and attenuation factor (b) versus gas saturation at the corresponding relaxation peaks as in (c), for spherical and fractal patches in sandstones with different porosities (29% in red, 19% in blue). Panels (c) and (d) show the attenuation factor and P-wave velocity, respectively, as function of frequency, based on spherical patch geometry. The dotted vertical lines indicates the seismic frequency range, while the green vertical line marks the reference frequency of 30 Hz.

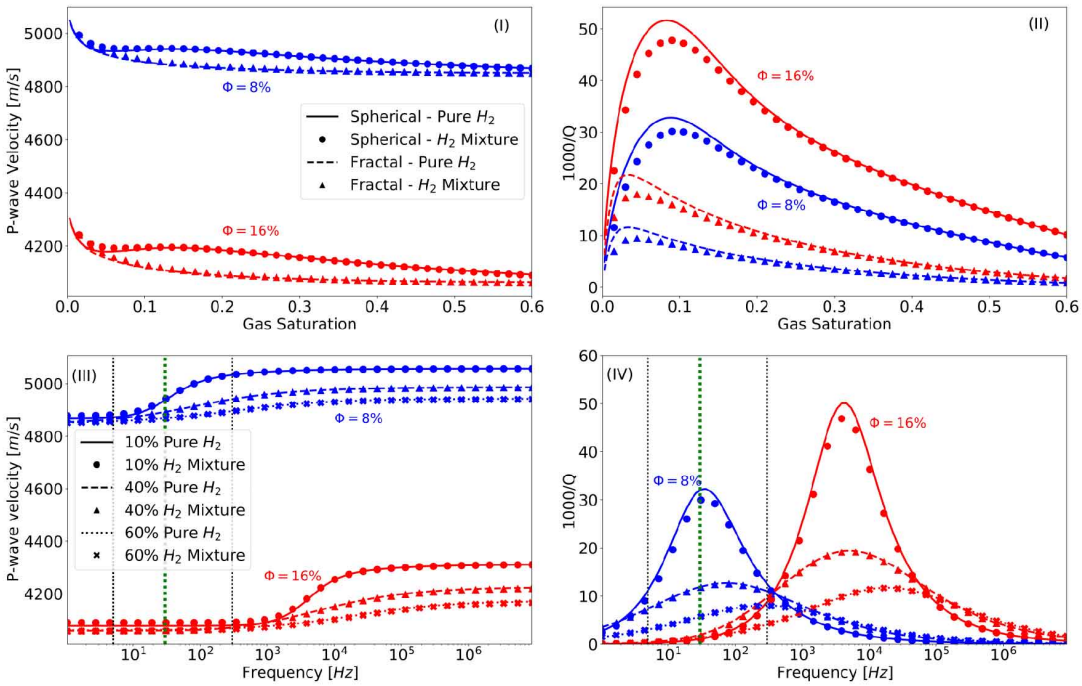

Figure 6.1.2: P-wave velocity (a) and attenuation factor (b) as a function of gas saturation at the corresponding relaxation peaks as in (c), for different patch geometries in limestones with different porosities (16% in red, 8% in blue). Panels (c) and (d) show the attenuation factor and P-wave velocity, respectively, as functions of frequency, based on spherical patch geometry. The dotted vertical lines indicate the seismic frequency range, while the green vertical line marks the reference frequency of 30 Hz.

Conclusions

This study offers a detailed analysis of frequency-dependent P-wave velocity dispersion and attenuation responses using Johnson's spherical and fractal patches, for saline aquifer and depleted reservoir during seasonal hydrogen storage. Patch geometries significantly affect the mesoscopic attenuation response, where fractal patches introduce stronger P-wave variation and lower attenuation peak compared to spherical patches, especially at lower saturations and in low-porosity and low-permeability media. Higher attenuation and velocity dispersion occur at low gas saturations (10%), due to high bulk modulus contrasts between hydrogen and brine. The presence of hydrogen mixtures with cushion gas leads to slightly reduced attenuation compared to pure hydrogen, especially at low saturations. Our modelling for sandstones and limestones indicates that frequency-dependent seismic analysis can offer quantitative constraints on hydrogen-partially saturated zone, under different rock properties and fluid mobility conditions. The modelling can be extended to possible leakage that may occur from the reservoir through the caprock. Further studies should investigate loss mechanisms

associated with mesoscopic heterogeneities in the solid frame. Additionally, integrating frequency-dependent Q-factor for partially saturated media into seismic forward modelling and FWI algorithm, should improve amplitude prediction due to hydrogen injection, enhancing feasibility studies for monitoring purpose.

Bibliography

K. C. Bijay, L. P. Frash, N. M. Creasy, C. W. Neil, P. Purswani, W. Li, M. Meng, U. Iyare, and M. R. Gross. 2024. Laboratory study of cyclic underground hydrogen storage in porous media with evidence of a dry near-well zone and evaporation induced salt precipitation. *International Journal of Hydrogen Energy* 71 (2024), 515–527. https://doi.org/10.1016/j.ijhydene.2024.05.234

J. V. M. Borgomano, L. Pimienta, J. Fortin, and Y. Guéguen. 2017. Dispersion and attenuation measurements of the elastic moduli of a dual-porosity limestone. *Journal of Geophysical Research: Solid Earth* 122, 4 (2017), 2690–2711. https://doi.org/10.1002/2016JB013816

R. A. Chadwick, P. Zweigel, U. Gregersen, G. A. Kirby, S. Holloway, and P. N. Johannessen. 2004. Geological reservoir characterization of a CO_2 storage site: The Utsira Sand, Sleipner, northern North Sea. *Energy* 29 (2004), 1371–1381. https://doi.org/10.1016/j.energy.2004.03.071

Samuel Chapman, Jan V M Borgomano, Beatriz Quintal, Sally M Benson, and Jerome Fortin. 2022. Mass transfer between fluids as a mechanism for seismic wave attenuation: experimental evidence from water–CO2 saturated sandstones. *Geophysical Journal International* 230, 1 (02 2022), 216–234. https://doi.org/10.1093/gji/ggac067

D. Gei, J. M. Carcione, and S. Picotti. 2024. The physics of seismic propagation in aquifers partially saturated with H_2. Comparison with the cases of CO_2 and CH_4. *Bulletin of Geophysics & Oceanography (BGO)* 65, 4 (2024), 1–22. https://doi.org/10.4430/bgo00470

Y.X. He, S.X. Wang, C. Sun, G.Y. Tang, and W. Zhu. 2021. Analysis of the frequency dependence characteristics of wave attenuation and velocity dispersion using a poroelastic model with mesoscopic and microscopic heterogeneities. *Geophysical Prospecting* 69, 6 (2021), 1260–1281. https://doi.org/10.1111/1365-2478.13101

D. L. Johnson. 2001. Theory of frequency dependent acoustics in patchy saturated porous media. *Journal of the Acoustical Society of America* 110 (2001), 682–694. https://doi.org/10.1121/1.1381021

Masao Kimura. 2014. Grain-size dependence of shear wave speed dispersion and attenuation in granular marine sediments. *The Journal of the Acoustical Society of America* 136, 1 (06 2014), EL53–EL59. https://doi.org/10.1121/1.4885478

J. Lohrenz, B. G. Bray, and C. R. Clark. 1964. Calculating viscosities of reservoir fluids from their compositions. *Journal of Petroleum Technology* 16 (1964), 1171–1176. https://doi.org/10.2118/915-PA

Gary Mavko, Tapan Mukerji, and Jack Dvorkin. 2009. *The Rock Physics Handbook* (2 ed.). Cambridge University Press, Cambridge, UK. https://doi.org/10.1017/CBO9780511626753 511 pp.

Johannes Miocic, Niklas Heinemann, Katriona Edlmann, Jonathan Scafidi, Fatemeh Molaei, and Juan Alcalde. 2023. Underground hydrogen storage: a review. *Geological Society, London, Special Publications* 528, 1 (2023), 73–86. https://doi.org/10.1144/SP528-2022-88

Stefano Picotti, José M. Carcione, J. Germán Rubino, Juan E. Santos, and Fabio Cavallini. 2010a. A viscoelastic representation of wave attenuation in porous media. *Computers & Geosciences* 36, 1 (2010), 44–53. https://doi.org/10.1016/j.cageo.2009.07.003

S. Picotti, J. M. Carcione, J. G. Rubino, J. E. Santos, and F. Cavallini. 2010b. A viscoelastic representation of wave attenuation in porous media. *Computers & Geosciences* 36, 1 (2010), 44–53. https://doi.org/10.1016/j.cageo.2009.07.003

Manuel Queißer and Satish C. Singh. 2013. Localizing CO2 at Sleipner — Seismic images versus P-wave velocities from waveform inversion. *GEOPHYSICS* 78, 3 (2013), B131–B146. https://doi.org/10.1190/geo2012-0216.1

J. Germán Rubino, Danilo R. Velis, and Mauricio D. Sacchi. 2011. Numerical analysis of wave-induced fluid flow effects on seismic data: Application to monitoring of CO2 storage at the Sleipner field. *Journal of Geophysical Research: Solid Earth* 116, B3 (2011). https://doi.org/10.1029/2010JB007997

Chao Sun, Jérôme Fortin, Jan V. M. Borgomano, Shangxu Wang, Genyang Tang, Tom Bultreys, and Veerle Cnudde. 2022. Influence of Fluid Distribution on Seismic Dispersion and Attenuation in Partially Saturated Limestone. *Journal of Geophysical Research: Solid Earth* 127, 5 (2022), e2021JB023867. https://doi.org/10.1029/2021JB023867

A. S. Teja and P. Rice. 1981. Generalized corresponding states method for the viscosities of liquid mixtures. *Industrial & Engineering Chemistry Fundamentals* 20, 1 (1981), 77–81. https://doi.org/10.1021/i100001a015

J. E. White. 1975. Computed seismic speeds and attenuation in rocks with partial gas saturation. *Geophysics* 40 (1975), 224–232. https://doi.org/10.1190/1.1440520

H. Yu, J. Ba, J. Carcione, J. S. Li, G. Tang, X. Y. Zhang, X. Z. He, and H. Ouyang. 2014. Rock physics modeling of heterogeneous carbonate reservoirs: Porosity estimation and hydrocarbon detection. *Applied Geophysics* 11 (2014), 9–22. https://doi.org/10.1007/s11770-014-0413-9

Chapter 7

Active Seismic Monitoring during CO_2 Injection at Svelvik CO_2 Field Lab

7.1 Introduction

As part of the PhD program, I led a geophysical project aimed at testing the integration of seismic and electromagnetic methods for the detection and quantification of CO_2 leakage at the Svelvik CO_2 Field Lab, Norway. This geophysical campaign was part of the SBEM (Svelvik Borehole Electromagnetic Monitoring) campaign, carried out between 24^{th} May and 9^{th} June 2025. The fieldwork was carried out in collaboration with Elisa Ligas, PhD student at UniTs, and Giacomo Roncoroni, Post-doctoral Researcher at UniTs. The planning and writing phase of the project proposal was also supported by my supervisors Michele Pipan and Emanuele Forte.

The SBEM project was carried out in collaboration with SINTEF, particularly through the contributions of Marcin Duda and Michael Jordan (Research Scientists and Field Lab representatives), who provided both seismic acquisition equipment and on-site assistance throughout the project period at the Svelvik CO_2 Field Lab. This work was partially supported by the FUSE project[1]. The SBEM project was funded by GEO-INQUIRE[2].

[1] Open Infrastructure on Future Underground Hydrogen Storage (FUSE), funded by the Regione Autonoma Friuli Venezia Giulia (L.R. 13/2023), CUP J93C24001980002.

[2] Geo-INQUIRE is funded by the European Commission under project number 101058518 within the HORIZON-INFRA-2021-SERV-01 call.

7.1.1 Purpose of the SBEM project

The SBEM project proposes a feasibility study for the near-surface characterization and monitoring of the Svelvik CO_2 Field Lab (SFL), combining Electrical Resistivity Tomography (ERT), Ground Penetrating Radar (GPR), and active seismic surveys. The objective was the characterization and imaging of the near-surface overburden and caprock of the SFL with GPR, in order to accurately mapping the geological boundaries and identifying lithologic variations that might affect the ability of the caprock to retain CO_2, as well as to detect possible CO_2 migration and leakage using seismic methods. In fact, previous CO_2 injection campaigns at the SFL have shown that the injected CO_2 migrates upwards and northwards from the injection point, as observed in time-lapse cross-well seismic surveys (Jordan et al., 2022). Complementary chemical tracer surveys[3] conducted using shallow soil sampling wells, also detected CO_2 at the surface, beyond the area typically covered by cross-well seismic surveys (personal communication from SINTEF researchers).

Seismic method is sensitive to CO_2 migration in the deep subsurface, while it is not expected to be sensitive in the shallower near-surface where small amount of CO_2 is eventually expected. By conducting GPR surveys, we aimed to assess whether GPR can be able to detect small amount of CO_2 that migrate through the overburden. In the areas not covered by cross-well time-lapse seismic surveys, only small amounts of CO_2 are expected, making seismic methods likely insensitive to its presence. The idea was therefore to explore whether GPR could complement seismic monitoring in the near-surface zone, assessing its potential to detect small amounts of CO_2 migrating through the overburden.

Due to time constraints and delays during the acquisition campaign, only limited work has been carried out on the collected datasets at the time of writing this thesis. In this chapter, selected examples of time-lapse seismic data collected with hydrophones and DAS are presented, while GPR and ERT data are omitted as they are beyond the main scope of the PhD work and will be used in future researches.

7.2 Description of the Svelvik CO_2 Field Lab

7.2.1 Geology

The Svelvik CO_2 Field Lab (SFL) is a small-scale test site owned by SINTEF[4] and is part of the European Carbon Dioxide Capture and Storage Laboratory Infrastructure

[3] See RESMAN Energy - "Using Chemical Tracers to Verify Secure Geological Storage"
[4] https://www.sintef.no

(ECCSEL[5]) for CO_2 Capture, Utilisation, Transport and Storage (CCUS) research. The SFL was specifically designed for controlled CO_2 injection experiments and for developing and testing technologies for detection and quantification of CO_2 storage.
The SFL occupies a non-active part of a sand and gravel quarry, located in an east-west running sandy ridge of recessional moraine (Figure 7.2.1), fluvial and marine sediments deposited in Holocene (SINTEF). The sandy aquifer is more than 200 m thick, with its geometry locally affected by undulating bedrock topography. The uppermost, phreatic aquifer holds fresh groundwater, while deeper parts are brackish and thought to be directly influenced by seawater (SINTEF). The geology of the SFL comprises unconsolidated sandy sediments with local gravel and boulders down to about 35 m depth, underlain by interbedded sand, silt, and clay layers of highly variable permeability. While below 35 m there is an alternation of layers of sand, silt and clay. Figure 7.2.2 displays the clay content (V_{cl}) and the grain-size distribution at well #1. V_{cl}, estimated from the gamma-ray log, identifies the presence of an aquifer around 65 m depth (NTNU, 2018). Distinct intervals with high V_{cl} are evident, notably the caprock that seals the top of Sand Zone 1 at roughly 35 m depth. Past experiments (i.e., the Pre-ACT project, Eliasson et al. (2018) or Jordan et al. (2022)) have highlighted peculiar behaviour of the CO_2 migration: (i) CO_2 migrated rapidly upward through the formation from the injection depth; (ii) CO_2 accumulated around well M3 beneath a mud-rich layer at approximately 37 m depth; (iii) leakage occurred toward the surface outside the injection well (personal communication from SINTEF researchers). These findings confirms the presence of the mud-rich horizon around 37 m depth that serves as a shallow caprock that trap migrating CO_2 from the injection point. Then, after the stop of injection the CO_2 continues its migration northward and upward, and the field site return to the pre-injection condition. This well-characterized layout and geology-guided gas migration provide an ideal setting for SBEM project to test high-resolution electromagnetic and seismic monitoring techniques in a real CO_2 injection scenario, and transfer it to leakage detection and leakage quantification in deep storage reservoir.

[5] https://www.eccsel.org

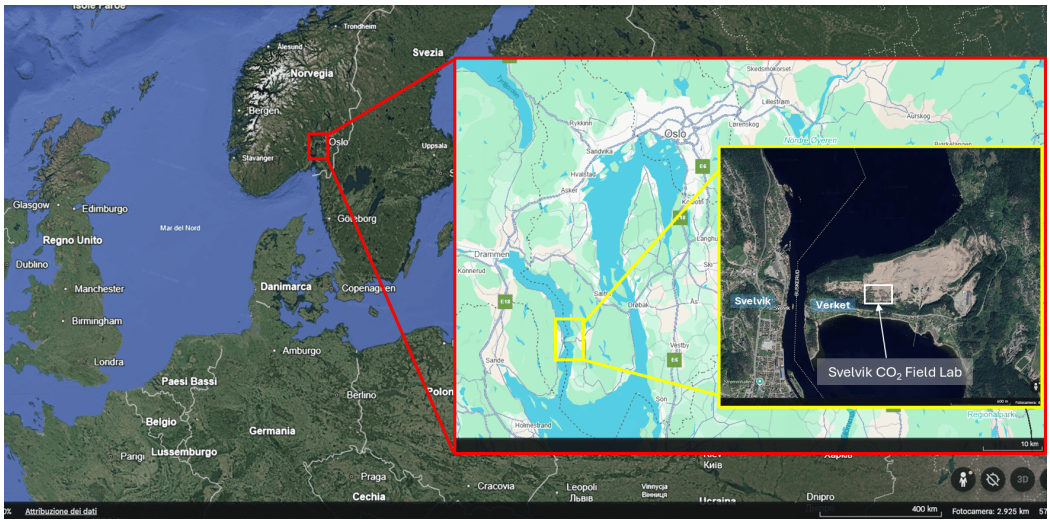

Figure 7.2.1: Multi-scale locator maps of southern Norway. The red square highlights the Oslo region. The yellow square is the satellite image showing Verket with the Svelvik ridge in Drammensfjorden, which is an east-west running sandy ridge of recessional moraine where the test site is located. The white square highlights the exact location of the SFL that occupies a non-active part of a sand and gravel quarry.

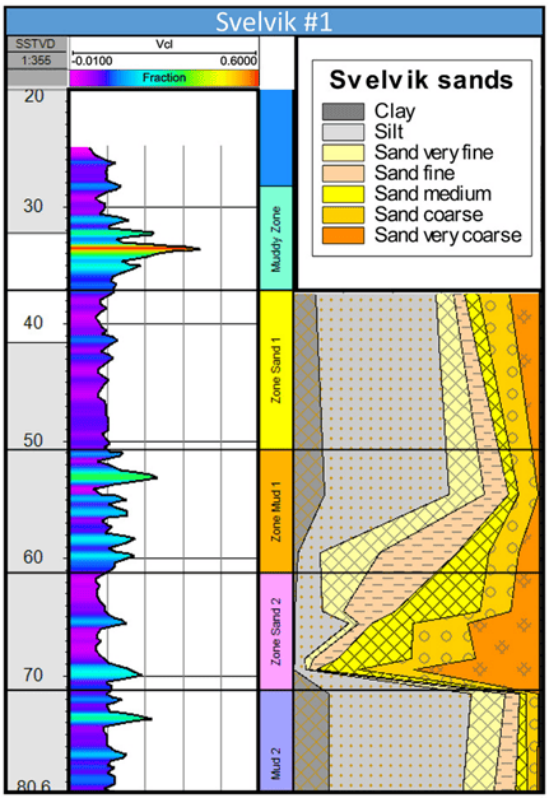

Figure 7.2.2: Gamma Ray log derived clay content (V_{cl}) log and grain size distributions from well #1 for the Svelvik site (Wuestefeld and Weinzierl, 2020).

7.2.2 Methods: test site and instrumentation setup

The SFL consists of a deep appraisal well (#1, up to 330 m), an injection well (#2, up to 90 m), and four monitoring wells (M1 to M4, up to 100 m) positioned at the corners of a rhombus with the injection well in the centre (Figure 7.2.3). The injection well is designed for injecting CO_2 at 64-65 meters depth. The monitoring wells are PVC cased to a depth of approximately 100 m. The inside of the casing is available for non-permanent instrumentation, allowing us to perform cross-well seismic and GPR borehole surveys, as well as Vertical Seismic Profile (VSP) and Vertical Radar Profile (VRP). Behind the casing, each monitoring well is equipped with research fibre-optic cables comprising straight (LIN) and helically wound (HWC) fibres (Figure 7.2.4). These configurations enable various Distributed Acoustic Sensing (DAS) measurements with different directional sensitivities, allowing comparative analyses of their performance under different acquisition settings.

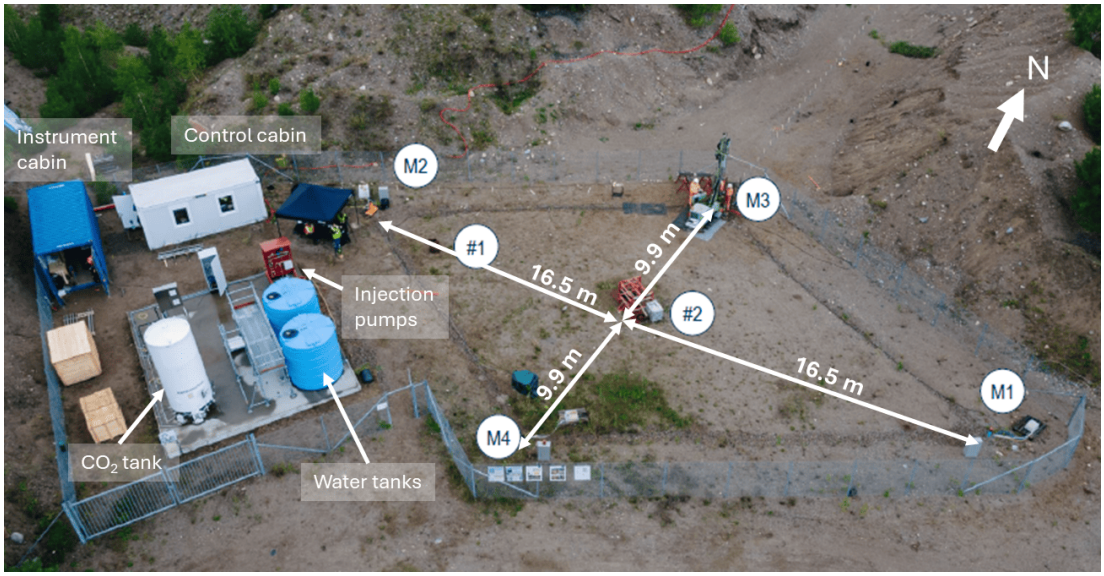

Figure 7.2.3: Drone photo showing the Svelvik CO_2 Field Lab and position of the most important facilities. Control and instrument cabin in the upper left of the photo is the place where instruments and data storage systems for downhole sensors are located. The locations of the wells and their distances are highlighted with markers and labels. Image courtesy of SINTEF.

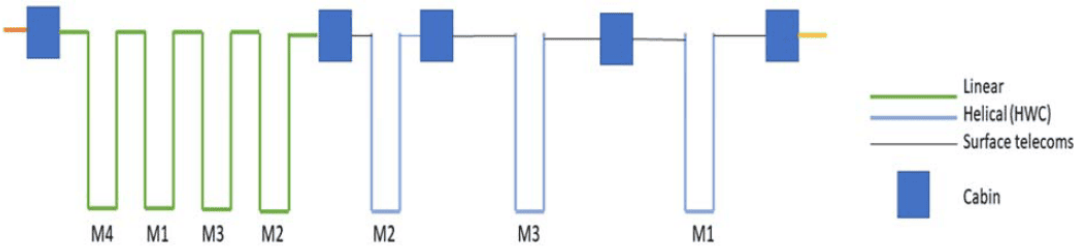

Figure 7.2.4: Sketch of the configuration of DAS cables in wells at SFL. Source: Koedel et al. (2022) DAS fibre-optic cable loop used in data acquisition. Boreholes are labelled (M1-M4) and the type of cable (linear, helical or standard telecommunications) is indicated. The cables are spliced together to form one interrogation loop. The interrogator is housed in the control cabin.

DAS system overview

Distributed Fibre Optic Sensing (DFOS) comprises a set of techniques where a fibre-optic cable, traditionally employed for data transmission, serves as the sensor capable of measuring various parameters like temperature (Distributed Temperature Sensing - DTS), strain (Distributed Strain Sensing - DSS), or vibrations (Distributed Acoustic Sensing - DAS) (Hartog, 2017). The application of fibre-optics to detect acoustic waves through DAS is a relatively recent innovation in this category of measurement methods. In DAS technique, Rayleigh backscattering of light caused by nano-scale irregularities within the optical fibres is utilized to detect variations in strain along the fibre that correlate with passing acoustic waves (Lindsey and Martin, 2021; Mei et al., 2024). An interrogator device positioned at one end of the fibre emits pulsed laser EM waves (Figure 7.2.5). As the emitted waves encounter imperfections in the fibre, phase shifts in the backscattered signal (light) occur over defined sections of the cable, referred to as the gauge length. This process enables the spatially resolved measurement of strain or strain-rate, conveying information about the average acoustic field sampled at consistent intervals along the fibre (Lindsey and Martin, 2021). Parameters such as sampling resolution can be modified according to application requirements and cable constraints. In summary, DFOS represents a significant advancement in monitoring techniques that utilize fibre optics, enabling precise and extensive data gathering for various applications, including seismic monitoring, structural health evaluations, and environmental assessments, ultimately contributing to enhanced safety and performance in numerous fields.

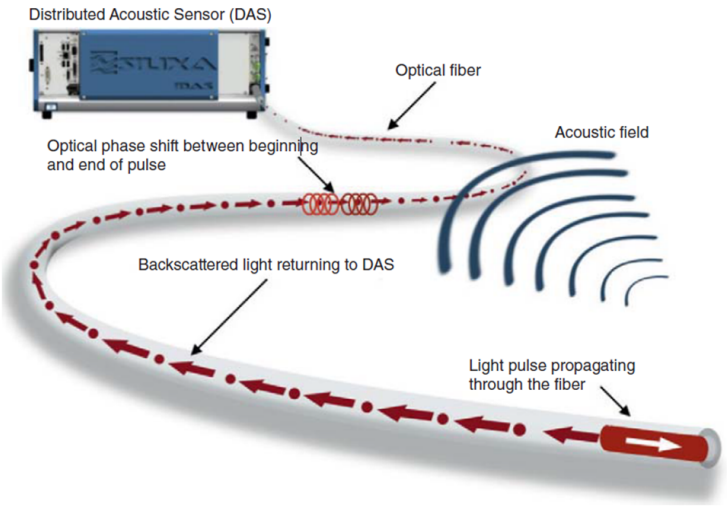

Figure 7.2.5: Principle of operation of the Distributed Acoustic Sensing (DAS) (SPE, 2014).

However, the operational range for acoustic field sensing with these cables can be influenced by several factors, including the distance to the interrogator, fibre attenuation leading to unsatisfactory signal-to-noise ratios, and the necessary sampling rate. The latter requires that each light pulse must allow adequate time for round-trip travel to the designated segment of the cable before the next pulse is emitted.
DAS data provide several advantages as compared to the traditional seismic sensors (i.e., geophones or hydrophones), including higher spatial resolution and higher temporal resolution. They also allow continuous recording along the full length of the cable. A key limitation, however, is that DAS records only a single component, since it is sensitive only to strain changes along the fibre axis (Figure 7.2.6). The response of DAS to P- and S-waves depends on the incidence angle θ between the wavefront and the fibre axis (Willis et al., 2016). As shown in Eqs. 7.1 and 7.2, the P-wave sensitivity is maximal when the wavefront propagates parallel to the fibre, whereas the S-wave response peaks at intermediate angles and vanishes when the propagation is either parallel or perpendicular to the fibre axis (Figure 7.2.6).

$$D_P(\theta) = \cos^2(\theta), \tag{7.1}$$

$$D_S(\theta) = \sin(\theta)\cos(\theta). \tag{7.2}$$

This leads to a weaker response for P-waves arriving nearly perpendicular to the cable, which is what commonly occurs in cross-well seismic surveys where sources and

receivers are placed at comparable depths within two (or more) boreholes. To address this, helically wound cables (HWC) have been developed, in which the fibres are wrapped around the cable core to improve sensitivity and decrease directionality (Kuvshinov, 2016). The Svelvik CO_2 Field Lab provides a valuable testbed to compare measurements from both straight and helically wound fibre-cables, assessing their suitability for cross-well and VSP applications. DAS technology is widely employed for VSP or Cross-hole surveys for energy exploration and has also been successfully used to monitor CO_2 plumes at carbon storage sites (Halladay et al., 2018; Yurikov et al., 2022; Bacci et al., 2017; Koedel et al., 2022).

More complex directionality factor should include the distance of the cable to the source, the frequency of the signal, and the gauge length (GL). The GL is a key parameter in DAS systems as represents the length of optical fibre over which the signal is averaged to obtain the distributed measurement (i.e., the distributed dynamic strain) (Maass et al., 2024). Choosing the GL requires a trade-off between GL length and spatial resolution: a longer GL improves the signal-to-noise ratio but reduces spatial resolution and may introduce distortion; a shorter GL offers higher resolution but lower signal-to-noise and can be adjusted in post-processing if needed. As a general rule, it is recommended to use a spatial sampling interval $\Delta x = GL/2$ to properly register the entire signal (Sayed et al., 2024).

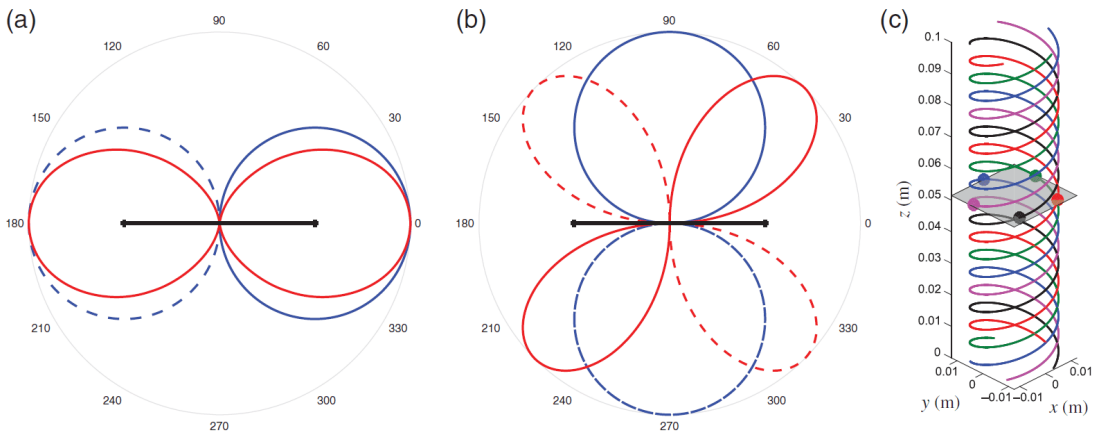

Figure 7.2.6: Source Zhan (2019): (a) Red lines show directional sensitivity of DAS to P wave for a straight fibre section aligned along the horizontal axis (black lines). Solid and dashed lines mean positive and negative, respectively. The directional sensitivity of a conventional seismometer's horizontal component is shown in blue lines as references. (b) Same as (a) but for S waves. (c) A helically wound fibre-optic cable design that can provide better broadside DAS sensitivity than straight fibres. Figure from Lim Chen Ning and Sava (2018).

7.3 Geophysical campaign overview

During our campaign at the SFL, a comprehensive dataset of baseline, injection, and post-injection integrated geophysical surveys was acquired within a time-lapse framework. Identical instrument setups and survey geometries were adopted throughout the campaign to ensure direct comparability between datasets, as all other survey parameters were kept constant. This time-lapse strategy enabled tracking the CO_2 plume evolution over time allowing the identification of potential seismic or radar anomalies that might indicate leakage beyond the expected boundaries or other peculiar behaviours. Two main survey categories were conducted:

1. **Electrical and Electromagnetic (EM) surveys**, including surface Electrical Resistivity Tomography (ERT), Vertical Radar Profile (VRP), surface GPR, and Cross-Well GPR measurements.

2. **Seismic surveys**, consisting of Cross-Well and Vertical Seismic Profile (VSP) acquisitions. All seismic acquisition equipment were provided by SINTEF.

We conducted the seismic surveys in parallel with GPR, using source–receiver geometries that mirrored the radar configurations, in order to compare and integrate the two datasets. However, this chapter focuses exclusively on the seismic data, while GPR results are not discussed as they fall outside the main scope of this thesis.

To give an overview of the seismic campaign, the timeline of the seismic surveys is summarized in Table 7.1. The injection ran for four days, from 30/05 at 16:52 to 03/06 at 16:50. Accordingly, the surveys on 28/05 and 30/05 serve as the pre-injection baseline (BL1 and BL2, respectively). Surveys from 31/05 to 03/06 correspond to the injection period (MO1 to MO4), and the survey on 04/06 represents the post-injection survey (MO5). The last monitoring survey planned for 05/06 was cancelled due to the P-wave source failure. Shot coverage varies day by day, with shallowest and deepest source depths present only on selected monitor dates. See Table 7.1 for detailed schedule. Hydrophones were only deployed during surveys MO3 and MO5.

Table 7.1: Injection phase, source depth, and sensors coverage by survey date. Gray cells indicate data not recorded. HP stands for hydrophones. (* HP spacing 1 m; † HP spacing 2 m).

		28/05 BL1	30/05 BL2	31/05 MO1	01/06 MO2	02/06 MO3	03/06 MO4	04/06 MO5	05/06 MO6
Injection phase	pre-								
	during-								
	post-								
Source depth in M4 [m]	3–34								
	35–45								
	46–55								
Sensors	DAS								
	HP					*		†	

For the cross-well measurements, a borehole P-wave sparker source SBS42 (Geotomographie GmbH) was always deployed in well M4 at various depths to generate seismic waves. These waves were recorded in well M3 using borehole hydrophone strings BHC5 (Geotomographie GmbH), and in all monitoring wells equipped with permanently installed straight and helical Distributed Acoustic Sensing (DAS) fiber-optic cables interrogated by an ASN OptoDAS C01-S interrogator (ASN). The recording parameters for both DAS and geophones are summarized in Table 7.2, while Figure 7.3.1 provides an overview of the survey setting.

Parameter	**Hydrophones**	**DAS**
Channels / Gauge length	2x12 hydrophone string	2.04 m
Spacial sampling	1 m / 2 m	1.02 m
Sampling rate	16 kHz	4 kHz
Recording length	512 ms	10000 ms

Table 7.2: Seismic data recording parameters.

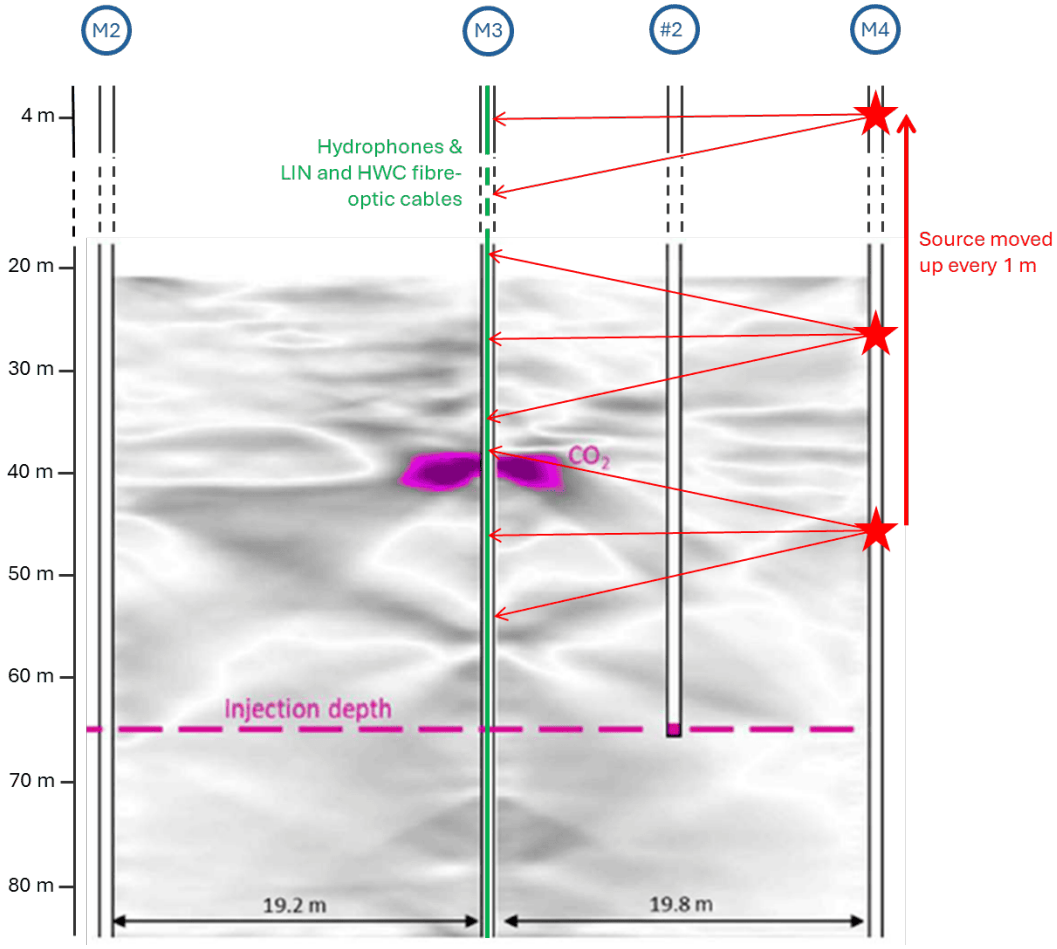

Figure 7.3.1: Cross-well surveying configuration adopted during the seismic surveys employing seismic sources in borehole M4 (red stars), conventional hydrophones in M3, and DAS cables in all the monitoring boreholes (M1-M4) to image the migration of the injected CO_2. The DAS vertical resolution, guided by the gauge length, is about 1.02 m. Cross section in the background from Jordan et al. (2022) shows time-lapse velocity anomalies derived from seismic first-arrival-time tomography. Pink areas indicate 4D low-velocity anomalies corresponding to a velocity decrease of at least 3% (Jordan et al., 2022).

7.3.1 Seismic data: DAS & Hydrophones

Raw DAS data were registered as a continuous signal arriving throughout the length of the cables. Figure 7.3.2 shows an example of seismic signal recorded as a loop along the entire length of both Straight (LIN) and Helical (HWC) fibre-cables. The P-wave source was shot 6-times at 55 m depth in M4, and then the records have been stacked to improve the signal-to-noise ratio (SNR). The direct P-wave is clear down to 0.025 s, while from 0.06 s the S-waves appears. Initial preprocessing on raw DAS data included: (i) Data Extraction of the loops through both straight and helical fibres and their

associated boreholes, (ii) Stacking of repeated shots at the same depth; (iii) Splitting of data into down-going and up-going segments for each borehole; (iiii) Stacking of down-going and up-going segments for each borehole.

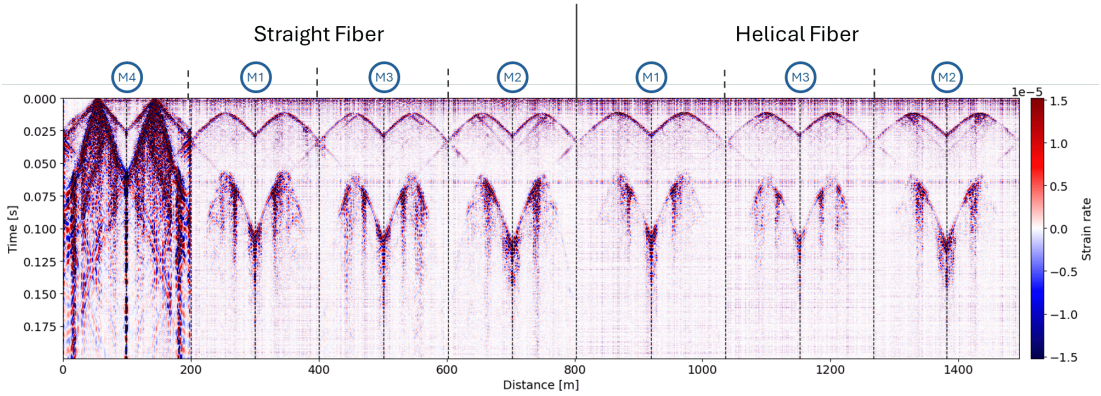

Figure 7.3.2: DAS strain-rate record along the entire fibre-optic cable crossing wells M4-M1-M3-M2 (Straight Fiber sections) and M1–M3–M2 (Helical Fiber sections). Dashed vertical lines and blue labels mark the positions of each well segment.

Linear and Helical DAS performance comparison

Figure 7.3.3 shows a comparison between linear (LIN) and helical (HWC) DAS records in M3, employing P-wave source at 45 m depth. Figure 7.3.3.a shows baseline survey on 28/05/2025 recorded with LIN cable, while Figure 7.3.3.b shows baseline survey on 28/05/22025 recorded with HWC cable. Figure 7.3.3.c and Figure 7.3.3.d show the same but for the monitor survey on 04/06/2025. The comparison between the LIN and HWC measurements reveals several differences in the recording performance of P- and S-wave arrivals. In particular, the P-wave direct arrivals are clearly identifiable in both the cable configurations. However, at depths where the incident wavefronts from the source are nearly perpendicular to the cable orientation, the HWC configuration, as expected, provides enhanced visibility of these arrivals, owing to its improved directional sensitivity. In addition to P-waves, S-waves were also generated and effectively recorded by the DAS configurations from 0.06 s, despite the source being designed to emit primarily P-waves. In this case, the LIN cable exhibits higher S-wave amplitudes than the HWC one, suggesting that the S-wave particle motion is predominantly oriented along the vertical direction, to which the LIN cable is more sensitive.

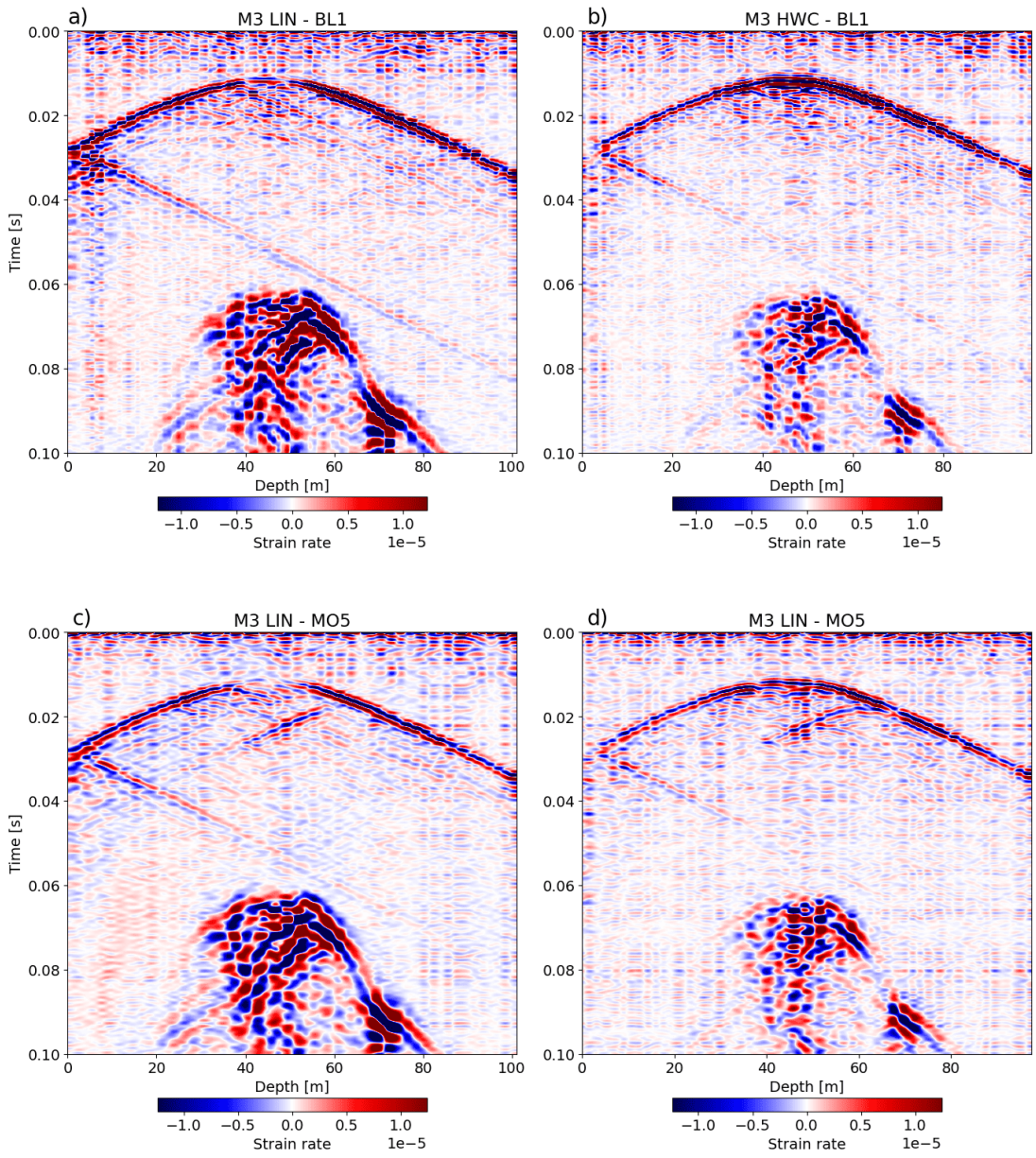

Figure 7.3.3: Comparison between LIN and HWC DAS recordings: (a) baseline survey BL1 acquired with LIN and (b) with HWC, while in (c) the monitor survey MO5 acquired with LIN, and HWC in (d). As indicated by the x-axis, the recordings are collected along the entire length of well M3.

Hydrophones and DAS performance comparison

During the seismic monitoring campaign at the SFL, borehole hydrophones were also deployed to enable a direct comparison with the DAS measurements. The hydrophones were deployed only in well M3. Due to the length of the hydrophone strings (24 m), the hydrophone recordings in both MO3 and MO5 cover depths from 3 to 50 m. Hydrophones spacing varies between MO3 and MO5 surveys (see Table 7.1). Due to logistical constraints, no baseline survey was acquired with the hydrophones.

Figure 7.3.4 presents a comparison between hydrophone recordings (Figure 7.3.4.a-d), and DAS recordings for both LIN (Figure 7.3.4.b-e) and HWC configurations (Figure 7.3.4.c-f), using a P-wave source deployed at 45 m depth in M4. Panels (a-b-c) correspond to the MO3 survey, with hydrophones spaced at 1 m intervals, while panels (d-e-f) show the MO5 survey, where the hydrophone spacing was increased to 2 m. The DAS data were band-pass filtered between 100 and 1700 Hz to attenuate high-frequency noise, whereas the hydrophone data were left unprocessed, except for stacking of the six repeated shots. Moreover, S-waves are detected by DAS, which is more sensitive to shear deformation, whereas they are not expected in the hydrophone recordings.

Some considerations on seismic feature changes in time-lapse DAS data due to CO_2 injection are reported in Section 4.2, Figure 4.2.3. One particular feature consistently observed across all surveys is a strong linear signal, already visible in BL1 and BL2 and highlighted by the black arrows in Figure 7.3.4. This event is preliminarily interpreted as a guided wave, generated at the ground/air interface by the direct wave coming from the deep source, which then propagates downward along the entire length of M3 well as a direct arrival. Its travel-time linearly increases with increasing depth along the well, being recorded from both DAS and hydrophones positioned along the well M3.

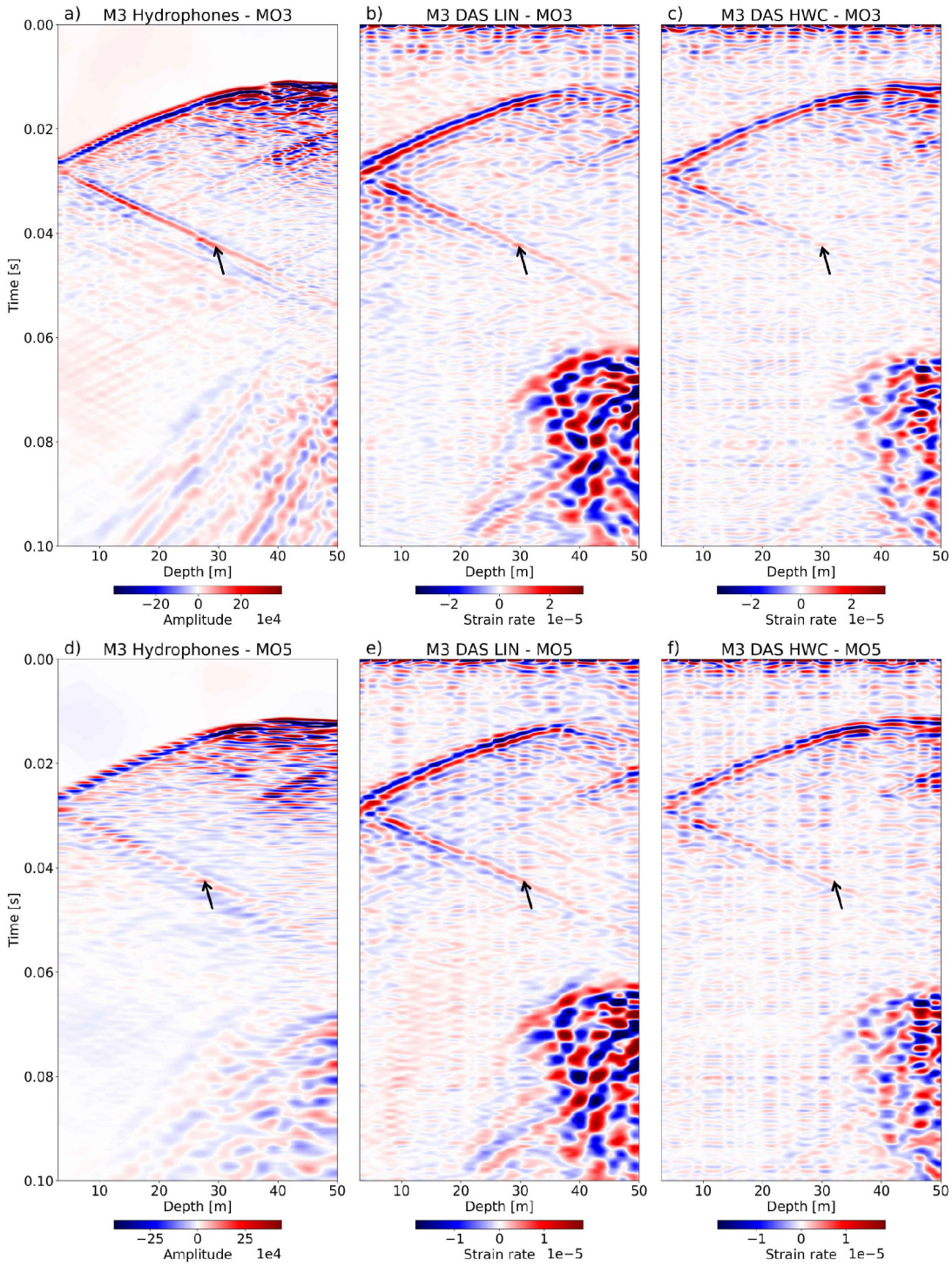

Figure 7.3.4: Comparison between hydrophone and DAS recordings collected in well M3 for MO3 survey (Panels a-b-c) with hydrophones spacing of 1 m, and MO5 survey (Panels d-e-f) with hydrophone spacing of 2 m. In both cases, the DAS data are shown for the LIN and HWC cable configurations. The P-wave source was positioned at 45 m depth. DAS recordings were cropped for plot purpose between same depth range covered by hydrophones string in well M3.

7.4 Conclusions

The active seismic monitoring campaign conducted at the Svelvik CO_2 Field Lab successfully demonstrated the feasibility of integrating Distributed Acoustic Sensing (DAS) and conventional hydrophone surveys for near-surface CO_2 monitoring. The time-lapse acquisition strategy allowed for a direct comparison between the baseline and injection/post-injection phases, ensured by the consistent survey geometry. The permanent DAS installation within the casing provided high repeatability of the measurements, ensuring that observed changes were not related to variations in instrumentation or sensors geometries.

The DAS system, installed in both straight (LIN) and helically wound (HWC) configurations, proved capable of capturing high-quality seismic data with accurate spatial sampling and extensive depth coverage. The comparison between LIN and HWC fibres confirmed the higher sensitivity to P-waves of the helical geometry due to the nearly perpendicular incidence of the wavefront, while the linear fibre provided stronger responses to S-waves, consistent with its axial sensitivity. The use of hydrophones allowed benchmarking of the DAS performance. The results confirmed that the DAS shows greater sensitivity to shear deformation, while the hydrophones provide clearer arrivals of P-waves.

Overall, the campaign validated the operational readiness of the DAS system for repeated, cost-effective time-lapse surveys at CO_2 storage sites. The DAS data proved highly suitable for CO_2 monitoring, as also demonstrated in Section 4.2, where the developed framework applied to the DAS dataset yielded promising results. These findings confirm the potential of DAS as a reliable and sensitive tool for detecting and tracking CO_2 migration. The datasets acquired at the Svelvik CO_2 Field Lab will therefore serve as a valuable benchmark for testing the methodologies developed in this thesis, as well as for developing and validating new approaches aimed at quantitative assessment of CO_2 migration and leakage phenomena.

Bibliography

ASN. 2025. ASN - Alcatel Submarine Networks. https://www.asn.com/fiber-sensing/. Accessed on 16 Sep 2025.

Vicente Oropeza Bacci, Simon O'Brien, Jordan Frank, and Mark Anderson. 2017. Using a walk-away DAS time-lapse VSP for CO2 plume monitoring at the Quest CCS Project. *CSEG Recorder* 42, 3 (2017), 18–21. https://csegrecorder.com/articles/view/using-a-walk-away-das-time-lapse-vsp-for-co2-sub-plume-monitoring

Peder Eliasson, Pierre Cerasi, Anouar Romdhane, Jim White, Cornelia Schmidt-Hattenberger, Stefan Carpentier, Alv-Arne Grimstad, and Ane Elisabet Lothe. 2018. Pressure control and conformance management for safe and efficient CO2 storage–an overview of the Pre-ACT project. In *14th Greenhouse Gas Control Technologies Conference Melbourne*. SSRN Electronic Journal, Online, 21–26. https://doi.org/10.2139/ssrn.3365876

Geotomographie GmbH. 2025. Geotomographie website: Seismic tomography equipment. https://geotomographie.de/equipment/. Accessed on 16 Sep 2025.

A. Halladay, V. Orpeza Bacci, S. O'Brien, and K. Hindriks. 2018. Results From The Second Monitor DAS VSP At Quest CCS. *EAGE* 2018, 1 (2018), 1–5. https://doi.org/10.3997/2214-4609.201802981

Arthur Hartog. 2017. *An Introduction to Distributed Optical Fibre Sensors*. CRC Press (Taylor and Francis), Boca Raton. https://doi.org/10.1201/9781315119014

Michael Jordan, Peder Eliasson, Wolfgang Weinzierl, Cathrine Ringstad, Martin Raphaug, Alv-Arne Grimstad, and Cornelia Schmidt-Hattenberger. 2022. Learnings from the Pre-ACT campaign at the Svelvik CO2 Field Lab, In GHGT-16 conference. *Available at SSRN: https://ssrn.com/abstract=4286508* 1, 1–8. https://doi.org/10.2139/ssrn.4286508

Uta Koedel, Anna Stork, Peter James Thomas, Wen Zhou, Ari David, Hansruedi Maurer, Hagen Soeding, and Thomas Fechner. 2022. Seismic Cross-hole Surveying with Conventional Seismic and Distributed Acoustic Sensing (DAS) at the Svelvik Test-site. In *Proceedings of the 16th Greenhouse Gas Control Technologies Conference (GHGT-16)*. GHGT, Lyon, France, 23–24. https://doi.org/10.2139/ssrn.4274670

B.N. Kuvshinov. 2016. Interaction of helically wound fibre-optic cables with plane seismic waves. *Geophysical Prospecting* 64, 3 (2016), 671–688. https://doi.org/10.1111/1365-2478.12303

Ivan Lim Chen Ning and Paul Sava. 2018. High-resolution multi-component distributed acoustic sensing. *Geophysical Prospecting* 66, 6 (2018), 1111–1122. https://doi.org/10.1111/1365-2478.12634

Nathaniel J. Lindsey and Eileen R. Martin. 2021. Fiber-Optic Seismology. *Annual Review of Earth and Planetary Sciences* 49, Volume 49, 2021 (2021), 309–336. https://doi.org/10.1146/annurev-earth-072420-065213

Regina Maass, Sven Schippkus, Céline Hadziioannou, Benjamin Schwarz, Philippe Jousset, and Charlotte Krawczyk. 2024. Stacking of Distributed Dynamic Strain Reveals Link Between Seismic Velocity Changes and the 2020 Unrest in Reykjanes. *Journal of Geophysical Research: Solid Earth* 129, 6 (2024), e2023JB028320. https://doi.org/10.1029/2023JB028320

Ying Mei, Xiaojun Yang, Rui Du, Yisong Zhang, Ruiyan Li, and Xuechao Tian. 2024. Structural deformation monitoring based on distributed fiber optic sensors. In *Advanced Fiber Laser Conference (AFL2023)*, Pu Zhou (Ed.), Vol. 13104. International Society for Optics and Photonics, SPIE, Shenzhen, 131046Q. https://doi.org/10.1117/12.3023848

NTNU (Ed.). 2018. *Modelling Medium- Depth CO2 Injection at the Svelvik CO2 Field Laboratory in Norway*. NTNU, Trondheim, Norway. https://ntnuopen.ntnu.no/ntnu-xmlui/handle/11250/2562292 Accessed: 2025-10-03.

Ali Sayed, Ran Bachrach, Anna Titova, and Gabriele Busanello. 2024. Research note: Choosing gauge length for surface distributed acoustic sensing. *Geophysical Prospecting* 72, 8 (2024), 2893–2901. https://doi.org/10.1111/1365-2478.13555

SINTEF. 2024. ECCSEL Svelvik CO_2 Field Lab website. https://www.sintef.no/projectweb/svelvik-co2-field-lab/. Accessed 16 Sep 2025.

SPE (Ed.). 2014. *Borehole Flow Monitoring using a Non-intrusive Passive Distributed Acoustic Sensing (DAS)*. SPE Annual Technical Conference and Exhibition, Vol. SPE Annual Technical Conference and Exhibition. Amsterdam, The Netherlands. https://doi.org/10.2118/170844-MS

Mark Willis, DavidBarfoot, AndreasEllmauthaler, XiangWu, OscarBarrios, CemalErdemir, SimonShaw, and DanQuinn. 2016. Quantitative quality of distributed acoustic sensing vertical seismic profile data. *The Leading Edge* 35, 7 (2016), 605–609. https://doi.org/10.1190/tle35070605.1

Andreas Wuestefeld and Wolfgang Weinzierl. 2020. Design considerations for using Distributed Acoustic Sensing for cross-well seismics: A case study for CO2 storage. *Geophysical Prospecting* 68, 6 (2020), 1893–1905. https://doi.org/10.1111/1365-2478.12965

Alexey Yurikov, Konstantin Tertyshnikov, Sinem Yavuz, Pavel Shashkin, Roman Isaenkov, Evgenii Sidenko, Stanislav Glubokovskikh, Paul Barraclough, and Roman Pevzner. 2022. Seismic monitoring of CO2 geosequestration using multi-well 4D DAS VSP: Stage 3 of the CO2CRC Otway project. *International Journal of Greenhouse Gas Control* 119 (2022), 103726. https://doi.org/10.1016/j.ijggc.2022.103726

Zhongwen Zhan. 2019. Distributed Acoustic Sensing Turns Fiber-Optic Cables into Sensitive Seismic Antennas. *Seismological Research Letters* 91, 1 (12 2019), 1–15. https://doi.org/10.1785/0220190112

Chapter 8

Conclusions

This thesis has addressed the development and application of innovative geophysical methodologies for the monitoring of underground geological storage sites, with a particular focus on carbon-dioxide and hydrogen. The overarching objective was to improve the characterization and quantification of subsurface processes occurring during and after fluid injection and storage, by combining the predictive power of physics-based approaches with the efficiency and adaptability of data-driven methods. Throughout the different chapters, this research has explored how seismic monitoring, rock-physics modelling, and deep learning analyses can be integrated into a coherent framework capable of providing more reliable and interpretable insights into subsurface storage systems.

The work first demonstrated the potential of data-driven strategies for reservoir monitoring, presenting a deep learning workflow based on convolutional neural networks designed to estimate the spatial distribution of injected CO_2 plumes from time-lapse seismic data (Pantaleo et al., 2023, 2024a). By enhancing the network with multi-scale feature extraction using two-dimensional continuous wavelet transforms, the predictions achieved both improved accuracy and interpretability, underlining the role of deep learning in accelerating plume characterization and reducing the reliance on manual analysis. In parallel, attention was devoted to the design of cost-effective monitoring strategies that could reduce the operational burden of repeated seismic acquisitions. Leveraging pre-trained ResNet models arranged in a Siamese architecture, combined with UMAP for dimensionality reduction and k-nearest neighbours for classification, a framework was proposed that automatically distinguishes between baseline and monitor surveys (Pantaleo and Pipan, 2025a,b). Application to Distributed Acoustic Sensing (DAS) cross-well data from the Svelvik CO_2 Field Lab confirmed the ability of this approach to detect anomalies with fewer repeated geophysical surveys, thereby reducing

costs without sacrificing monitoring reliability and accuracy.

Beyond purely data-driven techniques, this thesis also introduced a novel inversion strategy in which full-waveform inversion is parametrized directly in terms of petrophysical variables linked to elastic parameters through rock-physics models (Pantaleo et al., 2024b; Pantaleo and Pipan, 2025d). Leveraging automatic differentiation, this rock-physics–constrained FWI formulation efficiently computes the gradients required for the inversion, helping mitigate the cross-talk between elastic parameters by focusing the inversion on petrophysical parameters directly related to fluid saturation. Applications to underground gas storage scenarios demonstrated that this approach enhances sensitivity to gas injection and provides a more physically interpretable description of subsurface changes than conventional elastic inversion. Complementing this, the thesis also investigated the impact of patchy gas saturation on seismic dispersion and attenuation, showing through rock-physics modelling that heterogeneous distributions of CO_2 and hydrogen in porous media can produce significant frequency-dependent effects (Pantaleo and Pipan, 2025c). These findings remark the importance of incorporating mesoscopic fluid-flow mechanisms into monitoring and inversion workflows to capture realistic seismic responses.

Overall, the findings of this thesis underscore the necessity of integrating rock-physics theory, seismic modelling, and machine learning techniques to achieve robust monitoring of geological storage. By combining physics-driven and data-driven methods, it is possible to achieve higher-resolution, more interpretable, and more cost-effective monitoring solutions. The research highlights that such hybrid and integrated approaches improve the reliability of time-lapse seismic interpretation, reduce acquisition and processing costs through the use of intelligent representations, and strengthen the physical interpretability of inversion results by constraining them within specific petrophysical frameworks. At the same time, the work demonstrates that methodologies initially designed for CO_2 storage can be effectively extended to underground hydrogen storage and even to the exploration of naturally occurring hydrogen accumulations, thereby broadening their relevance within the wider energy transition.

Despite these advances, several open challenges remain for future investigation. Data-driven methods need to be scaled up to larger and more diverse datasets in order to achieve the level of generalization required for routine application to field data. Integration of multi-physics monitoring techniques, including seismic, electromagnetic, gravity, and geochemical surveys, represents another key direction to reduce uncertainties and provide more comprehensive assessments of the storage capabilities. Advances in high-performance computing and differentiable programming are expected to play

a central role in enabling real-time monitoring and decision support, which are critical steps for operational risk management. Finally, specific attention must be paid to hydrogen storage, where cyclic injection, weaker seismic contrasts, and chemical or microbial reactivity pose unique additional challenges that require dedicated monitoring workflows research.

In conclusion, this thesis has contributed to the development and validation of a new generation of geophysical monitoring methodologies that combine the interpretability and robustness of physics-based modelling with the efficiency and adaptability of machine learning. By advancing our ability to image, quantify, and interpret the dynamic behaviour of injected fluids in the subsurface, the work supports the safe and large-scale deployment of geological storage solutions. Such advances reinforce the crucial role of geosciences in enabling a secure and sustainable low-carbon energy future, where underground storage of CO_2 and hydrogen will play a central role in both climate change mitigation and energy system flexibility.

Bibliography

Giovanni Pantaleo, Attilio Molossi, and Michele Pipan. 2023. Application of Deep Learning in the Estimation of CO_2 Saturation Maps. In *EAGE PeGe2023 Conference Proceedings*. European Association of Geoscientists & Engineers, EAGE, Porto, Portugal, 1–5. https://doi.org/10.3997/2214-4609.202335061

Giovanni Pantaleo, Attilio Molossi, and Michele Pipan. 2024a. Estimation of CO_2 Saturation Maps from Synthetic Seismic Data Using a Deep-Learning Method with a Multi-Scale Approach. *Geoenergy* 2, 1 (2024), 1–13. https://doi.org/10.1144/geoenergy2023-057

Giovanni Pantaleo and Michele Pipan. 2025a. Assessment of a Deep Learning Framework for Time-Lapse Seismic Monitoring. In *EGU General Assembly 2025*. EGU, European Geosciences Union, Vienna, Austria, 1–1. https://doi.org/10.5194/egusphere-egu25-882 EGU25-882; 27 Apr–2 May 2025.

Giovanni Pantaleo and Michele Pipan. 2025b. Enhancing Early CO_2 Leakage Detection Using Pre-Trained Deep Learning Models. In *EAGE World CCUS Conference 2025 Conference Proceedings*, Vol. 2025. European Association of Geoscientists & Engineers, EAGE, Bergen, Norway, 1–5. DOI to be assigned. Available at https://www.earthdoc.org/content/papers/10.3997/2214-4609.202522134.

Giovanni Pantaleo and Michele Pipan. 2025c. Frequency-Dependent Seismic Analysis for Hydrogen Storage in Porous Media. In *International Meeting for Applied Geoscience and Energy (IMAGE25)*. SEG, Houston, TX, 1–5. DOI to be assigned. Available at https://imageevent.aapg.org/portals/26/abstracts/2025/4316783.pdf.

Giovanni Pantaleo and Michele Pipan. 2025d. Optimization of Rock-Physics Inversion via FWI and Deep Learning Tools. In *43rd National Conference of the GNGTS*. GNGTS, Bologna, Italy, 1–5. https://gngts.ogs.it/

Giovanni Pantaleo, Giacomo Roncoroni, and Michele Pipan. 2024b. Monitoring Elastic Parameters Changes During Underground Hydrogen Storage Using Rock Physics Parametrized FWI. In *EAGE GET24 Conference Proceedings*. European Association of Geoscientists & Engineers, EAGE, Rotterdam, The Netherlands, 1–5. https://doi.org/10.3997/2214-4609.202421200